Flexural-Torsional Buckling of Double Angle Joist and Joist Girder Chords

Edward J. Sippel, Graduate Research Assistant[1]

Ronald D. Ziemian, Professor [2]

Hannah B. Blum, Assistant Professor[1]

[1] Department of Civil and Environmental Engineering

University of Wisconsin - Madison

[2] Department of Civil and Environmental Engineering

Bucknell University

August 2022

Executive Summary

Open-web steel joists are often fabricated from components with relatively high slenderness ratios to efficiently support loading. As a result, joists are susceptible to buckling instabilities in the webs and the double angle chords. The current SJI design provisions for steel joists require the consideration of flexural buckling but exclude any mention of flexural-torsional buckling modes for double angle members, which differs from AISC's design provisions. This study evaluates the underlying SJI assumption that flexural-torsional buckling can be safely neglected in joist design. This report summarizes the results of the theoretical elastic and inelastic buckling behavior of double angles and the finite element modeling of complete joists and joist girders as well as isolated chord segments.

A theoretical buckling investigation was completed to identify double angle cross sections that appeared to be susceptible to flexural-torsional buckling. The elastic buckling analysis identified instances where flexural-torsional buckling behavior was expected to control for a wide slenderness range at low stresses. Based on the current AISC design provisions, this result identified multiple sections susceptible to flexural-torsional buckling. However, this study considered the methodology behind AISC's exemption for single angle flexural-torsional buckling to determine if the same behavior was observed in double angles. While accounting for the observed shear stiffness in buckled columns and nominal torsional stiffness, multiple double angle cross sections, specifically compact geometries, were controlled by flexural buckling. Nevertheless, numerous slender double angle cross sections were still found to theoretically exhibit flexural-torsional buckling. The historical performance of joists indicated that double angle chords are adequately designed by the current SJI Specifications;

therefore, finite element modeling was completed to verify whether or not flexural-torsional buckling was observed.

Finite element models of the joist and joist girders were created to evaluate the behavior of double angle chords including continuity and web connection effects. The joist modeling procedure was validated against previously reported full steel joists experimental results including web-to-chord connection variations, support and bracing conditions, and loading application. These validation models were able to accurately predict the bending stiffness of the joist and the different buckling failure modes of the webs. The main study evaluated 18 different chord sizes, which were split among one joist and two joist girder models, to observe a range of buckling behavior. It was observed that the inelastic buckling load regularly exceeded the compression member capacity calculated using the SJI design provisions. The double angle chord captured a significant amount of twist of the individual angles; however, global flexural-torsional buckling was not found to be a prevalent factor.

Additional finite element modeling was used to verify the observations from the full joist models. Isolated double angle chord segments were evaluated for the same nominal effective length included in the full joist model for both a pinned and fixed end condition. The elastic buckling results highlighted the importance of the local buckling of individual angles between connection points and a global flexural-torsional response greater than the assumed elastic behavior. The inelastic buckling analysis regularly captured local buckling of the individual chord angles leading to a flexural buckling failure. Similar to the full joist models, the isolated chord investigation observed compression member capacities greater than the flexural buckling limit and overly conservative predictions when considering flexural-torsional buckling.

The increased buckling capacity was attributed to an increased torsional stiffness of the composite section, which is typically not considered in design. A variable amount of composite behavior was observed through finite element modeling of cantilevered double angle chords subjected to a discrete end rotation. The addition of even a single tie at midspan was found to have a significant

increase in stiffness, which continued to linearly increase proportional to the spacing between ties. A brief parametric study was completed to isolate the underlying behavior using parallel plates instead of the more complex angle cross sections. The increased torsional stiffness was attributed to a composite warping response. The transfer of torsion through the tie connection allowed equal and opposite bending moments to develop in the chord, similar to the forces carried by the flanges of an I-beams in torsion. If the appropriate forces could not be transmitted through the tie connections, minimal increases in torsional stiffness were observed in the composite section.

The results of this study indicate that the SJI approach of only considering flexural buckling with local buckling reductions seems to be an appropriate design approach for joist chords. The joist chord connections result in an increased torsional stiffness, which is complemented by increased torsional restraint due to continuity and the web members. These factors cause global flexural-torsional buckling behavior to be less significant than the current AISC Specification design approach. The individual twisting of angles cannot be eliminated, but this behavior is accounted for in the local buckling reductions. Neglecting flexural-torsional buckling in design of double angles relies on providing the appropriate chord-to-chord connections to ensure the composite response and incorporating adequate local buckling reductions. Further details are provided in the Recommendation section of the report.

Contents

List of Figures

List of Tables

1. Introduction

Open-web steel joist and joist girders are economical steel structures that can be used in a variety of applications. The efficient use of material often results in the use of slender elements that are susceptible to buckling under compression. The current Steel Joist Institute (SJI) Standard Specification for K-Series, LH-Series, DLH-Series Open Web Steel Joists and for Joist Girders (SJI 100-2020) [1] requires that the design capacity of hot-rolled sections account for flexural and local buckling effects. These requirements contrast with the current provisions of the American Institute of Steel Construction (AISC) Specification for Structural Steel Buildings [2] which additionally require consideration of flexural-torsional buckling. For non-doubly symmetric members such as angles and double angles, flexural-torsional buckling can often lead to significantly lower design capacities at short lengths. A study on double angle buckling by Simpson Gumpertz & Heger Inc. [3] noted that the flexural-torsional behavior required by the AISC Specification produced overly conservative results at low slenderness ratios while the SJI Specification resulted in somewhat unconservative capacities for some geometries. Since that study occurred, modifications have been made to provisions regarding local buckling reductions and modified slenderness of built-up members; however, the major global buckling discrepancy between the two Specifications has not been addressed. This report summarizes an investigation into the behavior of double angles used for joist and joist girder chords including the theoretical response and a numerical parametric study of full-scale joists and joist chord segments. The joist modeling validation is also discussed and final recommendations are presented.

2. Theoretical Buckling Behavior

Steel members in compression typically fail due to buckling, which is a geometric instability caused by a member reaching a limiting capacity where additional load cannot be supported without excessive deformations. In an perfectly-straight elastic member, buckling failure is associated with a bifurcation point at which a member would suddenly move as depicted in Fig. 2.1. However, realistic members include some imperfections from residual stresses, cross-section variations, or an initial misalignment that cause the member to deflect prior to the ultimate load. At lower stresses, the imperfect response can be largely elastic and reach similar capacities as the perfect column, but at high stress levels yielding occurs, which reduces the maximum load the column can support. Buckling instability covers a range of behaviors that are affected by the cross-section properties. The following sections define the various buckling modes and how they are accounted for in design according to the SJI and AISC Specifications.

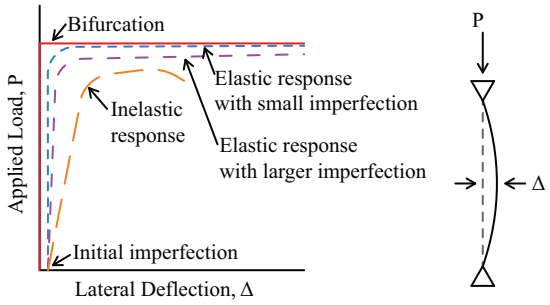

Figure 2.1: Typical buckling behavior

2.1. Buckling Modes

The foundation of compression member design is elastic buckling that incorporates the global limits of flexural, torsional, or combined flexural-torsional buckling and local effects. The critical flexural buckling stress about the x-axis, f_x, and about the y-axis, f_y, are calculated by Eq. 2.1 and Eq. 2.2, respectively. Torsional buckling occurs due to twisting about the shear center with a critical torsional buckling stress, f_z, determined by Eq. 2.3;

$$f_x = \frac{\pi^2 E}{(L/r_x)^2} \tag{2.1}$$

$$f_y = \frac{\pi^2 E}{\left(L/r_y\right)^2} \tag{2.2}$$

$$f_z = \frac{GJ + \pi^2 E C_w / L^2}{r_0^2 A} \tag{2.3}$$

where E is the modulus of elasticity, G is the shear modulus, $r_x = \sqrt{I_x/A}$ and $r_y = \sqrt{I_y/A}$ are the radii of gyration about the x- and y- axes, I_x and I_y are the moments of inertia about the principal x- and the y-axes, A is the cross-sectional area, J is the torsion constant, C_w is the warping constant, L is the unbraced length, and r_0 is the polar radius of gyration about the shear center which is calculated by Eq. 2.4;

$$r_0^2 = r_x^2 + r_y^2 + x_0^2 + y_0^2 \tag{2.4}$$

where (x_0, y_0) are the coordinates of the shear center relative to the centroid.

In an arbitrary section, the flexural and torsional buckling modes can interact which introduces flexural-torsional buckling. This interaction is defined by Eq. 2.5 where the three roots

of the equation are the critical buckling stresses, f_{el} [4]. When the shear center and centroid are coincident, Eq. 2.5 reduces to uncoupled flexural and torsional buckling modes with the minimum value controlling the behavior. When the shear center and centroid are not coincident, which occurs in double angle cross sections, the interaction of buckling modes results in a new lower buckling stress.

$$(f_{el} - f_x)\left(f_{el} - f_y\right)(f_{el} - f_z) - f_{el}^2\left(f_{el} - f_y\right)\frac{x_0^2}{r_0^2} - f_{el}^2\left(f_{el} - f_x\right)\frac{y_0^2}{r_0^2} = 0 \tag{2.5}$$

Slender cross- section elements experience local buckling, which is incorporated into hot-rolled member design based on the plate buckling stress, f_L , given by Eq. 2.6;

$$f_L = \frac{0.425\pi^2 E}{12(1-\nu^2)}\left(\frac{t}{b}\right)^2 \tag{2.6}$$

where ν is the Poisson's ratio, t is the thickness of the angle leg, and b is the leg width. For unstiffened elements such as the legs of single and double angles, the failure mode assumes uniform one-way compression on a pin supported plate with one edge supported and the other unsupported.

The above relationships can be used to compare the elastic response for various cross sections. Only equal-leg double angles spaced with one inch between the vertical legs as shown in Fig. 2.2 were considered. Table 2.1 summarizes the chord double angle dimensions evaluated for this study, which are representative of joist designs per SJI. The investigation accounts for equal effective lengths for all buckling modes and a C_w equal to twice a single angle, which will be discussed in greater detail in Section 2.4. As shown in Fig. 2.3 and Fig. 2.4, flexural-torsional response controls the buckling behavior of double angles at shorter lengths which transitions into a flexural buckling limit state at longer lengths. This pattern can be seen for all cross sections in Appendix B. Despite this trend, the elastic response alone is not enough to determine the importance of flexural-torsional

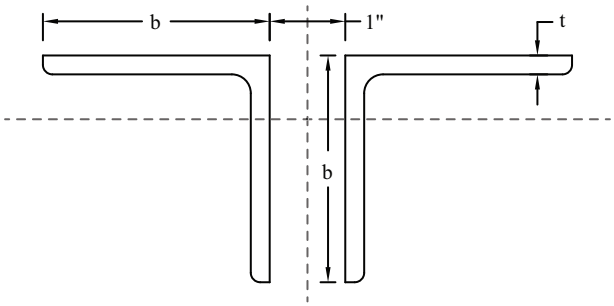

Figure 2.2: Typical double angle chord geometry

Table 2.1: Angle dimensions considered

Leg (in)	Thickness (in)								
1.25	0.109	0.115	0.125	0.188					
1.5	0.109	0.115	0.123	0.137	0.141	0.155	0.17	0.188	0.25
1.75	0.115	0.125	0.143	0.155	0.17	0.188	0.25		
2	0.125	0.143	0.156	0.163	0.176	0.188	0.205	0.216	0.23
2 (cont.)	0.248	0.25	0.281	0.313					
2.5	0.188	0.212	0.23	0.25	0.28	0.313			
3	0.188	0.227	0.25	0.281	0.29	0.313	0.375		
3.5	0.287	0.313	0.344	0.375					
4	0.25	0.313	0.344	0.375	0.438	0.5			
5	0.438	0.5							
6	0.438	0.5	0.563	0.625	0.75	0.875	1		
8	0.5	0.546	0.625	0.75	1	1.125			

buckling in design as the elastic buckling strength is regularly greater than the yield stress making inelastic behavior a critical factor.

2.2. Inelastic Flexural Buckling

Building upon the elastic buckling response, inelastic buckling design per both the SJI Specification [1] and the AISC Specification [2] utilizes a tangential buckling approach based on flexural buckling behavior to convert the limiting elastic buckling stress, F_e, to the critical buckling stress, F_{cr}. At low compressive buckling stresses, the behavior remains largely elastic and can be determined using Eq. 2.7. When F_e exceeds $\frac{4}{9}$ of the yield stress, F_y, inelastic buckling behavior

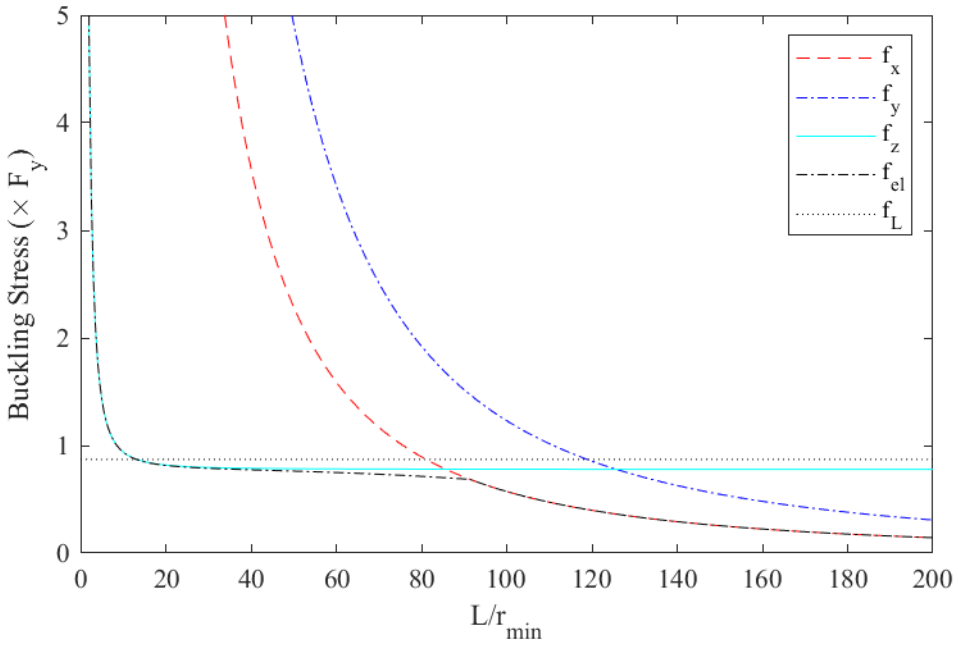

Figure 2.3: Elastic buckling of 2-L8"x8"x0.5" with significant flexural-torsional behavior

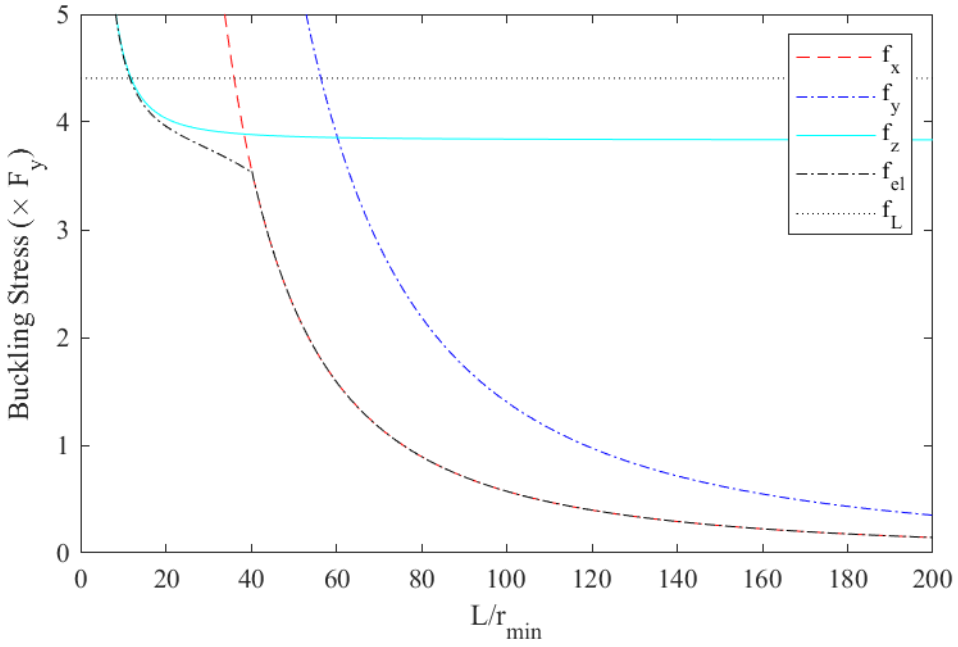

Figure 2.4: Elastic buckling of 2-L8"x8"x1.125" with minimal flexural-torsional behavior

controls and is represented by Eq. 2.8.

$$F_{cr} = 0.877F_e \quad \text{for } \frac{F_y}{F_e} > 2.25 \tag{2.7}$$

$$F_{cr} = \left(0.658^{F_y/F_e}\right) F_y \quad \text{for } \frac{F_y}{F_e} \leq 2.25 \tag{2.8}$$

An alternative method of presenting this relationship would be to use a reduction factor, τ, to directly calculate the tangential buckling response by modifying E [5]. Rearranging Eqs. 2.7 and 2.8, the F_{cr} can instead be defined as the limiting elastic buckling capacity times τ given by Eq. 2.9.

$$\tau = \begin{cases} 0.877 & \text{if } \frac{F_{cr}}{F_y} \leq 0.877/2.25 \\ \frac{1}{\ln(0.658)} \frac{F_{cr}}{F_y} \ln\left(\frac{F_{cr}}{F_y}\right) & \text{otherwise} \end{cases} \tag{2.9}$$

Lastly, a modification factor that accounts for strength reduction due to local buckling is included. The current SJI Specification and the prior AISC Specification [6] utilized a single slenderness reduction factor, Q, according to Eq. 2.10;

$$Q = \begin{cases} 1.0 & \text{if } \lambda_e \leq 0.45\sqrt{\frac{E}{F_y}} \\ 1.34 - 0.76\lambda_e\sqrt{\frac{F_y}{E}} & \text{if } 0.45\sqrt{\frac{E}{F_y}} < \lambda_e \leq 0.91\sqrt{\frac{E}{F_y}} \\ 0.53\frac{E}{F_y}\left(\frac{1}{\lambda_e}\right)^2 & \text{if } 0.91\sqrt{\frac{E}{F_y}} < \lambda_e \end{cases} \tag{2.10}$$

where λ_e is the slenderness of the angle leg, b/t.

For double angles, the single lowest Q factor associated with any unstiffened element is used to uniformly reduce the capacity of the entire section. This local buckling limitation is incorporated by replacing F_y in Eq. 2.7, 2.8, and 2.9 with QF_y and the remaining calculations are completed as normal. The 2016 AISC Specification introduced a different approach requiring the original F_{cr}

to act over an effective area of the cross section based on plate buckling. While the different local buckling provisions alter the final capacities, the impact of this variation is not discussed in further detail in this report because the focus of this study is on the current SJI requirements.

2.3. Inelastic Flexural-Torsional Buckling

The design buckling calculations have been limited to flexural buckling since it is the foundation of compression member design. The current SJI Specification allows for the effects of flexural-torsional buckling to be neglected for double and single angles, and, as a result, only flexural buckling need be considered. The AISC Specification incorporates a similar exception for single angles, but requires the consideration of flexural-torsional buckling for double angles. The capacity is conservatively calculated by using the minimum elastic buckling response considering flexural and flexural-torsional buckling modes using Eq. 2.5 and applies the same flexural buckling reduction shown in Eq. 2.7 and 2.8. However, this approach does not account for the strength associated with the shear stiffness as identified in previous testing and numerical studies [5, 7, 8, 9]. Unlike the softening longitudinal behavior, shear stiffness has been found to remain effectively constant until full yield of the section, which can result in higher and more realistic torsional buckling capacities. The inelastic shear and longitudinal responses can be combined by modifying Eq. 2.5 with the appropriate tangential stiffness reduction factor, τ for the longitudinal behavior and τ_G for the shear behavior, resulting in Eq. 2.11 where the minimum solution is the inelastic critical buckling stress, f_{in}. Previous work by Galambos [5] determined that accounting for the increased stiffness meant flexural-torsional buckling was unlikely to control the design of single angles when accounting for the interaction of flexural buckling and local buckling. That study also determined that some double angles were susceptible to flexural-torsional buckling and recommended continuing to consider the

relevant provisions for the design of double angles.

$$\begin{aligned}(f_{in} - f_x\tau)\left(f_{in} - f_y\tau\right)\left(f_{in} - \frac{\tau_G GJ + \tau\pi^2 EC_w/L^2}{r_0^2}\right) \\ -f_{in}^2\left(f_{in} - f_y\tau\right)\frac{x_0^2}{r_0^2} - f_{in}^2\left(f_{in} - f_x\tau\right)\frac{y_0^2}{r_0^2} = 0\end{aligned} \tag{2.11}$$

2.4. Inelastic Buckling Study

Galambos's [5] recommendation for double angles covered a wide array of geometries including both unequal- and equal-leg sections, multiple spacings between the vertical legs of the angles, and different connection methods. For this study, a more limited configuration was considered to investigate the impact of flexural-torsional behavior in joist and joist girder chords. Only equal-leg double angles spaced with one inch between the vertical legs were considered. Details of the geometry and representative sizes are provided in Fig. 2.2 and Table 2.1 above.

This flexural-torsional buckling study included variations in the shear stiffness via two values for τ_G and in the warping stiffness of double angles via three values for C_w. In line with previous research [5, 8, 10], an upper limit of $\tau_G = 1.0$ was used to capture the full shear stiffness of the section as minimal reduction was observed. A reduction was estimated as $\tau_G = 0.877$ to account for imperfections and residual stresses based on critical elastic flexural buckling. The minimum value for C_w was defined based on AISC's [2] conservative design recommendation that C_w of double angles can be taken as 0 and the shear center, S_{low}, is positioned along the axis of symmetry at the middle of the horizontal flanges similar to a tee section as shown in Fig. 2.5. An alternative conservative recommendation by the Canadian Institute of Steel Construction [11] uses the same shear center position but references a C_w equal to twice that of the single angle. Limited information was

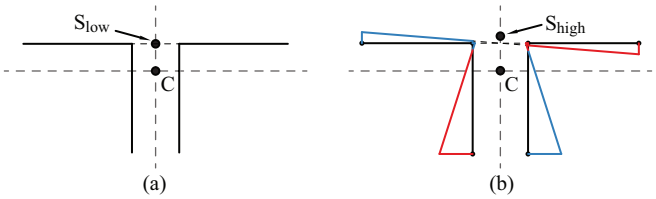

Figure 2.5: Assumed double angle warping behavior (a) AISC/CISC (b) Est. upper bound

available on the composite twist response of double angles; therefore, an estimate of a fully composite behavior was determined using a thin-walled approximation by assuming a connection between the angle heels with no thickness which resulted in a new shear center, S_{high}, and a significantly increased C_w, by more than a factor of 100 in some configurations. These three C_w values were considered to investigate the impact of warping stiffness and are identified as $C_w = 0$, Low C_w, and High C_w, respectively.

For each alternative C_w, four inelastic buckling curves were determined for lengths up to 200 times the minimum radius of gyration. The upper bound was determined considering flexural buckling effects in line with the current SJI Specification and labeled “FB". The lower bound for capacity was determined considering both flexural and torsional buckling effects aligned with the AISC Specification and labeled “FTB". Two intermediate solutions were found using the τ_G factors discussed above to capture the increased shear stiffness in torsional buckling. The results labeled “$\tau_G = 1.0$" account for the maximum increase in strength while the results labeled “$\tau_G = 0.877$" include a small reduction to account for imperfections. All calculations included local buckling reductions based on the SJI provisions, which employ the previously mentioned Q-factor.

The study identified multiple double angle cross sections expected to be controlled by flexural buckling over flexural-torsional buckling. Compact sections, such as the 2-L8"x8"x1" shown in Fig. 2.6, were controlled by flexural buckling about the x-axis if accounting for the increased shear stiffness. However, this trend was not absolute and flexural-torsional buckling became the controlling mechanism as the legs became more slender as depicted in Fig. 2.7 and Fig. 2.8.

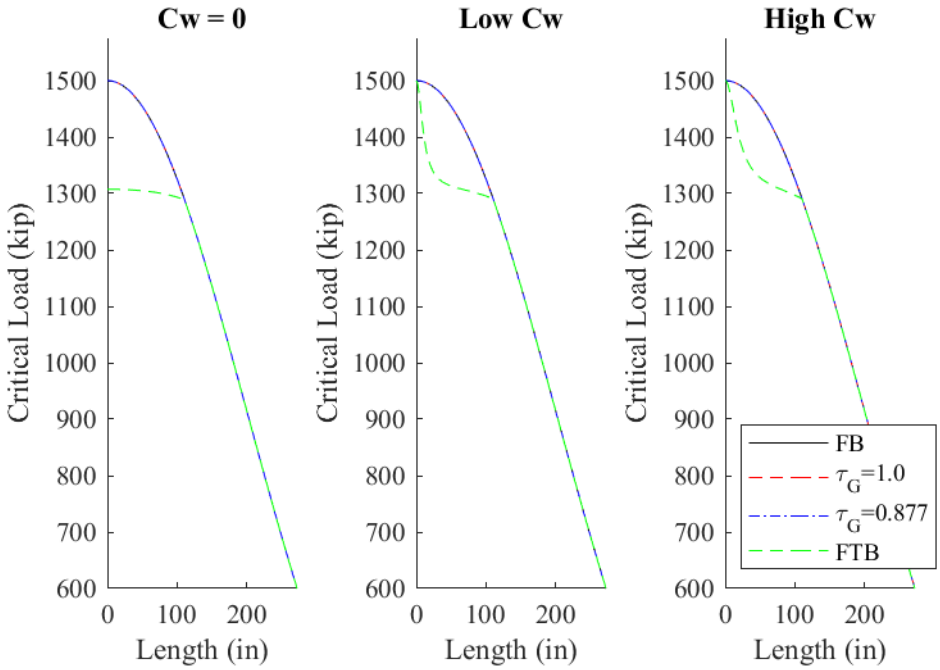

Figure 2.6: Inelastic buckling of a 2-L8"x8"x1" controlled by flexural buckling

Accounting for a non-zero C_w significantly increased the capacity in flexural-torsional buckling, especially when considering a composite response. Despite the increases indicated, multiple double angle cross sections were still controlled by flexural-torsional buckling with significant reductions from the flexural buckling capacity. The complete data set is provided in Appendix C.

2.5. Discussion

The flexural-torsional buckling provisions within the current AISC Specification appear to not take full advantage of known available strength. The conservative approach of utilizing the same elastic-inelastic relationship for flexural and torsional behavior, however, is straight forward. Nevertheless, the capacity of multiple double angle cross sections was observed to be significantly underestimated, as shown in Fig. 2.6. This reduction is compounded with the recommendation

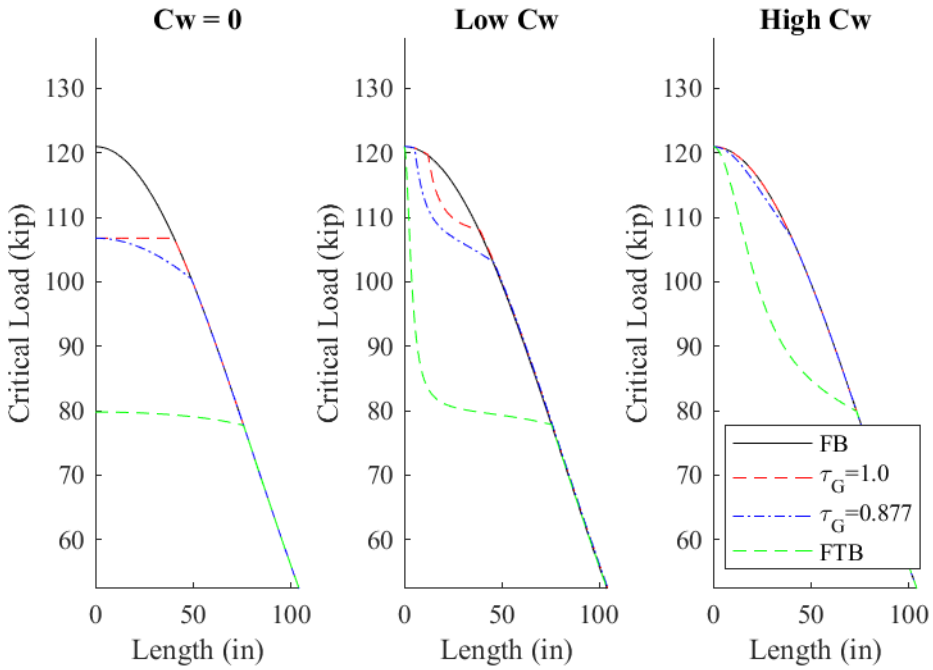

Figure 2.7: Inelastic buckling of a 2-L3"x3"x0.227" with limited critical flexural-torsional buckling

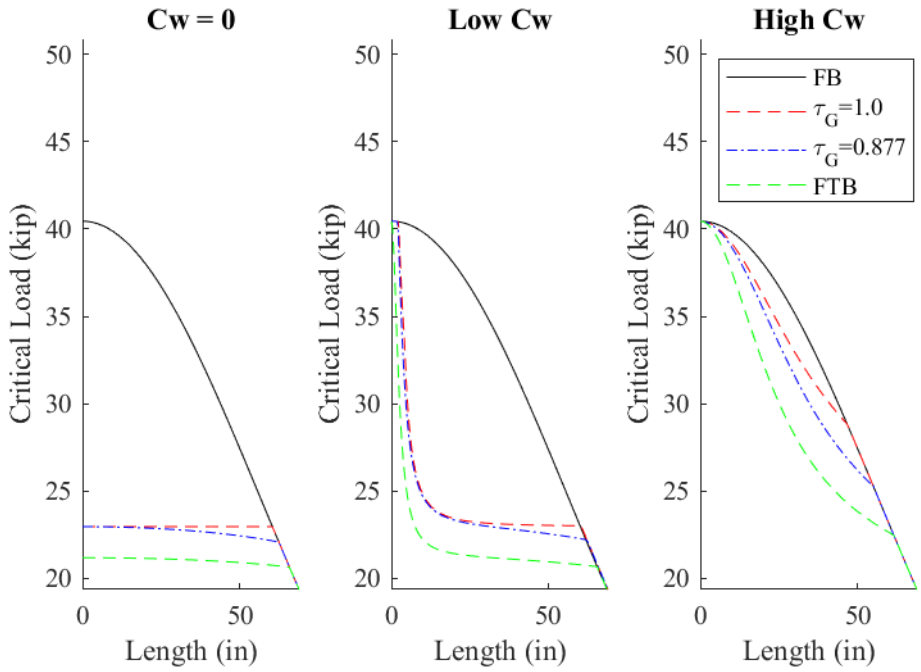

Figure 2.8: Inelastic buckling of a 2-L2"x2"x0.125" with significant flexural-torsional buckling

to ignore the C_w of double angles. Without detailed recommendations for determining torsional stiffness for composite members, treating double angles with a warping stiffness and shear center position similar to tee sections appears reasonable for a conservative design. However, this ignores a significant contribution of stiffness, especially when the two angles can act as a composite member as identified in Section 5.4. The consideration of both parameters, increased shear stiffness and composite behavior, reduces the likelihood of flexural-torsional buckling controlling the member capacity.

This inelastic study alone does not support the design approach of neglecting flexural-torsional buckling in all double angles similar to the prior work by Galambos [5]. Even after accounting for known conservatism in design, multiple double angle cross sections were observed to have a range of lengths where the controlling behavior was flexural-torsional buckling, which was significantly lower than the flexural buckling capacity. This result does not align with the well-established history of existing joist performance and various production testing that indicate joists and joist girders are adequately designed by only considering flexural buckling. As a consequence, further investigation using advanced finite element models was implemented to validate the theoretical results by evaluating systems where flexural-torsional buckling was expected to control the response.

3. Joist Modeling Validation

The joist finite element modeling procedure was validated using previous work by Yost et al. [12, 13] that tested a series of 16-foot (4.88 m) long, 18 inch (460 mm) and 30 inch (760 mm) deep steel joists until failure via web member buckling. The 30 inch deep joist exhibited in-plane flexural buckling behavior, while the 18 inch deep joist captured twisting and bulging associated with flexural-torsional behavior. Results of the validation process follow.

3.1. Modeling Approach

The joists were constructed with 2-L2"x2"x0.125" double angle chords, crimped end L1"x1"x0.125" single angle webs, and an end 7/8-inch (22 mm) solid rod diagonal as depicted in Fig. 3.1 with details taken from the original joist designs. The joists were both laterally supported and loaded along the top chord at the panel points.

Advanced finite element models of the full joist models were developed in Abaqus [14] including multiple material models, connection methods, and imperfections. All structural angles were modeled using S4R shell elements while the rod sections were represented by C3D8R solid elements. The joist was evaluated using four different material models shown in Fig. 3.2. All models considered E = 29,000 ksi (200 GPa) and F_y = 50 ksi (345 MPa). The base material model was an elastic-plastic relationship following Eurocode 3 with a post yield modulus of elasticity equal to $E/10,000$ [15]. For the second model, another Eurocode 3 material model was implemented considering linear strain-hardening that began immediately after yield with a stiffness of $E/100$ until

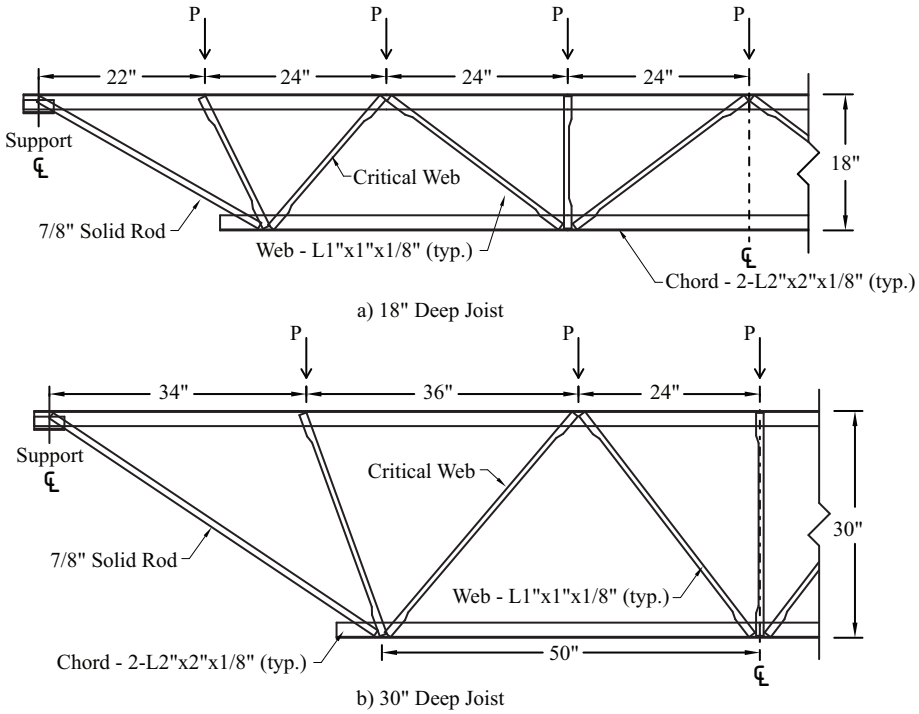

Figure 3.1: Validation study joist geometry (Adapted from manufacturer's design package)

the ultimate stress was reached at 65 ksi (448 MPa). The third material model was a trilinear approach accounting for an initial perfect plasticity after yield. Strain-hardening started at 10 times the yield strain and was approximated by a linear transition to an ultimate strain of 0.15 in/in and ultimate stress of 65 ksi (448 MPa), which is an effective stiffness of E/267. The fourth material model was a realistic reference stress-strain curve for A992-50 taken from literature [16].

The flare bevel weld connecting the solid rod web to the double angle chord was modeled using a surface to surface tie over the approximate welded area as depicted in Fig. 3.3. The web connections required consideration of the crimped geometry of the web members as shown in Fig. 3.4 and modeling of the fillet weld, Fig. 3.5. The fillet weld was modeled as either: (1) the entire face of the welded region was treated as bonded to the chord (the red area) or (2) only the edge along the physical fillet weld was connected (the blue line). Additionally, each connection alternative was modeled as excluding or including contact between the members resulting in four connection models

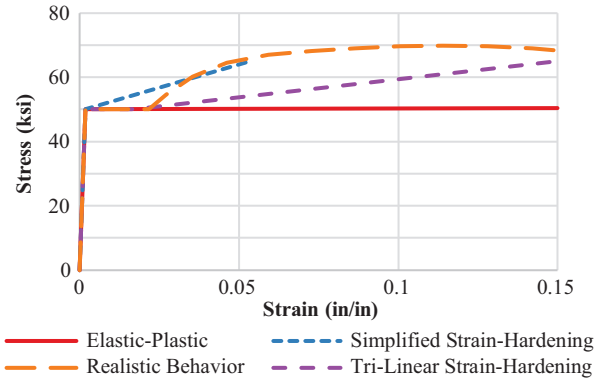

Figure 3.2: Material models for joist modeling

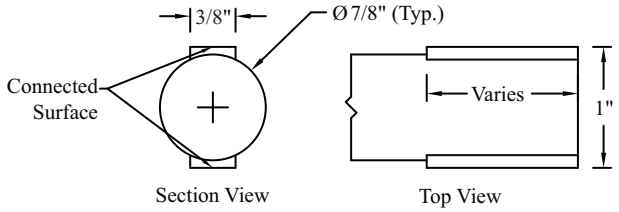

Figure 3.3: Typical solid rod to angle connection model

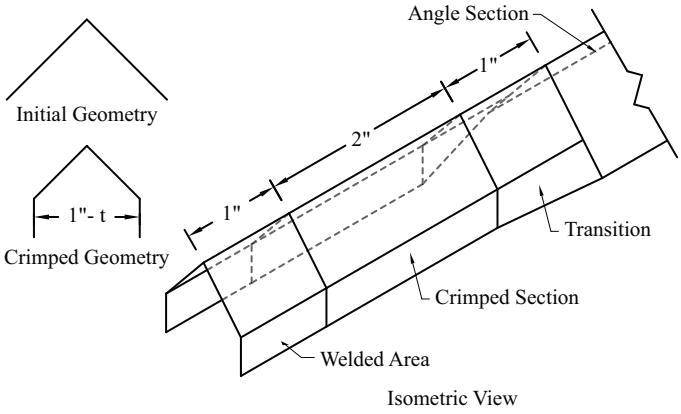

Figure 3.4: Crimped web geometry

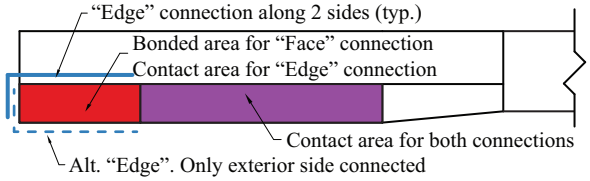

Figure 3.5: Crimped web end weld model

Table 3.1: Imperfections considered in modeling validation study

Case	Out-of-plane	In-Plane	Rotation
1	L/1000	0	0°
2	L/1000	L/1000	0°
3	L/1000	L/1000	1/100°
4	L/1000	L/1000	1/50°
5	L/750	0	0°
6	L/750	L/750	0°
7	L/750	L/750	1/100°
8	L/200	0	0°
9	L/200	L/200	0°
10	L/200	L/200	1/100°

(the purple area plus the red area for edge connection).

Imperfections were applied to the joist in a half wavelength, sinusoidal distribution along the undeformed length of webs and to the chords between the panel points. Various combinations of in-plane translation, out-of-plane translation, and a rotation were considered in the validation process incorporating translations of $L/1000$, $L/750$, and $L/250$ and rotations of $1/100°$ and $1/50°$ as summarized in Table 3.1. Elastic eigenbuckling imperfections were not implemented as the eigenbuckling results provided irrelevant displacements due to the unsupported bottom chord.

3.2. Web Buckling Results

3.2.1 Material Model Selection Considering Connection Variations

The failure loads and load-deflection information from Yost et al. [12, 13] was used to validate the choice of material and connection model for the joist. When including a $L/1000$ out-of-plane imperfection, all combinations of material and connection models captured a similar joist stiffness until approaching failure. Only minimal increases in stiffness occurred due to utilizing the face connection or considering contact. With regard to the elastic-plastic material model, the

Table 3.2: Ultimate load variation due to connection and material models

	Maximum Applied Load, P, (kip)							
Joist Size		18" Deep				30" Deep			
	Yost et al. [13]	2.35	2.61	2.70		2.81	2.88	3.35	
	Connection Model	Edge	Face	Edge + C	Face + C	Edge	Face	Edge + C	Face + C
Mat. Model	Elastic-Plastic	2.25	2.44	2.39	2.69	3.02	3.25	3.30	3.47
	Simplified Str.-Hard.	2.20	2.46	2.41	2.68	3.03	3.27	3.30	3.47
	Tri-Linear Str.-Hard.	2.32	2.50	2.46	2.72	3.05	3.36	3.33	3.46
	Realistic	2.28	2.48	2.42	2.68	3.03	3.29	3.30	3.47

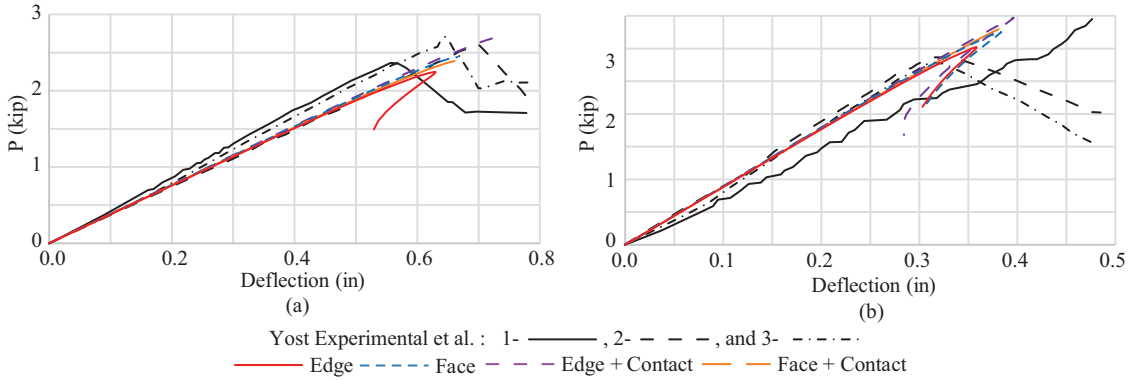

Figure 3.6: Load-displacements results of validation modeling

computational results were found to be in agreement with the softest of the 18 inch deep joists and the stiffest of the 30 inch deep joists as shown in Fig. 3.6(a) and 3.6(b), respectively. As summarized in Table 3.2, minimal increase in strength were observed due to including strain-hardening, which is neglected in typical steel member design and inelastic modeling provisions per AISC [2].

3.2.2 Connection Model Selection Including Imperfection Effects

The ultimate load, summarized in Table 3.3 which considered various imperfections, and failure mode of the webs determined using the computational results were in agreement with the experimental behavior. The 18 inch deep steel joist failed in a twisting and bulging mode as shown in Fig. 3.7. The models consistently failed near the web mid-height while the experimental failure was closer to the crimped geometry transition. It is hypothesized that the different failure position is

Table 3.3: Effect of connection model and imperfection on ultimate load

Maximum Applied Load, P, (kip)									
Joist Size		18" Deep				30" Deep			
	Yost et al. [13]	2.35	2.61	2.70		2.81	2.88	3.35	
	Conn. Model	Edge	Face	Edge + C	Face + C	Edge	Face	Edge + C	Face + C
Imperfection Case	1	2.25	2.44	2.39	2.69	3.02	3.25	3.30	3.47
	2	2.20	2.38	2.31	2.58	2.82	3.07	3.11	3.17
	3	2.20	2.38	2.31	2.58	2.82	3.07	3.10	3.17
	4	2.20	2.38	2.33	2.58	2.82	3.07	3.11	3.16
	5	2.24	2.44	2.36	2.67	3.02	3.23	3.30	3.46
	6	2.16	2.36	2.30	2.52	2.79	2.99	3.01	3.07
	7	2.16	2.36	2.30	2.54	2.79	3.00	3.01	3.07
	8	2.15	2.31	2.26	2.44	2.94	3.13	3.17	3.26
	9	1.93	2.05	2.00	2.12	2.22	2.35	2.32	2.39
	10	1.93	2.05	2.01	2.13	2.22	2.35	2.32	2.39

a consequence of the modeling assumptions including (1) the largest imperfections at midspan and (2) not accounting for residual stresses due to the crimping process. The 30 inch deep steel joist was controlled by an in-plane flexural buckling failure mode depicted in Fig. 3.8. The buckled geometry shown resulted from the edge connection without contact model and the elastic-plastic material relationship. By varying the imperfection, it was possible to observe how the the buckling behavior changed. As expected, larger initial imperfections led to smaller ultimate loads. The inclusion of the in-plane imperfection caused a greater load reduction as it amplified the observed failure modes. The addition of the imperfection rotations improved the post-buckling modeling of the joists without a significant change in the failure load. From this analysis, it was determined to continue with the typical $L/1000$ for imperfection displacements as realistic larger values were considered to not have a significant effect.

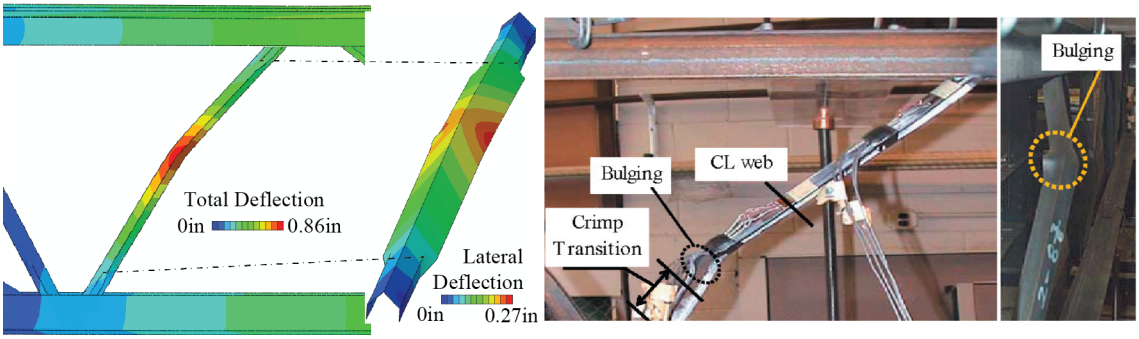

Figure 3.7: Twisting and bulging of 18" deep joist diagonal at failure. (a) Model (b) Yost et al. [13]

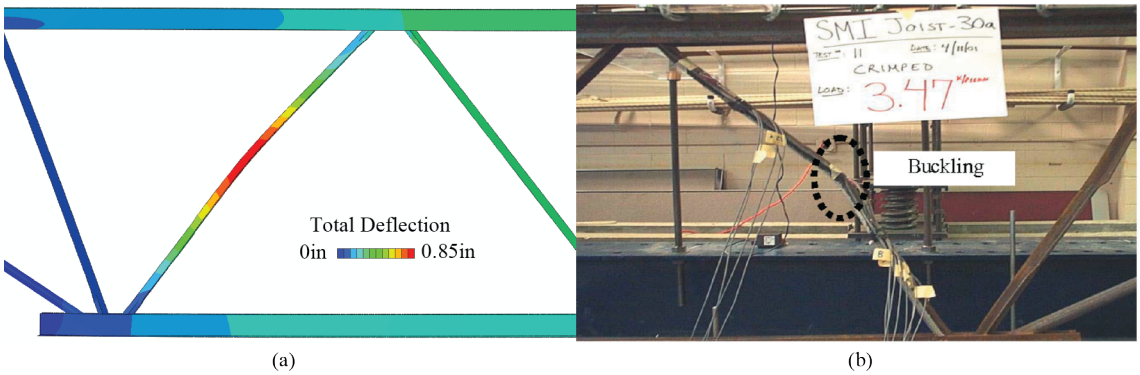

Figure 3.8: Flexural buckling of 30" deep joist diagonal at failure. (a) Model (b) Yost et al. [13]

3.3. Discussion

The initial validation has shown that it is possible to accurately model the behavior of steel joist structures including flexural and torsional buckling behaviors at failure. The overall geometry of the joist defined the general stiffness of the structure, but the details of the connections were still a key parameter in defining the ultimate stability of the system. While all connection models resulted in appropriate failure loads, the exclusion of contact captured similar failure modes, provided a more conservative result, and improved run times. It was decided not to use the face connection alternative as it was uncertain how the greater bonded area would correlate to the edge connection alternative. The larger web sizes would provide a sizeable area that would result in a substantially stiffer connection than the edge connection only. Furthermore, the buckled geometry of 30 inch deep joist including contact captured an unexpected in-plane downwards flexural buckling failure, which was unlikely to occur. As mentioned previously, minimal benefits were observed due to strain-hardening; therefore, the edge connection without contact and the elastic-plastic material relationship were used for the remainder of the study.

As noted above, elastic eigenbuckling imperfections were not implemented in the validation modeling. The elastic buckling results consistently indicated that the chord was expected to buckle before the webs, which was contrary to the inelastic analysis. A closer investigation of the webs indicated that substantially yielding was occurring at the end of the webs prior to failure, as shown in Fig. 3.9. The reduced restraint at the end of the member lowered the required buckling load, which would be expected to occur when inelastic flexural-torsional buckling controls. Along those lines, capturing an accurate distribution of stresses at the connection allowed for the appropriate portion of the member to yield. For this chord study, capturing the yielding of the web connections becomes important as it will alter the restraint of the chord members.

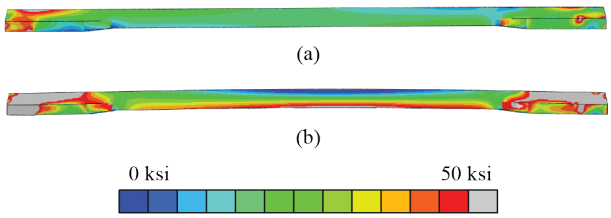

Figure 3.9: Yielding of web diagonal at failure. Von Mises stress at (a) 50% of P_{max} and (b) P_{max}

4. Full Joist and Joist Girder Buckling Study

A buckling study utilizing full joists and joist girders models was completed to investigate the effects of flexural-torsional buckling including continuity and connection effects, which considered 18 different cross sections divided into three groups based on leg width detailed in Sections 4.1.1, 4.1.2, and 4.1.3. Each group was evaluated for a reference joist or joist girder that was designed to have the chords fail in compression before the webs. The desired model behavior was verified for the largest chord size in each group. Then, only the chord sizes were modified to capture a range of behavior including sections anticipated to be controlled by flexural-torsional buckling based on the analysis in Section 2.4. A discussion of the overall modeling parameters and specific model group details are followed by the inelastic buckling results of all models.

4.1. General Modeling Provisions

Each joist and joist girder was modeled as a simply-supported span with the appropriate lateral bracing to test buckling of the bottom chord including continuity and connection effects. The webs were sized to not fail in buckling prior to the chords. Based on the results from the validation study in Chapter 3, the double angle, single angle, and crimped angle members were modeled with SR4 shell elements and the solid rod webs were modeled using C3D8R solid elements. The web to chord connections utilized the edge connection model without contact to simulate the fillet welds. The double angle chords were connected using vertical segments of 7/8-inch solid rods modeled similar to the end diagonal members as shown in Fig. 4.1.

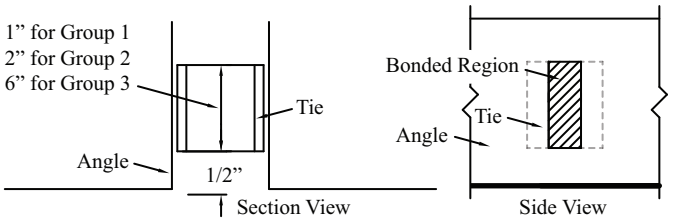

Figure 4.1: Tie between angle chord details

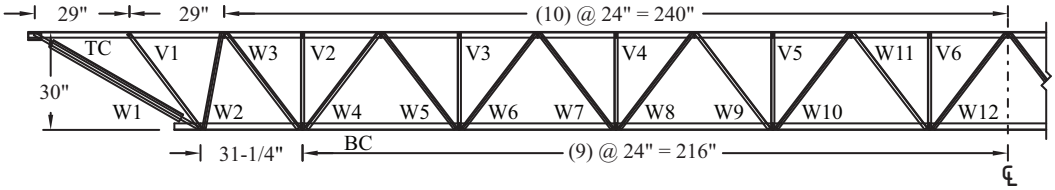

Figure 4.2: Elevation view of Group 1 - Joist A

The joists were modeled as nominal 50 ksi (345 MPa) yield steel with an elastic-plastic relationship (Fig. 3.2). Imperfections were applied to the structures in a sinusoidal pattern to each chord with a half wavelength between the panel points incorporating a $L/1000$ displacement out-of-plane, a $L/1000$ displacement in-plane, and a 1° rotation. Each model was evaluated in a Riks load-controlled analysis to allow for a consistent distribution of load.

4.1.1 Group 1 Details - Joist A

For Group 1, a 50-foot long, 30 inch deep joist, as shown in Fig. 4.2 with members listed in Table 4.1, was subjected to uniform uplift to investigate buckling of the bottom chord. Table 4.2 lists the seven different bottom chord double angle cross sections considered for this group. All chord sizes were expected to fail by flexural-torsional buckling at a nominal 4-foot unbraced length.

The joists were modeled as a simply-supported span with the top chord laterally supported on one chord angle at 12 inch o.c. and the bottom chord braced at all panel points. The bottom chord bracing was achieved by incorporating a horizontal bracing angle, which was laterally supported at the ends. A uniformly distributed load was applied over the entire length of the joist top chord via

Table 4.1: Joist A member sizes

Label	Cross Section
TC	2-L1-3/4"x1-3/4"x0.170"
BC	See Table 4.2
W1	7/8" Rod + L2-1/2"x2-1/2"x3/16"
W2	CC1-1/4"x1-1/4"x0.188"
W3	CC1-1/2"x1-1/2"x0.25"
W4	CC1-1/2"x1-1/2"x0.138"
W5-W12	CC1-1/4"x1-1/4"x0.125"
V1-V6	L1"x1"x0.109"

CC = Continuously crimped angle

Table 4.2: Group 1 joist bottom chord cross section alternatives

Leg (in)	Thickness (in)				Theoretical Failure
2	0.125	0.115	0.109	0.094	Flexural-torsional
1.75	0.125	0.115	0.109		Flexural-torsional

equal point loads on the interior 25% of the cross section as shown in Fig. 4.3.

4.1.2 Group 2 Details - Joist Girder B

For Group 2, a 45-foot long, 28 inch deep joist girder, as shown in Fig. 4.4 with members listed in Table 4.3, was subjected to concentrated point loads in uplift to investigate buckling of the bottom chord. Table 4.4 lists the five different bottom chord double angle cross sections considered in the study. The three thicker cross sections were expected to fail in flexural buckling, and the two thinner cross section in flexural-torsional buckling, at a nominal 5-foot unbraced length.

The joist girder model for Group 2 is a simply supported span with a discretely braced top and bottom chord at the panel points. A modified 60-inch section of Group 1 joist was used to model

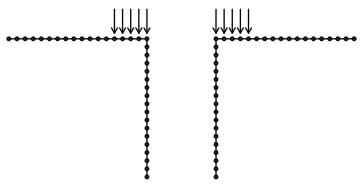

Figure 4.3: Uniform loading approximation on Group 1 top chord angles

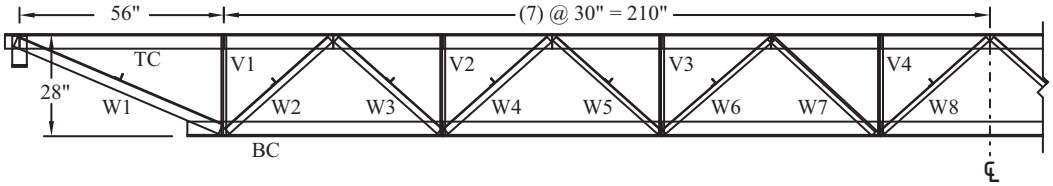

Figure 4.4: Elevation view of Group 2 - Joist girder B

Table 4.3: Joist girder B member sizes

Label	Cross Section
TC, BC	See Table 4.4
W1	2-L3"x3"x0.375"
W2	2-L2"x2"x0.375"
W3, W4	2-L2"x2"x0.25"
W5, W6	2-L1-1/2"x1-1/2"x0.25"
W7	CC2"x2"x0.25"
W8	2-L1-1/2"x1-1/2"x0.227"
V1, V2	CC1-1/2"x1-1/2"x0.170"
V3	CC1-1/2"x1-1/2"x0.188"
V4	CC1-1/2"x1-1/2"x0.138"

CC = Continuously crimped angle

Table 4.4: Group 2 joist girder chord cross section alternatives

Leg (in)	Thickness (in)			Theoretical Failure
4	0.375	0.344	0.3125	Flexural
4	0.25	0.1875		Flexural-torsional

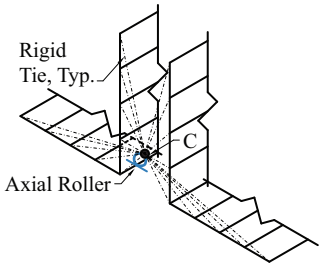

Figure 4.5: Rigid tie on joist chord segment for axial restraint

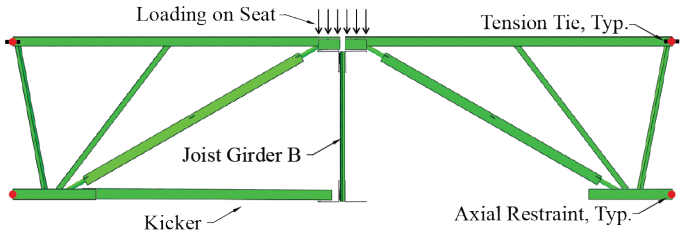

Figure 4.6: Joist girder B joist seat and lateral bracing support

the joist bearing on joist girder interaction and to provide lateral support as shown in Fig. 4.6. The top and bottom chord of each joist section had a separate rigid tie between a reference node at the centroid and all end nodes on the double angle as shown in Fig 4.5 to allow for axial force to develop in the chords. These reaction forces combined with the L2"x2"x0.25" kicker on one side of the joist girder to provide lateral support to the bottom chord. A kicker was not provided to the second side to avoid creating a moment continuity between the supported joists. The point loading of the joist girder was achieved by applying discrete loads over the length of the seat to the top chord of the modified Group 1 joist section, which allowed the flexibility of the joist seat and joist girder top chord to define the force distribution. Lastly, a 1"x0.25" tension tie was pin connected to the rigid tie at the end of the modified joist section top chords to ensure deformations occurred throughout the joist girder instead of only locally at the seat which would cause large rotations of the joist section.

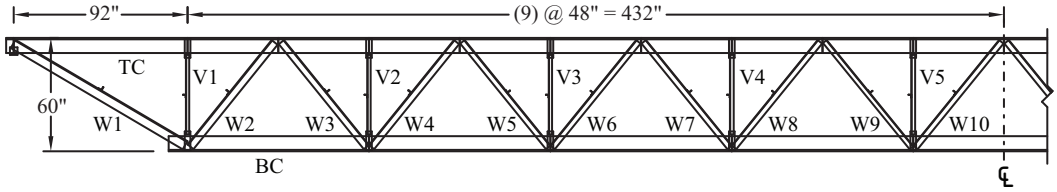

Figure 4.7: Elevation view of Group 3 - Joist girder C

Table 4.5: Joist girder C member sizes

Label	Cross Section
TC , BC	See Table 4.6
W1	2-L5"x5"x0.375"
W2	2-L5"x5"x0.625"
W3	2-L3-1/2"x3-1/2"x0.375"
W4	2-L4"x4"x0.5"
W5, W7, W8	2-L3"x3"x0.375"
W6	2-L3"x3"x0.5"
W9	2-L2-1/2"x2-1/2"x0.313"
W10	2-L3"x3"x0.227"
V1, V3	2-L1-3/4"x1-3/4"x0.170"
V2	2-L1-3/4"x1-3/4"x0.155"
V4, V5	2-L2"x2"x0.163"

4.1.3 Group 3 Details - Joist Girder C

For Group 3, a 88-foot long, 60 inch deep joist girder, as shown in Fig. 4.7 with members listed in Table 4.5, was subjected to concentrated point loads in uplift to investigate buckling of the bottom chord. Table 4.6 lists the six different bottom chord double angle cross sections considered in the study. With a nominal 8-foot unbraced length, the three thicker cross sections were expected to fail in flexural buckling, while the three thinner cross section were expected to fail in flexural-torsional buckling.

The joist girder models for Group 3 were created in the same manner as Group 2. Due to

Table 4.6: Group 3 joist girder chord cross section alternatives

Leg (in)	Thickness (in)			Theoretical Failure
8	0.75	0.625	0.546	Flexural
8	0.50	0.438	0.375	Flexural-torsional

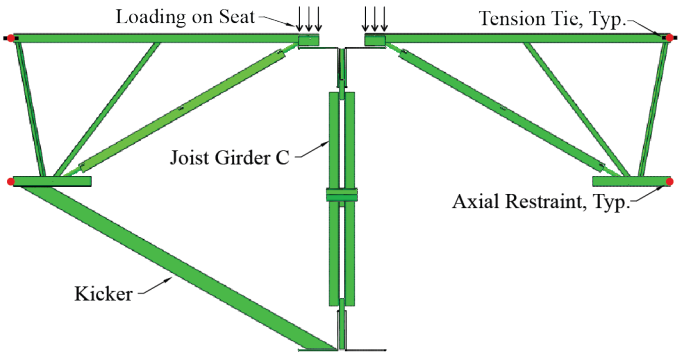

Figure 4.8: Joist Girder C joist seat and lateral bracing support

the greater depth of the joist girder C, illustrated in Fig. 4.8, and increased applied loads, the chords of the modified Group 1 joist section were increased to 0.25" thick and the kicker was increased to a L3"x3"x0.25". Additionally, plasticity was eliminated from the Group 1 joist section seat material model as the applied load exceed the yield stress of the seat angles. The standard elastic-plastic stress-strain relationship described in Section 4.1 was still implemented for the remainder of the model.

4.2. Results of Full Joist and Joist Girder Modeling

The joist and joist girder chords exhibited a number of complex displacement patterns at the maximum loading noted in Table 4.7. The joist chord capacity was consistently observed to be greater than or equal to the SJI Specification's flexural buckling limit, including the effective length factor defined by SJI. A similar average ratio for the modeled to design capacity, 1.11 and 1.13, was found for the expected controlling failure mode of flexural buckling or flexural-torsional buckling, respectively. However, greater variability was noted for flexural-torsional buckling, COV=0.10, compared to flexural buckling, COV=0.04. Despite this difference, the predominant deformation of the chord was consistently in the vertical direction due to the span deflection and twisting of the

Table 4.7: Full joist and joist girder modeling inelastic buckling results

Expected Buckling Mode		Cross Section	Model (k)	SJI Design (k)	Model/SJI
	Flexural-Torsional	2-L2"x2"x0.125"	36.87	30.2	1.22
		2-L2"x2"x0.115"	32.09	26.9	1.19
		2-L2"x2"x0.109"	28.55	23.4	1.22
		2-L2"x2"x0.094"	19.90	19.4	1.03
		2-L1.75"x1.75"x0.125"	30.42	25.1	1.21
		2-L1.75"x1.75"x0.115"	28.03	22.6	1.24
		2-L1.75"x1.75"x0.109"	26.33	20.1	1.31
		2-L4"x4"x0.25"	164.9	140.6	1.17
		2-L4"x4"x0.188"	86.9	87.5	0.99
		2-L8"x8"x0.5"	660.5	592	1.12
		2-L8"x8"x0.438"	502.7	480	1.05
		2-L8"x8"x0.375"	359.6	364	0.99
	Flexural	2-L4"x4"x0.375"	263.3	240.6	1.09
		2-L4"x4"x0.344"	243.0	216.9	1.12
		2-L4"x4"x0.313"	223.4	191.7	1.17
		2-L8"x8"x0.75"	1063	1024	1.04
		2-L8"x8"x0.625"	893.6	812	1.10
		2-L8"x8"x0.546"	759.8	673	1.13

chord angles as depicted in Fig. 4.9. The twisting of the chords included a combination of global and local twisting effects that made observations of post-buckling behavior difficult. The complex interaction was confirmed by evaluating the elastic buckling response, which captured five or more buckling modes within 5% of the first mode for each of the 2-in leg angles. Each mode indicated a combination of competing individual angle and composite chord lateral-torsional buckling shapes, all primarily located in the middle three spans.

4.3. Discussion

The buckling investigation considering full joists and joist girders indicated a variety of torsional responses within the chord making it difficult to define a simple controlling phenomenon. The individual angles were observed to twist independently with no consistent influence on the adjacent angle. During the analysis, it was considered that individual angle buckling might be

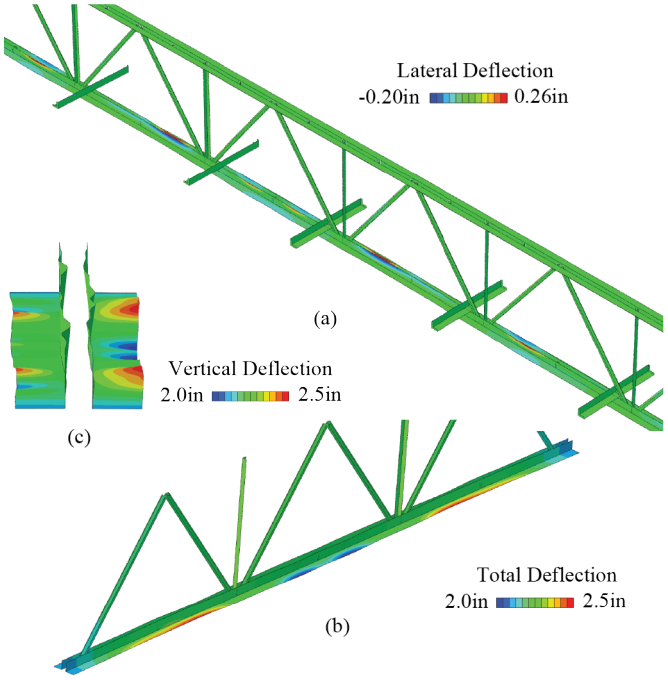

Figure 4.9: 2-L2"x2"x0.094" joist chord at failure. (a) Lateral displacement of full model. (b) Isometric view of bottom chord. (c) Angled end view of bottom chord.

controlling over the double angle response; however, it was later attributed to the local buckling. The flexural-torsional buckling of a single angle is equivalent to the local buckling of a single angle, which has no distinction from the local buckling of a double angle with a gap between the chords. Local buckling was expected to be encountered as the double angles susceptible to flexural-torsional buckling were slender. To clarify what behavior was observed, a chord buckling study, detailed in Chapter 5, was conducted to verify the calculated capacities and complex buckling modes.

5. Chord Segment Study

A simplified double angle chord segment buckling study was completed to validate the full joist modeling results while considering both elastic and inelastic buckling. The eighteen bottom chord cross sections from the full joist modeling, listed in Table 5.1 with the same group reference established in Chapter 4, were evaluated with the same nominal effective length, L, as the full-scale model with both a pinned-pinned and fixed-fixed boundary condition. This portion of the study varied the number of ties between the chords to account for differences in the composite behavior. While one connection between the double angle chords is typically adequate to meet the minimum requirements of a composite member per the SJI Specification, independent twisting of the individual angles was observed in the full joist investigation. The additional ties were included to capture a more fully composite response.

5.1. Modeling Details

The double angle chord segment models were based on the same modeling provisions as discussed in Section 4.1 using shell elements for the angles and solid elements for the ties. Each cross section was evaluated with 0, 1, 3, 7, 15, and 31 (replaced with 23 in Group 1) ties evenly spaced along the length of the chords. The first subset considered a simply supported boundary condition for bending about both the weak and strong axis with a length, L. The pinned boundary condition utilized a rigid tie between a reference node at the centroid and all end nodes on the double angle as shown in Fig 5.1(a). This node was then subjected to axial load to apply uniform compression

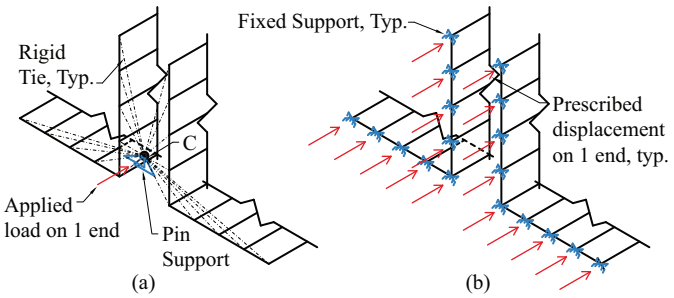

Figure 5.1: Chord segment end condition. (a) Pinned alternative (b) Fixed alternative

Table 5.1: Double angle chord dimensions

	Leg (in)	Thickness (in)						L (in)
Group 1	2	0.125	0.115	0.109	0.094			48
	1.75	0.125	0.115	0.109				
Group 2	4	0.375	0.344	0.313	0.25	0.188		60
Group 3	8	0.75	0.625	0.546	0.5	0.438	0.375	96

to each member. A consequence of this modeling approach was that the end of the members were fixed for warping, which resulted in a different theoretical effective length in flexural and torsional buckling. As an alternative, a second subset with fixed supports was considered where all end nodes of the member were individually fully restrained as shown in Fig 5.1(b) to have the same effective length for flexural and torsional buckling. This model was evaluated with a length of $2L$ to keep the same nominal effective length for flexural buckling as the baseline configuration. The fixed support model was loaded by providing a uniform axial displacement across the section. Each model was evaluated for elastic eigenbuckling and then inelastic buckling using the iterative-incremental Riks loading method with additional results provided in Appendix D. The first elastic buckling mode, regardless of the buckled shape, was used as an initial imperfection for the inelastic analyses with a consistent $L/1000$ imperfection for all models. An exception was made for the fixed end models with 0 ties because the unconnected angles behaved as separate models. To apply the first elastic mode imperfection to both angles, the first and second elastic buckling modes were applied. This was not required for the pin support as the angles interacted due to the rigid tie.

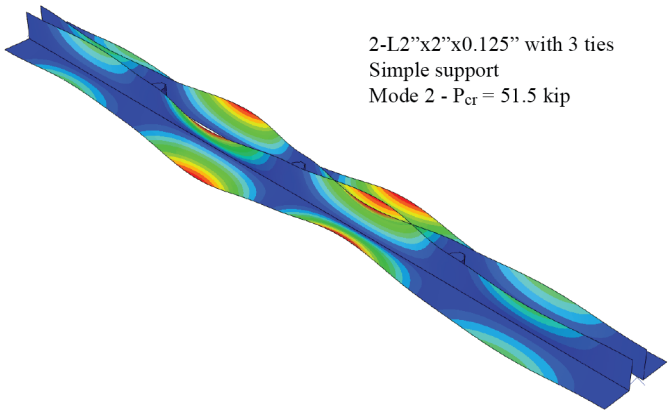

Figure 5.2: Individual angle flexural-torsional buckling displacement

5.2. Elastic Chord Behavior

The elastic buckling investigation depicted a variety of flexural, flexural-torsional, and local buckling responses. Global flexural-torsional buckling was only identified when the ties rotated along with the angles. Local buckling was observed as either twisting deformations in both flanges of one chord angle, which was classified as individual angles exhibiting flexural-torsional buckling as shown in Fig. 5.2, or different deformations in the horizontal and vertical flanges resulting in a non-90° angle between the flanges, which was classified as a distortional buckling mode as depicted in Fig. 5.3. This change in local buckling mode was not driven solely by consideration of higher buckling modes but also by the amount of tie connectivity between the chords. Considering the results for the 2-L2"x2"x0.125" in Table 5.2 and 5.3, distortional buckling behavior was largely limited to configurations with a significant number of connections between the angle members. For most practical joist applications, local buckling of the double angles resulted in single angle flexural-torsional buckling between the ties.

It was anticipated that the advanced finite element modeling would capture the same global buckling behavior described in Section 2 with additional local effects. Conforming to that expectation,

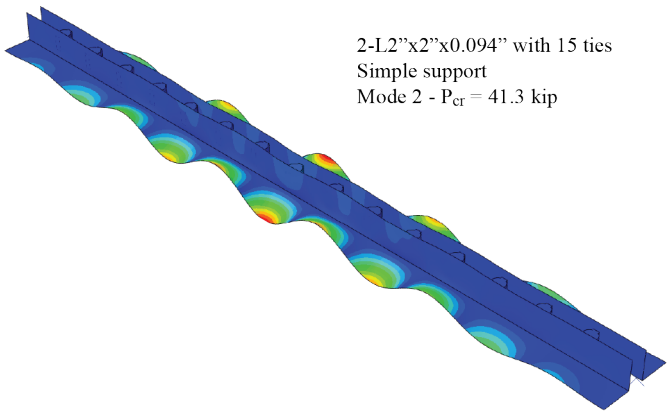

Figure 5.3: Distortional buckling displacement

Table 5.2: Elastic buckling of 2-L2"x2"x0.125" chord segment with simple support

Mode		Ties					
		0	1	3	7	15	23
1	P_{cr}	31.7 k	39.5 k	44.4 k	45.9 k	46.3 k	46.5 k
	Shape	g-FB+i-FTB	g-FB+i-FTB	g-FB	g-FB	g-FB	g-FB
2	P_{cr}	40.1 k	43.8 k	51.5 k	71.3 k	95.8 k	98.9 k
	Shape	g-FTB	i-FTB	i-FTB	i-FTB	D	D
3	P_{cr}	42.6 k	44.5 k	51.9 k	71.9 k	95.8 k	99.0 k
	Shape	i-FTB	i-FTB	i-FTB	i-FTB	D	D
4	P_{cr}	42.6 k	44.9 k	52.3 k	72.6 k	97.5 k	100.7 k
	Shape	i-FTB	i-FTB	i-FTB	i-FTB	D	D
5	P_{cr}	44.5 k	46.3 k	52.5 k	73.1 k	97.6 k	100.8 k
	Shape	i-FTB	g-FTB	i-FTB	i-FTB	D	D

FB = Flexural Buckling; FTB = Flexural-Torsional Buckling; D = Distortional
g = Global/composite response; i = Individual angle response

Table 5.3: Elastic buckling of 2-L2"x2"x0.125" chord segment with fixed support

Mode		Ties					
		0	1	3	7	15	23
1	P_{cr}	18.8 k	32.7 k	39.2 k	44.4 k	45.8 k	46.0 k
	Shape	i-FB	g-FTB	g-FTB	g-FB	g-FB	g-FB
2	P_{cr}	18.8 k	38.6 k	39.3 k	47.5k	65.3 k	84.5 k
	Shape	i-FB	i-FTB	g-FB+i-FTB	g-FTB	g-FTB	g-FTB
3	P_{cr}	33.4 k	38.8 k	43.1 k	51.1 k	70.6 k	89.7 k
	Shape	i-FTB	g-FB+i-FTB	g-FTB	i-FTB	i-FTB	g-FB
4	P_{cr}	33.4 k	39.8 k	43.3 k	51.3 k	70.8 k	90.7 k
	Shape	i-FTB	g-FTB	i-FTB	i-FTB	i-FTB	D
5	P_{cr}	38.1 k	39.8 k	43.7 k	51.5 k	71.1 k	90.8 k
	Shape	i-FB	i-FTB	g-FTB	i-FTB	i-FTB	D

FB = Flexural Buckling; FTB = Flexural-Torsional Buckling; D = Distortional
g = Global/composite response; i = Individual angle response

most cross sections from Group 2 and Group 3 failed in elastic global flexural-torsional buckling, regardless of inelastical response. Despite the apparent agreement, the observed buckling capacity was greater than the theoretical value with ties spaced at $L/2$, which would have been expected to be reduced due to local effects. Group 1 provided a more complex result. For example, a 2-L2"x2"x0.125" would theoretically flexural-torsional buckle around 26 kips, but the advanced model with fixed end supports was able to reach 39.2 kips before failing in global flexural-torsional buckling. While the pinned variation failed at a similar load of 39.5 kips, flexural buckling with individual angle flexural-torsional buckling was now observed to be the controlling mode. For many of the Group 1 cross sections, flexural buckling replaced global flexural-torsional behavior, especially when considering the pinned boundary condition.

Additional ties were observed to consistently increase buckling capacity, but the effect varied by buckling modes. Flexural buckling exhibited initial gains due to composite behavior, but an excessive number of ties produced a negligible increase in strength. Reducing the spacing between ties increased the individual flexural-torsional response until the strength of the unsupported horizontal flange limited capacity, which aligned with a new controlling failure mode. In this study, no limit for increased elastic global flexural-torsional buckling capacity was observed.

5.3. Inelastic Chord Behavior

An iterative-incremental inelastic buckling analysis was conducted, and the results indicated that the double angle cross sections primarily failed in flexural buckling, which was typically initiated by the local twisting of the individual angle sections. The buckling strength increased with additional ties, see Table 5.4, which restrained the twist of individual chords up to a limit where distortion of the flange preceded the onset of buckling as highlighted in Fig. 5.4 and Fig. 5.5. The benefit of

increased strength with the addition of more ties was greater in more slender cross sections. Some global twisting was observed at failure, such as Fig. 5.5(a), where the initial imperfection was a flexural-torsional buckling mode; however, it was generally accompanied with a flexural response at failure as well. Complete results of the inelastic buckling study based on the first elastic buckling mode imperfection are available in Appendix D.2. Note that some entries have a second value in the footnote, as done in Table 5.4, providing the buckling capacity based on a different initial imperfection to verify the jump in capacity was due to the study methodology and not other underlying behavior.

To directly compare the results of the simplified chord models with the full joist models presented in Section 4.2, the number of ties in the simplified chord models was limited to practical numbers such as ties spaced at $L/2$ and $L/4$. It was found that the buckling capacity results, presented in Table 5.5, were in agreement between the two models for both pinned and fixed boundary conditions. The design limits of both flexural and flexural-torsional buckling were found to underestimate the modeled strength. As the section slenderness increased, the conservatism of the flexural buckling prediction was reduced.

The inelastic model results provided an interesting deviation from the typical design assumptions. The various full and isolated joist models incorporated different effective lengths for flexural-torsional buckling; however, each exhibited comparable torsional behavior and similar ultimate capacities. The additional warping restraint in the simply supported alternative should have caused flexural buckling to be more dominant compared to the other modeling alternatives. As a result, it was theorized the stiff connection between the chords and the continuity of the chords provide similar warping restraint that would typically be conservatively ignored in design.

Table 5.4: Inelastic buckling of simply supported chord

Cross Section	Axial buckling load (kip) for (#) ties					
	0	1	3	7	15	31
2-L8"x8"x0.75"	1120	1130	1130	1130	1130	1110
2-L8"x8"x0.625"	932	931	944	948	952	948
2-L8"x8"x0.546"	781	783	809	824	833 [1]	816
2-L8"x8"x0.5"	659 [2]	644	717	743	764 [3]	738
2-L8"x8"x0.438"	491 [4]	486	572	606	628	626
2-L8"x8"x0.375"	350 [5]	346	418	475	498	505

[*] Evaluations with different elastic buckling mode resulted in reduced buckling load
[1] Mode 2 = 824 k
[2] Mode 4 = 617 k
[3] Mode 3 = 742 k
[4] Mode 4 = 457 k
[4] Mode 4 = 321 k

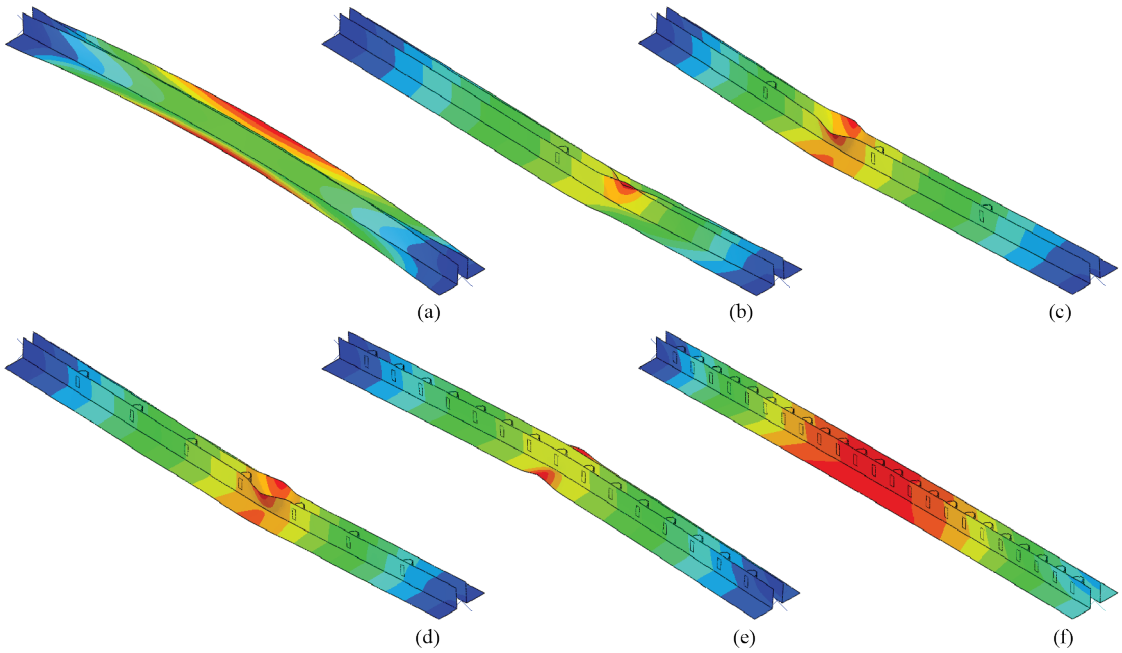

Figure 5.4: Composite behavior effect on inelastic buckling in a 2-L2"x2"x0.094" with (a) 0, (b) 1, (c) 3, (d) 7, (e) 15 and (f) 23 ties

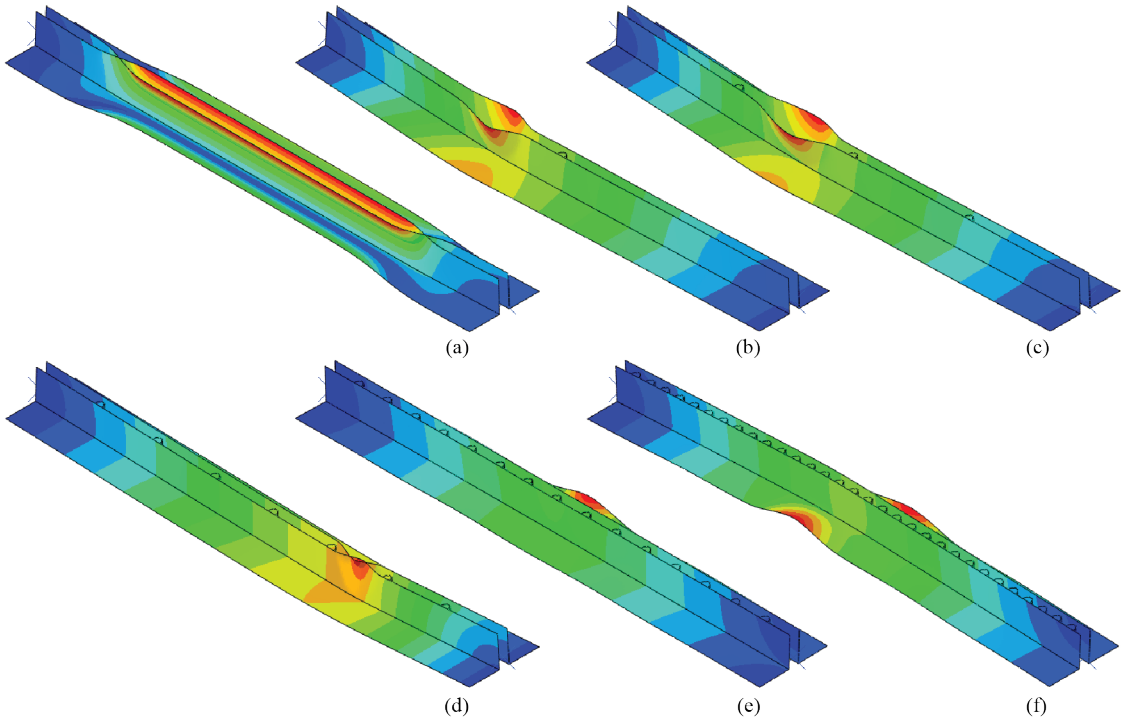

Figure 5.5: Composite behavior effect on inelastic buckling in a 2-L4"x4"x0.25" with (a) 0, (b) 1, (c) 3, (d) 7, (e) 15 and (f) 31 ties

Table 5.5: Buckling capacity comparison between modeling and code values

Cross Section	Maximum Model Compression (kip)					Design* (kip)	
	Ties at $L/2$			Ties at $L/4$		FB	FTB
	Joist	Pinned	Fixed	Pinned	Fixed		
2-L2"x2"x0.125"	36.7	34.4	36.7	36.4	35.6	28.3	24.1
2-L2"x2"x0.115"	32.1	31	30.8	33.3	30.7	25.2	20.4
2-L2"x2"x0.109"	28.5	25.7	27.3	25.3	26.6	23.3	18.3
2-L2"x2"x0.094"	19.9	18.5	19.2	18.3	21.5	18.4	13.4
2-L1.75"x1.75"x0.125"	30.2	25	25.5	26.3	26.1	22.8	23.0
2-L1.75"x1.75"x0.115"	28.0	22.8	23.3	24.3	24.1	20.6	19.5
2-L1.75"x1.75"x0.109"	26.3	21.5	22.0	23	22.9	19.3	17.5
2-L4"x4"x0.375"	263	273	282	271	284	241	220
2-L4"x4"x0.344"	242	253	259	257	261	217	191
2-L4"x4"x0.313"	223	230	234	232	237	192	162
2-L4"x4"x0.25"	165	156	167	156	179	141	106
2-L4"x4"x0.188"	87.4	82.7	87.1	87.4	101	87.5	58.7
2-L8"x8"x0.75"	1063	1130	1136	1130	1139	1024	901
2-L8"x8"x0.625"	890	931	947	944	952	812	661
2-L8"x8"x0.546"	733	783	803	809	821	674	513
2-L8"x8"x0.5"	659	644	679	717	718	592	430
2-L8"x8"x0.438"	505	486	499	572	544	480	325
2-L8"x8"x0.375"	360	346	344	418	389	364	229

* Effective length factors taken as k=1 for all calculations

5.4. Double Angle Chord in Torsion

The previous buckling results where indicative of an increased torsional stiffness due to increasing composite behavior of the cross section. This behavior was evaluated by subjecting double angle chord segments to a defined twist to determine an effective torsional stiffness. This analysis was accomplished by updating the boundary conditions of the simply supported double angle models described in Section 5.1. The model construction still incorporated the rigid tie at both ends of the member causing each end to be fixed for warping. One end of the angle was fully fixed to create a cantilever, and the unsupported end was subjected to a torsional rotation of 0.01 radians. The torsional reaction moments from a second-order elastic Riks analysis are listed in Table 5.6 in addition to the theoretical torsion results using the thin-walled section properties described in Section 2.4. These

Table 5.6: Reaction moments for torsional study

	Theoretical Moment (in-lb)			Model Moment (in-lb) for (#) ties					
Cross Section	C_w=0	Low C_w	High C_w	0	1	3	7	15	23 or 31
2-L2"x2"x0.125"	11.7	11.7	18.7	14.2	17.1	22.5	31.7	49.1	66.0
2-L2"x2"x0.115"	9.2	9.2	15.3	11.4	14.1	19.1	27.7	44.1	59.8
2-L2"x2"x0.109"	7.8	7.8	13.5	10.0	12.5	17.3	25.6	41.2	56.3
2-L2"x2"x0.094"	5.0	5.0	9.6	6.8	9.1	13.3	20.8	34.9	48.3
2-L1.75"x1.75"x0.125"	10.2	10.2	15.1	11.8	14.2	19.2	28.2	45.5	62.6
2-L1.75"x1.75"x0.115"	8.0	8.0	12.3	9.4	11.7	16.3	24.8	41.0	56.9
2-L1.75"x1.75"x0.109"	6.8	6.8	10.8	8.2	10.4	14.8	22.9	38.5	53.7
2-L4"x4"x0.375"	498	530	643	544	592	686	849	1180	1810
2-L4"x4"x0.344"	386	411	511	428	470	552	696	990	1560
2-L4"x4"x0.313"	291	309	396	329	365	435	559	817	1330
2-L4"x4"x0.25"	150	160	222	179	204	252	340	528	915
2-L4"x4"x0.188"	64	68	110	83	100	130	186	308	569
2-L8"x8"x0.75"	4980	5380	5970	5360	5660	6240	7210	8990	12090
2-L8"x8"x0.625"	2910	3140	3590	3200	3420	3860	4600	5990	8450
2-L8"x8"x0.546"	1950	2110	2480	2190	2360	2700	3310	4460	6540
2-L8"x8"x0.5"	1500	1620	1950	1710	1860	2150	2670	3700	5550
2-L8"x8"x0.438"	1010	1100	1360	1180	1290	1520	1950	2790	4350
2-L8"x8"x0.375"	638	691	901	762	849	1020	1340	2010	3280

results highlighted that the modeled torsional stiffness was normally greater than the assumed 'Low C_w' condition.

Two different effective section properties were calculated for each model based on the results in Table 5.6 as discussed in further detail in Appendix E. An effective torsional stiffness, J_e, was determined neglecting warping. An effective warping stiffness, $C_{w,e}$, was calculated accounting for the fixed warping at the boundaries and the nominal torsional stiffness. While these section properties would not coexist, each value provides different context for how much the stiffness increased. As indicated by Table 5.6, the double angle finite element models without ties exhibited an increase in torsional stiffness compared to the theoretical pure twist behavior due to the composite behavior at the end. The increase varied with the cross-section thickness with some of the thicker sections only experiencing a 7% increase in J_e compared to the nominal J while thin sections saw increases up to 30%. The increased torsional stiffness became more pronounced as ties were included as shown in Fig. 5.6 and Fig. 5.7. The inclusion of a single tie resulted in a measurable increase in stiffness

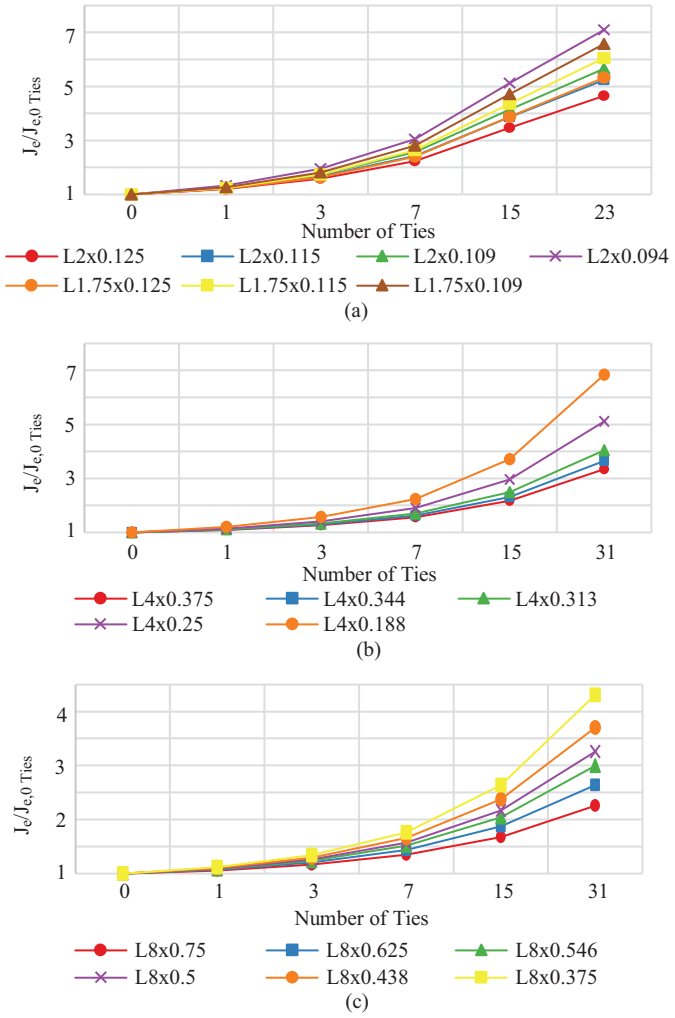

Figure 5.6: Influence of composite behavior on J_e of double angles

causing $C_{w,e}$ to at least double for all cross sections which translated to more than a 20% jump in J_e for Group 1 (see Table 5.1). The compact sections included as part of Group 2 and 3, which were expected to fail in flexural buckling, has smaller, but still substantial increases in stiffness. The effective cross-section properties of all cross sections were found to linearly increase proportional to the spacing between ties. This increased torsional stiffness aligns with the previous results that torsional behavior becomes less critical with additional connections between the angles.

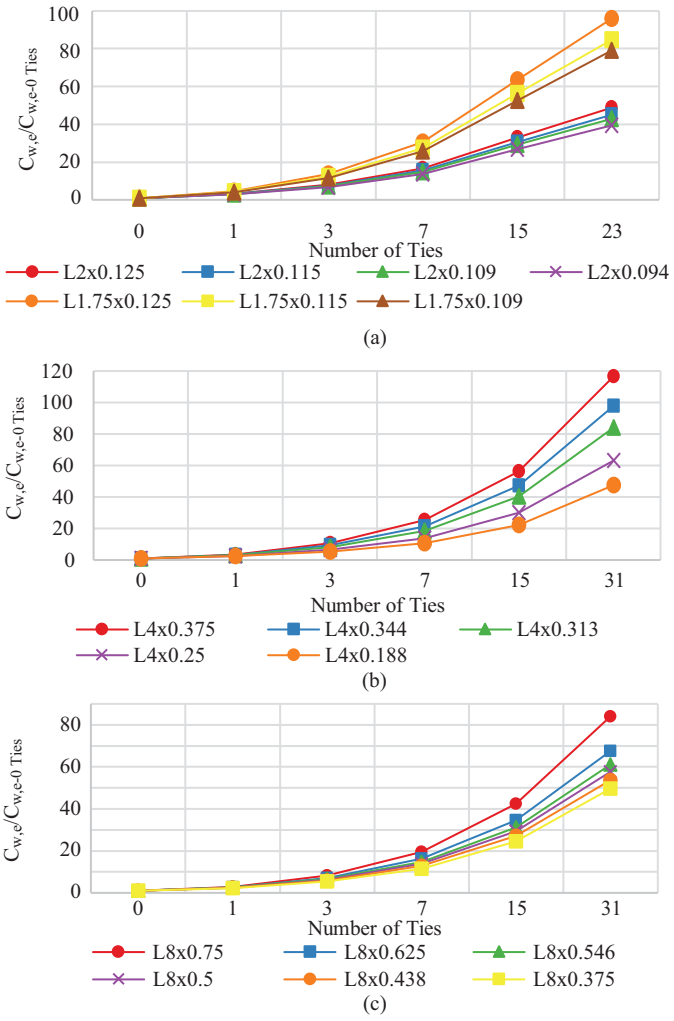

Figure 5.7: Influence of composite behavior on C_w of double angles

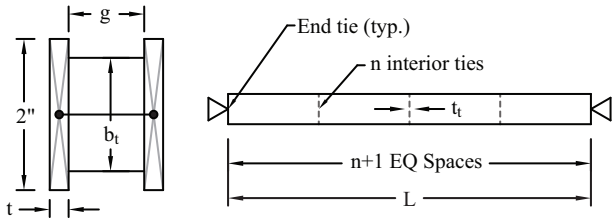

Figure 5.8: Geometry of parallel plates in torsion

Table 5.7: Variables for parametric torsion study

Variable	Options						
L (in)	48	96					
t (in)	0.0833	0.100	0.125	0.167	0.250		
g (in)	0.5	1	2				
n_t	0	1	2	3	7	15	31
b_t (in)	0.125	1.5					
t_t (in)	0.125	0.5					
Tie End	Fixed	Pinned					

5.5. Parallel Plates in Torsion

A line element study was completed to improve the understanding of the underlying mechanics causing the behavior in Section 5.4. A simplified example of 2-inch rectangular plates connected by intermediate ties, Fig 5.8, was considered to isolate the composite behavior response. The limited parametric study considered the influence of length, thickness, spacing of plates, and tie variations as detailed in Table 5.7.

The parametric study considered cantilevered parallel plates subjected to a defined rotation to determine a J_e when evaluated with MASTAN2 [17]. Each side plate was defined as 96 warping continuous line elements with the ends free to warp. Connection ties were divided into two line elements with free warping. A tie was provided at the end of the cantilevered plates in addition to n_t ties evenly spaced along the model as illustrated in Fig 5.8. The system was supported by a fully fixed support applied at the middle of one end tie, while the other end tie was subjected to a torsional rotation of 0.01 radians. The “Tie End" condition defined whether the ties were fixed or pinned for

Table 5.8: J_e/J_{nom} for 2" × t plates spaced 0.5" apart with (n_t) 1.5"x0.5" ties for L = 96 in

	t (in)	0.0833	0.1	0.125	0.167	0.25
	J_{nom} (in^3)	0.000772	0.00133	0.00260	0.00617	0.0208
Number of ties, n_t	0	1.04	1.03	1.02	1.01	1.01
	1	1.15	1.11	1.07	1.04	1.02
	2	1.31	1.22	1.14	1.08	1.04
	3	1.51	1.36	1.23	1.13	1.06
	7	2.63	2.10	1.68	1.36	1.14
	15	5.61	3.99	2.76	1.88	1.33
	31	12.64	8.31	5.13	2.97	1.70

bending moment to the plates. The corresponding connection was applied to both ends of the end ties; however, intermediate ties were only modified on one end to allow for shear force transfer between the plates in addition to axial forces and torsion.

Similar to the double angle study in Section 5.4, the parallel plate examples exhibited an increased torsional stiffness as additional ties were included. Table 5.8 shows that J_e was in agreement with the expected theoretical results, $J_{nom} = 2/3bt^3$, when no intermediate ties were included, but J_e significantly increased as additional ties were added. The thicker plate configurations were significantly stiffer than the thinner plate variations; however, the benefit of composite behavior was greater with thinner plates. The addition of one tie was found to increase the stiffness of the 0.083" plate variation by 10.4%, while only a 1.4% increase was observed with the 0.25" plate alternative. The torsional stiffness of the parallel plates was observed to be a function of the spacing between the ties as comparable results could be identified for the both model lengths when the tie spacing was equal, which can be found when comparing Table 5.8 to Table 5.9.

While the exact details of the mechanics were not evaluated in this study, the increased stiffness was attributed to a combined warping response. The rectangular plates behaved analogous to the flanges of an I-beam where the rectangular plates would support equal and opposite bending moments. That behavior was consistent with the results found by increasing the gap between the plates, summarized in Table 5.10, and reviewing the bending moment diagram shown in Fig. 5.9(a).

Table 5.9: J_e/J_{nom} for 2" × t plates spaced 0.5" apart with (n_t) 1.5"x0.5" ties for L = 48 in

	t (in)	0.0833	0.1	0.125	0.167	0.25
	J_{nom} (in^3)	0.000772	0.00133	0.00260	0.00617	0.0208
Number of ties, n_t	0	1.15	1.11	1.07	1.05	1.02
	1	1.53	1.37	1.24	1.14	1.06
	2	2.05	1.72	1.46	1.25	1.11
	3	2.68	2.13	1.70	1.37	1.15
	7	5.71	4.06	2.80	1.90	1.34
	15	12.80	8.42	5.20	3.01	1.71
	31	28.02	17.59	10.14	5.25	2.46

Table 5.10: J_e/J_{nom} for 2" × t plates spaced 2" apart with (n_t) 1.5"x0.5" ties for L = 48 in

	t (in)	0.0833	0.1	0.125	0.167	0.25
	J_{nom} (in^3)	0.000772	0.00133	0.00260	0.00617	0.0208
Number of ties, n_t	0	2.62	2.09	1.67	1.35	1.14
	1	5.50	3.90	2.68	1.82	1.29
	2	8.71	5.85	3.73	2.29	1.44
	3	12.06	7.85	4.79	2.75	1.58
	7	25.87	16.01	9.06	4.60	2.15
	15	53.93	32.44	17.60	8.28	3.28
	31	110.14	65.25	34.60	15.59	5.53

The section was observed to become stiffer as the gap widened similar to the relationship between a deeper I-beams and an increased C_w. The plates experienced equal and opposite strong-axis bending moments which would be equivalent to the bimoment bending in an I-beam flange. Unlike the moment in an I-beam flange due to bimoment which would correspond to a point-loaded cantilever moment distribution, the plates exhibited a saw-tooth moment pattern. The change in moment was possible due to a transfer of torsion through the tie connection.

The proceeding interaction relied on the stiff tie elements to achieve the increased strength. When replacing the 1.5"x0.5" tie with a much softer 1/8"x1/8" element, the large torsional stiffness increases were not observed as indicated by Table 5.11. Additional connections between the angles still improved composite behavior, but the tie flexibility resulted in minimal benefit. In fact, the large deformations within the tie itself led to an apparent reduction in torsional stiffness. An alternative investigation considered the effect of eliminating torsional connections with the stiffer 1.5"x0.5" tie. As shown in Fig. 5.9(b), the plate elements were not able to develop the same strong axis bending

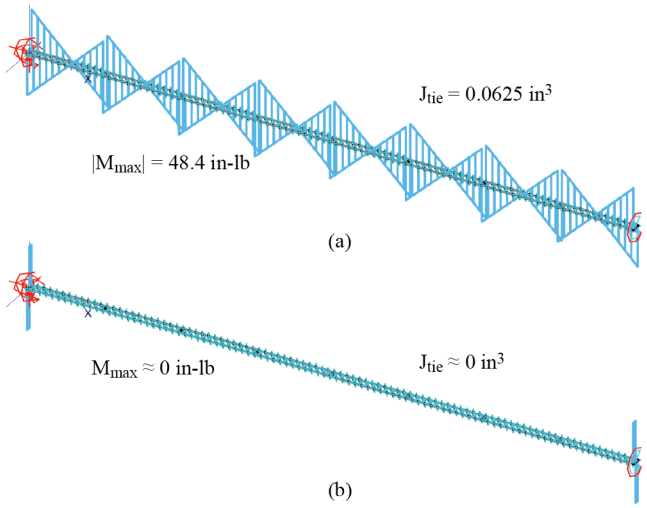

Figure 5.9: Strong-axis moment in parallel plates subjected to torsion. (a) Standard fixed tie connection (b) No torsion transferred through tie

Table 5.11: J_e/J_{nom} for 2" × t plates spaced 0.5" apart with (n_t) 1/8"x1/8" ties for L = 48 in

	t (in)	0.0833	0.1	0.125	0.167	0.25
	J_{nom} (in^3)	0.000772	0.00133	0.00260	0.00617	0.0208
Number of ties, n_t	0	0.92	0.87	0.76	0.55	0.25
	1	0.92	0.87	0.76	0.55	0.25
	2	0.92	0.87	0.76	0.56	0.25
	3	0.93	0.87	0.76	0.56	0.26
	7	0.93	0.88	0.77	0.58	0.28
	15	0.95	0.89	0.79	0.61	0.31
	31	0.97	0.91	0.82	0.66	0.36

response and the composite behavior was eliminated causing the section to only exhibit J_{nom} for the torsional stiffness.

5.6. The Effective of Increased Torsional Stiffness

The torsional stiffness of double angles is a combination of the twisting and warping response associated with the J and C_w, respectively. While there might be an small increase in J due to singly-symmetric sections twisting as a composite member, a significant portion of the increased

response was attributed to warping. To consider the impact of the increased section properties, the original inelastic buckling study from Section 2.4 was reevaluated with the nominal J and calculated $C_{w,e}$ from Section 5.4 for 1 tie between the chord for the members. The effective end restraint captured in the full joist and chord segment modeling was also considered by implementing the effective torsional buckling length factors of 1.0 and 0.5 with complete results in Appendix F. The tangential buckling response without the local buckling reduction, labeled '$\tau_G = 1.0$ w/o Q', was also plotted to understand the influence of local buckling reductions. As depicted in Fig. 5.10, the increased torsional restraint and torsional stiffness resulted in minimal difference between the expected behavior, line '$\tau_G = 1.0$', and the flexural buckling design provisions after the application of local buckling reductions. However, global flexural-torsional buckling was observed to be the controlling behavior for cross sections with high slenderness, $b/t > 16$, Fig. 5.11. In these instances, local buckling reductions were not large enough to simulate the low global flexural-torsional buckling capacity, which was so low that local buckling reductions do not apply. Although this observation indicates there is a limit when flexural-torsional buckling is critical, none of the representative cross-section sizes recommended by SJI exceeded the $b/t > 16$ limit, and therefore the limit only applied to the theoretical sizes considered in the extended study.

Flexural buckling reduced by local buckling was observed to regularly control the buckling capacity of double angles. This response was evaluated for the original representative cross-section sizes in Table 2.1 by utilized an approximate $C_{w,e}$ equal to 70% of the "High C_w" and a partial warping fixity with an effective torsion length factor of 0.7. The resulting buckling analysis, see App. F.2 for additional details, found most sections were controlled by flexural buckling. When flexural-torsional buckling did control, the capacity was found to be within 3% of the flexural buckling result.

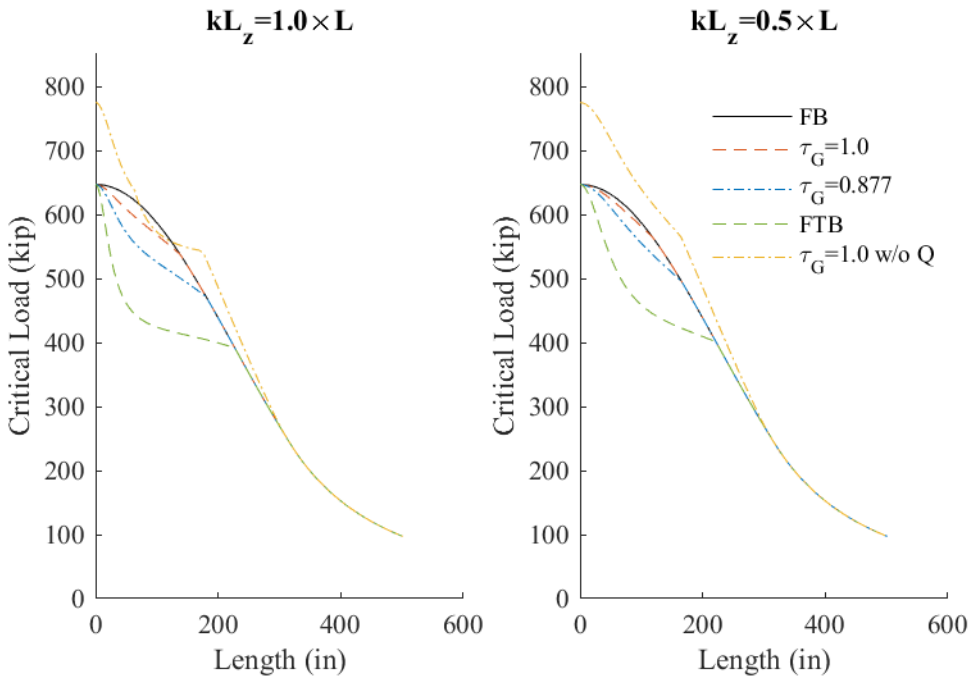

Figure 5.10: Theoretical buckling capacity of 2-L8"x8"x0.5" with effective section properties

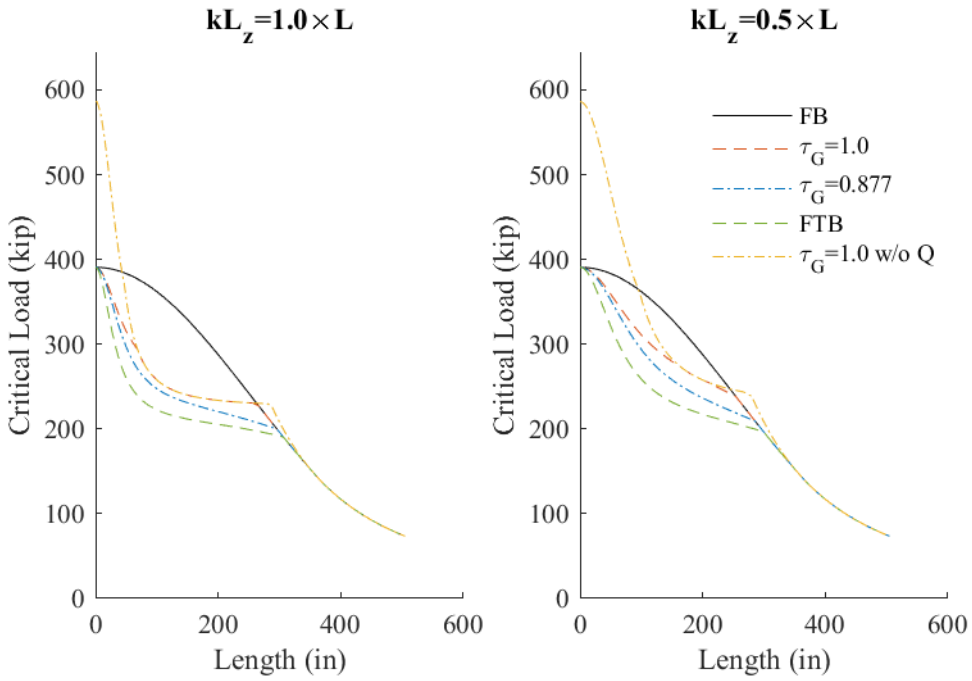

Figure 5.11: Theoretical buckling capacity of 2-L8"x8"x0.375" with effective section properties

5.7. Discussion

The torsional stiffness of composite members was observed to be greater than conventional design assumptions. While the double angle geometry exhibits similarities to a tee section, the separation between the vertical legs causes the analogy to fail for the description of warping and underestimates the member torsional stiffness. This underestimation of torsional stiffness causes flexural-torsional buckling to appear more critical in design provisions than it actually is as was demonstrated in Section 2.4. However, the warping behavior of the composite cross section requires the ability to adequate transfer the necessary forces. This investigation consider relatively stiff ties over the height of the double angle members, which would readily transfer torsion and moments between the chord angles. As shown in Section 5.5 with the parallel plates study, if the connection is too soft or unable to transmit torsion, like a single bolt, it may be appropriate to assume there is no benefit from composite behavior.

The increased torsional stiffness of the double angles considered in this study resulted in flexural buckling controlling the design behavior. However, that does not mean torsional behavior is not an important component of the limit state. All modeled cross sections were noncompact or slender, which requires the incorporation of local buckling reductions. This local buckling would equate to the flexural-torsional buckling mode of each angle as an independent member [18, 19]. For single angles, the flexural-torsional buckling condition does not need to be checked as the local buckling criteria adequately reduces the flexural buckling capacity to address torsional concerns [5, 18], and hence avoids penalizing the capacity of the member twice for the same effect. For double angles, standard engineering practice currently accounts for minimal torsional stiffness benefits, but applies the full penalty of non-compact sections. Therefore, designs according to the SJI Specification are only reduced due to local buckling while designs according to the AISC Specification are reduced

due to both global flexural torsional buckling and local buckling for similar behaviors. Determining an appropriate balance of these factors will be critical to establishing a uniform design approach for all double angle configurations.

6. Recommendations

6.1. Summary

This report summarizes a study on flexural-torsional buckling in double angle cross sections for joist and joist girder chords. An inelastic buckling investigation found that while flexural-torsional buckling is not as critical as treated by current AISC design procedures, flexural-torsional buckling is theoretically important for a number of double angle cross sections due to limited nominal torsional stiffness.

A series of double angles were evaluated using full joist finite element models that were expected to fail in flexural-torsional buckling with a total of three base models and eighteen different cross sections. The resulting analysis found that these chords were buckling at or above the SJI flexural buckling limits. The chord deformations were observed to have a combination of local behaviors interacting with the global buckling modes.

An isolated chord segment buckling study was completed to validate the joist study results. Elastic buckling evaluations indicated that local angle behavior between ties was a significant factor in defining the overall deformation of the cross sections. The resulting capacities were greater than the expected theoretical design-based results, while depicting both global and individual angle flexural-torsional buckling. This behavior was due to increased composite torsional stiffness, confirmed by additional modeling, but is often ignored in design. The increased torsional stiffness caused the inelastic buckling capacity to be controlled by flexural buckling with local twisting of the individual angles. A reevaluation of the original inelastic buckling calculations with updated section properties

and a reduced effective length for torsional buckling resulted in agreement between the observed behavior and the underlying theory.

6.2. Conclusion

The results of this study indicate that the SJI approach of only considering flexural buckling with local buckling reductions seems to be an appropriate design approach for joist chords. The joist chord configuration results in an increased torsional stiffness section property in addition to increased torsional restraint due to continuity and web members. All these factors cause global flexural-torsional buckling behavior to be less significant than the current AISC Specification design approach. The individual twisting of angles cannot be eliminated, but this behavior is accounted for in the local buckling reductions.

A recommendation to continue to design joist chords by considering flexural buckling with local buckling reductions and neglecting flexural-torsional buckling comes with a few significant limitations. First, the results of this study rely on the stiffness of the connection between the chord angles. The vertical solid steel tie provided a relatively stiff connection over the entire height of the chord angles allowing for a highly composite response. The effects of variables such as tie size, tie orientation, tie geometry, and angle-to-angle spacing were not thoroughly evaluated. A softer chord-to-chord connection could reduce the effective torsional stiffness, as shown in the composite plate study in Section 5.5, resulting in a drop in capacity. This would not be critical for all cross section sizes; however, when using thinner sections to create an efficient design, this issue would be present.

Local buckling would be another key consideration as this component is required to address flexural-torsional buckling concerns within the member as a whole and the individual angles. It

was observed that for double angle chords with high leg slenderness, $b/t > 16$, the local buckling reduction did not fully capture the anticipated torsional behavior. While such sections were indicated to not be common in joist chord applications per SJI, additional work would be needed to refine this constraint and any appropriate additional reduction to predict the expected capacity. It should be noted that all of this work utilized a nominal 50 ksi material. Any consideration of implementing a higher strength material could alter the local buckling reduction leading to a modified slenderness constraint.

Finally, the effective warping restraint developed in the chord is a necessary factor for the cross sections with intermediate torsional stiffness to be adequately designed when neglecting flexural-torsional buckling. The continuity of the chord and the web connections provide restraint that allows for additional load to be supported as the chord begins to approach the buckling limit. However, the parameters of this study implemented relatively stiff webs. The initial designs provided for this study, which had similar demand-to-capacity ratios for all members, required multiple web members to be increased in size to ensure the chords failed first in an inelastic finite element analysis of the full joist. Then, only the chord size was reduced in the subsequent analyses, which resulted in joists that incorporated larger than typical web sizes and thus more restraint provided by the webs. This study did not attempt to identify the critical web stiffness to brace the chord in torsion; however, utilizing a short unbraced double angle chord length would require strong web members which may minimize the concern.

Additional work should be completed to refine these limitations to provide more detailed recommendations on double angle chord construction to ensure the current design approach adequately predicts the capacity of compression members.

Bibliography

[1] SJI. *Standard Specifications: Load Tables and Weight Tables for Steel Joists and Joist Girders SJI 100-2020*. Steel Joist Institute, Florence, SC, 45th edition, 2020.

[2] AISC. *Specification for Structural Steel Buildings ANSI/AISC 360-16*. American Institute of Steel Construction, Chicago, IL, 2016.

[3] Simpson Gumpertz & Heger. Parameter Study to Assess Modifications to the SJI Design Equations for Buckling of HSLA-V Steels. Technical report, Simpson Gumpertz & Heger, Inc., San Francisco, CA, 2011.

[4] Nicholas S. Trahair. *Flexural-Torsional Buckling of Structures*. Spon, London; New York, 1st edition, 1993.

[5] Theodore V. Galambos. Design of axially loaded compressed angles. In *Proceedings of the 1991 SSRC Annual Stability Conference: "Inelastic Behavior and Design of Frames"*, pages 353–367, Chicago, IL, 1991. SSRC.

[6] AISC. *Specification for Structural Steel Buildings ANSI/AISC 360-10*. American Institute of Steel Construction, Chicago, IL, 2010.

[7] Theodore V Galambos. Inelastic lateral buckling of beams. *Journal of the Structural Division*, 89(5):217–242, 1963.

[8] S Kitipornchai and HW Lee. Inelastic buckling of single-angle, tee and double-angle struts. *Journal of Constructional Steel Research*, 6(1):3–20, 1986.

[9] Nicholas S. Trahair and Sritawat Kitipornchai. Buckling of inelastic I-beams under uniform moment. *Journal of the Structural Division*, 98(11):2551–2566, 1972.

[10] B. G. Neal. The lateral instability of yielded mild steel beams of rectangular cross-section. *Philosophical Transactions of the Royal Society of London. Series A, Mathematical and Physical Sciences*, 242(846):197–242, 1950.

[11] CISC. *Torsional Section Properties of Steel Shapes*. Canadian Institute of Steel Construction, 2002.

[12] Joseph Robert Yost, David W. Dinehart, Shawn P. Gross, Joseph J. Pote, and Brian Gargan. Strength and Design of Open Web Steel Joists with Crimped-End Web Members. *Journal of Structural Engineering*, 130(5):715–724, 2004.

[13] Joseph Robert Yost, David W. Dinehart, Shawn P. Gross, Joseph J. Pote, and James Deeney. Buckling Strength of Single-Angle Compression Members in K-Series Joists. *AISC Engineering Journal*, (2):141–152, 2006.

[14] Dassault Systems. *Abaqus/CAE*. V6.16, Johnston, RI: Dassault Systems, 2015.

[15] EN 1993-1-5. *Eurocode 3: Design of Steel Structures - Part 1-5: Plated Structural Elements*. European Committee for Standardisation, 2009.

[16] ASM International. *Atlas of Stress-Strain Curves*. ASM International, 2002.

[17] Ronald D. Ziemian, William McGuire, and Si-Wei Liu. *MASTAN2 v5.0.2*. 2019.

[18] Kim J.R. Rasmussen. Design of Angle Columns with Locally Unstable Legs (No. R830). Technical report, School of Civil Engineering, The University of Sydney, 2003.

[19] Behnam Behzadi-Sofiani, Leroy Gardner, M. Ahmer Wadee, Pedro B. Dinis, and Dinar Camotim. Behaviour and design of fixed-ended steel equal-leg angle section columns. *ce/papers*, 4(2-4):1096–1105, 2021.

[20] S. W. Liu, G. L. Gao, and R. D. Ziemian. Improved line-element formulations for the stability analysis of arbitrarily shaped open-section beam-columns. *Thin-Walled Structures*, 141:526–539, 2019.

[21] Paul A. Seaburg and Charles J. Carter. *Torsional analysis of structural steel members*. AISC,

1997.

Appendices

A. Warping Constant of Double Angles

Limited information was available on the warping constant, C_w, of a double angle section acting as a composite member. Typical considerations for the C_w include assuming that it is conservatively equal to zero [2] or using twice the value of an individual angle assuming no composite response [11]. In both application, the shear center is assumed to be located on the axis of symmetry in line with the horizontal flanges. While these values would provide useful lower estimates of strength, it was desired to have an upper bound solution accounting for a composite response of double angles. The following calculations summarize the approach used to determine the upper bound for C_w based on a thin-walled approximation.

Fig. A.1 illustrates the assumed geometry and orientation of the double angle member where b is the length of the horizontal leg, h is the length of the vertical leg, t is the thickness of the section, and g is the distance between the centerline of the vertical legs, which is the physical distance between the vertical legs plus t. The position of the centroid relative to the top flange, $\bar{y}$, is calculated per Eq. A.1.

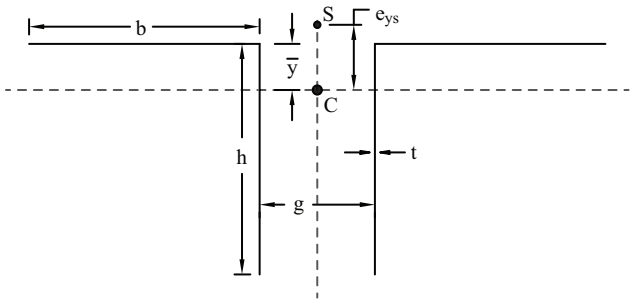

Figure A.1: Double angle cross section dimensions

$$\bar{y} = \frac{h^2}{2(b+h)} \tag{A.1}$$

With the cross section defined, it is possible to calculate the cross-sectional area, A, per Eq. A.2 and the area moments of inertia of the section, I_x and I_y, per Eq. A.3 and Eq. A.4, respectively. The product area moment of inertia, I_{xy}, is zero due to vertical axis symmetry about the vertical axis.

$$A = 2(b+h)t \tag{A.2}$$

$$I_x = 2\left(\frac{bt^3}{12} + bt\bar{y}^2 + \frac{h^3t}{12} + ht\left(\frac{h}{2} - \bar{y}\right)^2\right) \tag{A.3}$$

$$I_y = 2\left(\frac{b^3t}{12} + bt\left(\frac{b+g}{2}\right)^2 + \frac{ht^3}{12} + ht\left(\frac{g}{2}\right)^2\right) \tag{A.4}$$

Determination of the updated shear center and C_w required the evaluation of the warping constant of the cross-section. Typical thin-walled cross-section theory, as detailed in Liu et al. [20], requires a continuous cross section to properly define the warping parameters. For the double angle cross section, a connection between the heels of the angles was assumed to exist. While the connection forces the two angle sections to behave together, it was assumed that the connection had no thickness such that it did not further contribute to the stiffness of the cross section. Utilizing this tie, it was possible to determine the updated shear center position relative to the centroid as $(0, e_{ys})$ where e_{ys} is given by Eq. A.5.

$$e_{ys} = \frac{h^2\left(2b^3 + 3b^2g + 3bg^2 + 3g^2h\right)}{(b+h)\left(4b^3 + 6b^2g + 3bg^2 + 3g^2h + ht^2\right)} \tag{A.5}$$

The updated shear center position defined an normalized warping distribution as shown in Fig. A.2 which was used to determine the updated C_w estimate given in Eq. A.6.

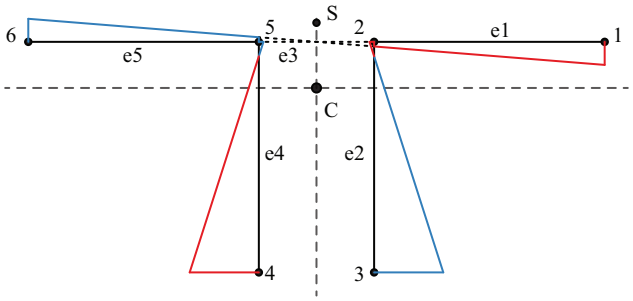

Figure A.2: Assumed combined warping behavior

$$
\begin{aligned}
C_w = & \frac{th^3}{12(b+h)^2\left(4b^3+6b^2g+3bg^2+3g^2h+ht^2\right)^2}\Big(9(2b+h/2)(b+h)^3g^6 \\
& +9(8b+5h)(b+h)^2b^2g^5+3(4b+h)(b+h)^2(10b^3+ht^2)g^4 \\
& +24(4b^3+ht^2)(b+h)^2b^2g^3+3b^2gh^3t^4+32b^3h^3t^4 \\
& +(32b^7+32b^6h+16b^4ht^2+16b^3h^2t^2+2h^2t^4b+13/2h^3t^4)(b+h)g^2\Big)
\end{aligned}
\tag{A.6}
$$

B. Elastic Behavior of Double Angles

This Appendix contains the plots for theoretical elastic buckling as described in Section 2.1. The evaluations consider a 1" gap between the vertical legs of the double angle members and utilizes a C_w of twice the value of the single angle section. The plots are normalized considering the F_y for buckling behavior and minimum radius of gyration for the length of the member. Each plot includes the flexural buckling stress about the x-axis, f_x; the flexural buckling stress about the y-axis, f_y; the torsional buckling stress, f_z; the controlling buckling stress from the interaction of flexural and torsional buckling, f_{el}; and the local buckling stress, f_L.

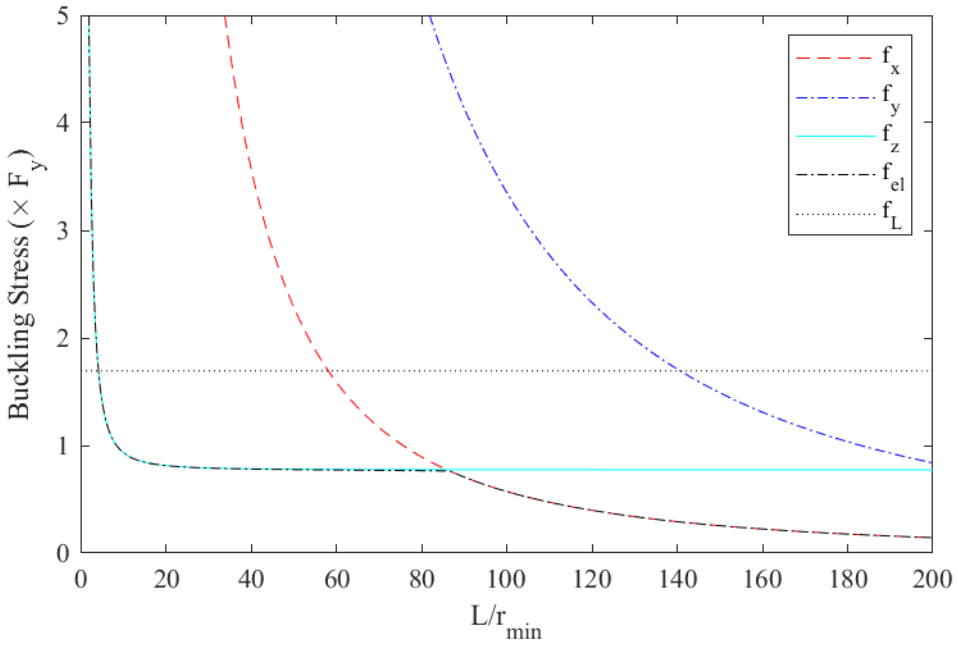

Figure B.1: Elastic buckling of 2-L1.25"x1.25"x0.109"

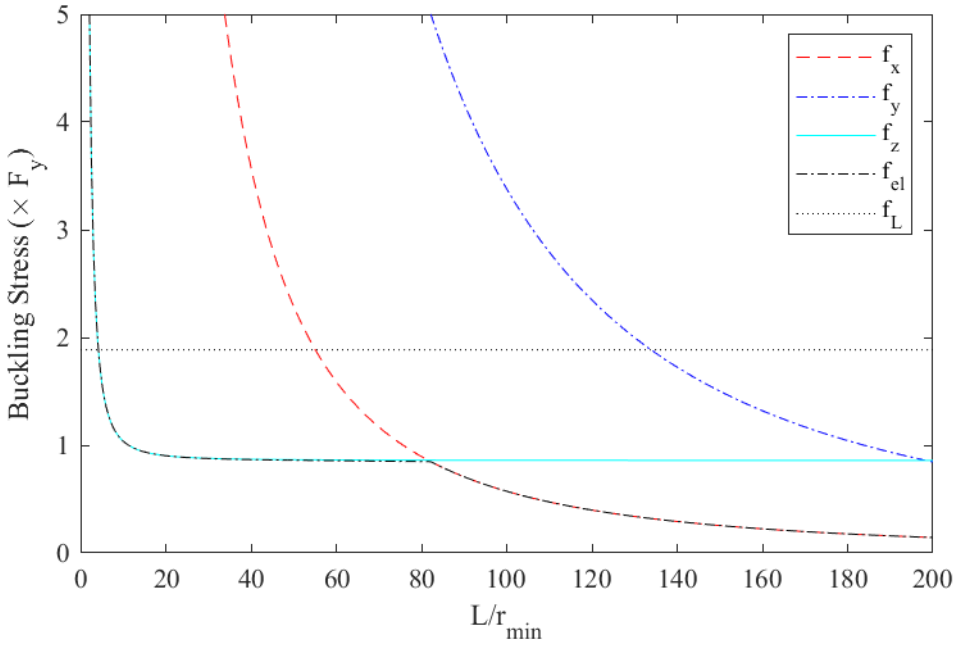

Figure B.2: Elastic buckling of 2-L1.25"x1.25"x0.115"

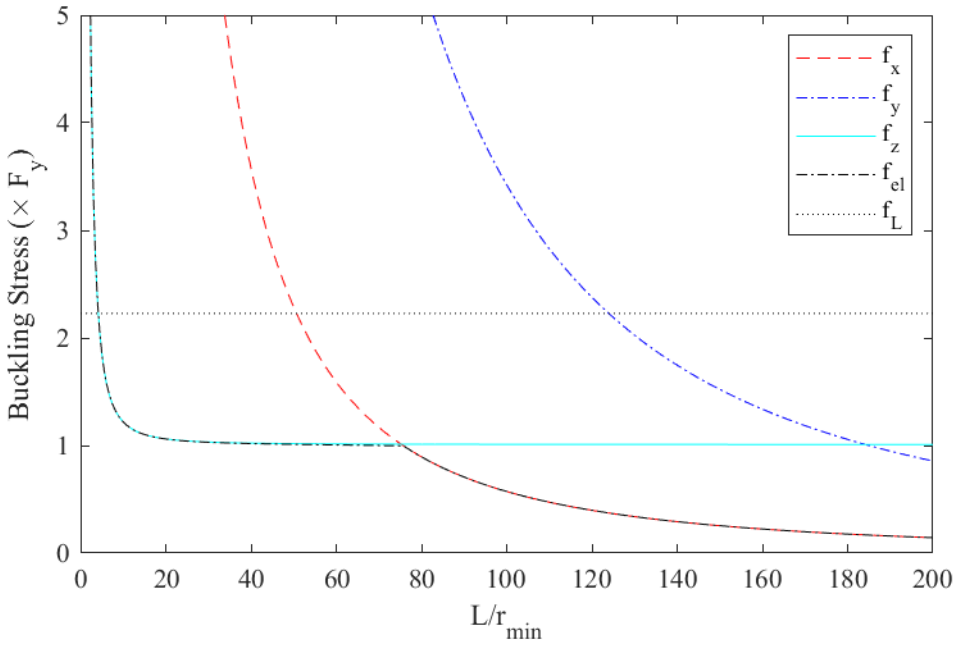

Figure B.3: Elastic buckling of 2-L1.25"x1.25"x0.125"

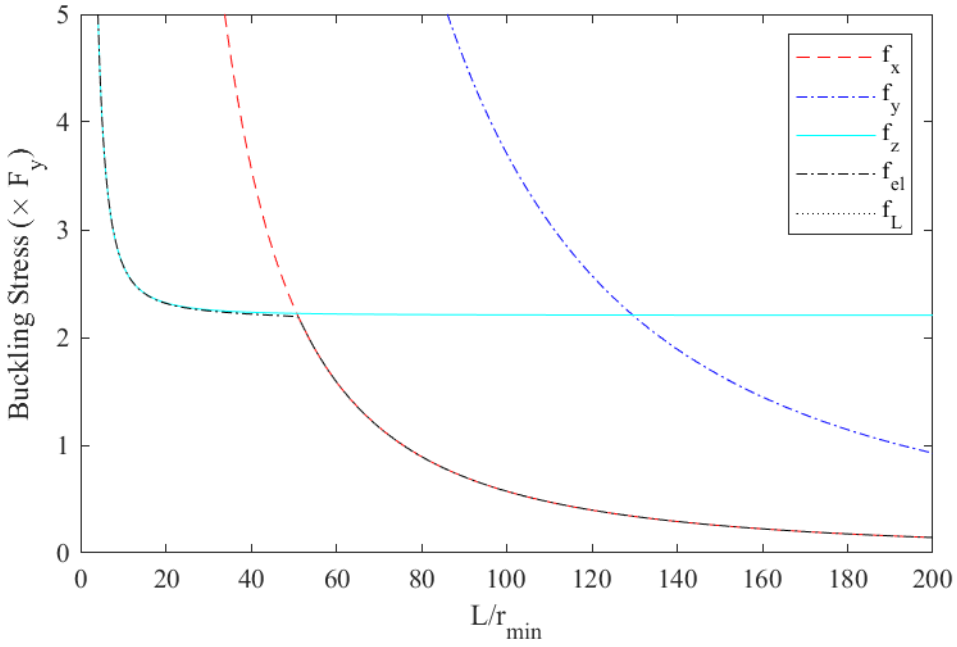

Figure B.4: Elastic buckling of 2-L1.25"x1.25"x0.188"

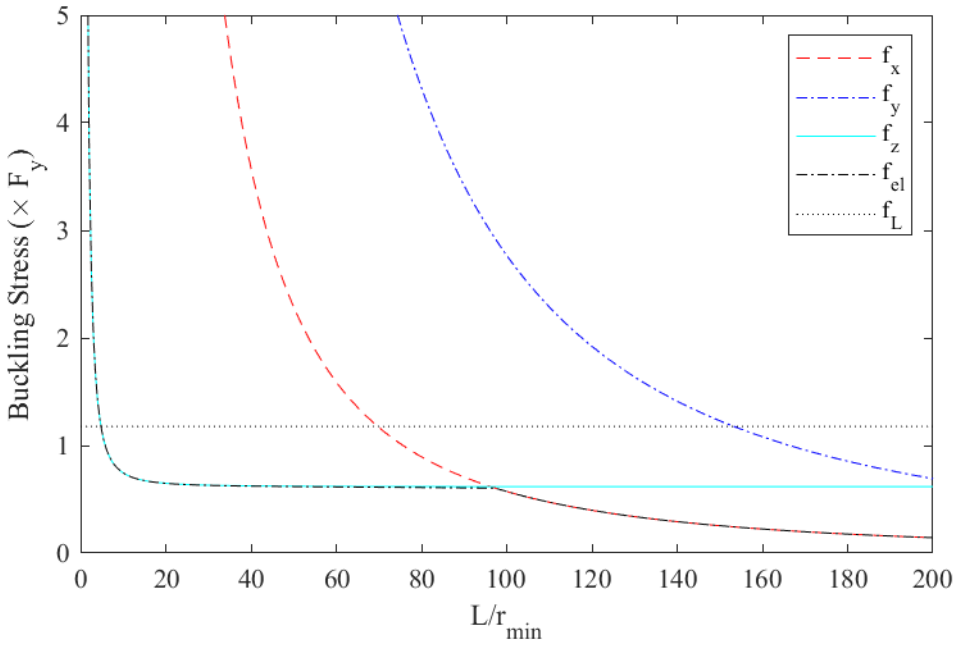

Figure B.5: Elastic buckling of 2-L1.5"x1.5"x0.109"

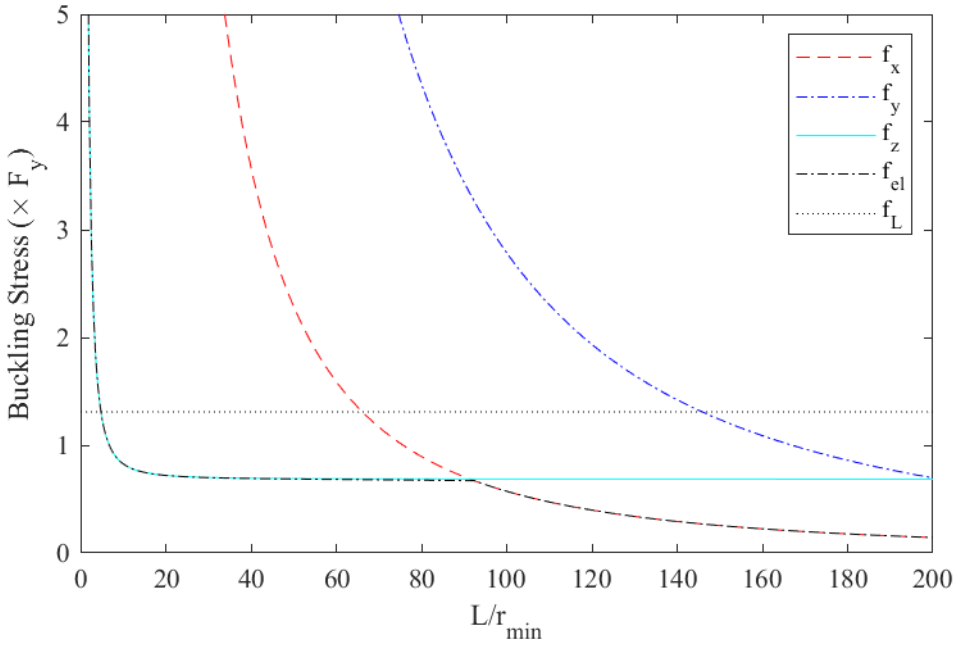

Figure B.6: Elastic buckling of 2-L1.5"x1.5"x0.115"

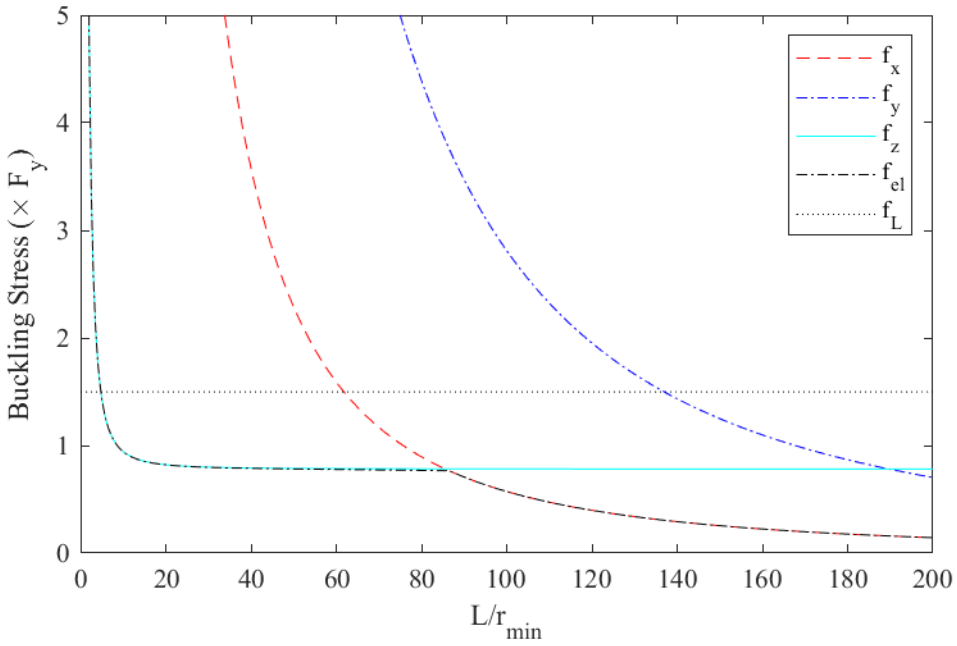

Figure B.7: Elastic buckling of 2-L1.5"x1.5"x0.123"

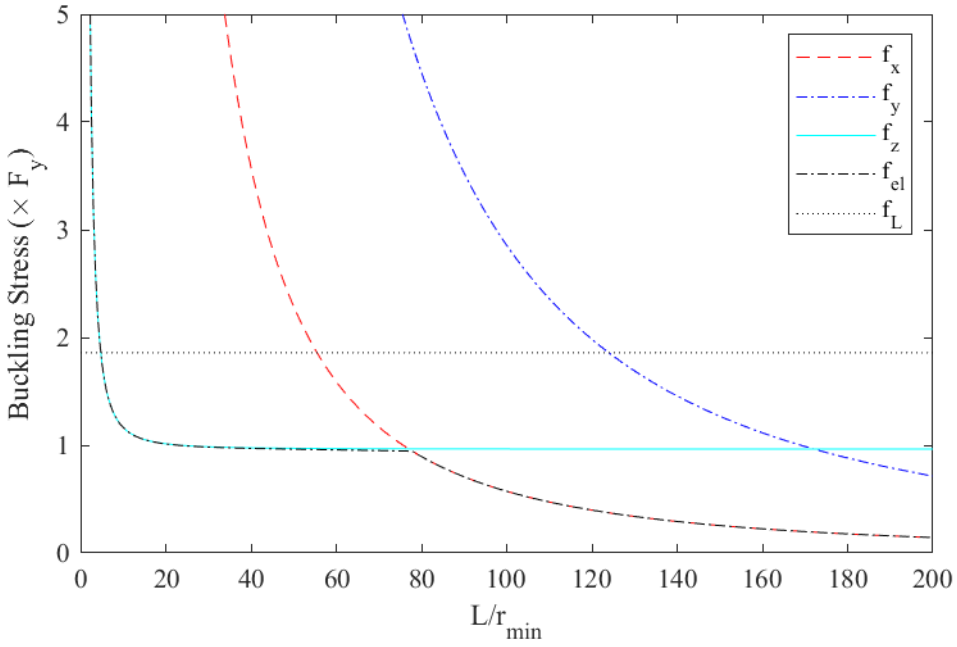

Figure B.8: Elastic buckling of 2-L1.5"x1.5"x0.137"

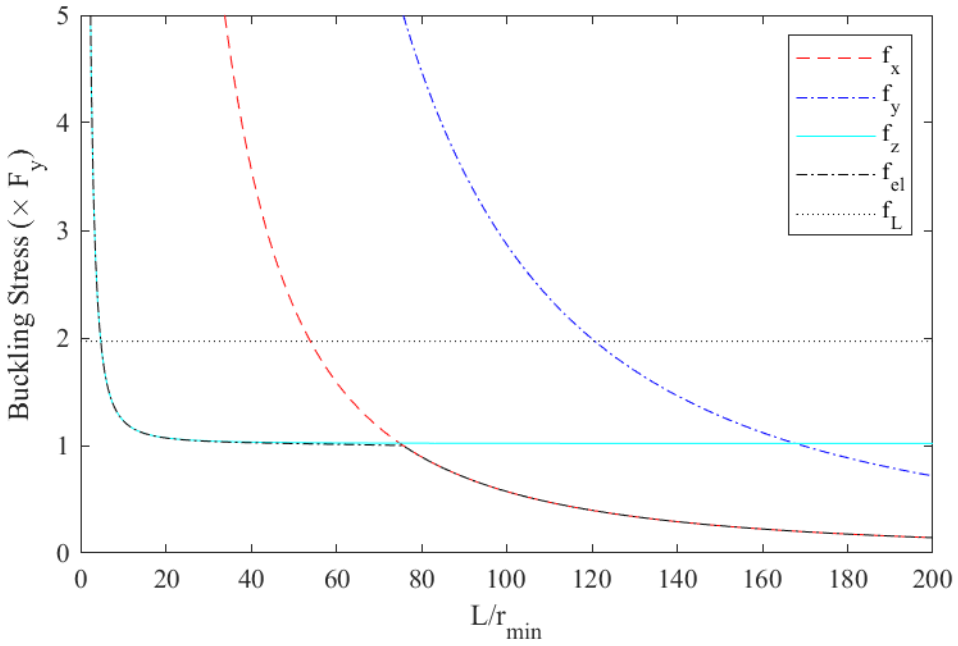

Figure B.9: Elastic buckling of 2-L1.5"x1.5"x0.141"

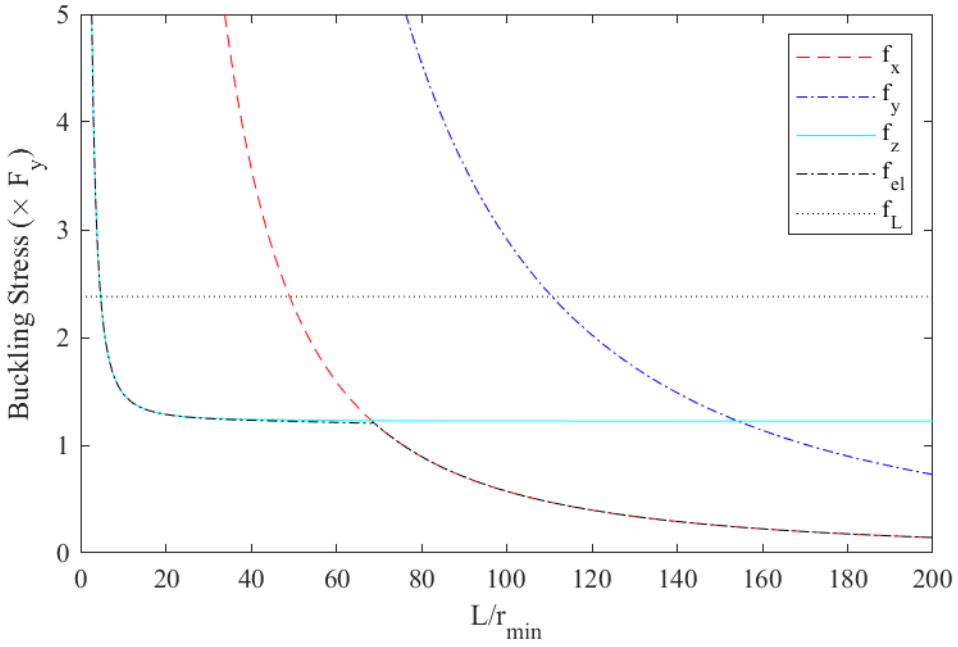

Figure B.10: Elastic buckling of 2-L1.5"x1.5"x0.155"

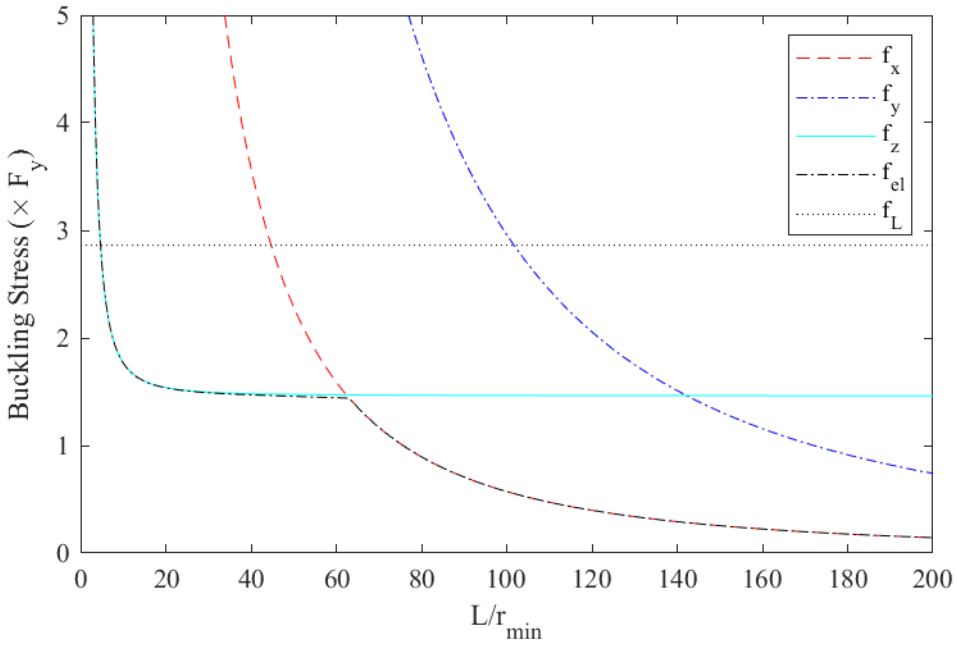

Figure B.11: Elastic buckling of 2-L1.5"x1.5"x0.17"

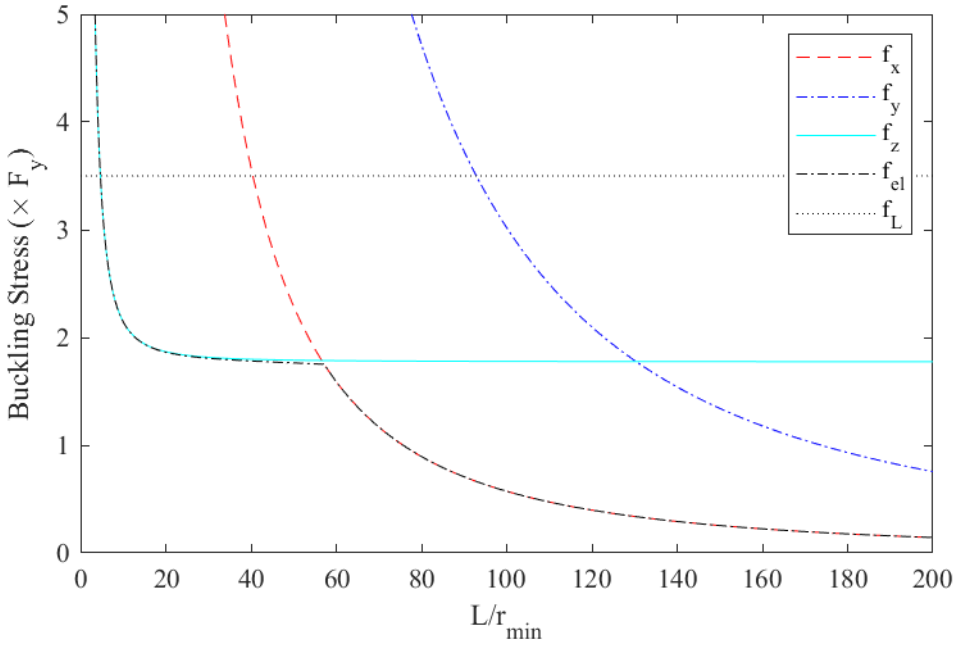

Figure B.12: Elastic buckling of 2-L1.5"x1.5"x0.188"

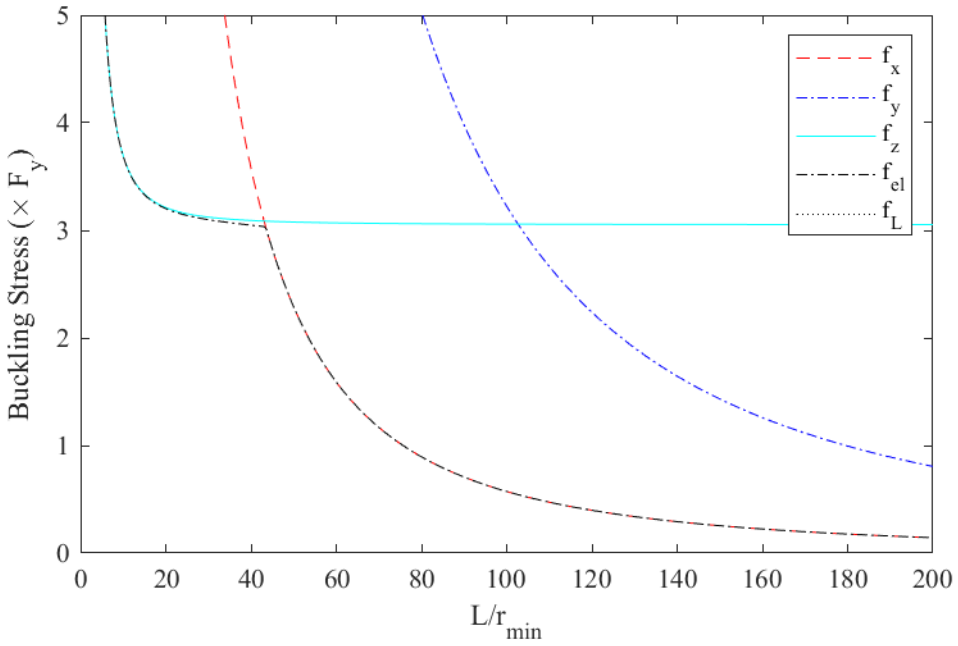

Figure B.13: Elastic buckling of 2-L1.5"x1.5"x0.25"

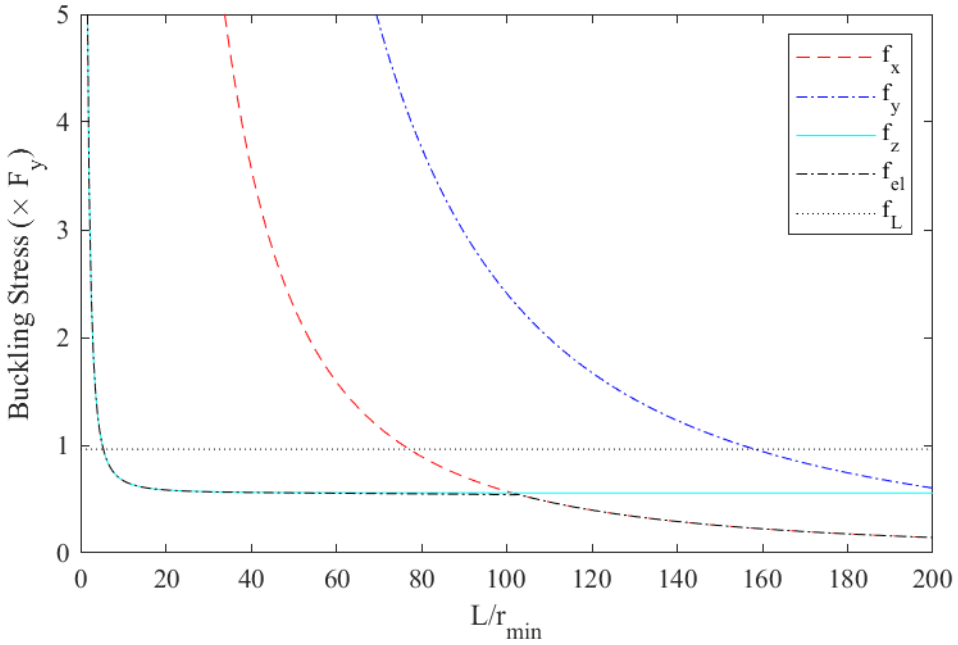

Figure B.14: Elastic buckling of 2-L1.75"x1.75"x0.115"

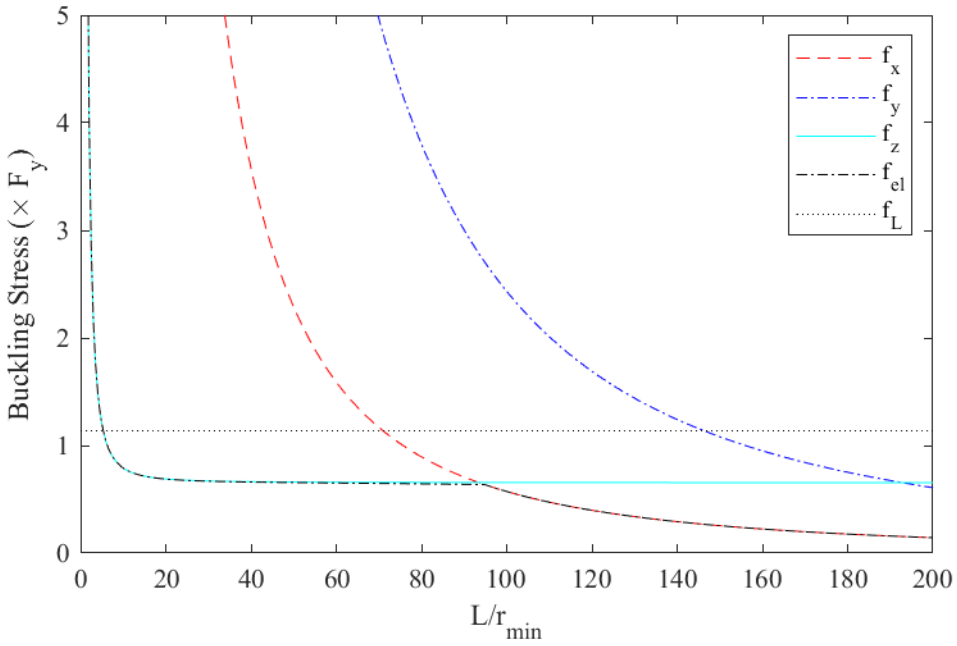

Figure B.15: Elastic buckling of 2-L1.75"x1.75"x0.125"

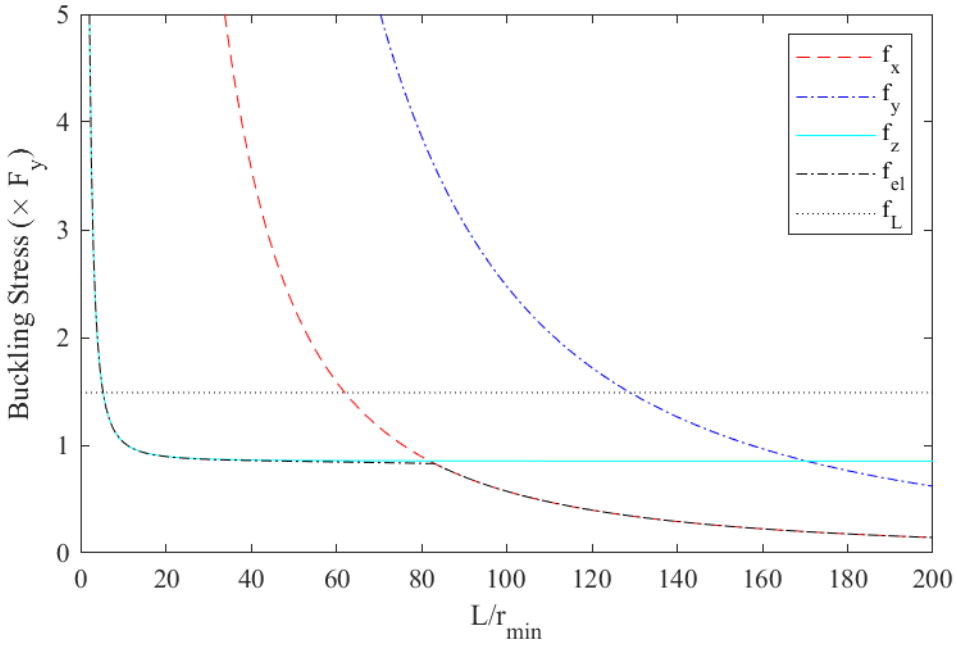

Figure B.16: Elastic buckling of 2-L1.75"x1.75"x0.143"

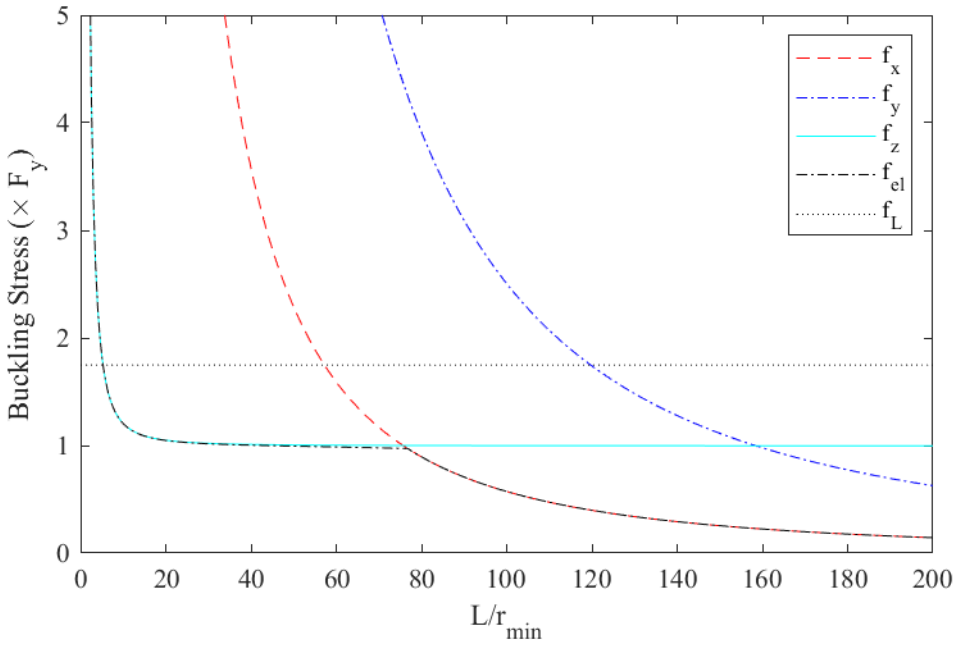

Figure B.17: Elastic buckling of 2-L1.75"x1.75"x0.155"

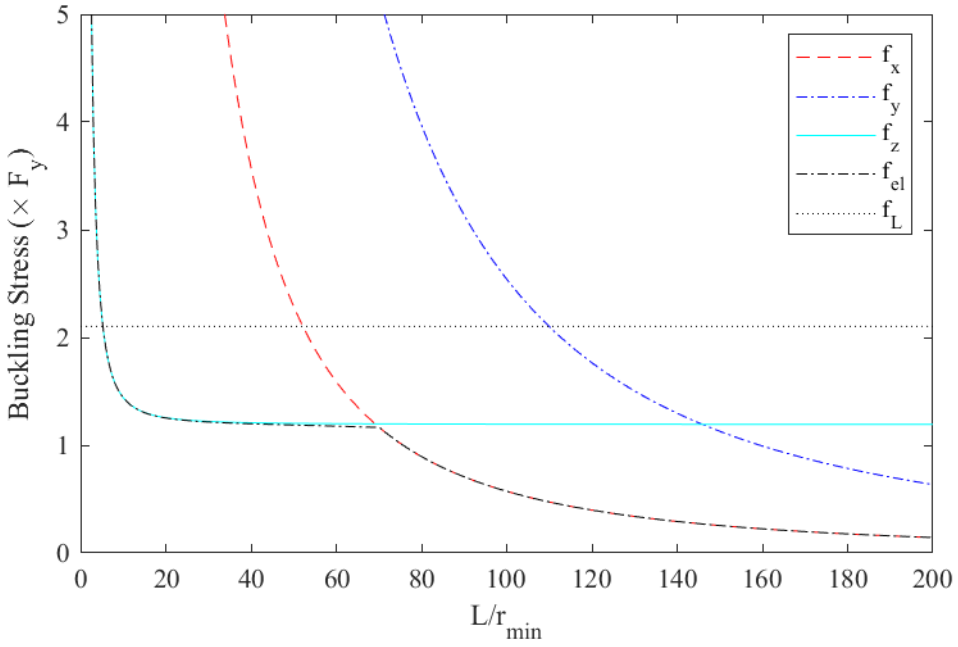

Figure B.18: Elastic buckling of 2-L1.75"x1.75"x0.17"

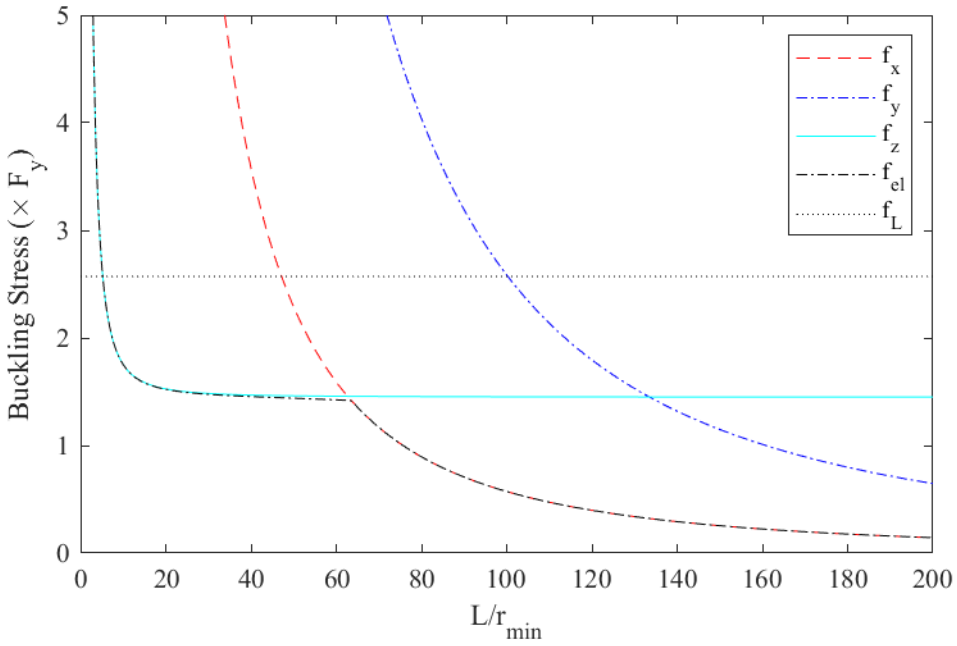

Figure B.19: Elastic buckling of 2-L1.75"x1.75"x0.188"

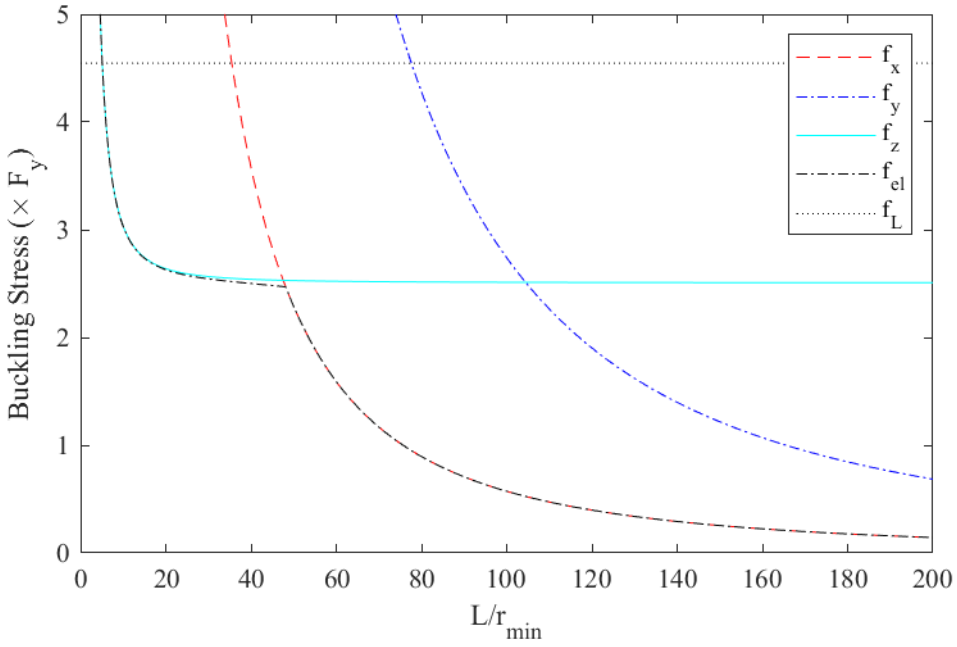

Figure B.20: Elastic buckling of 2-L1.75"x1.75"x0.25"

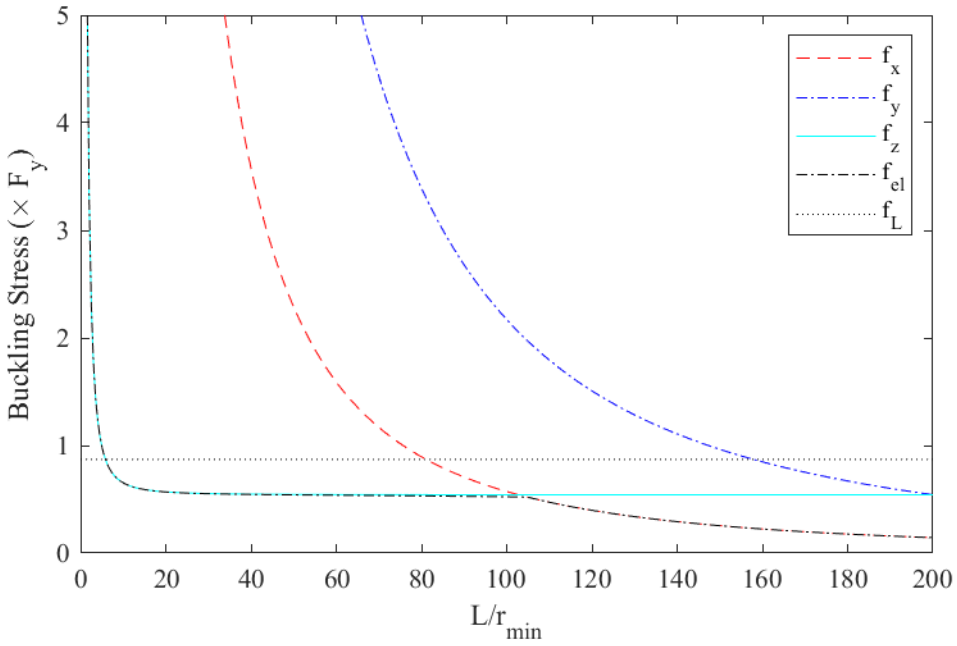

Figure B.21: Elastic buckling of 2-L2"x2"x0.125"

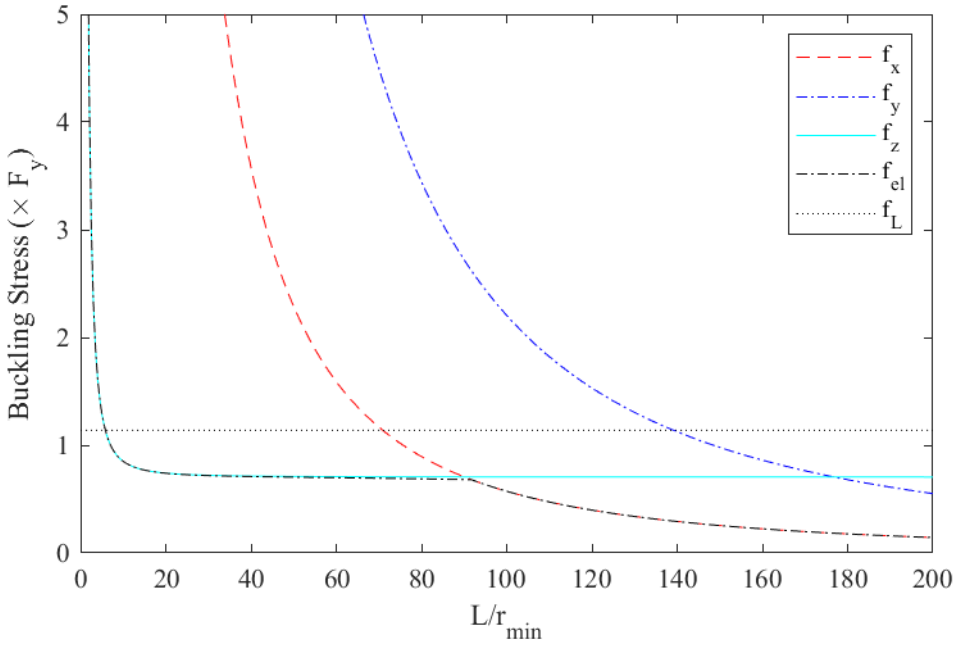

Figure B.22: Elastic buckling of 2-L2"x2"x0.143"

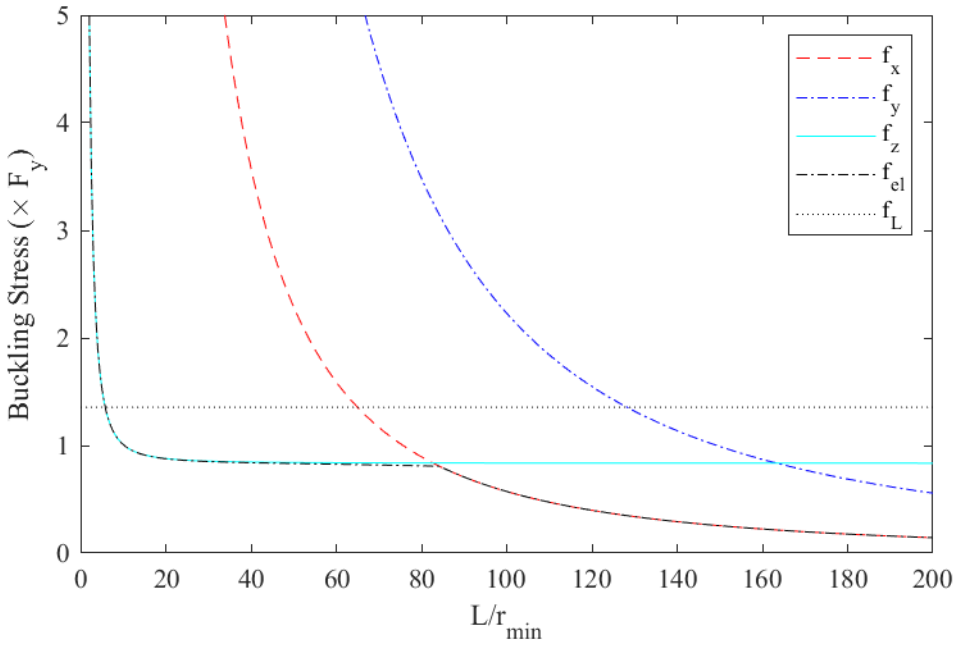

Figure B.23: Elastic buckling of 2-L2"x2"x0.156"

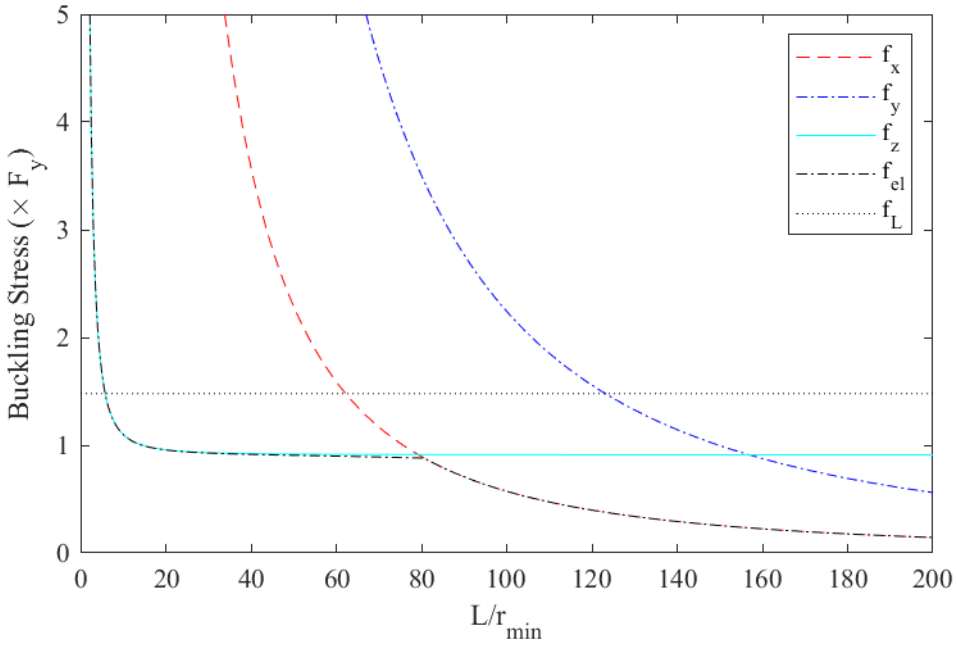

Figure B.24: Elastic buckling of 2-L2"x2"x0.163"

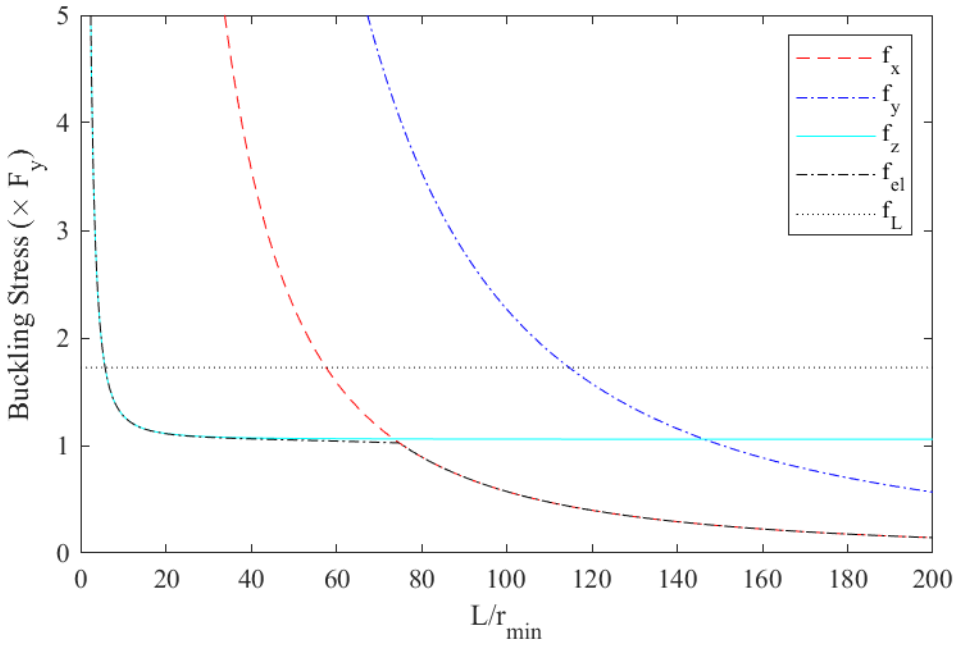

Figure B.25: Elastic buckling of 2-L2"x2"x0.176"

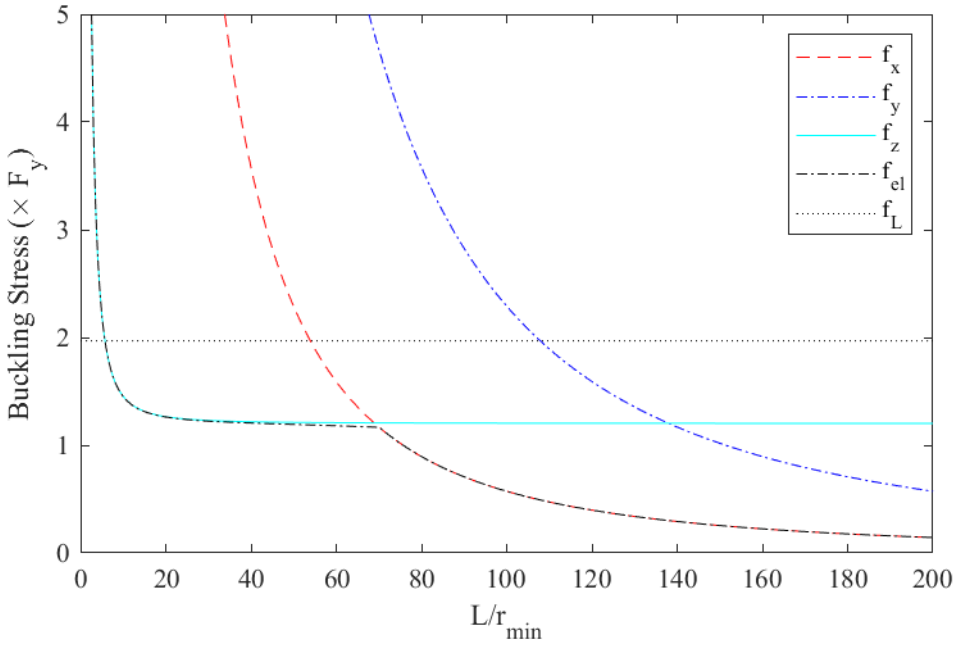

Figure B.26: Elastic buckling of 2-L2"x2"x0.188"

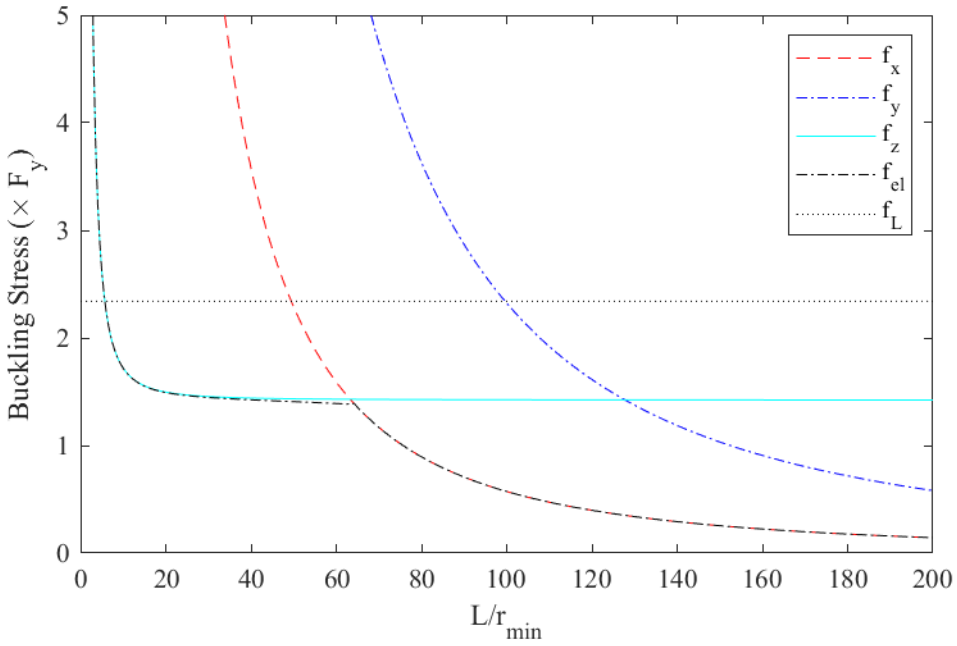

Figure B.27: Elastic buckling of 2-L2"x2"x0.205"

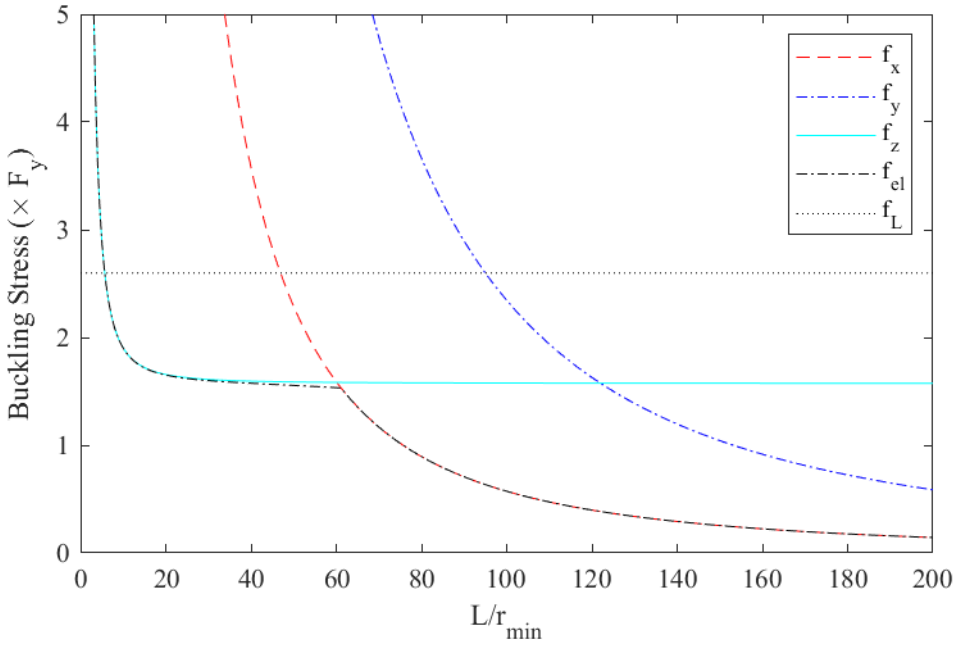

Figure B.28: Elastic buckling of 2-L2"x2"x0.216"

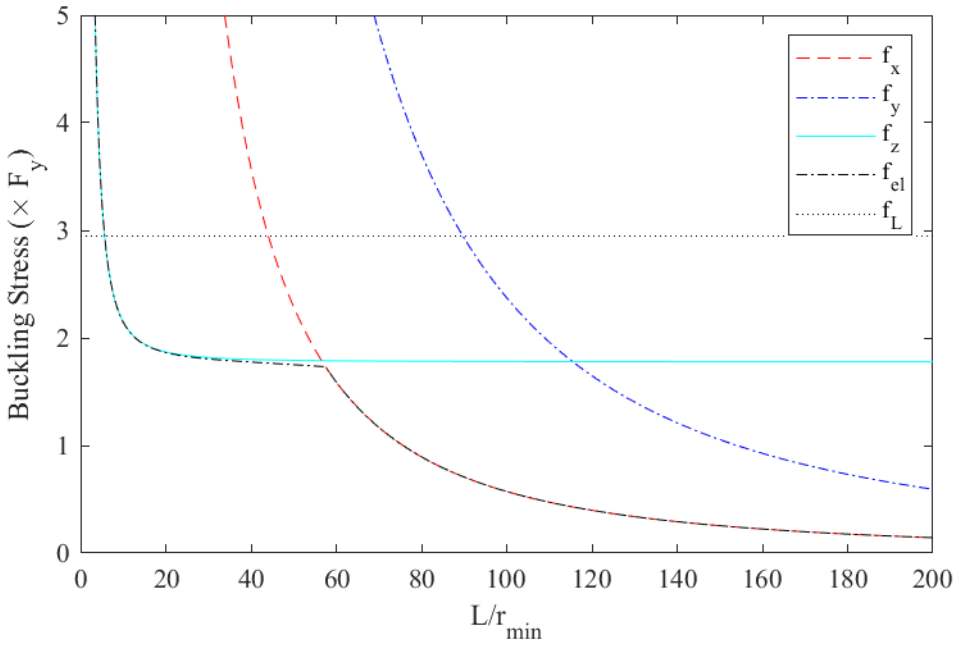

Figure B.29: Elastic buckling of 2-L2"x2"x0.23"

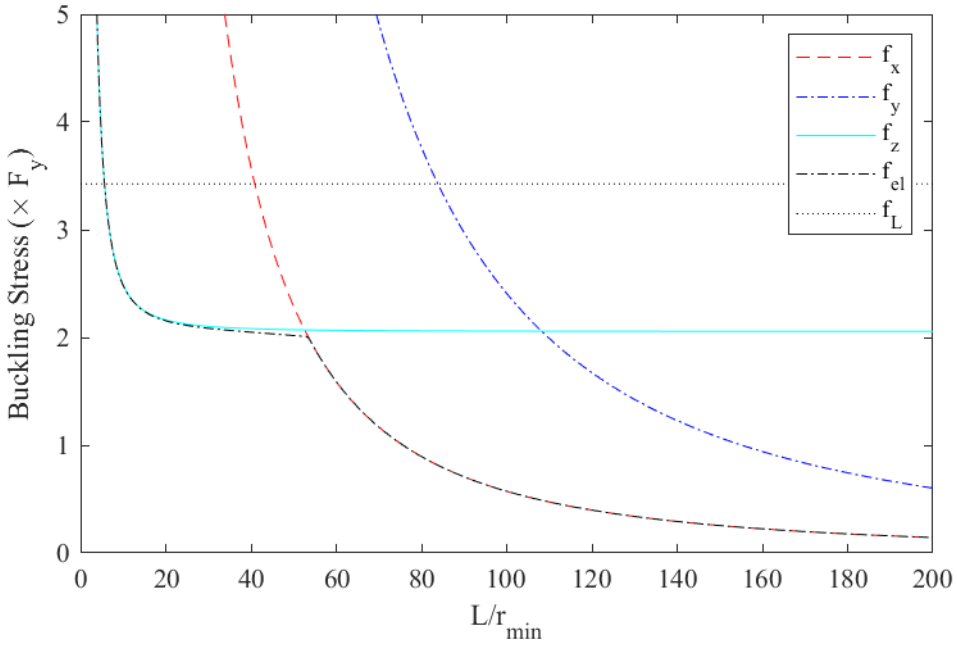

Figure B.30: Elastic buckling of 2-L2"x2"x0.248"

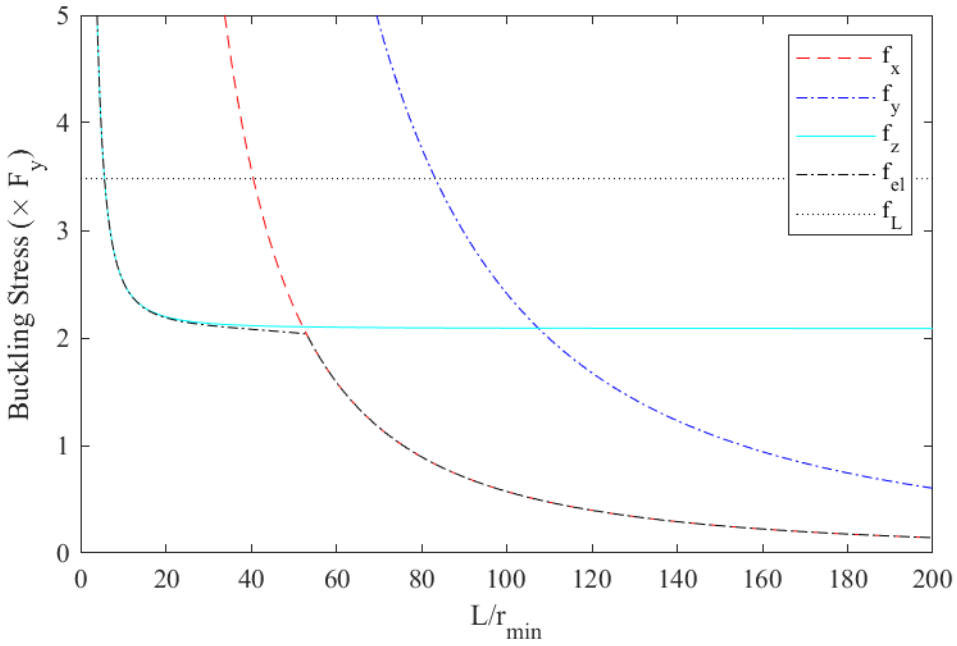

Figure B.31: Elastic buckling of 2-L2"x2"x0.25"

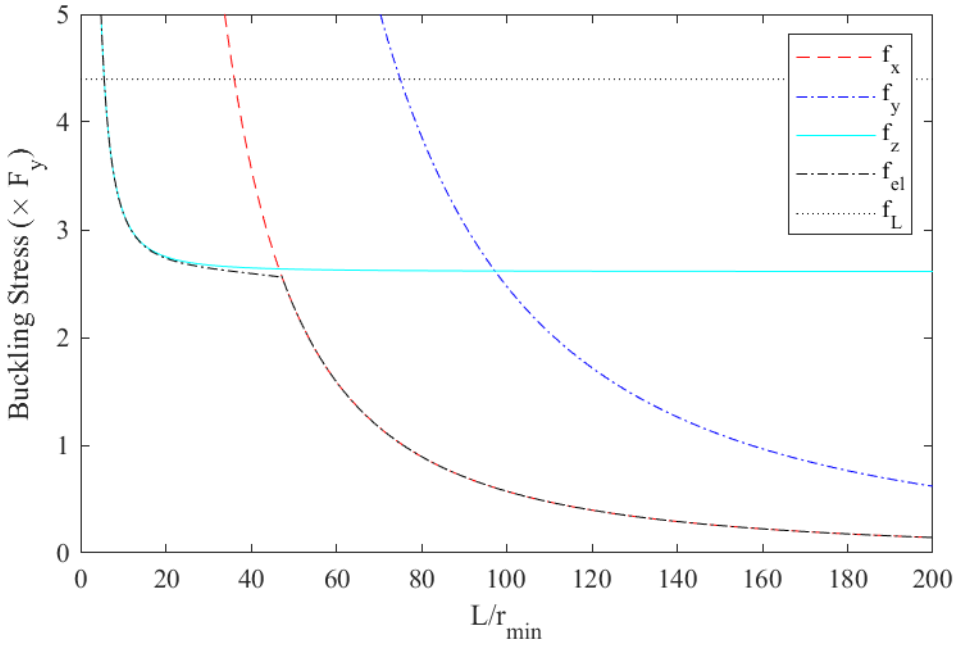

Figure B.32: Elastic buckling of 2-L2"x2"x0.281"

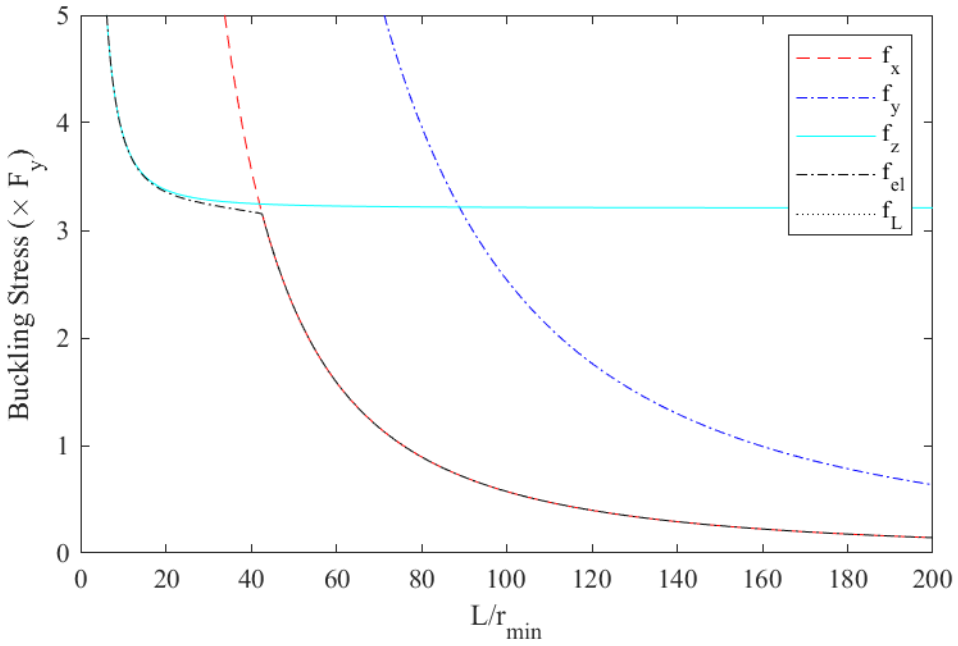

Figure B.33: Elastic buckling of 2-L2"x2"x0.313"

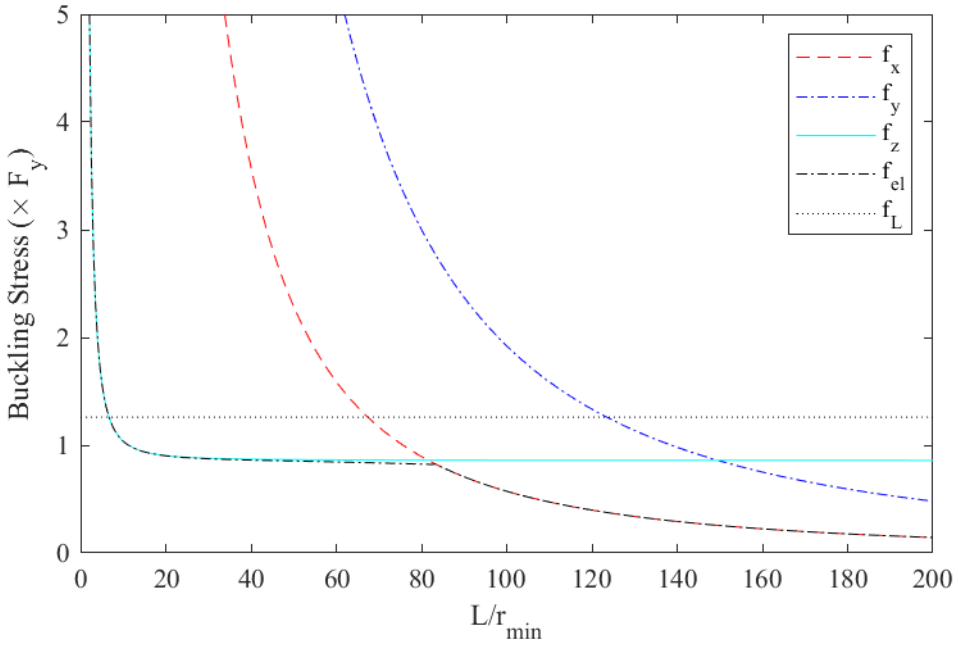

Figure B.34: Elastic buckling of 2-L2.5"x2.5"x0.188"

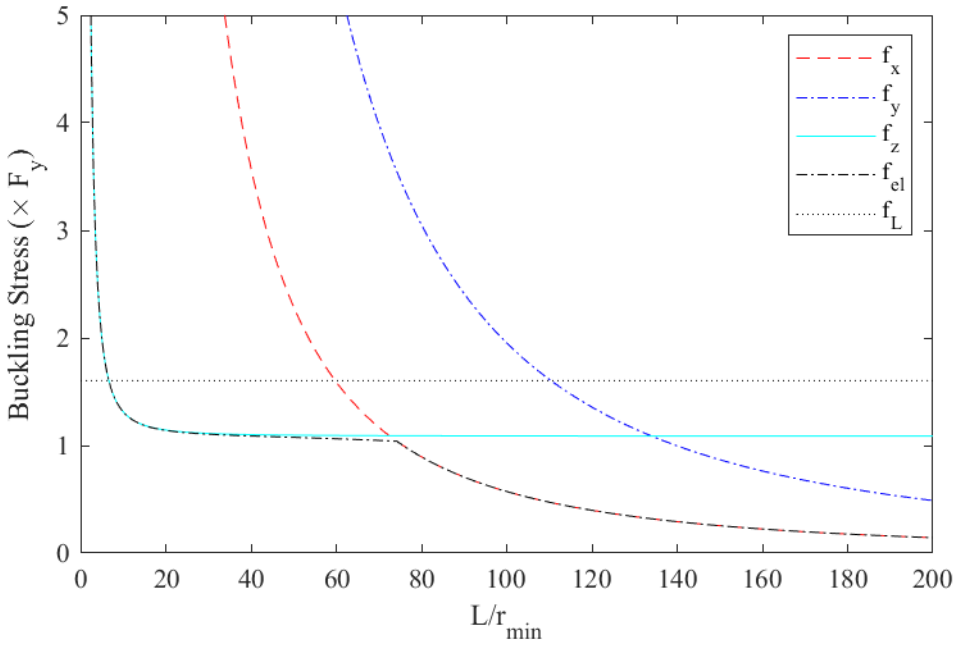

Figure B.35: Elastic buckling of 2-L2.5"x2.5"x0.212"

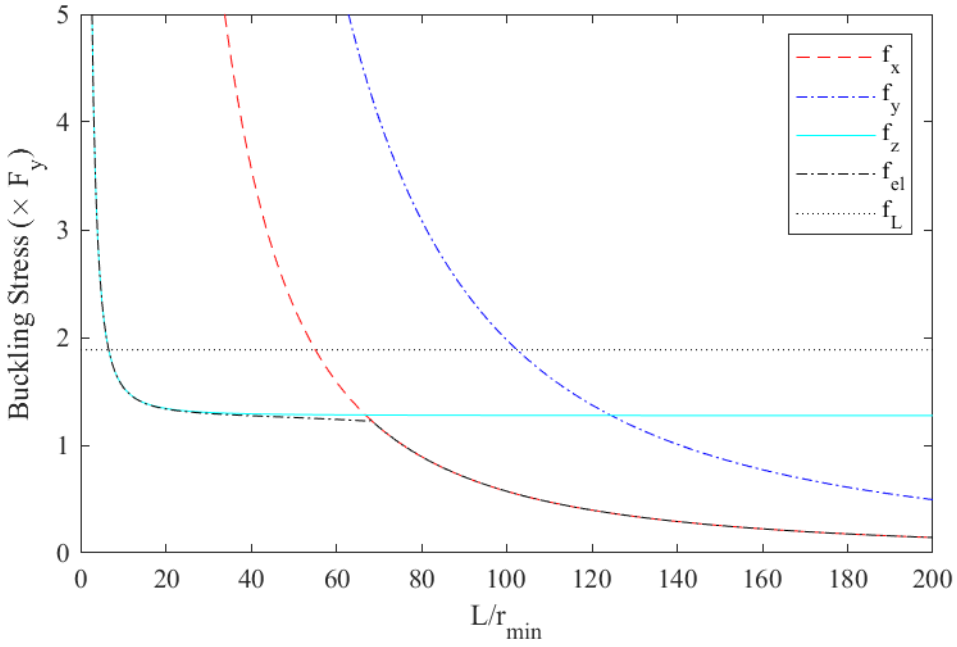

Figure B.36: Elastic buckling of 2-L2.5"x2.5"x0.23"

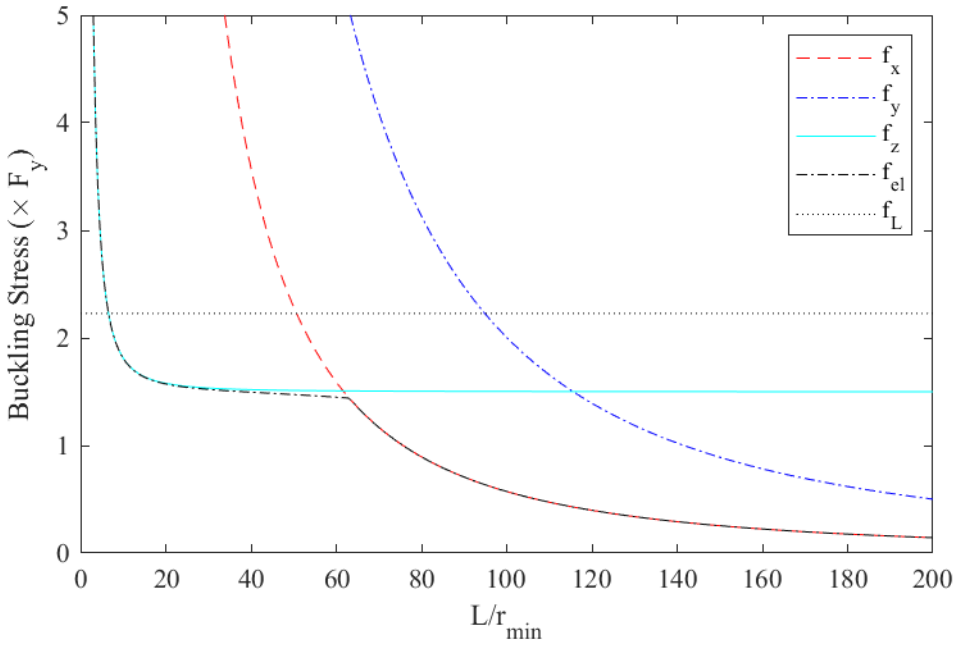

Figure B.37: Elastic buckling of 2-L2.5"x2.5"x0.25"

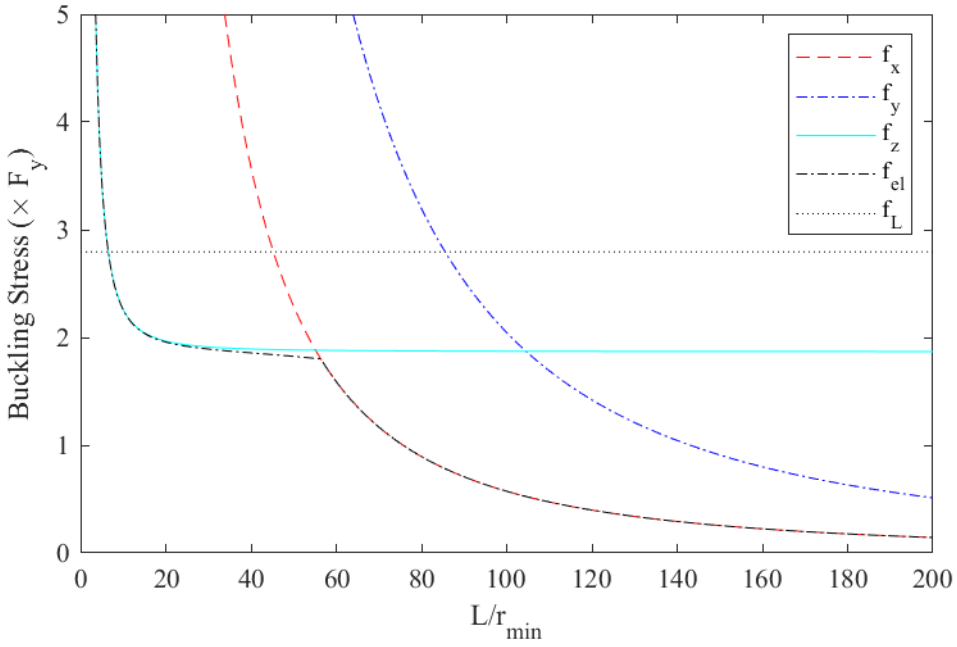

Figure B.38: Elastic buckling of 2-L2.5"x2.5"x0.28"

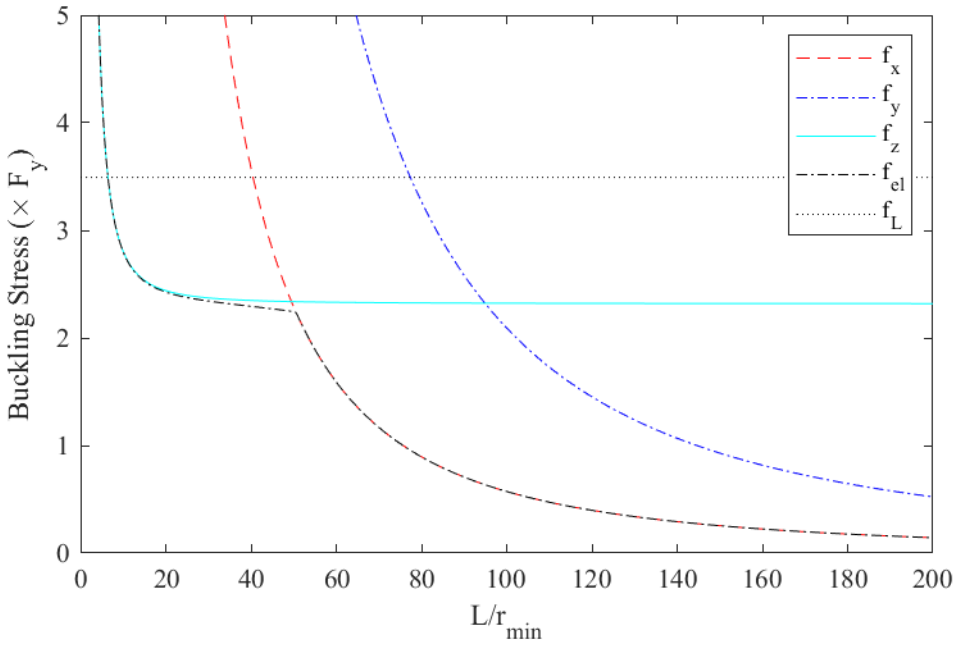

Figure B.39: Elastic buckling of 2-L2.5"x2.5"x0.313"

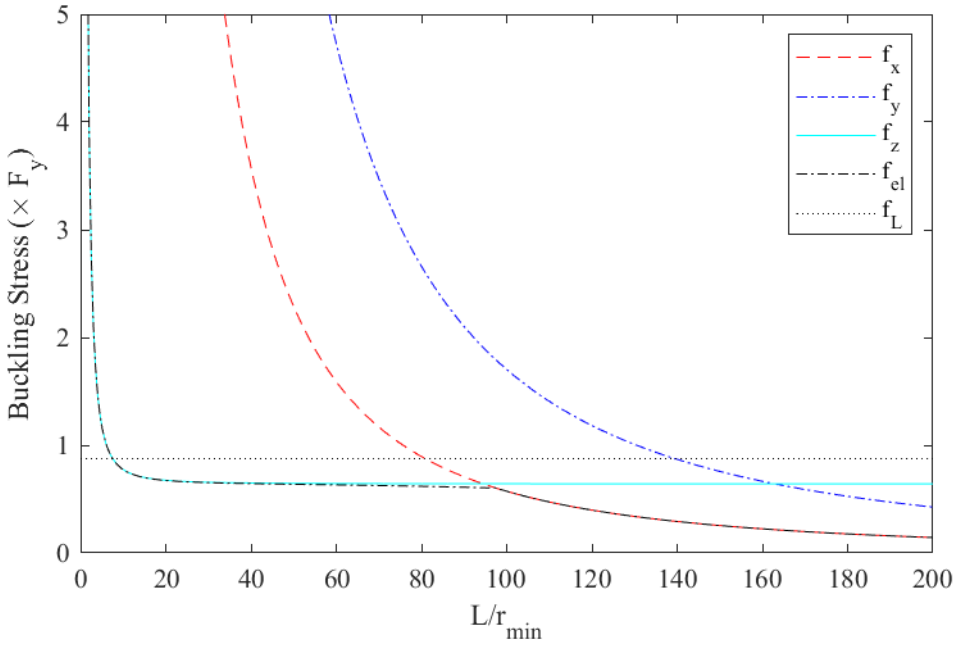

Figure B.40: Elastic buckling of 2-L3"x3"x0.188"

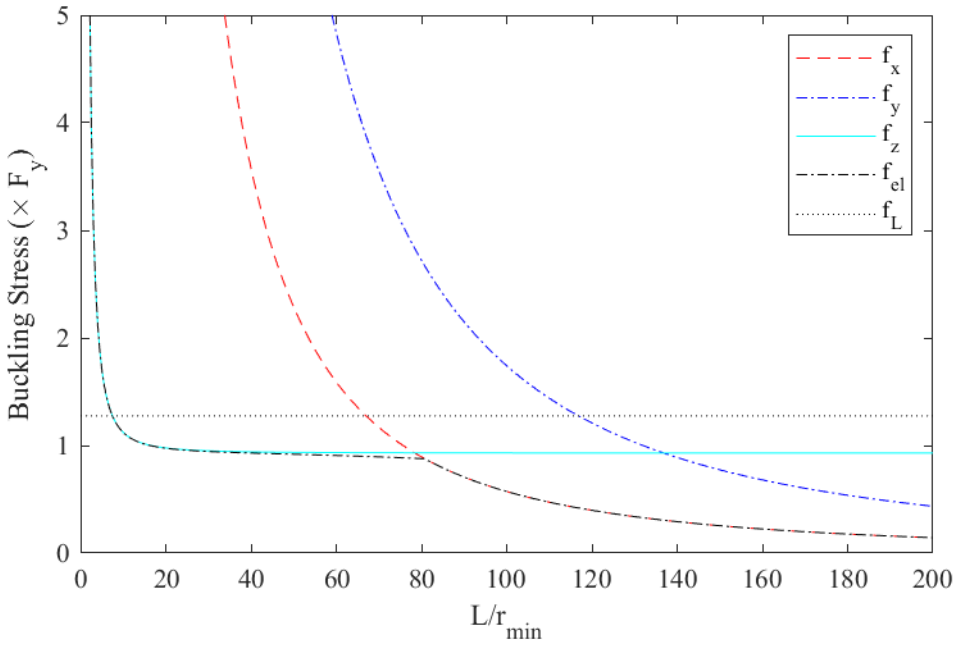

Figure B.41: Elastic buckling of 2-L3"x3"x0.227"

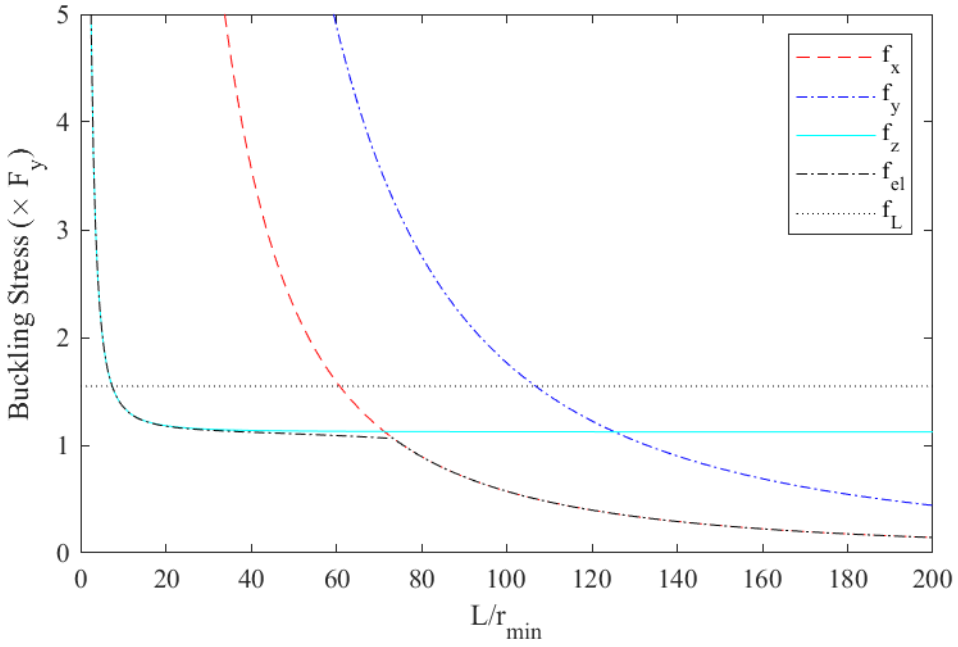

Figure B.42: Elastic buckling of 2-L3"x3"x0.25"

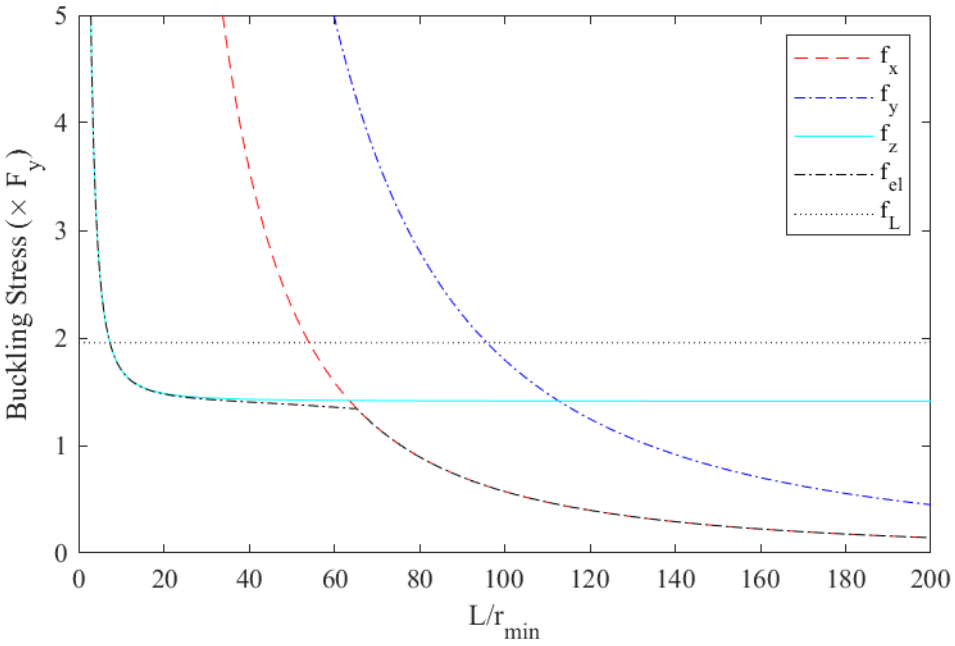

Figure B.43: Elastic buckling of 2-L3"x3"x0.281"

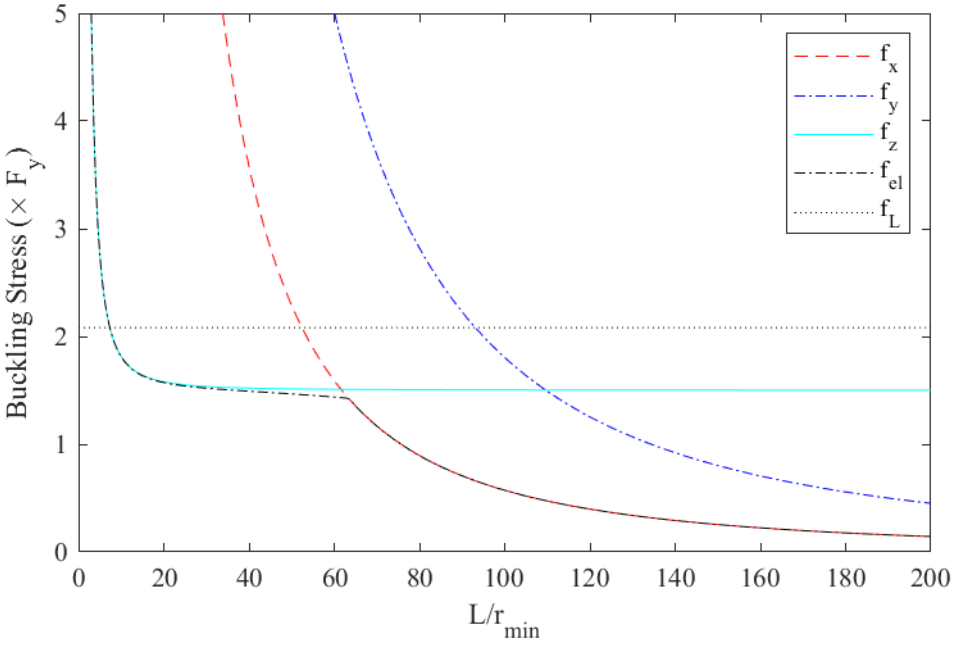

Figure B.44: Elastic buckling of 2-L3"x3"x0.29"

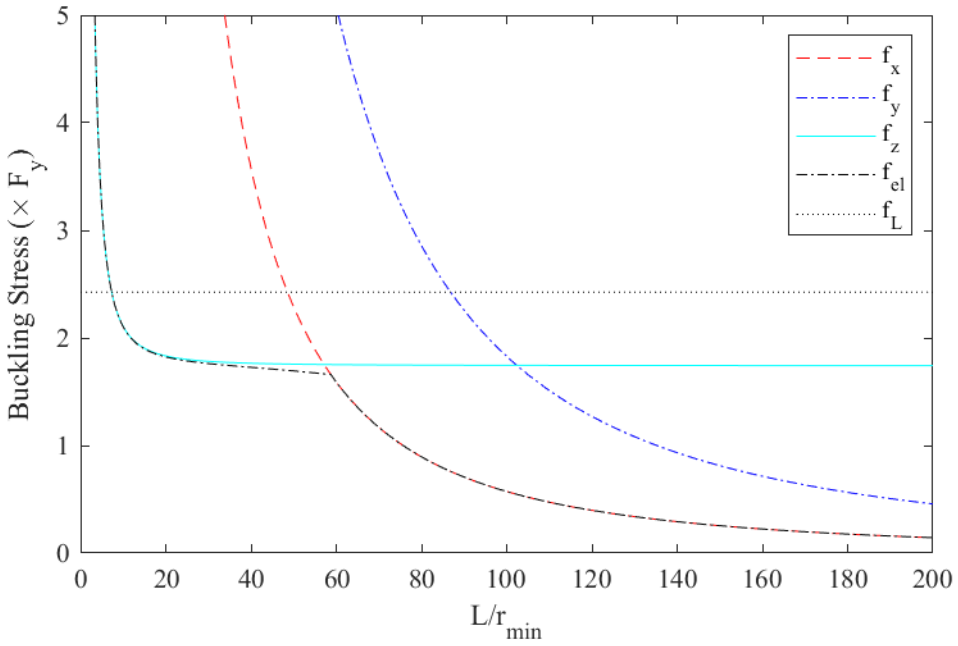

Figure B.45: Elastic buckling of 2-L3"x3"x0.313"

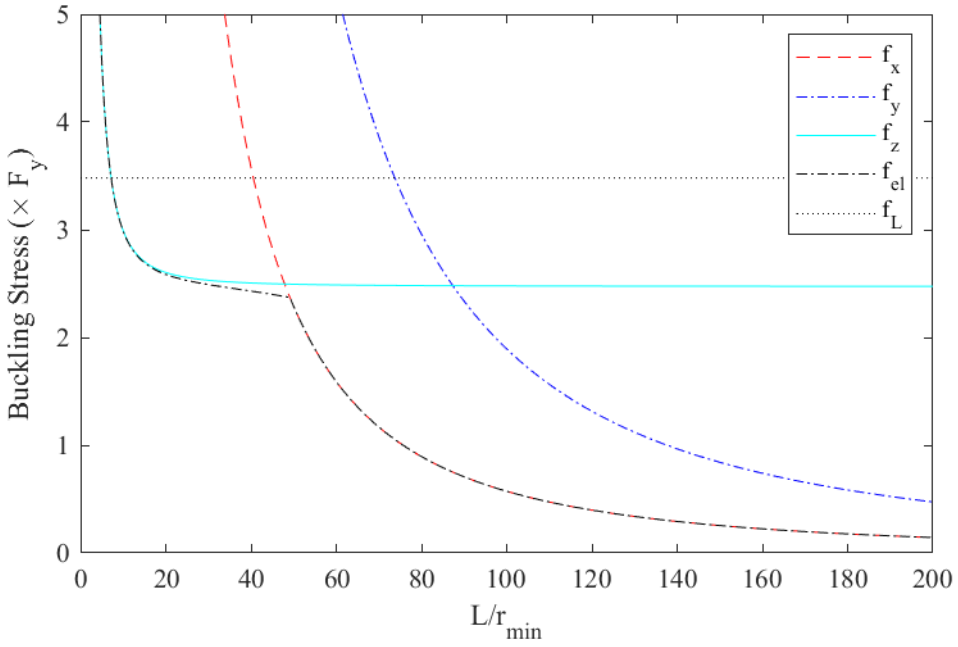

Figure B.46: Elastic buckling of 2-L3"x3"x0.375"

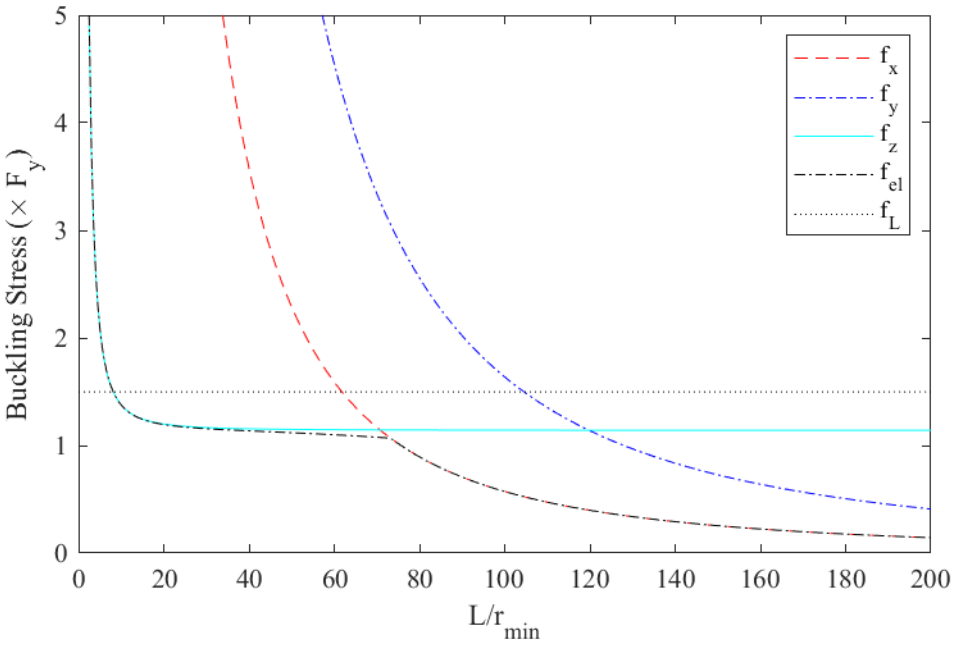

Figure B.47: Elastic buckling of 2-L3.5"x3.5"x0.287"

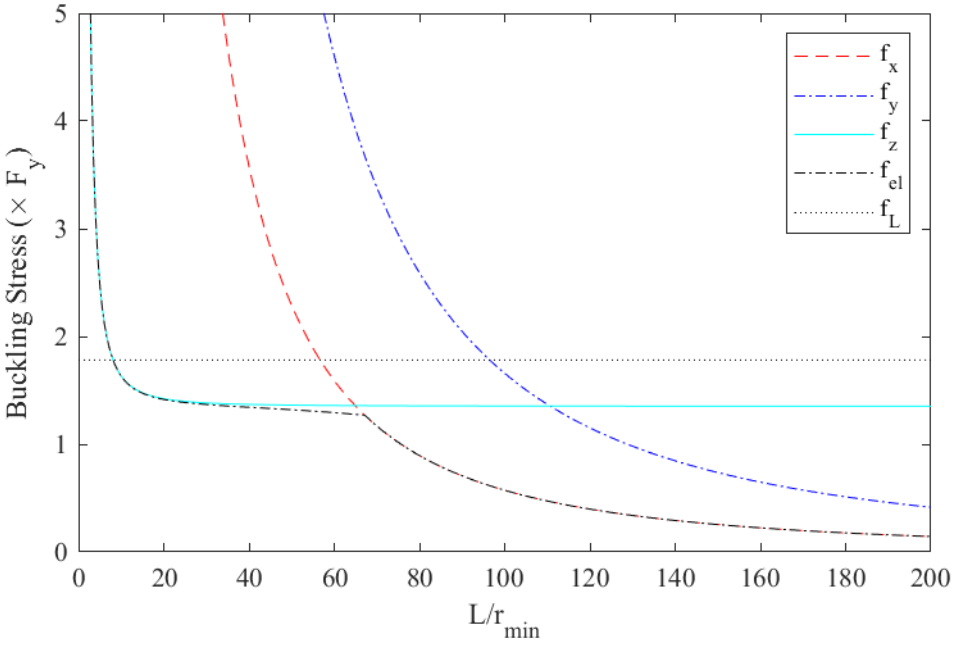

Figure B.48: Elastic buckling of 2-L3.5"x3.5"x0.313"

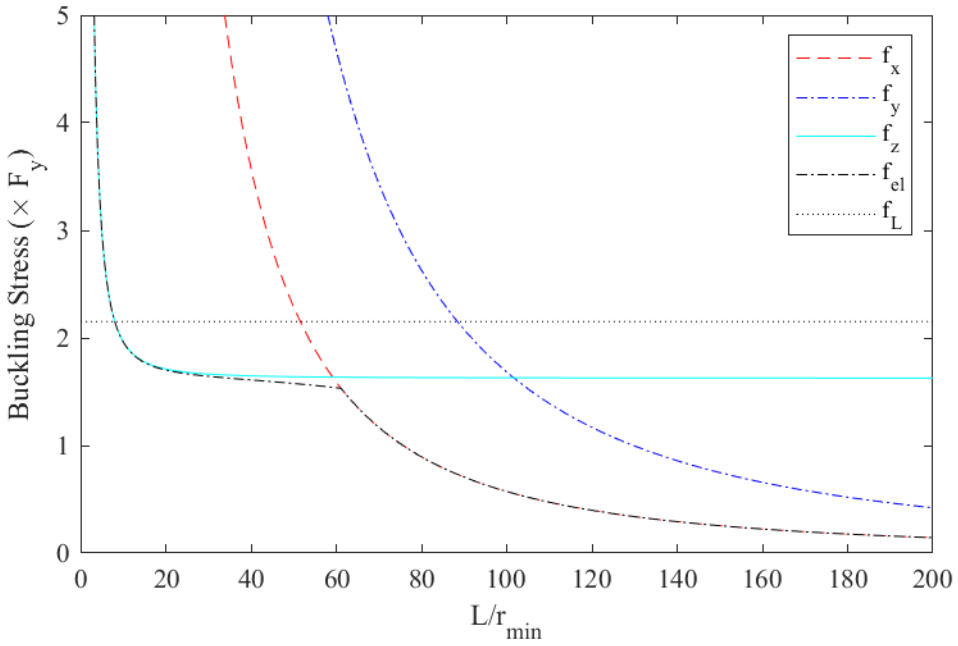

Figure B.49: Elastic buckling of 2-L3.5"x3.5"x0.344"

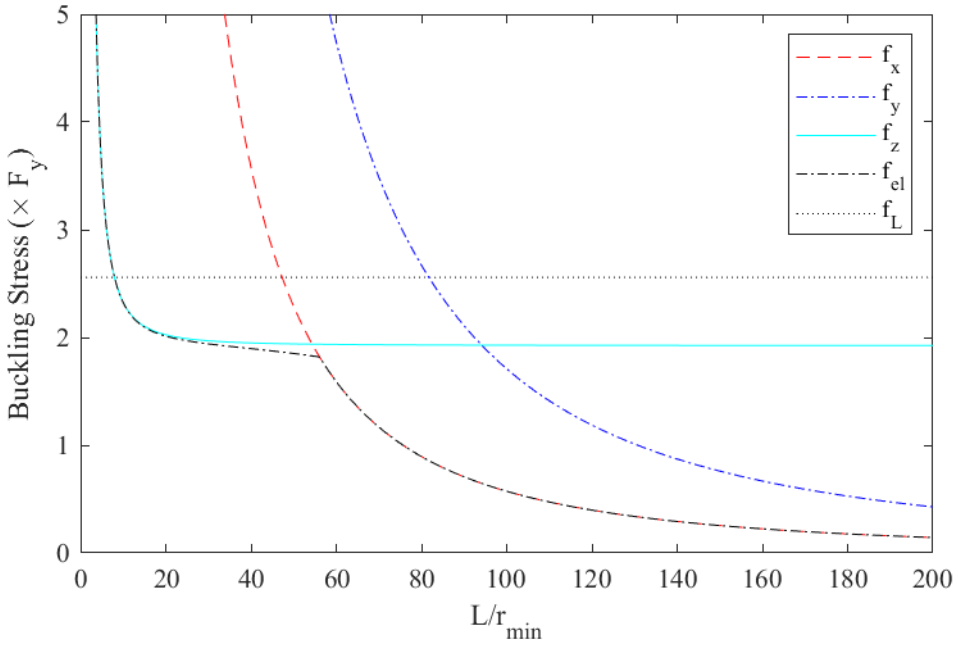

Figure B.50: Elastic buckling of 2-L3.5"x3.5"x0.375"

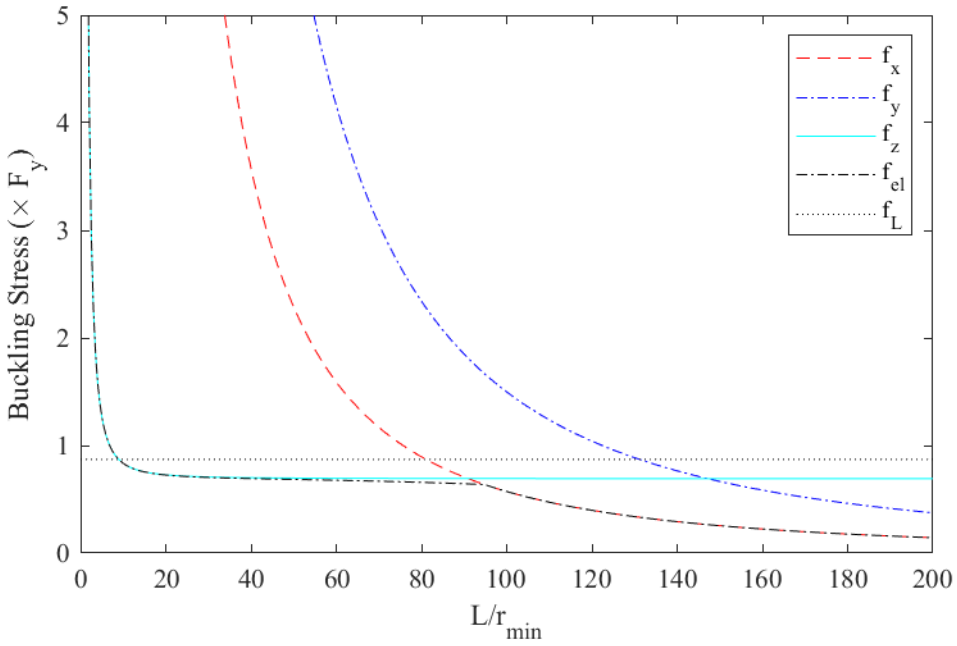

Figure B.51: Elastic buckling of 2-L4"x4"x0.25"

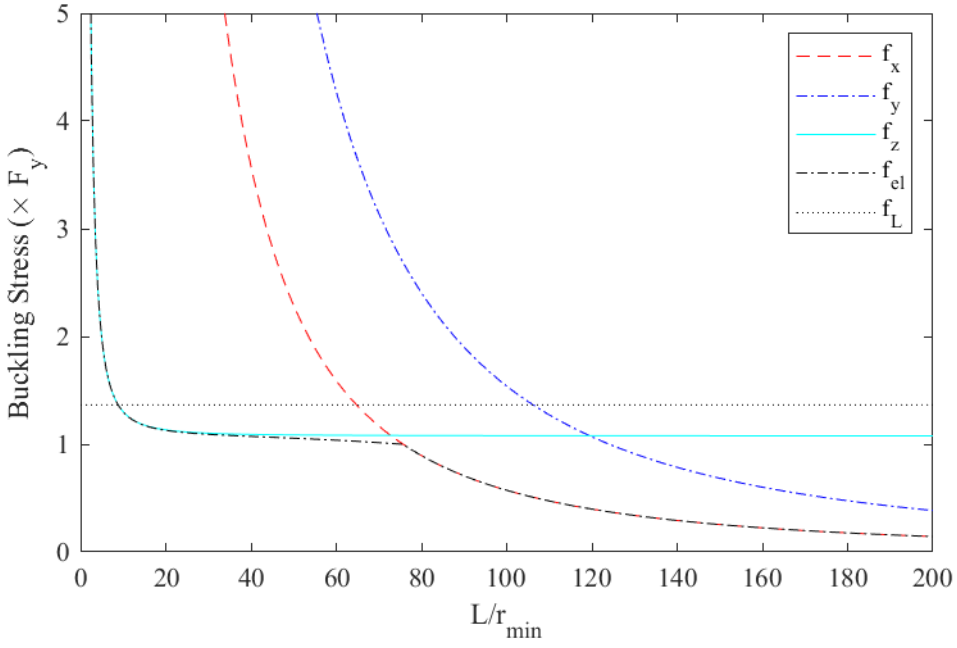

Figure B.52: Elastic buckling of 2-L4"x4"x0.313"

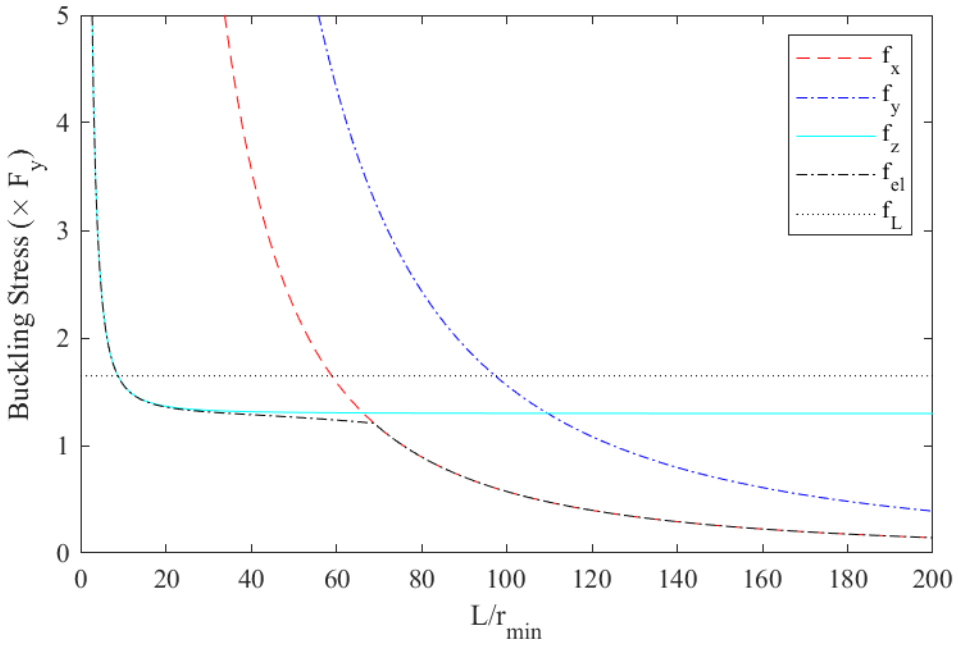

Figure B.53: Elastic buckling of 2-L4"x4"x0.344"

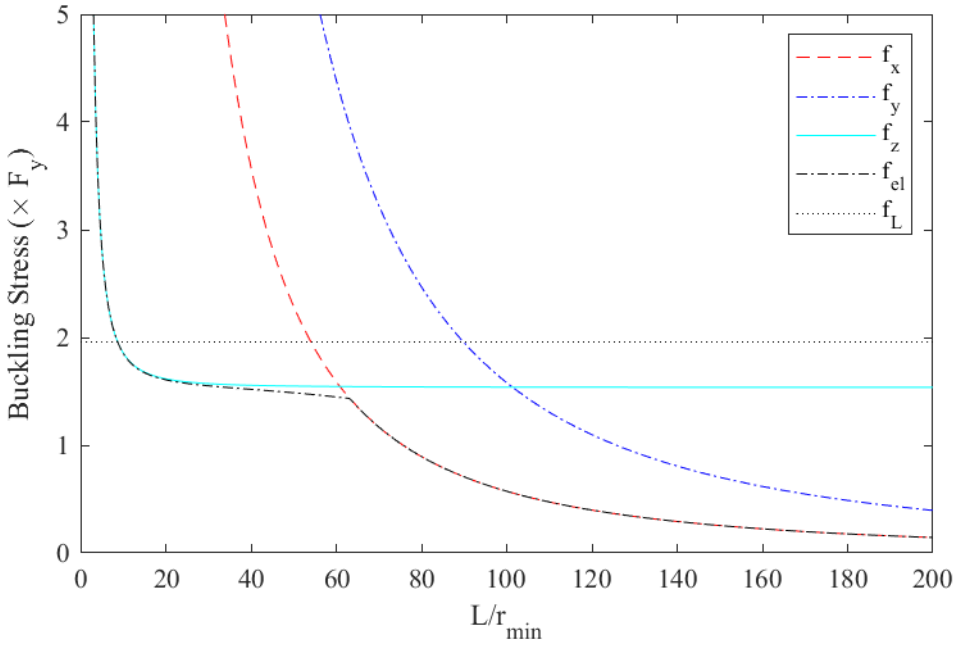

Figure B.54: Elastic buckling of 2-L4"x4"x0.375"

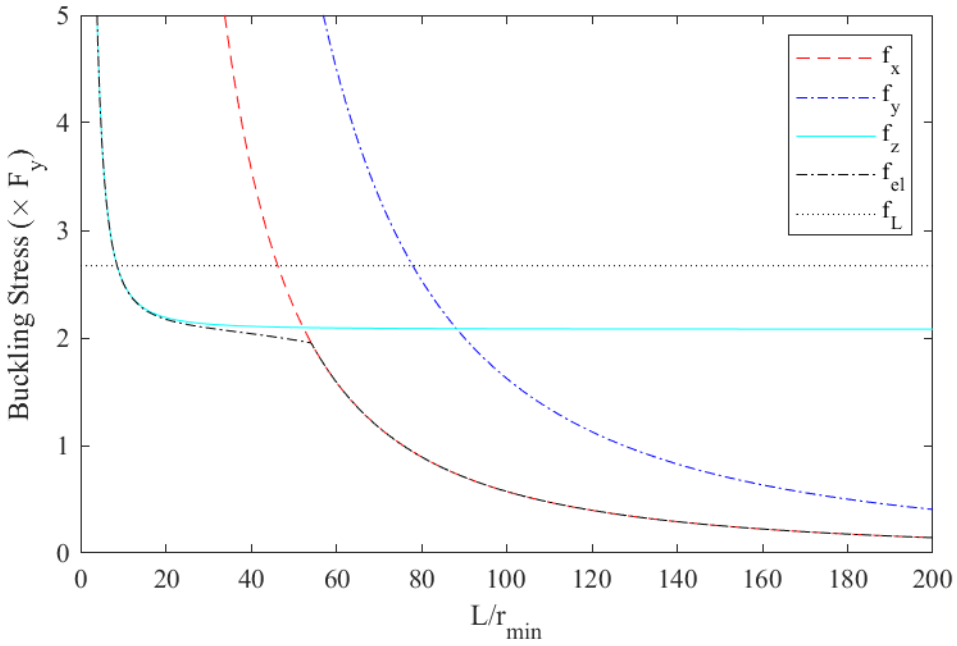

Figure B.55: Elastic buckling of 2-L4"x4"x0.438"

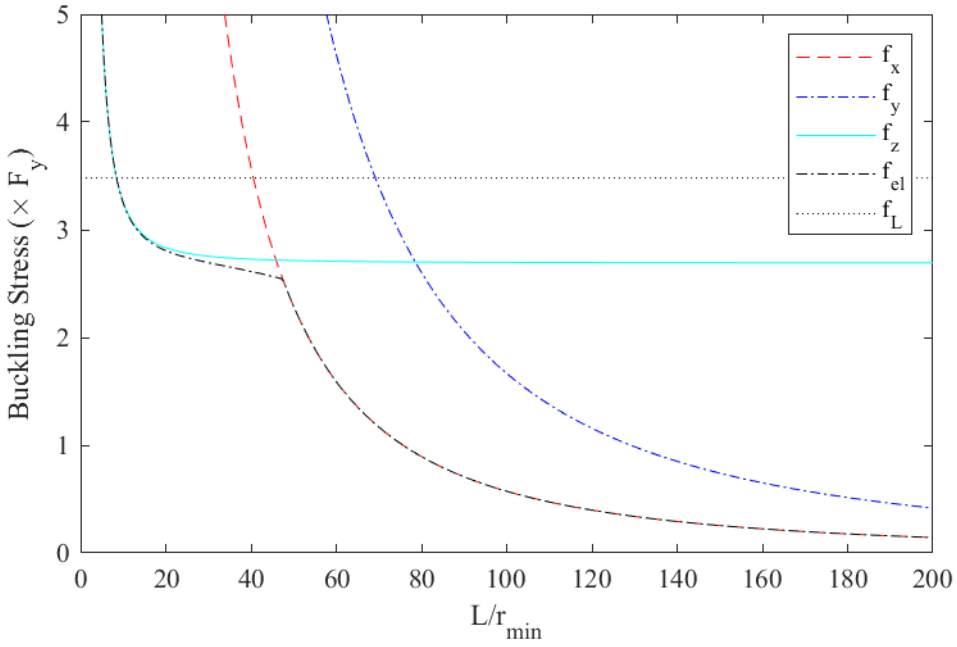

Figure B.56: Elastic buckling of 2-L4"x4"x0.5"

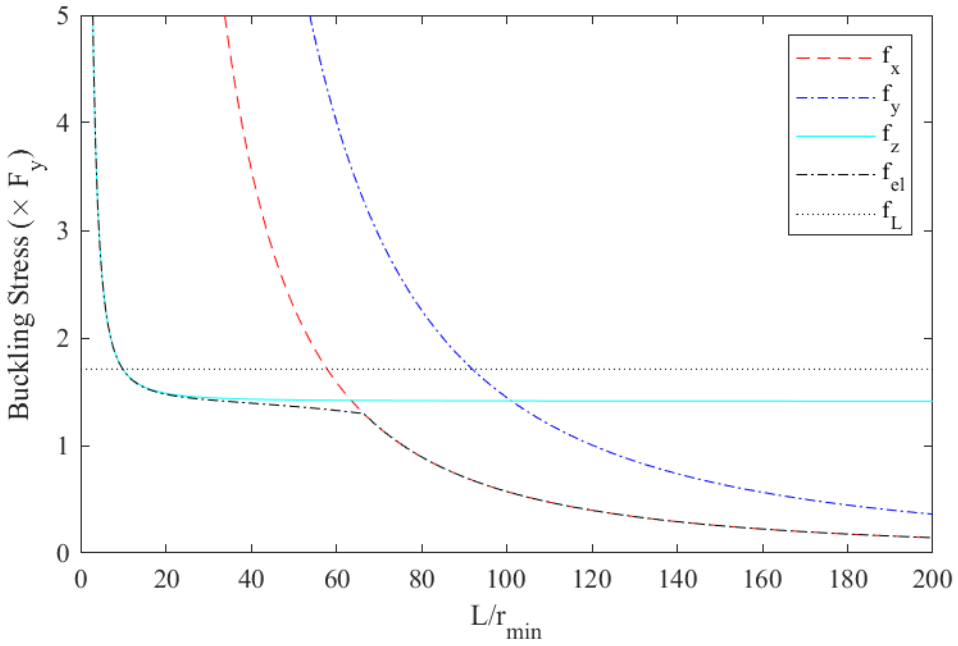

Figure B.57: Elastic buckling of 2-L5"x5"x0.438"

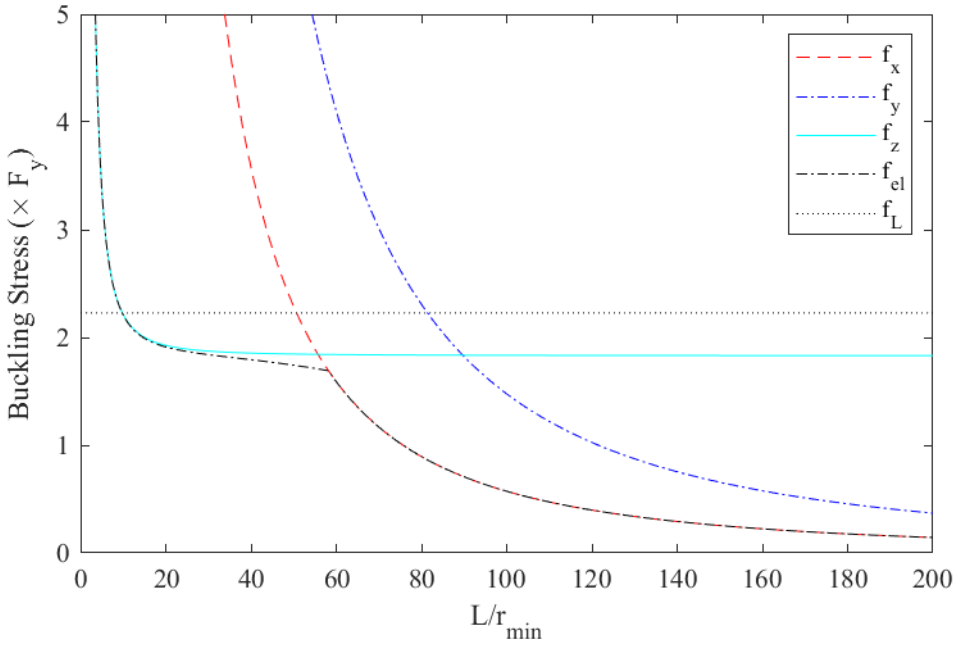

Figure B.58: Elastic buckling of 2-L5"x5"x0.5"

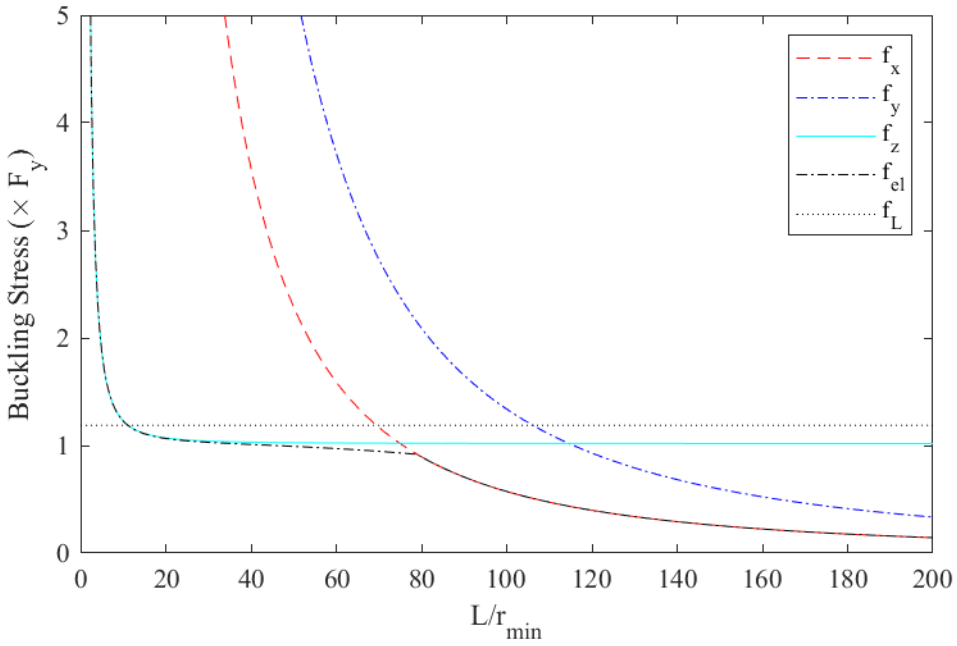

Figure B.59: Elastic buckling of 2-L6"x6"x0.438"

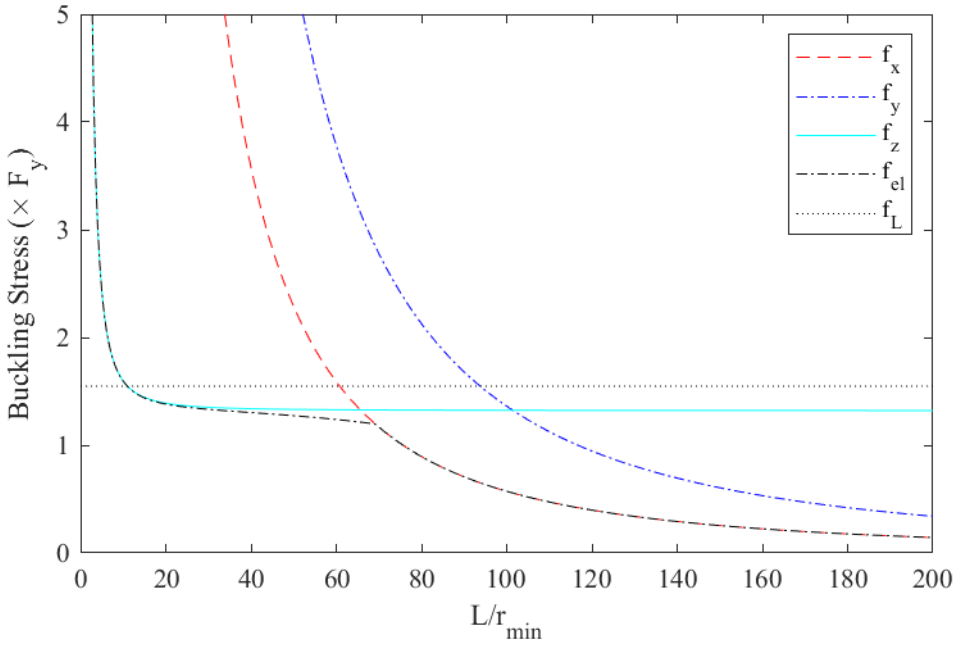

Figure B.60: Elastic buckling of 2-L6"x6"x0.5"

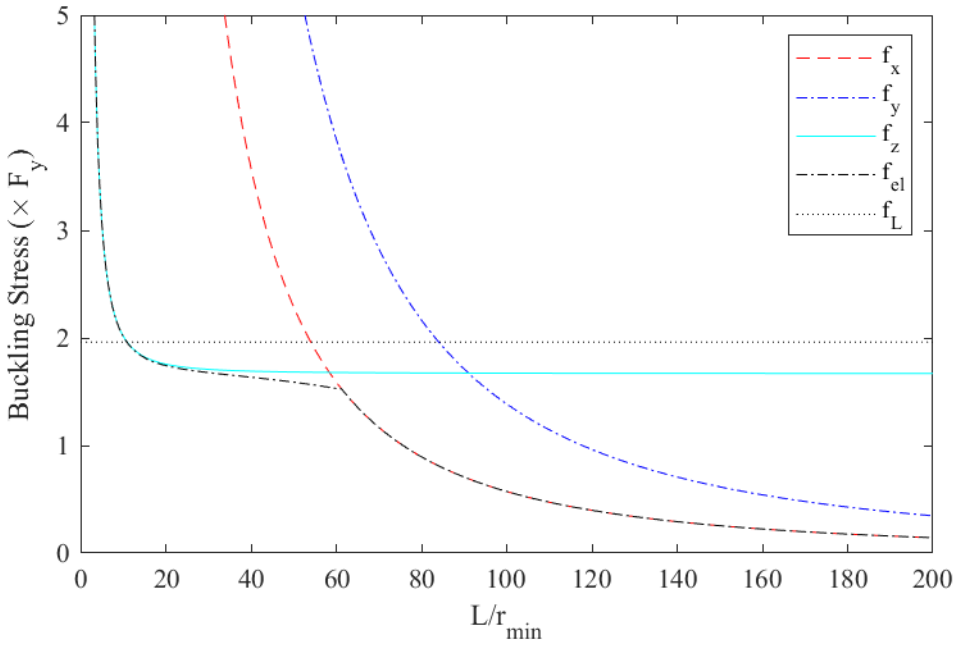

Figure B.61: Elastic buckling of 2-L6"x6"x0.563"

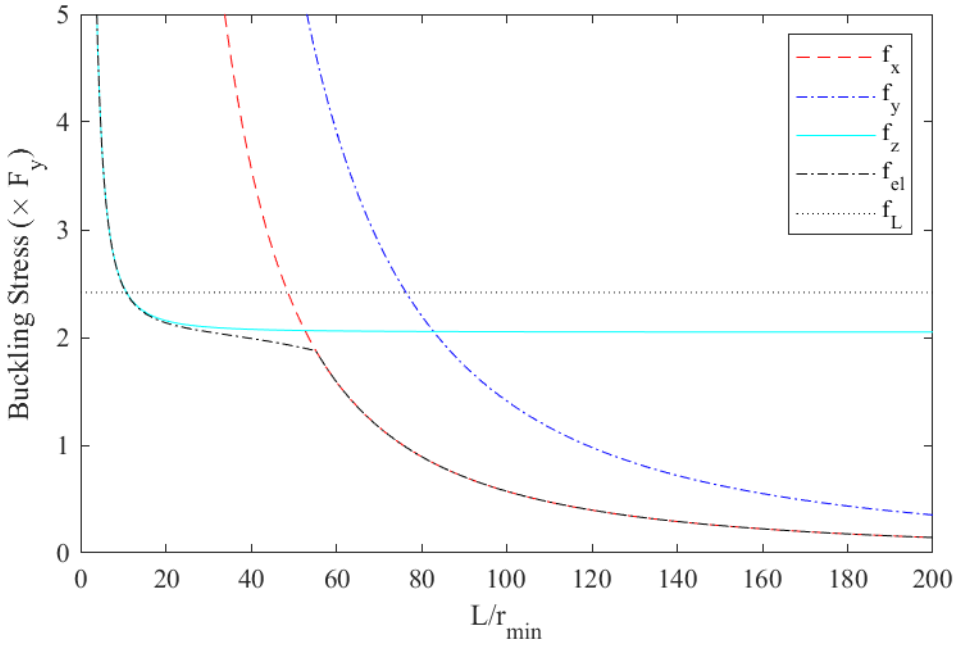

Figure B.62: Elastic buckling of 2-L6"x6"x0.625"

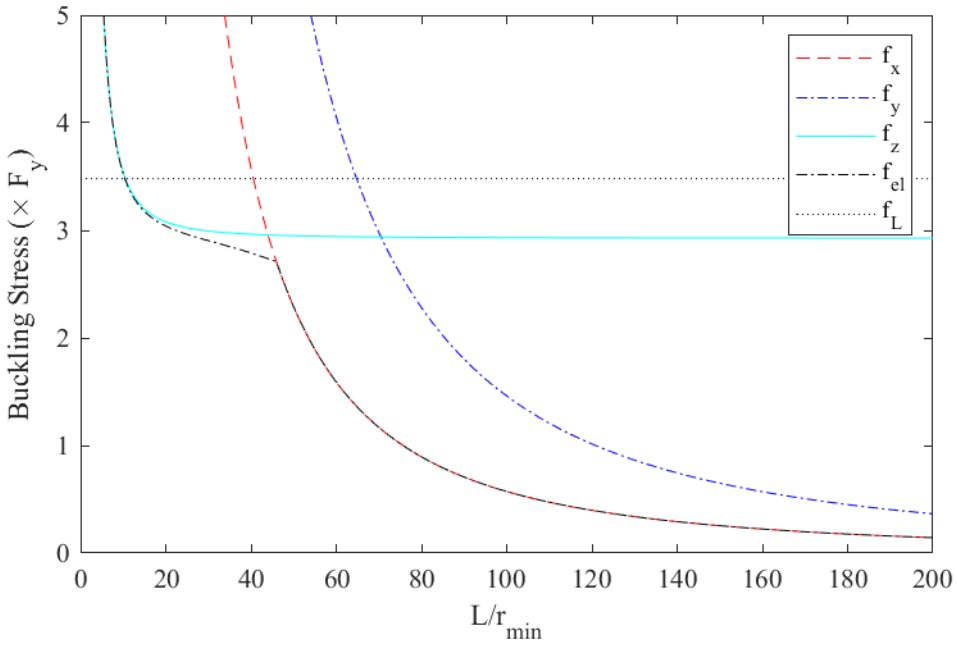

Figure B.63: Elastic buckling of 2-L6"x6"x0.75"

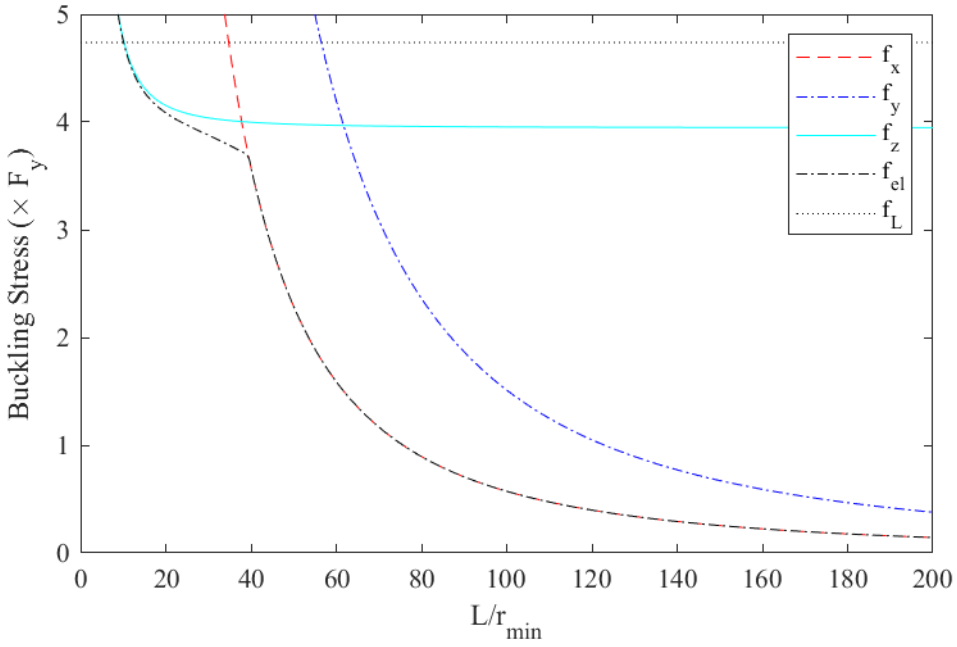

Figure B.64: Elastic buckling of 2-L6"x6"x0.875"

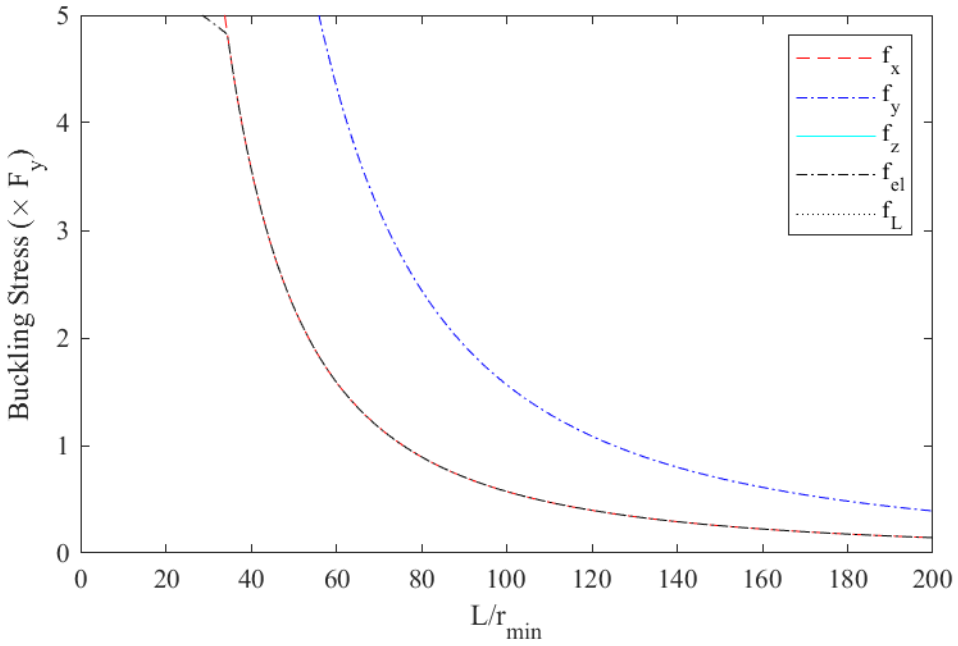

Figure B.65: Elastic buckling of 2-L6"x6"x1"

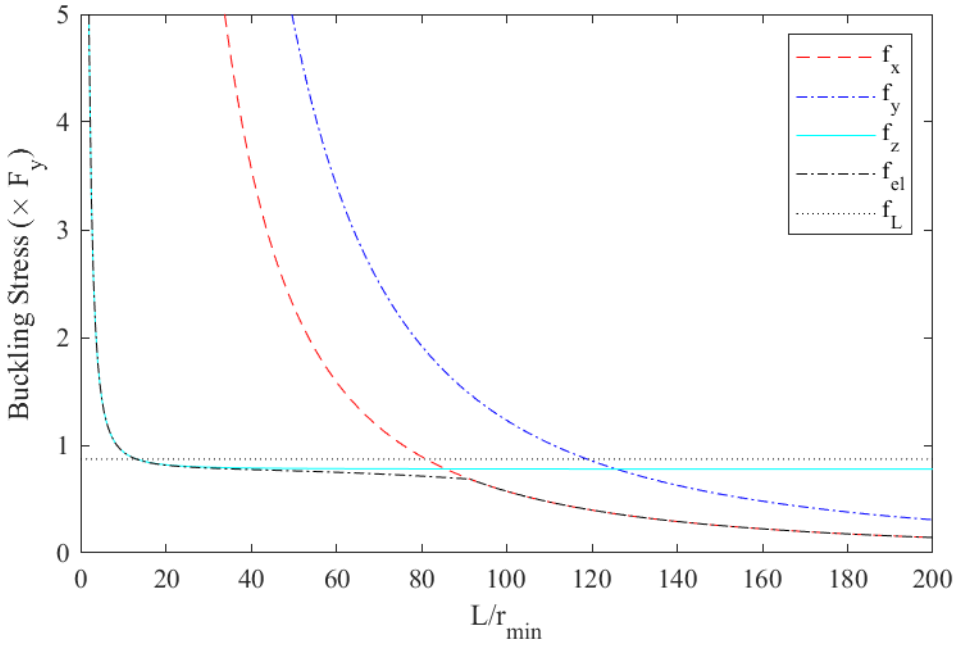

Figure B.66: Elastic buckling of 2-L8"x8"x0.5"

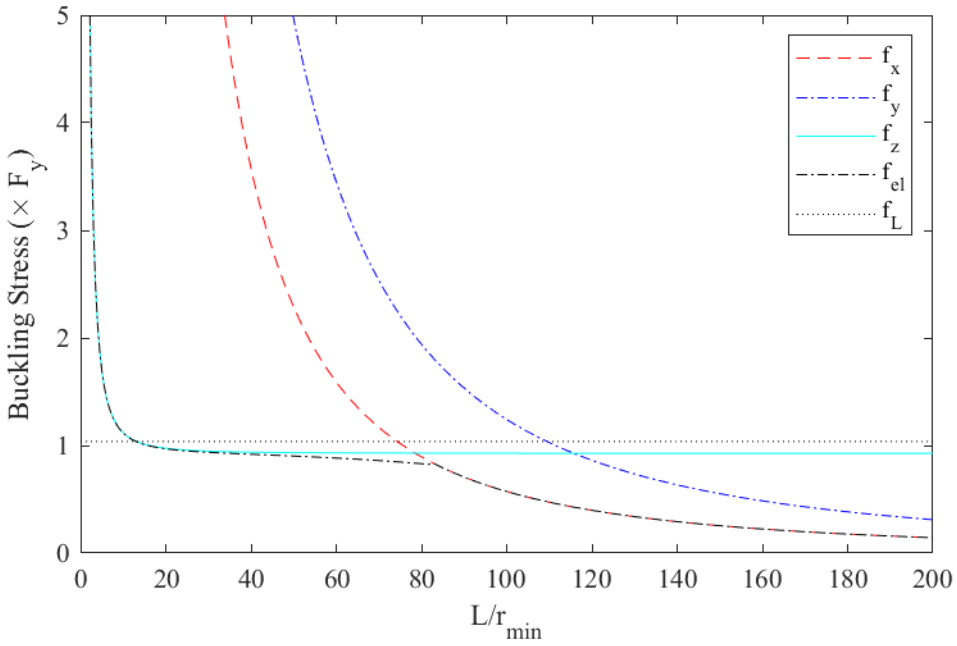

Figure B.67: Elastic buckling of 2-L8"x8"x0.546"

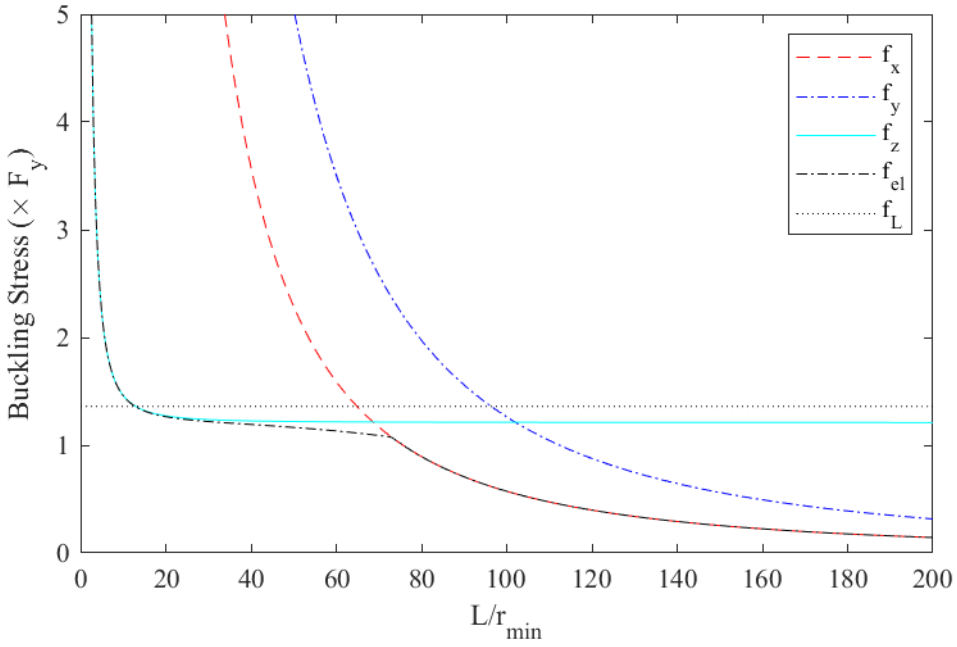

Figure B.68: Elastic buckling of 2-L8"x8"x0.625"

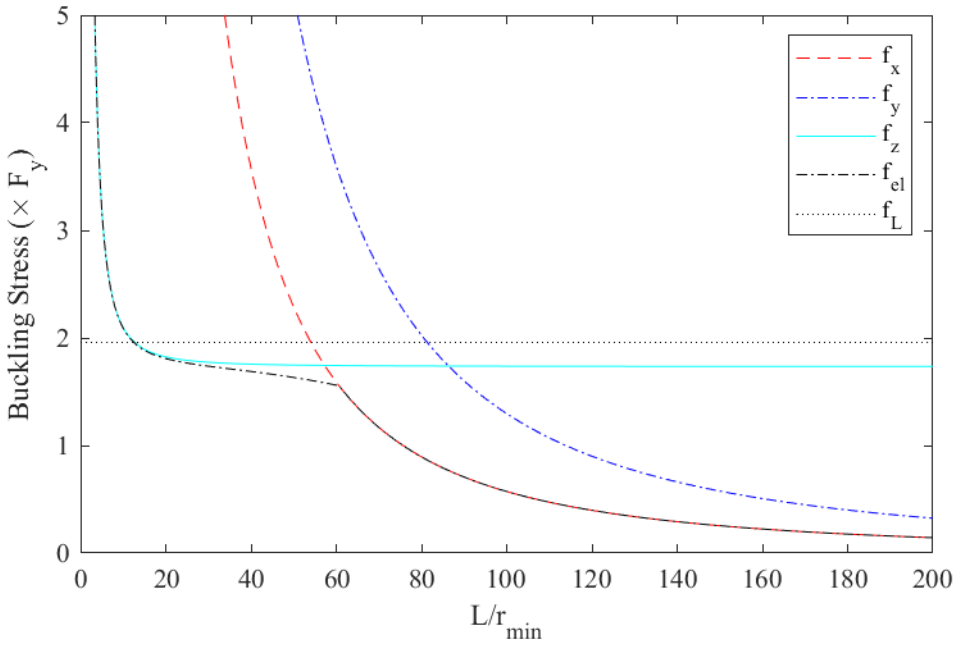

Figure B.69: Elastic buckling of 2-L8"x8"x0.75"

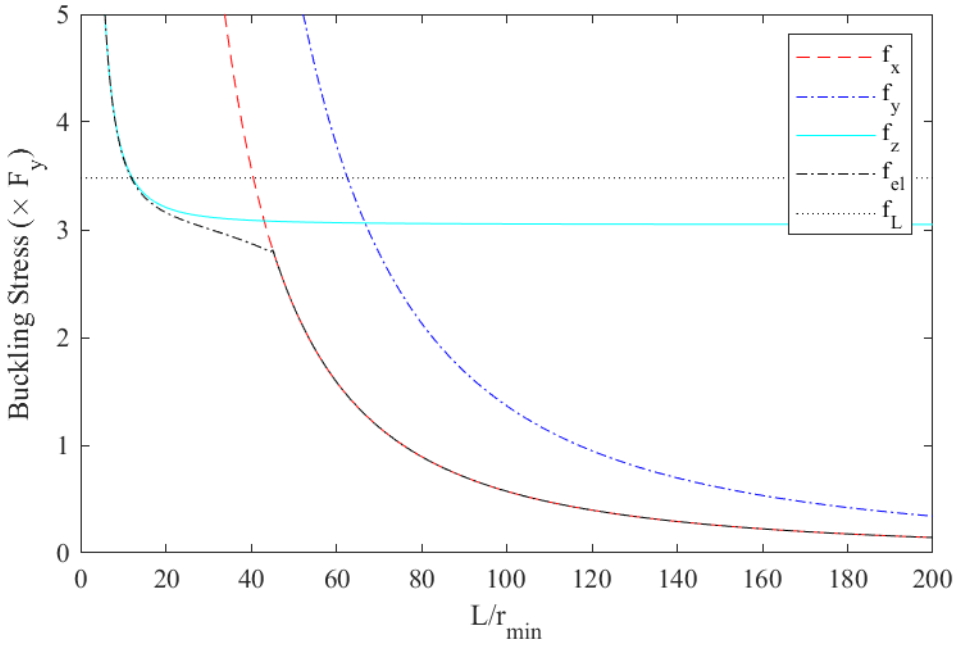

Figure B.70: Elastic buckling of 2-L8"x8"x1"

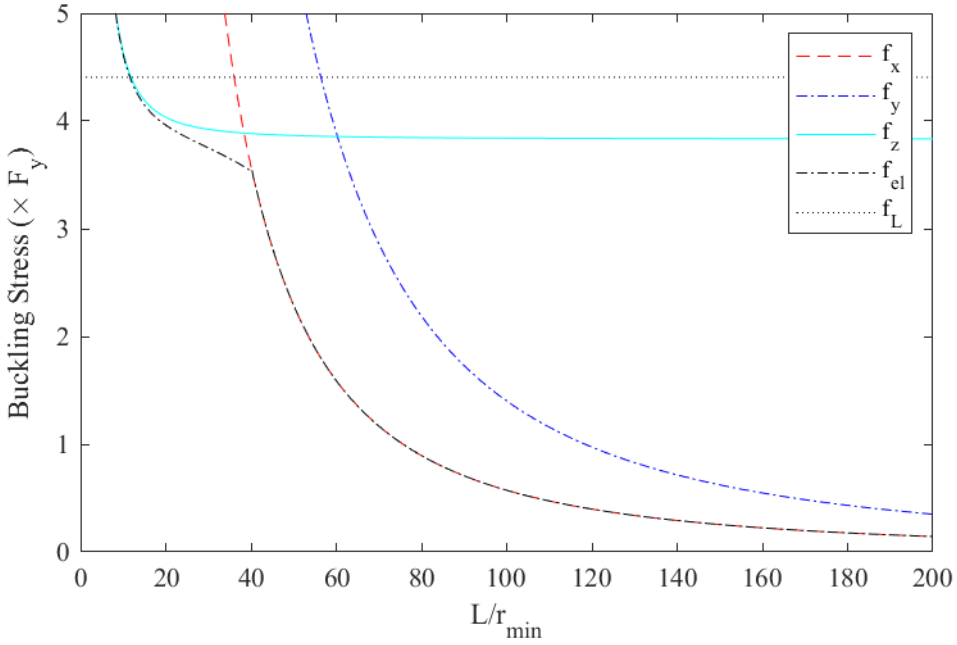

Figure B.71: Elastic buckling of 2-L8"x8"x1.125"

C. Nominal Buckling Behavior

This Appendix contains the plots for the theoretical inelastic buckling study described in Section 2.4 including variations in the shear stiffness via two values for τ_G and in the warping stiffness of double angles via three values for C_w. An upper limit of $\tau_G = 1.0$ was used to capture the full shear stiffness of the section as minimal reduction was observed. A reduction was estimated as $\tau_G = 0.877$ to account for imperfections and residual stresses based on critical elastic flexural buckling. The minimum value for C_w was defined based on AISC's [2] conservative design recommendation that C_w of double angles can be taken as 0 and the shear center is positioned along the axis of symmetry at the middle of the horizontal flanges. An alternative conservative recommendation by CISC [11] uses the same shear center position but references a C_w equal to twice that of the single angle. As discussed in Appendix A, an estimate of a fully composite behavior resulted in a new shear center and a significantly increased C_w. These three C_w values were considered to investigate the impact of warping stiffness and are identified as $C_w = 0$, Low C_w, and High C_w, respectively.

For each alternative C_w, four inelastic buckling curves were determined for lengths up to 200 times the minimum radius of gyration. The upper bound was determined considering flexural buckling effects in line with the current SJI Specification and labeled "FB". The lower bound for capacity was determined considering both flexural and torsional buckling effects aligned with the AISC Specification and labeled "FTB". Two intermediate solutions were found using the τ_G factors discussed above to capture the increased shear stiffness in torsional buckling. The results labeled "$\tau_G = 1.0$" account for the maximum increase in strength while the results labeled "$\tau_G = 0.877$" include a small reduction to account for imperfections. All calculations included local buckling

reductions based on the SJI provisions, which employ the previously mentioned Q-factor.

Note that some graphs will appear to not depict four separate lines and the intermediate values are plotted directly on the flexural buckling curve. This indicates that the effects of increased shear stiffness and an increased C_w is resulting in flexural buckling controlled behavior. Table C.1 summarizes this information where 'x' indicates flexural buckling controls for both "τ_G = 1.0" and "τ_G = 0.877" and 'o' indicates flexural buckling controls for only "τ_G = 1.0".

Table C.1: Sections Controlled by Flexural Buckling in Inelastic Buckling Analysis

	C_w = 0	Low C_w	High C_w
2-L1.25"x1.25"x0.109"			x
2-L1.25"x1.25"x0.115"			x
2-L1.25"x1.25"x0.125"			x
2-L1.25"x1.25"x0.188"	x	x	x
2-L1.5"x1.5"x0.109"			
2-L1.5"x1.5"x0.115"			o
2-L1.5"x1.5"x0.123"			o
2-L1.5"x1.5"x0.137"			x
2-L1.5"x1.5"x0.141"			x
2-L1.5"x1.5"x0.155"	x	x	x
2-L1.5"x1.5"x0.17"	x	x	x
2-L1.5"x1.5"x0.188"	x	x	x
2-L1.5"x1.5"x0.25"	x	x	x
2-L1.75"x1.75"x0.115"			
2-L1.75"x1.75"x0.125"			
2-L1.75"x1.75"x0.143"			o
2-L1.75"x1.75"x0.155"			x
2-L1.75"x1.75"x0.17"	x	x	x
2-L1.75"x1.75"x0.188"	x	x	x
2-L1.75"x1.75"x0.25"	x	x	x
2-L2"x2"x0.125"			
2-L2"x2"x0.143"			
2-L2"x2"x0.156"			o
2-L2"x2"x0.163"			o
2-L2"x2"x0.176"		o	x
2-L2"x2"x0.188"	x	x	x
2-L2"x2"x0.205"	x	x	x
2-L2"x2"x0.216"	x	x	x
2-L2"x2"x0.23"	x	x	x
2-L2"x2"x0.248"	x	x	x
2-L2"x2"x0.25"	x	x	x
2-L2"x2"x0.281"	x	x	x
2-L2"x2"x0.313"	x	x	x
2-L2.5"x2.5"x0.188"			o
2-L2.5"x2.5"x0.212"		x	x
2-L2.5"x2.5"x0.23"	x	x	x
2-L2.5"x2.5"x0.25"	x	x	x
2-L2.5"x2.5"x0.28"	x	x	x
2-L2.5"x2.5"x0.313"	x	x	x
2-L3"x3"x0.188"			
2-L3"x3"x0.227"			o
2-L3"x3"x0.25"	o	x	x
2-L3"x3"x0.281"	x	x	x
2-L3"x3"x0.29"	x	x	x
2-L3"x3"x0.313"	x	x	x
2-L3"x3"x0.375"	x	x	x
2-L3.5"x3.5"x0.287"	o	x	x
2-L3.5"x3.5"x0.313"	x	x	x
2-L3.5"x3.5"x0.344"	x	x	x
2-L3.5"x3.5"x0.375"	x	x	x
2-L4"x4"x0.25"			
2-L4"x4"x0.313"	o	x	x
2-L4"x4"x0.344"	x	x	x
2-L4"x4"x0.375"	x	x	x
2-L4"x4"x0.438"	x	x	x
2-L4"x4"x0.5"	x	x	x
2-L5"x5"x0.438"	x	x	x
2-L5"x5"x0.5"	x	x	x
2-L6"x6"x0.438"		x	o
2-L6"x6"x0.5"	x	x	x
2-L6"x6"x0.563"	x	x	x
2-L6"x6"x0.625"	x	x	x
2-L6"x6"x0.75"	x	x	x
2-L6"x6"x0.875"	x	x	x
2-L6"x6"x1"	x	x	x
2-L8"x8"x0.5"			
2-L8"x8"x0.546"			
2-L8"x8"x0.625"	x	x	x
2-L8"x8"x0.75"	x	x	x
2-L8"x8"x1"	x	x	x
2-L8"x8"x1.125"	x	x	x

x = FB controlling failure mode for both"τ_G = 1.0" and "τ_G = 0.877"
o = FB controlling failure mode only for "τ_G = 1.0"

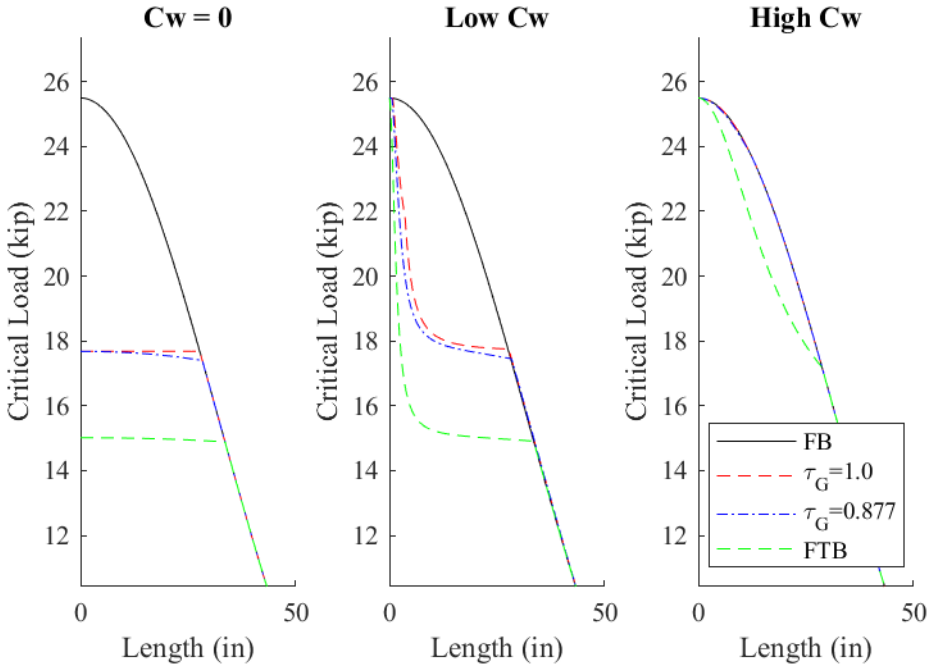

Figure C.1: Inelastic buckling of 2-L1.25"x1.25"x0.109"

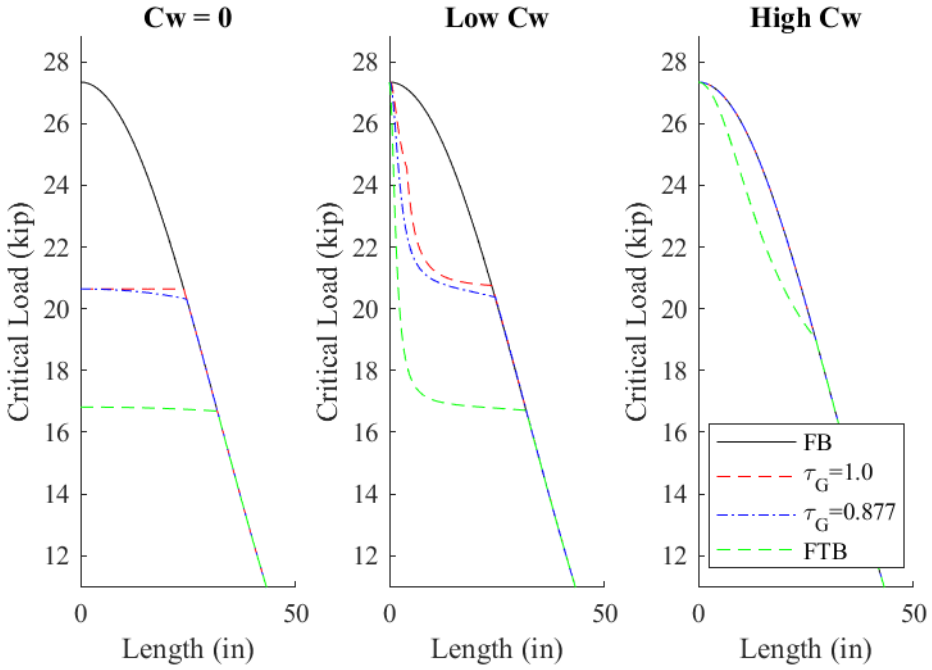

Figure C.2: Inelastic buckling of 2-L1.25"x1.25"x0.115"

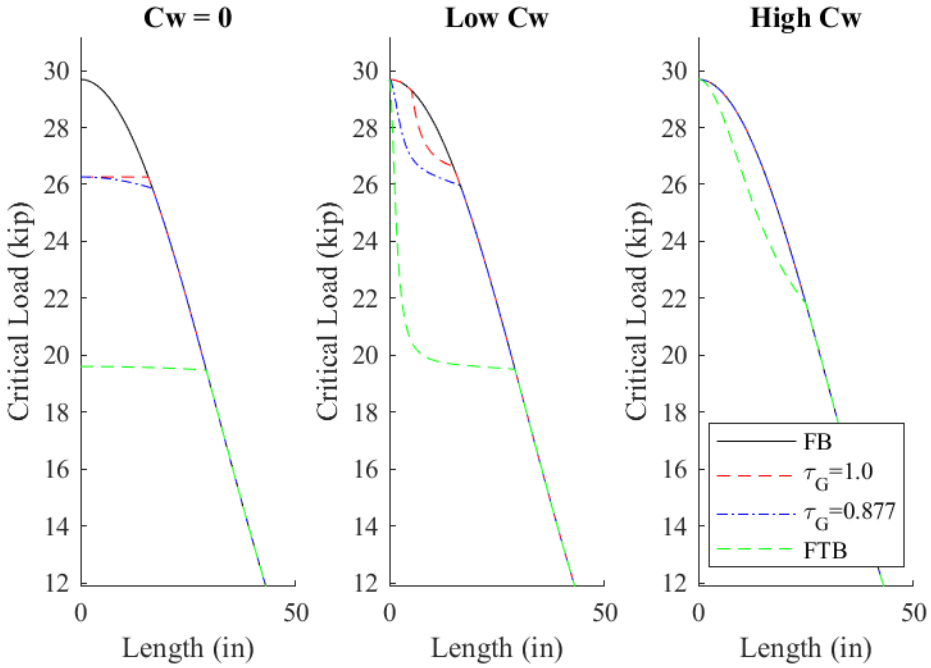

Figure C.3: Inelastic buckling of 2-L1.25"x1.25"x0.125"

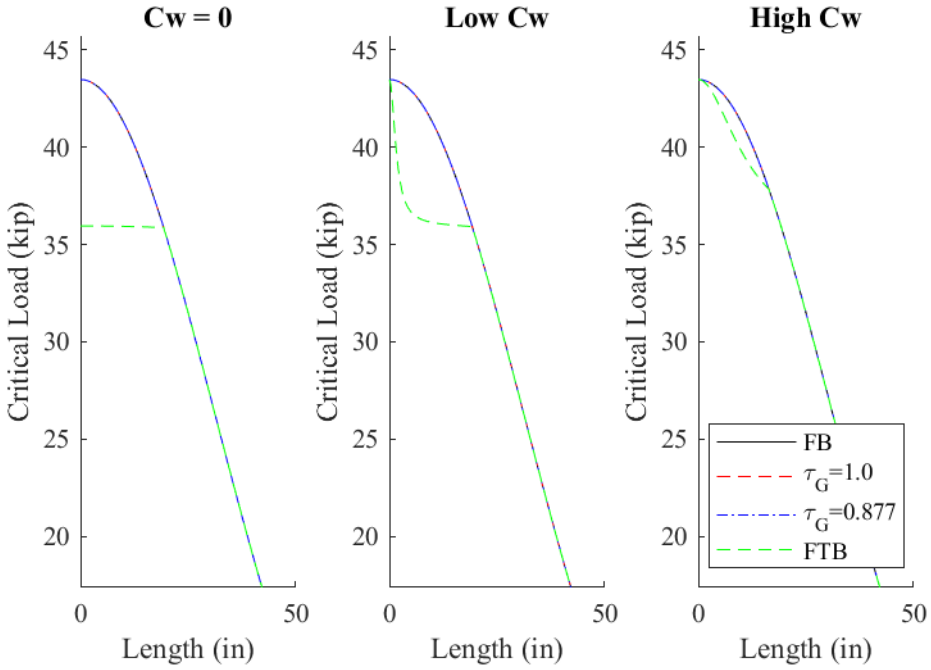

Figure C.4: Inelastic buckling of 2-L1.25"x1.25"x0.188"

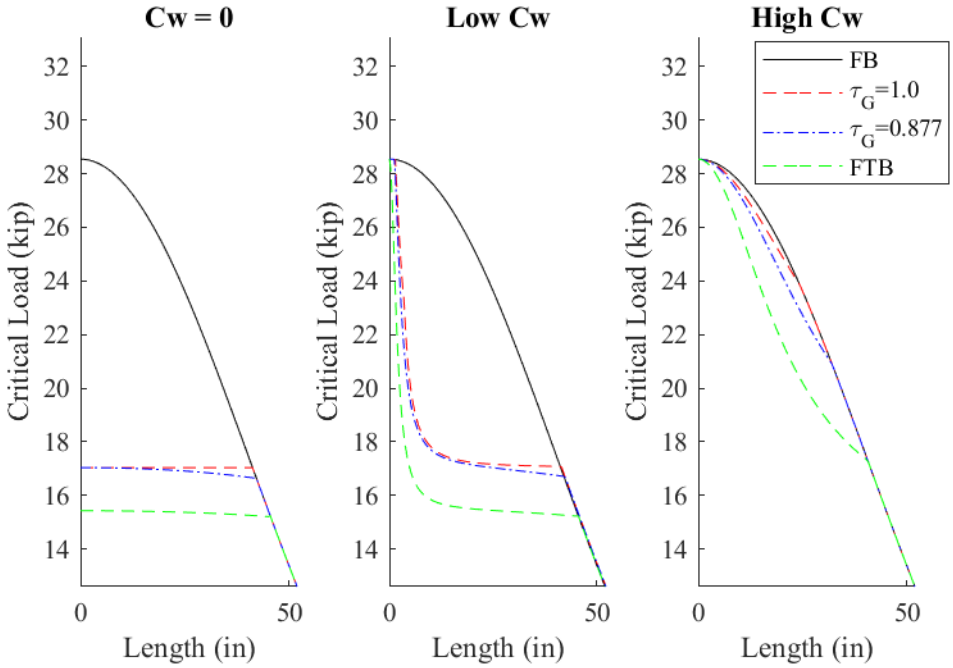

Figure C.5: Inelastic buckling of 2-L1.5"x1.5"x0.109"

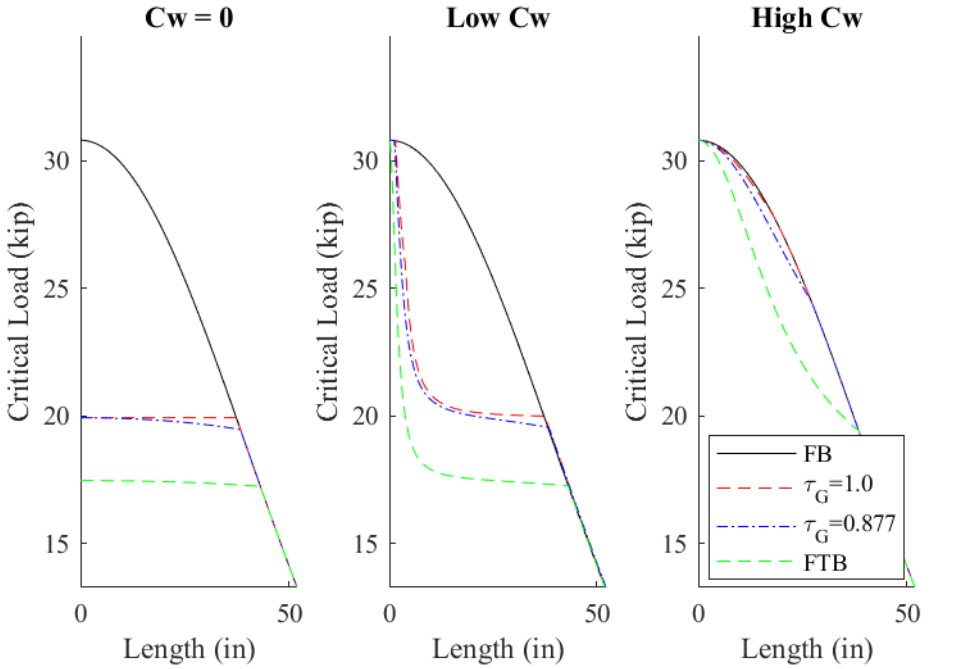

Figure C.6: Inelastic buckling of 2-L1.5"x1.5"x0.115"

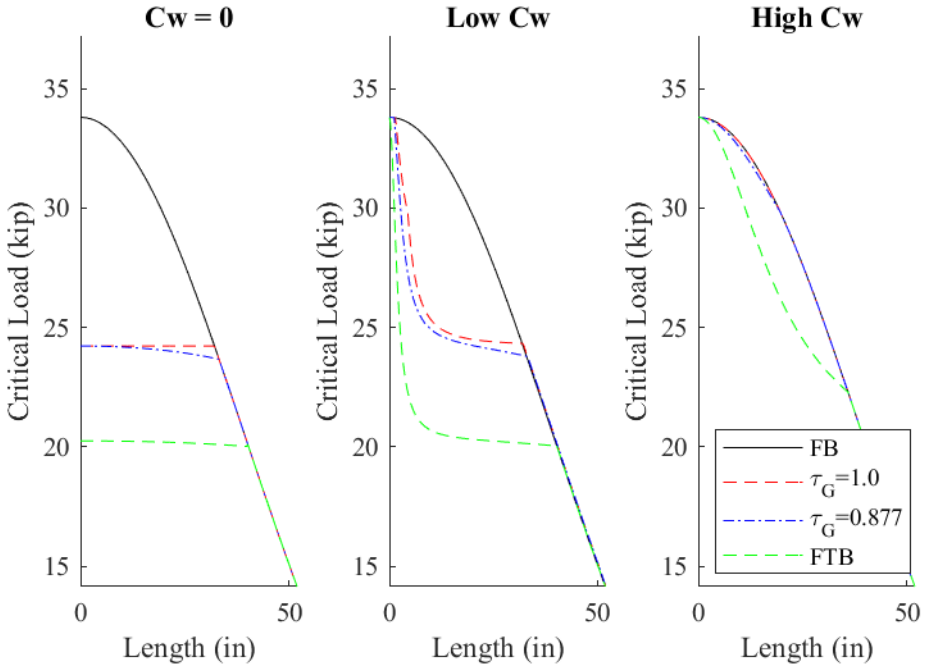

Figure C.7: Inelastic buckling of 2-L1.5"x1.5"x0.123"

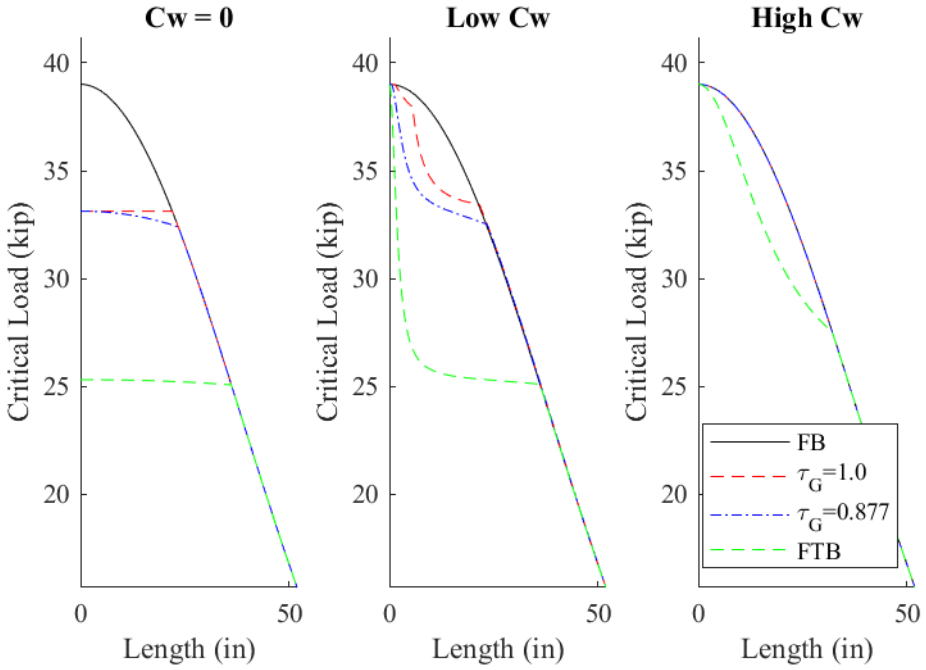

Figure C.8: Inelastic buckling of 2-L1.5"x1.5"x0.137"

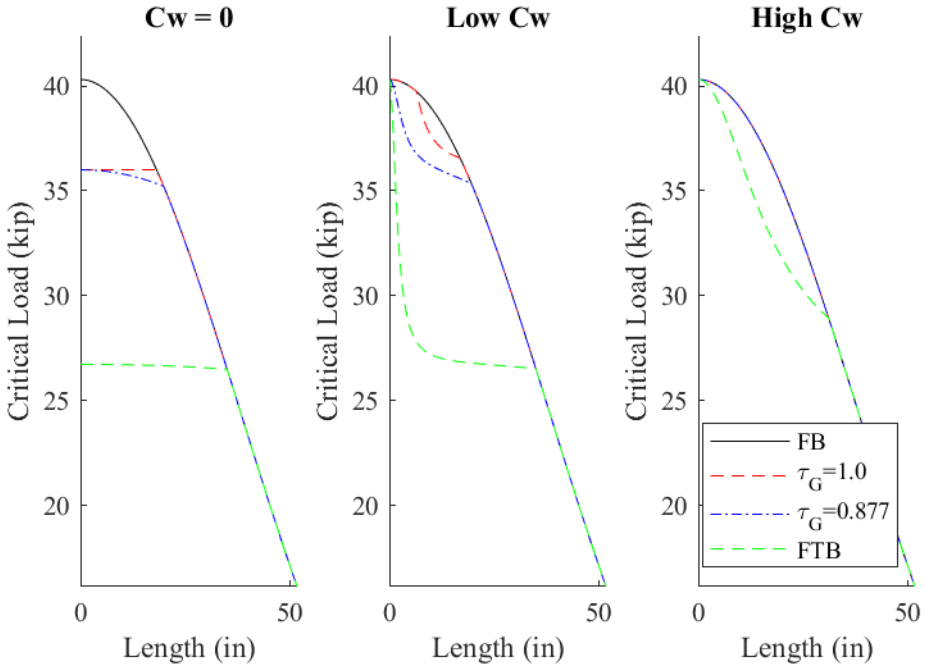

Figure C.9: Inelastic buckling of 2-L1.5"x1.5"x0.141"

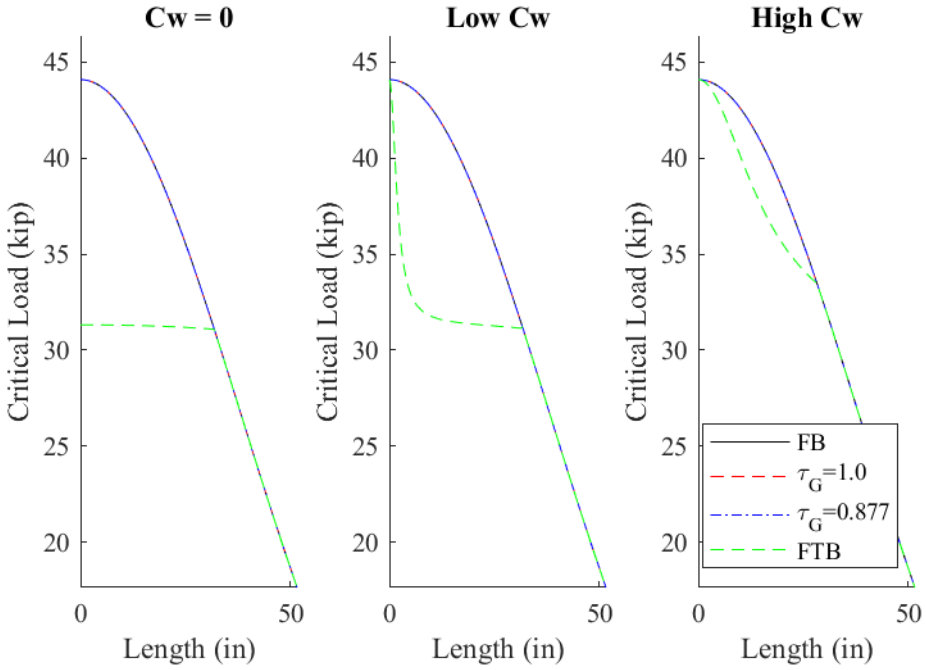

Figure C.10: Inelastic buckling of 2-L1.5"x1.5"x0.155"

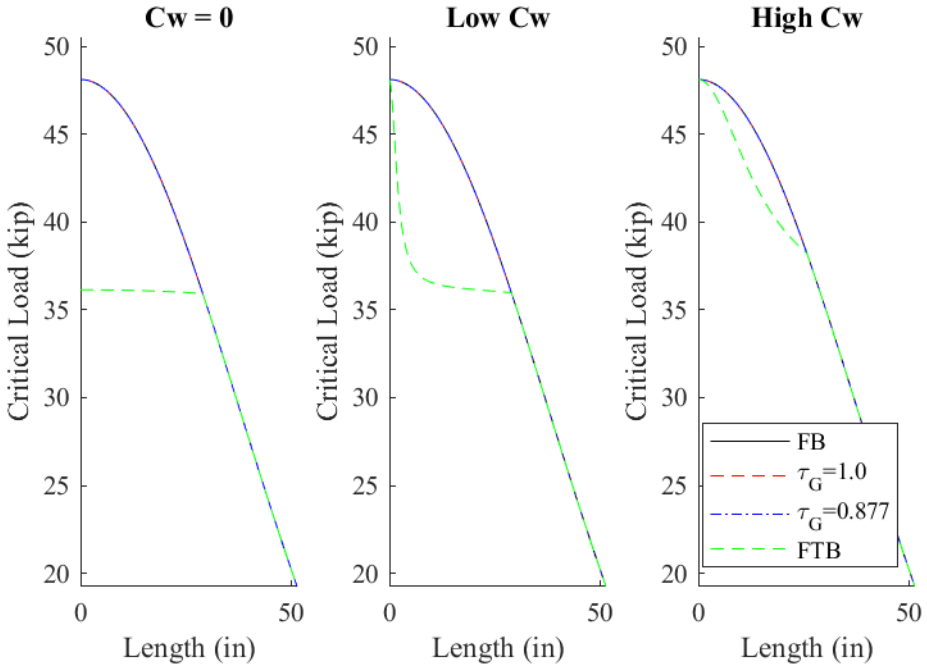

Figure C.11: Inelastic buckling of 2-L1.5"x1.5"x0.17"

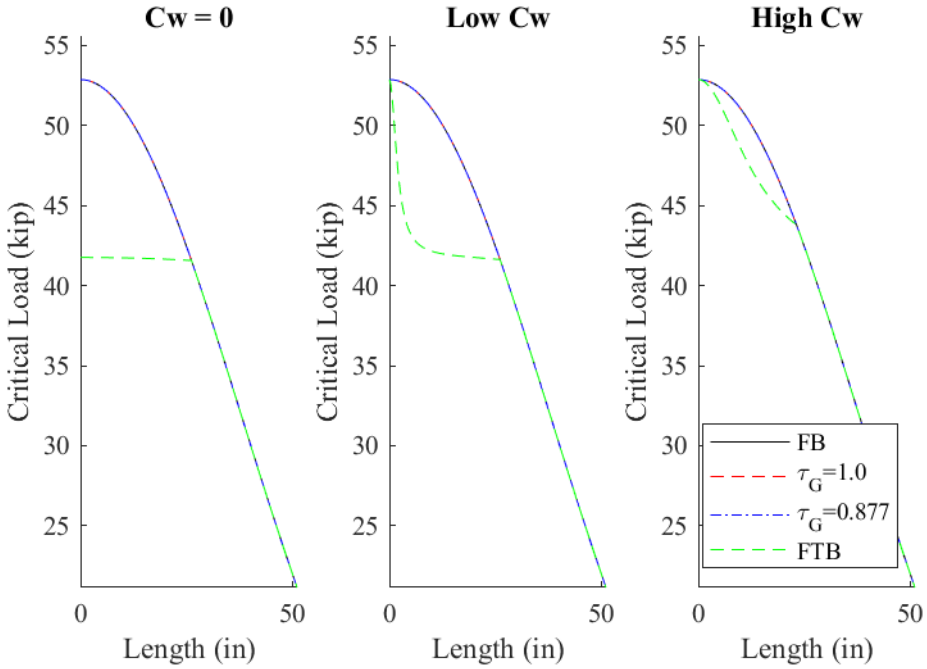

Figure C.12: Inelastic buckling of 2-L1.5"x1.5"x0.188"

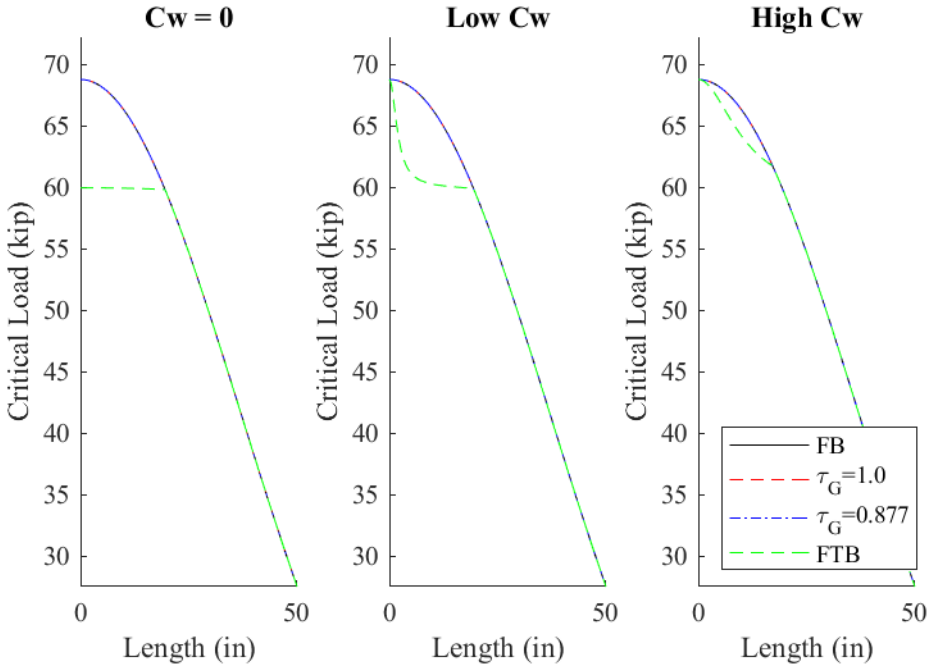

Figure C.13: Inelastic buckling of 2-L1.5"x1.5"x0.25"

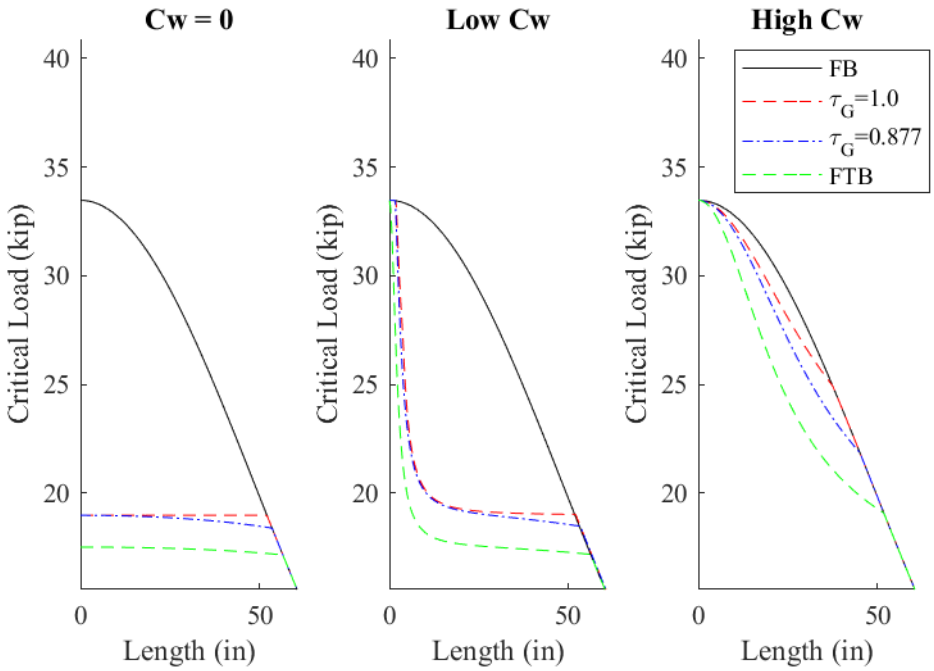

Figure C.14: Inelastic buckling of 2-L1.75"x1.75"x0.115"

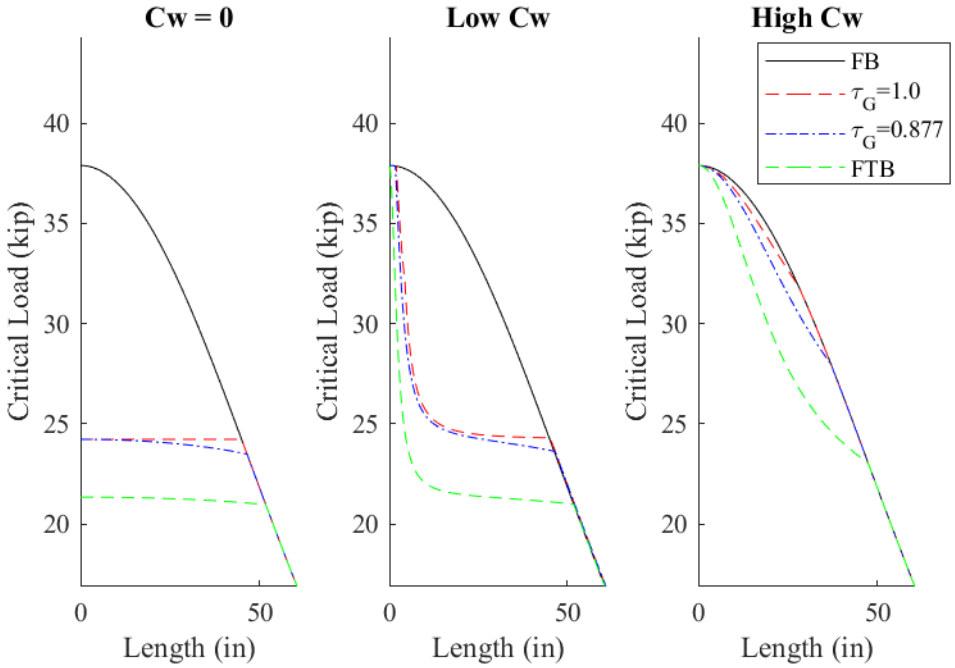

Figure C.15: Inelastic buckling of 2-L1.75"x1.75"x0.125"

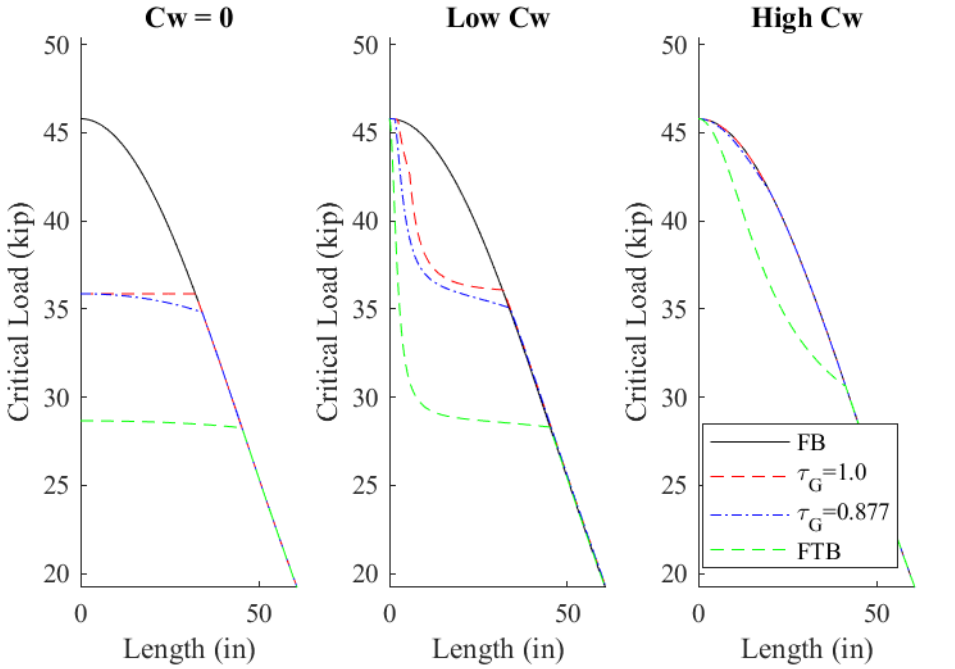

Figure C.16: Inelastic buckling of 2-L1.75"x1.75"x0.143"

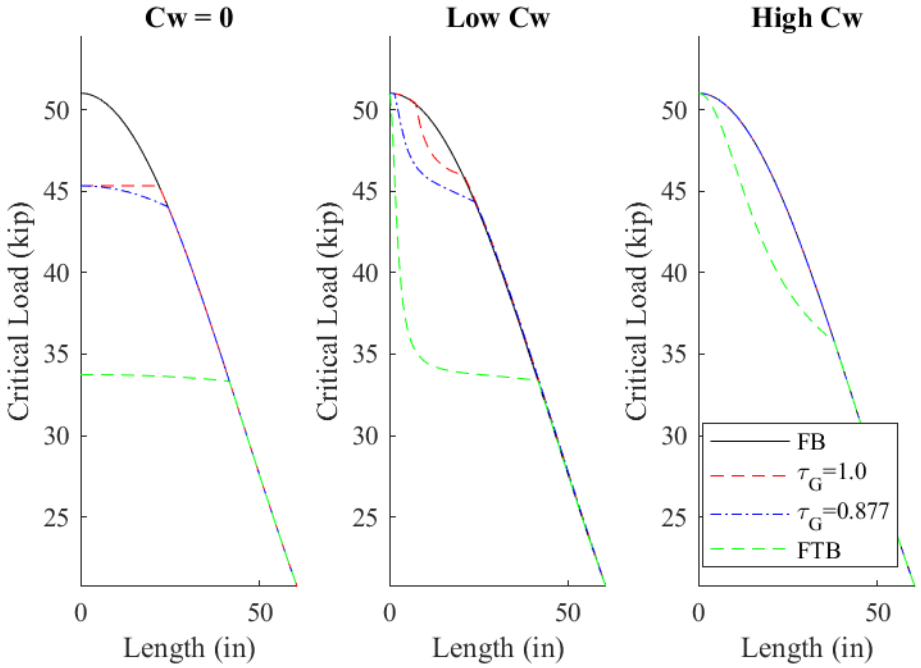

Figure C.17: Inelastic buckling of 2-L1.75"x1.75"x0.155"

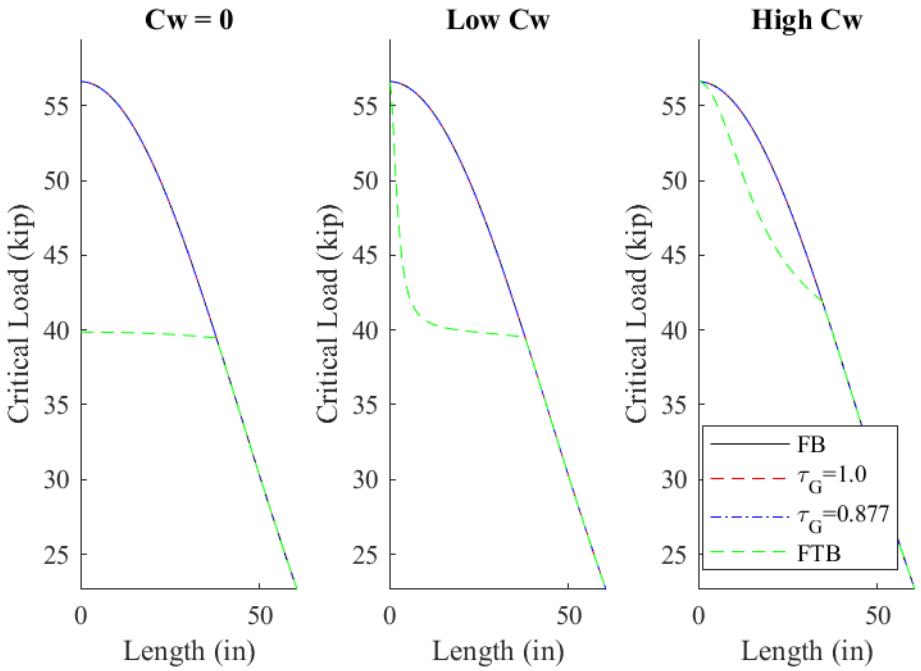

Figure C.18: Inelastic buckling of 2-L1.75"x1.75"x0.17"

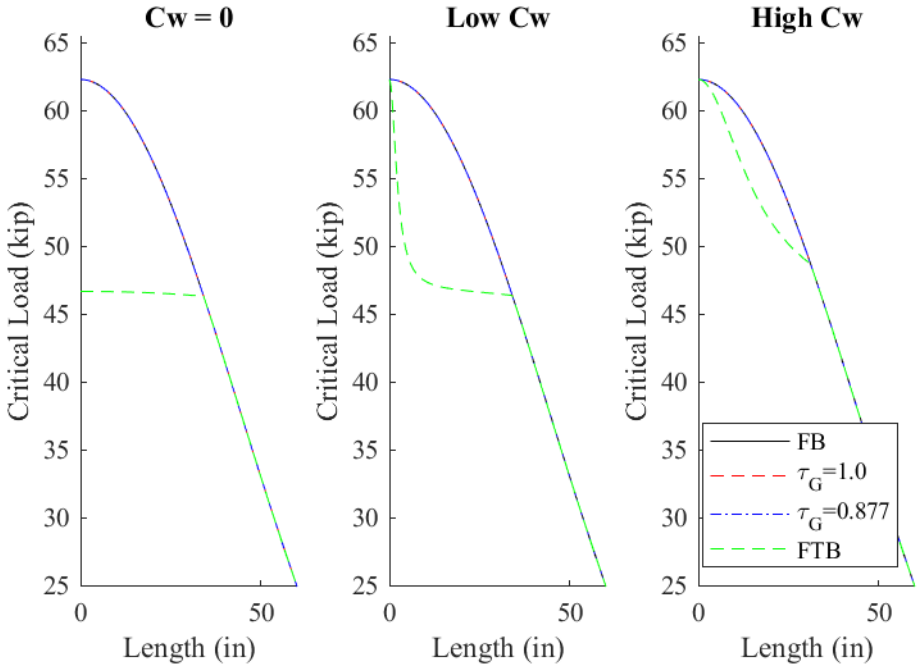

Figure C.19: Inelastic buckling of 2-L1.75"x1.75"x0.188"

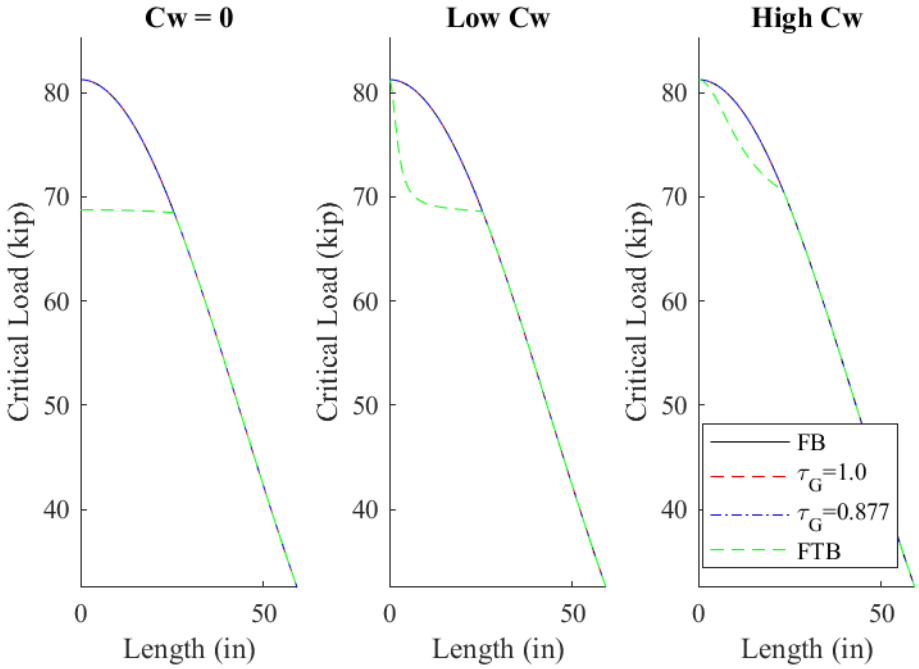

Figure C.20: Inelastic buckling of 2-L1.75"x1.75"x0.25"

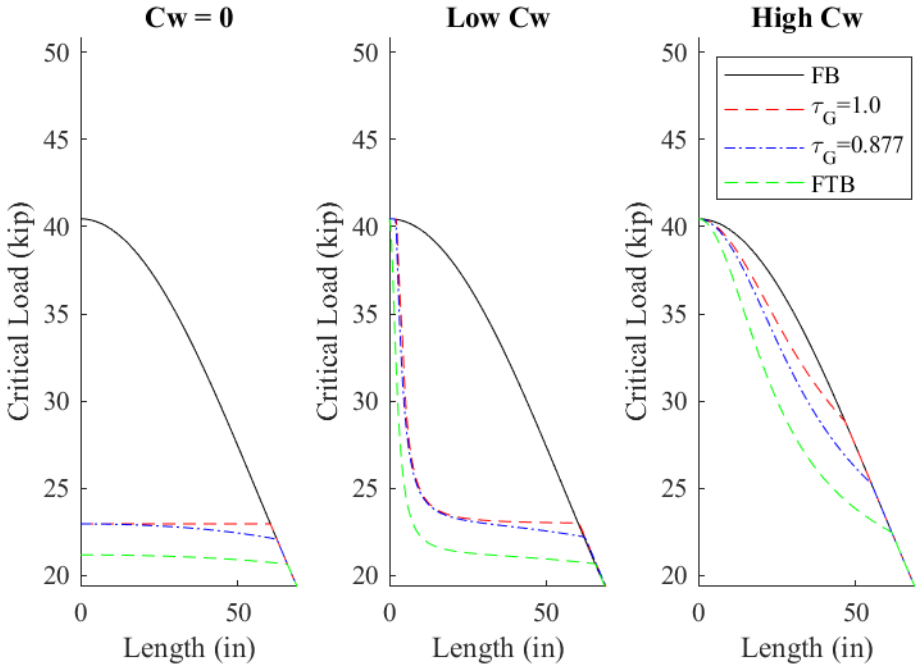

Figure C.21: Inelastic buckling of 2-L2"x2"x0.125"

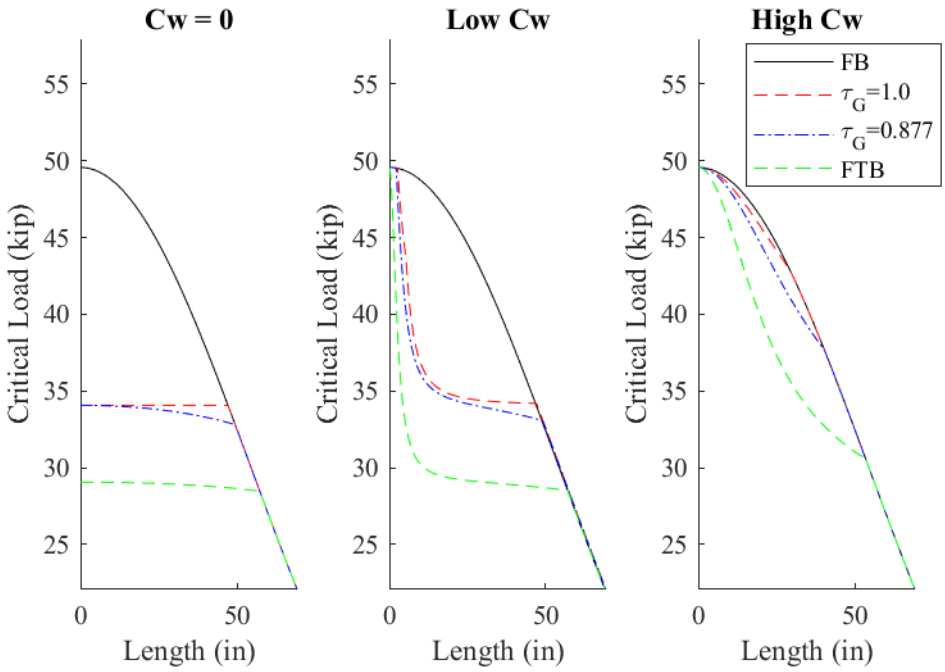

Figure C.22: Inelastic buckling of 2-L2"x2"x0.143"

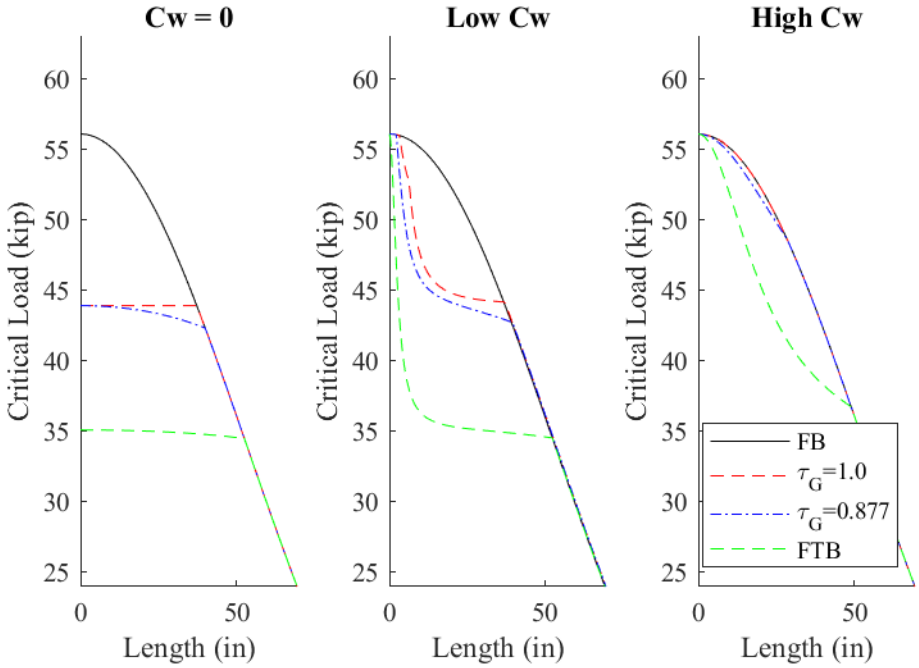

Figure C.23: Inelastic buckling of 2-L2"x2"x0.156"

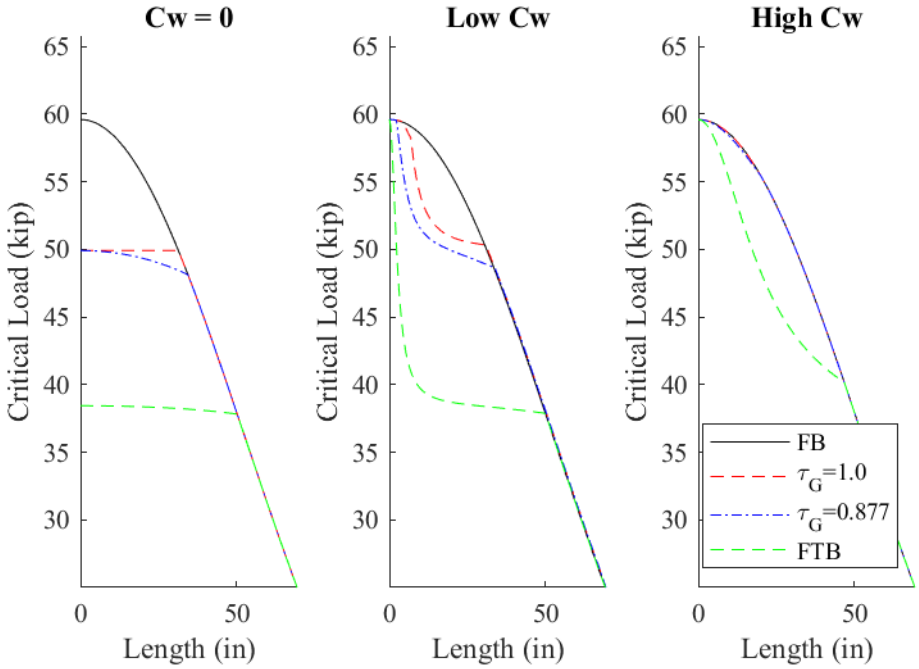

Figure C.24: Inelastic buckling of 2-L2"x2"x0.163"

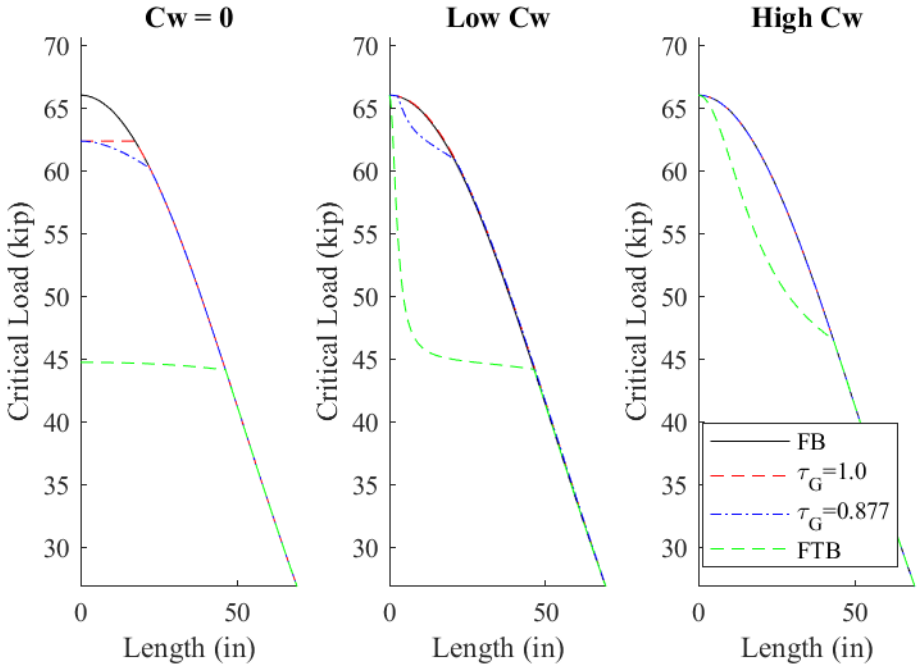

Figure C.25: Inelastic buckling of 2-L2"x2"x0.176"

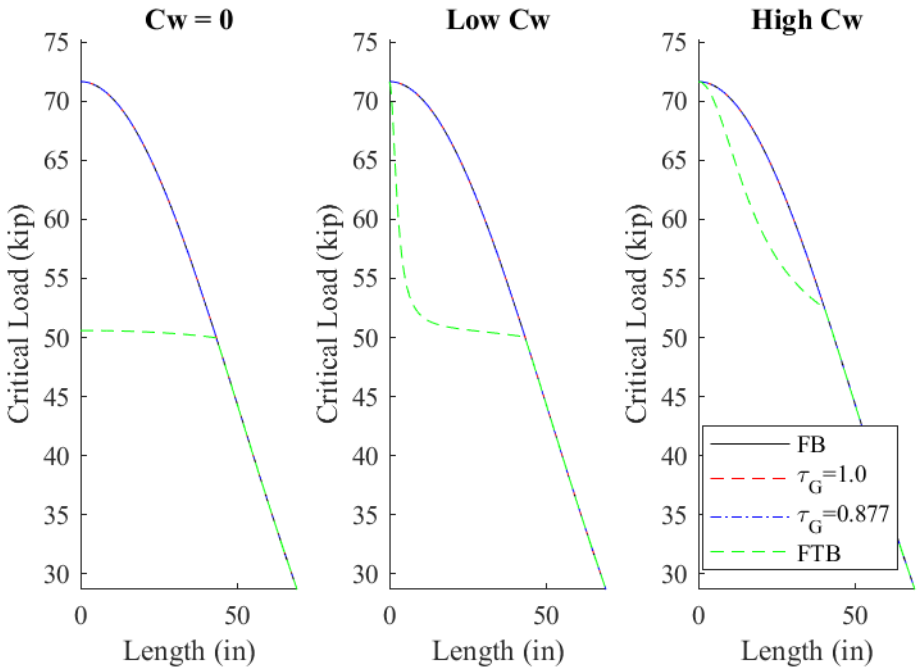

Figure C.26: Inelastic buckling of 2-L2"x2"x0.188"

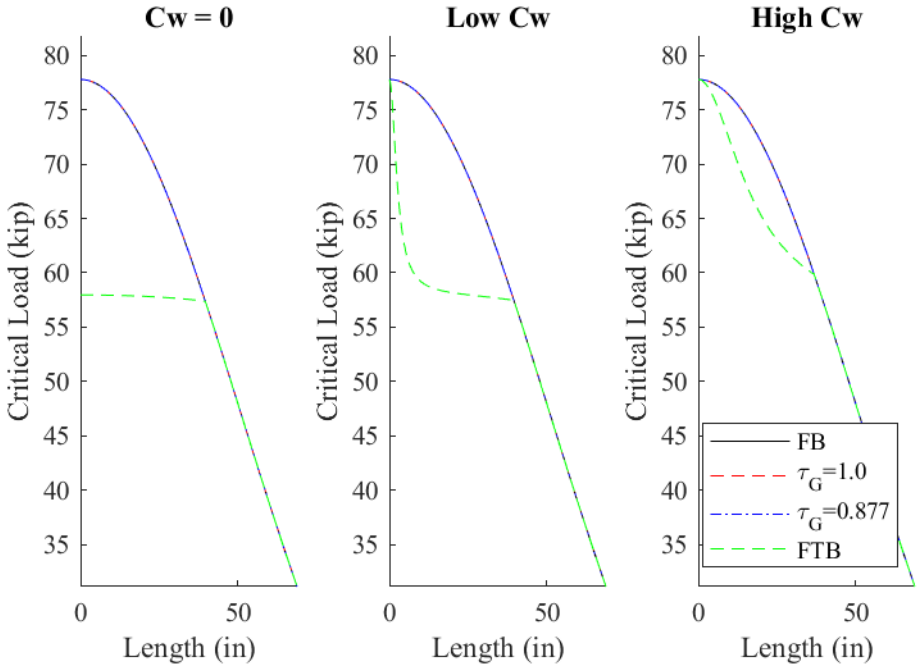

Figure C.27: Inelastic buckling of 2-L2"x2"x0.205"

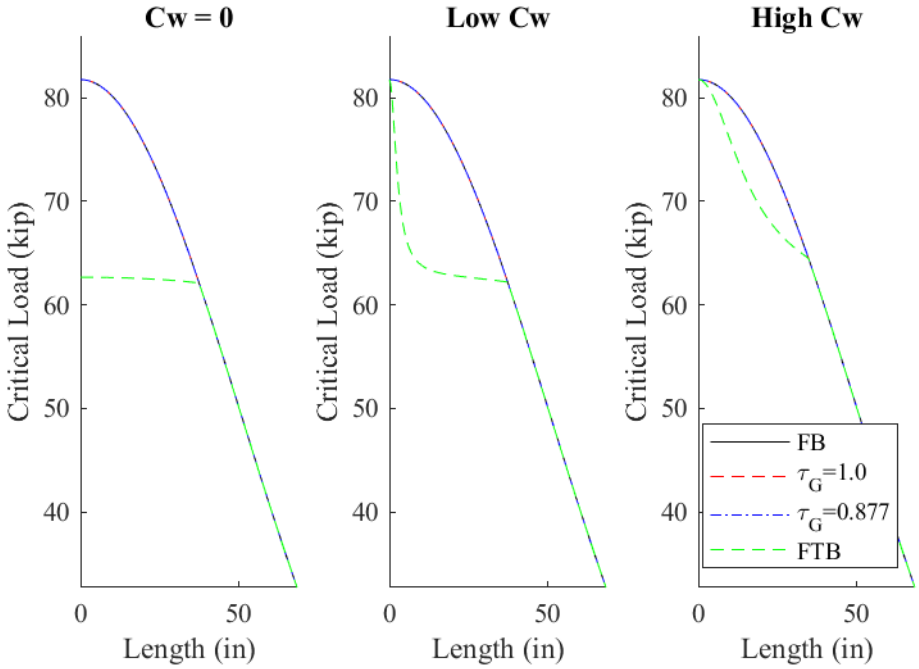

Figure C.28: Inelastic buckling of 2-L2"x2"x0.216"

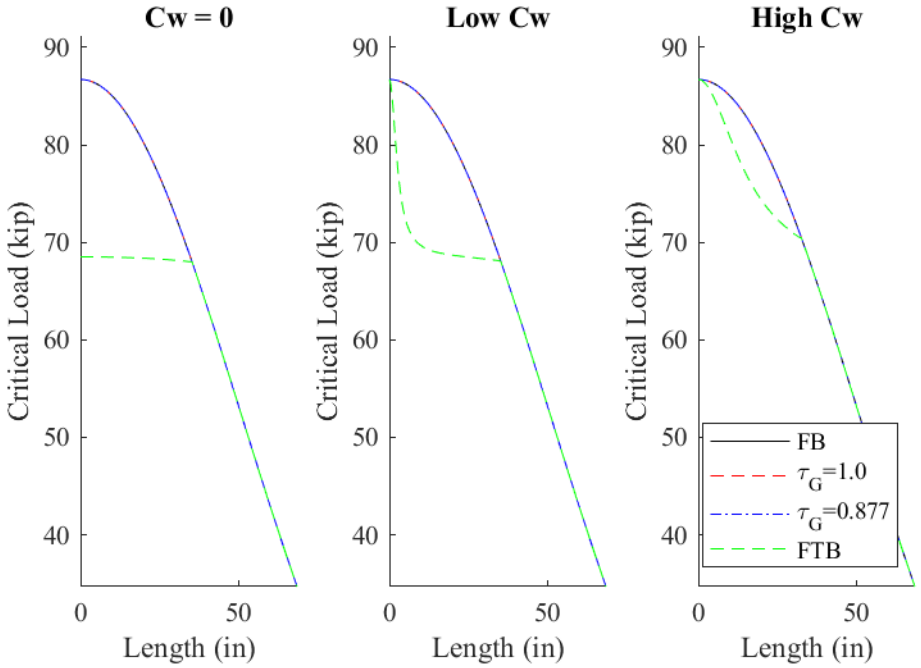

Figure C.29: Inelastic buckling of 2-L2"x2"x0.23"

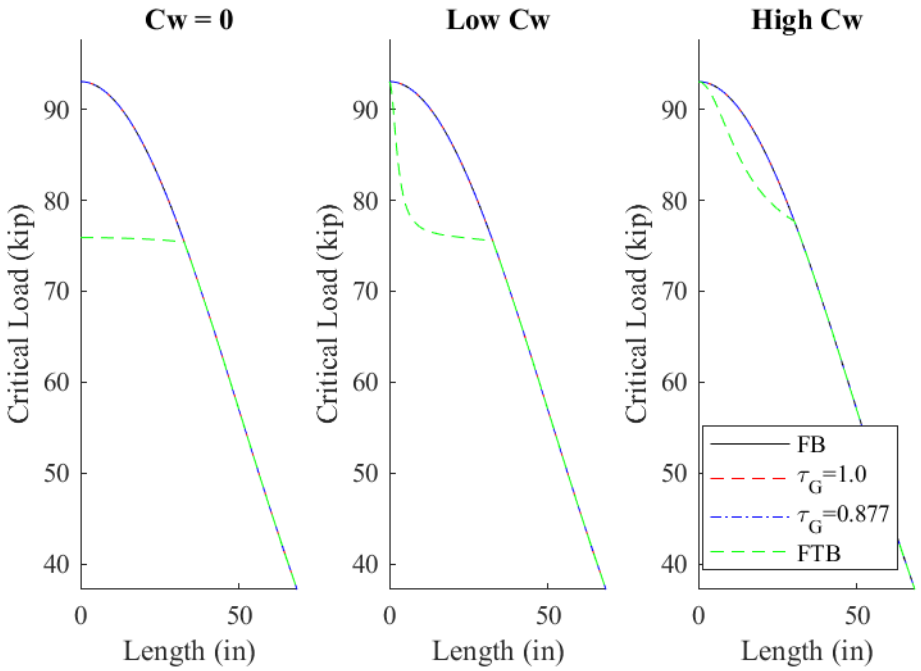

Figure C.30: Inelastic buckling of 2-L2"x2"x0.248"

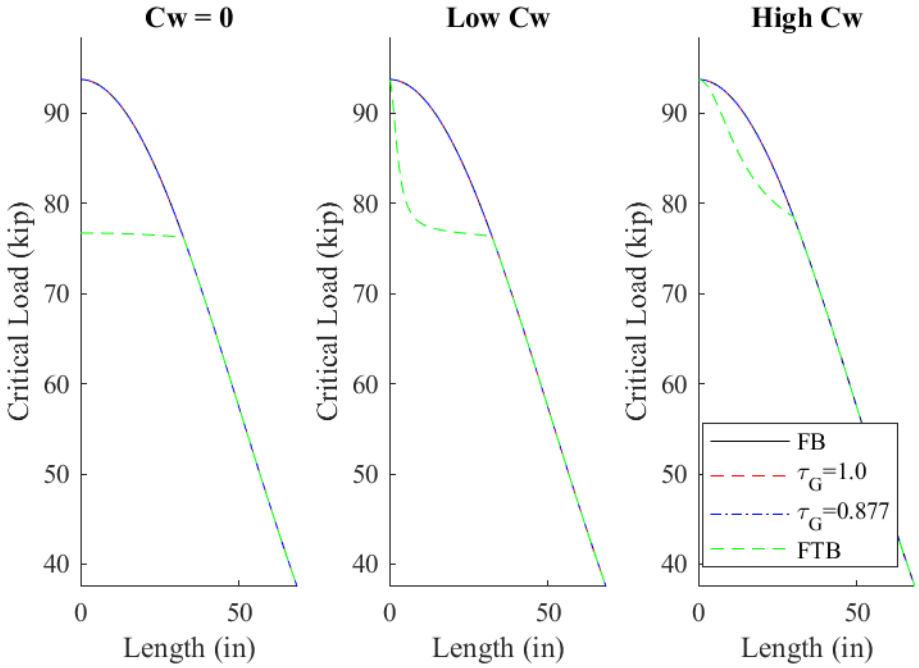

Figure C.31: Inelastic buckling of 2-L2"x2"x0.25"

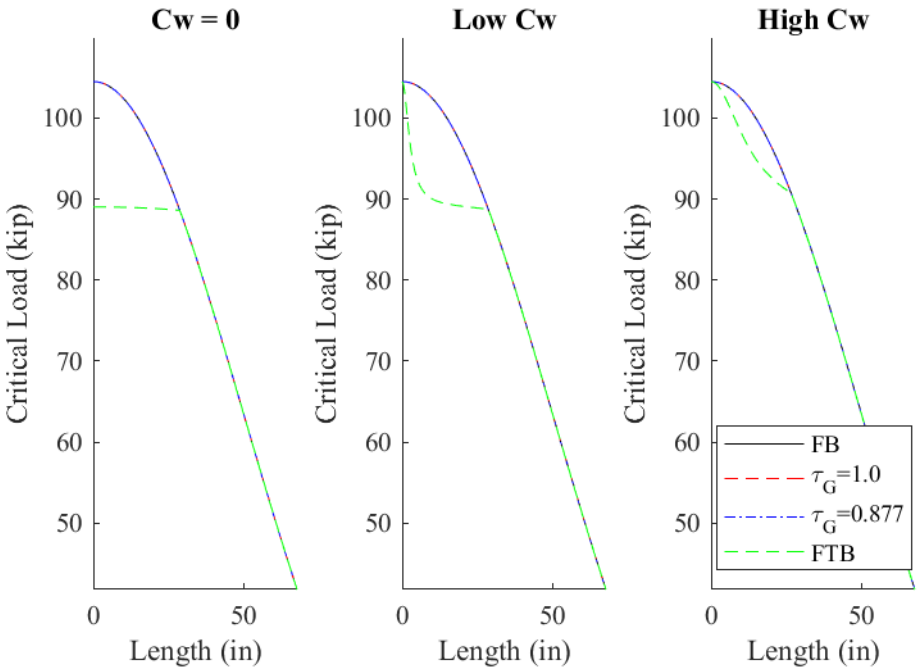

Figure C.32: Inelastic buckling of 2-L2"x2"x0.281"

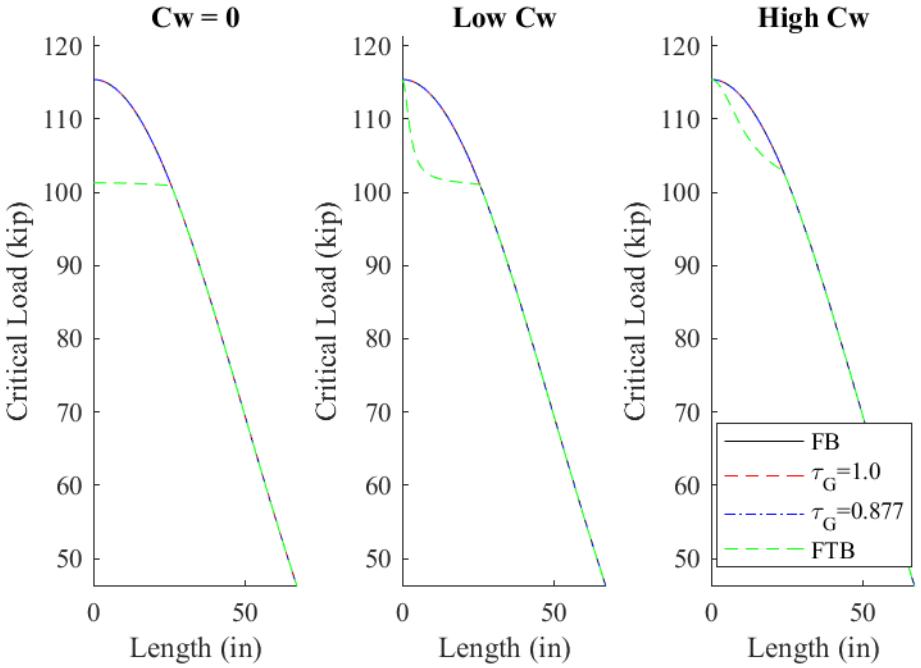

Figure C.33: Inelastic buckling of 2-L2"x2"x0.313"

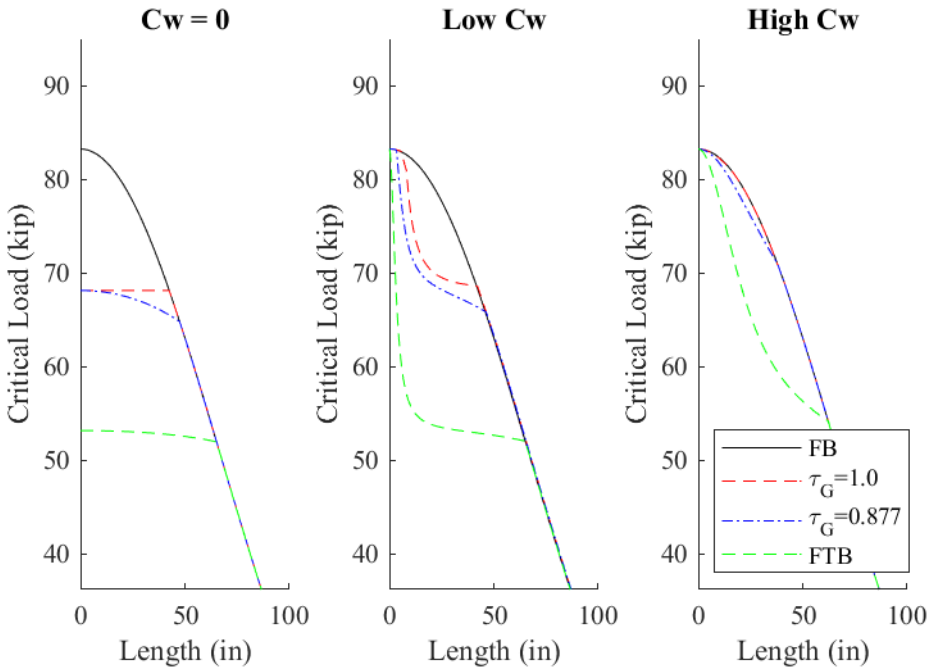

Figure C.34: Inelastic buckling of 2-L2.5"x2.5"x0.188"

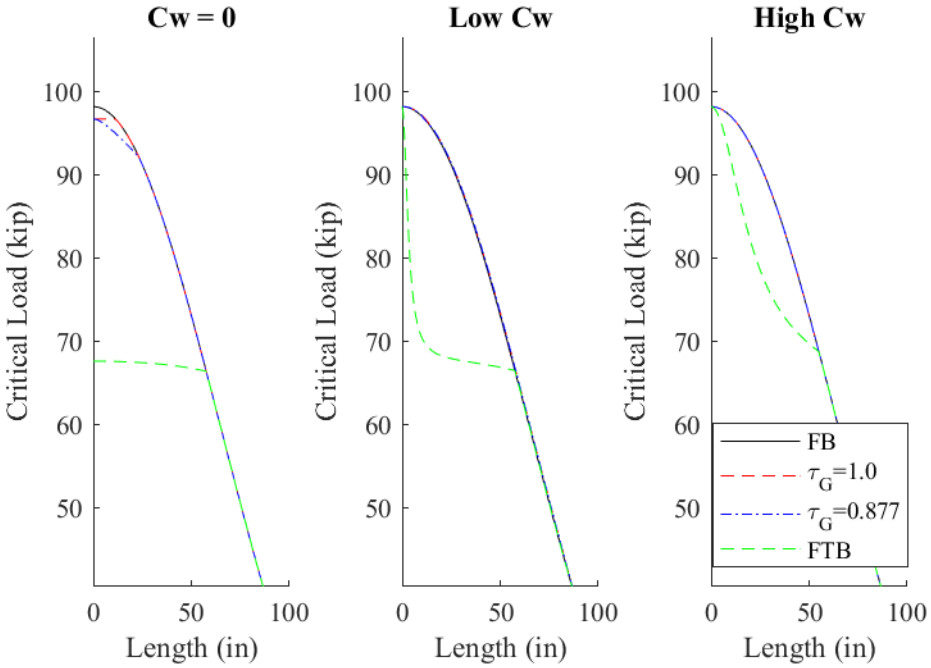

Figure C.35: Inelastic buckling of 2-L2.5"x2.5"x0.212"

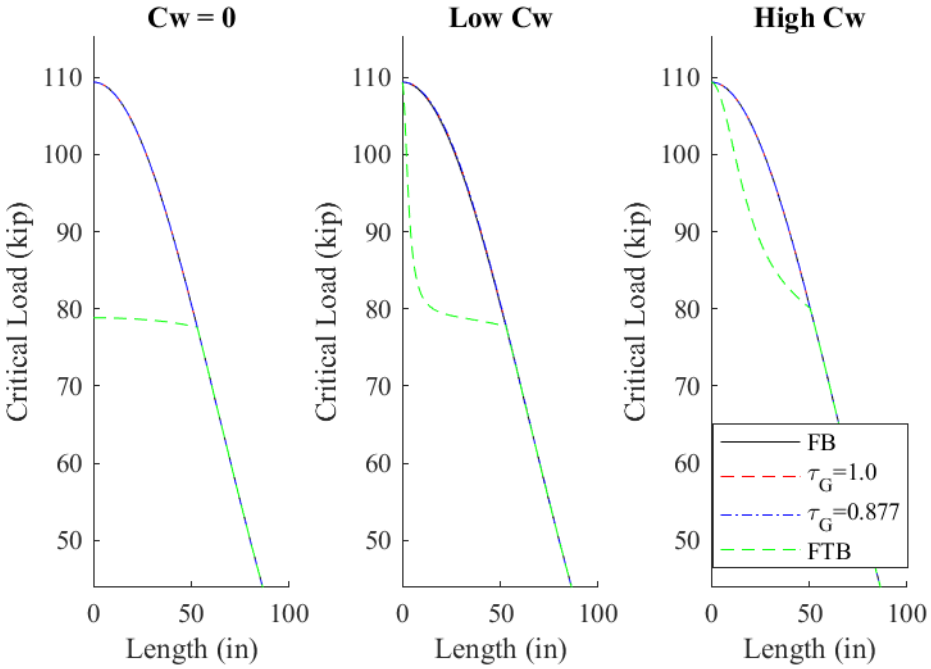

Figure C.36: Inelastic buckling of 2-L2.5"x2.5"x0.23"

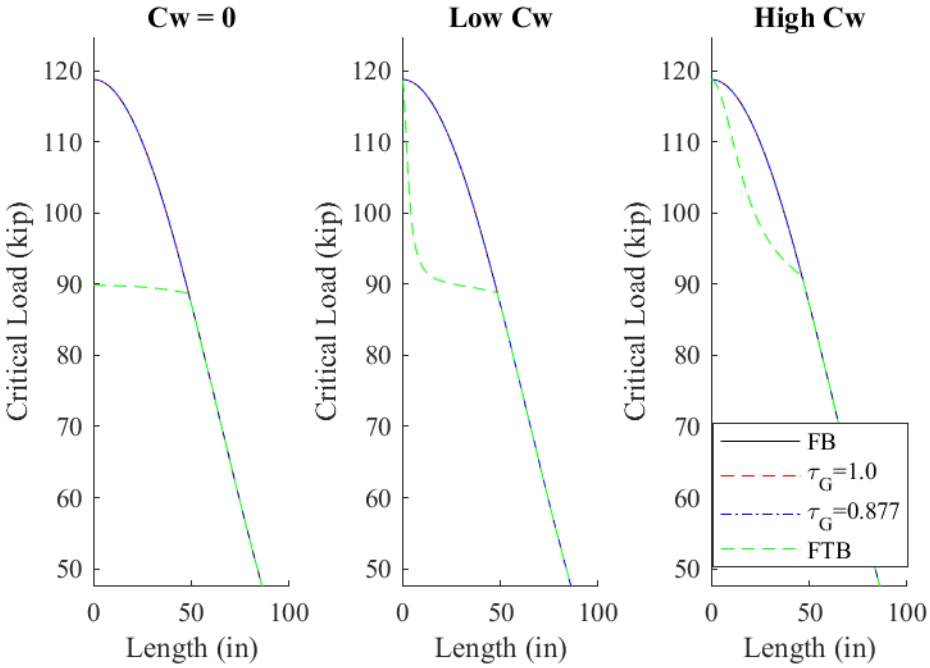

Figure C.37: Inelastic buckling of 2-L2.5"x2.5"x0.25"

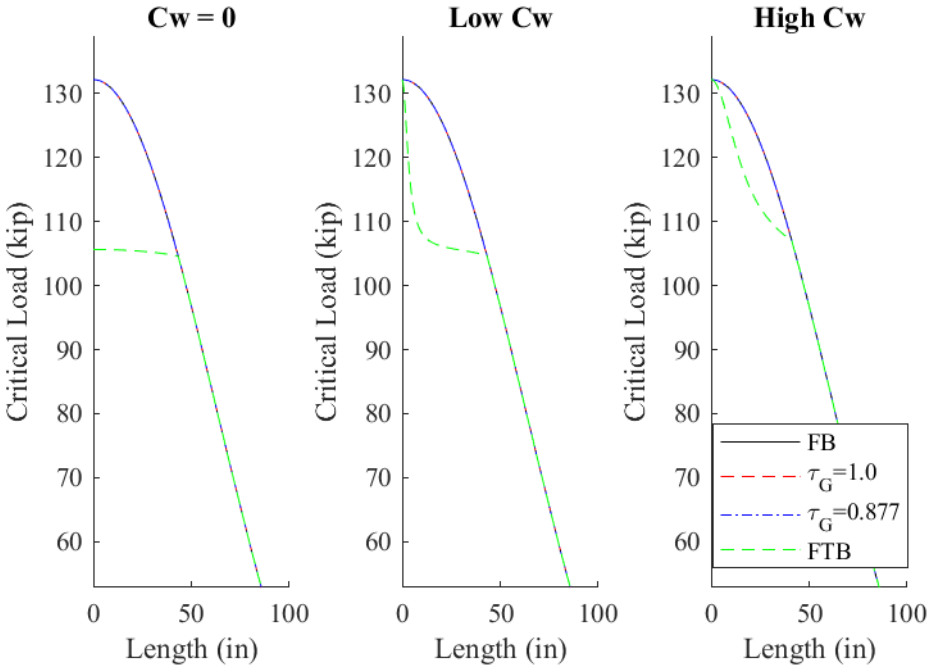

Figure C.38: Inelastic buckling of 2-L2.5"x2.5"x0.28"

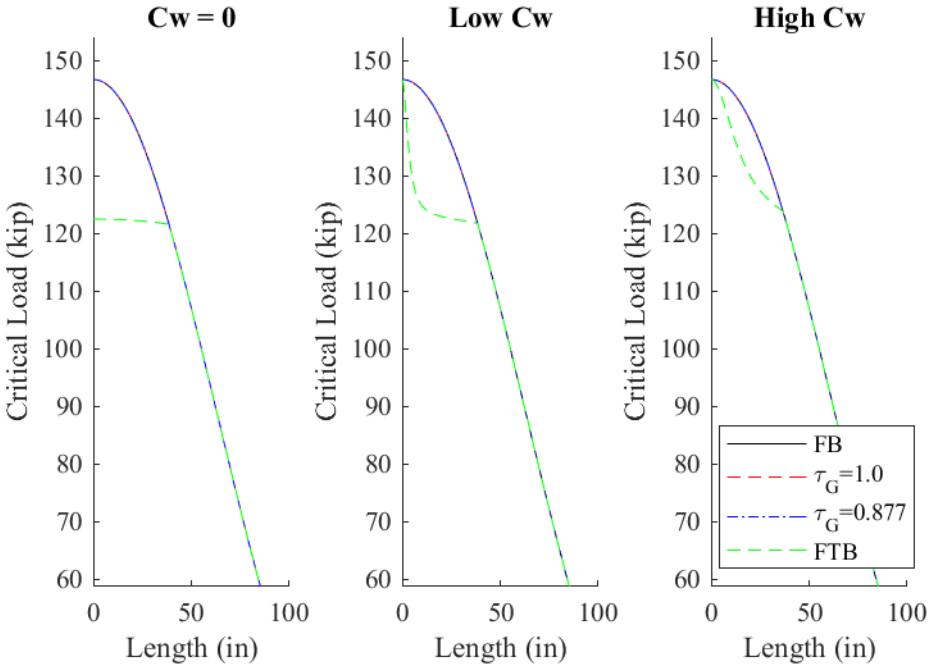

Figure C.39: Inelastic buckling of 2-L2.5"x2.5"x0.313"

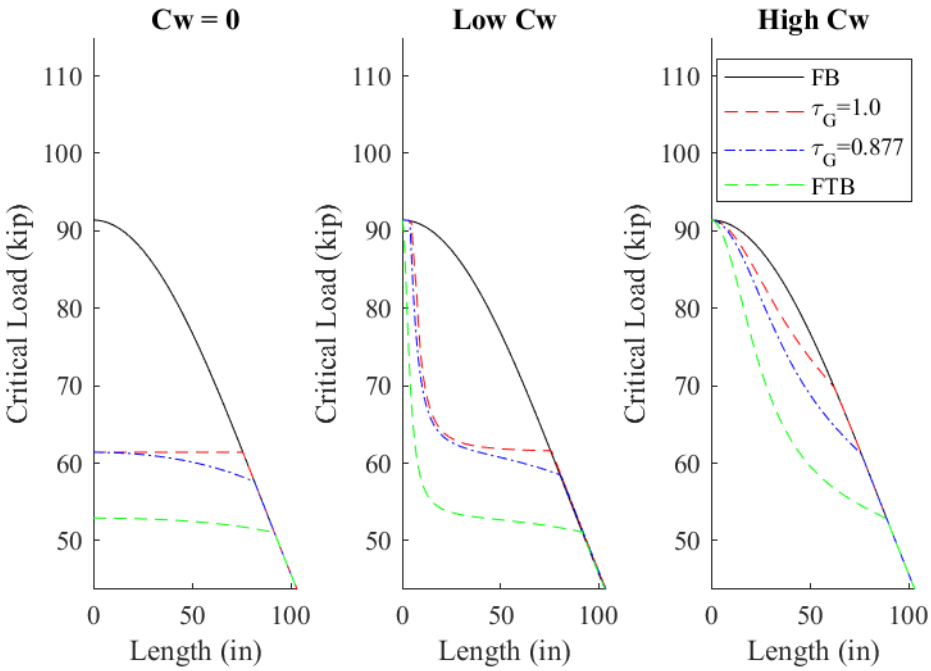

Figure C.40: Inelastic buckling of 2-L3"x3"x0.188"

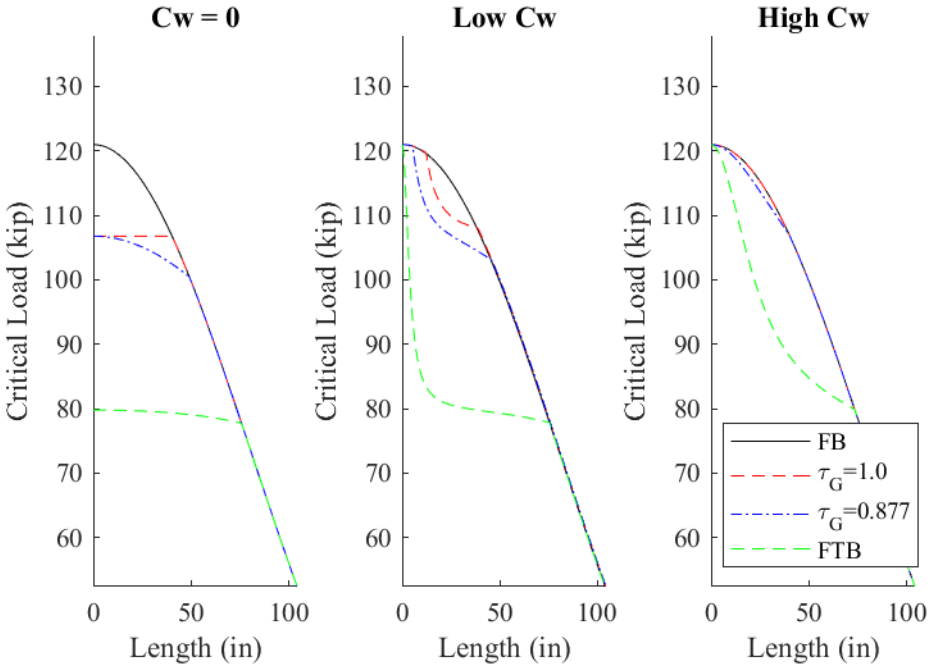

Figure C.41: Inelastic buckling of 2-L3"x3"x0.227"

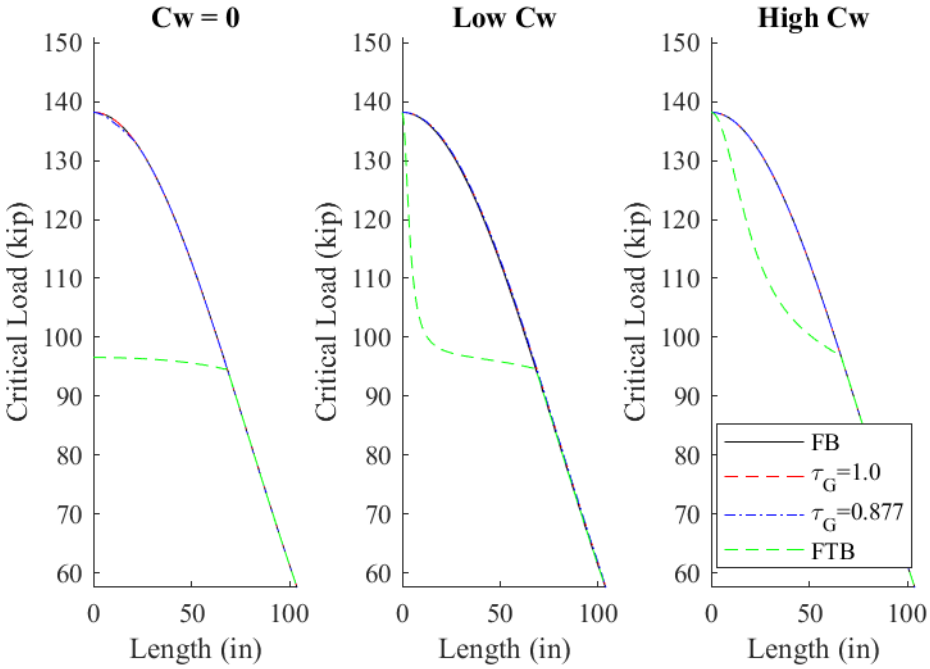

Figure C.42: Inelastic buckling of 2-L3"x3"x0.25"

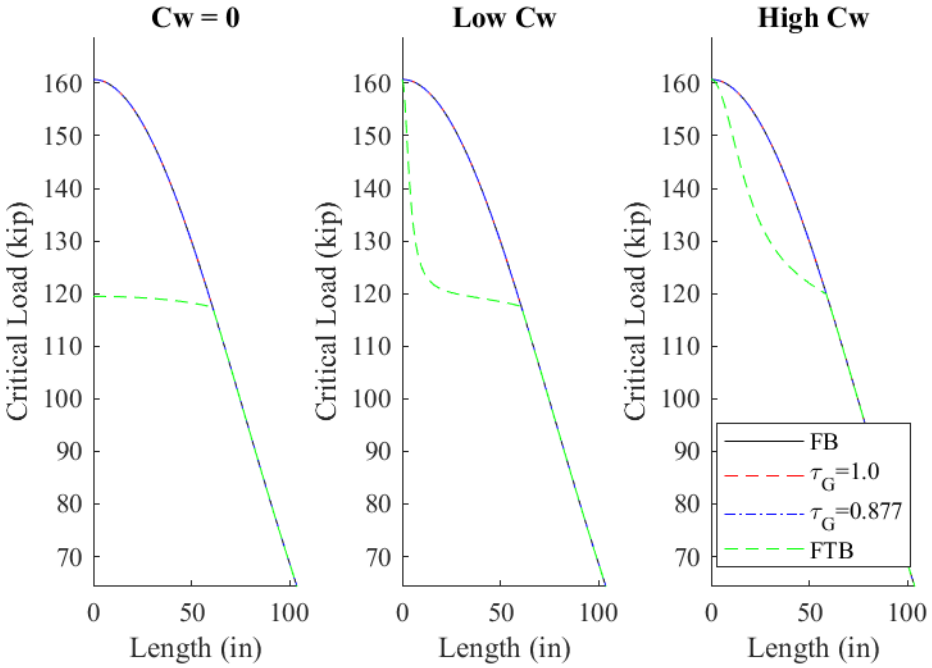

Figure C.43: Inelastic buckling of 2-L3"x3"x0.281"

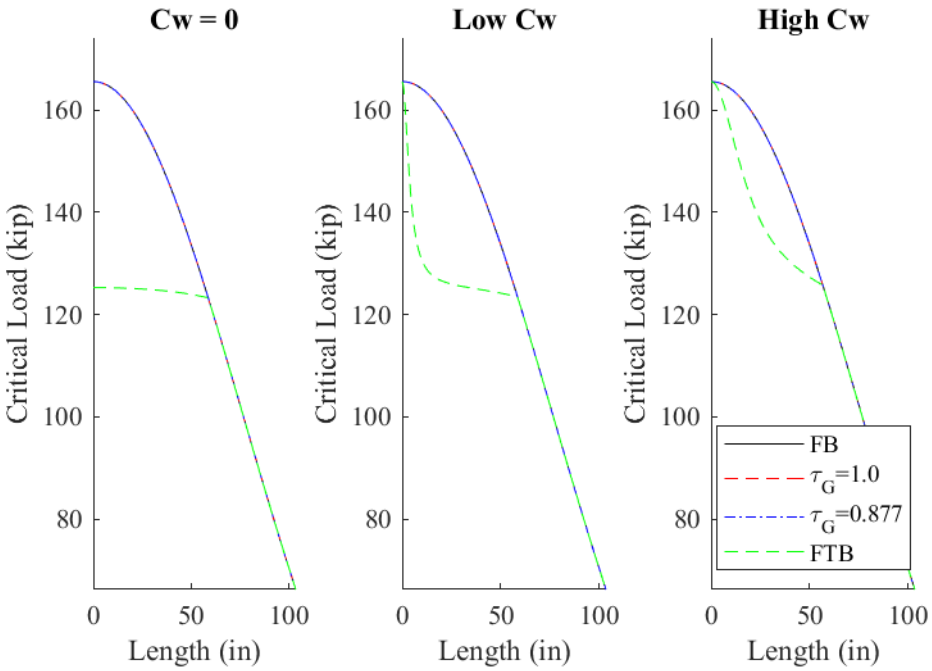

Figure C.44: Inelastic buckling of 2-L3"x3"x0.29"

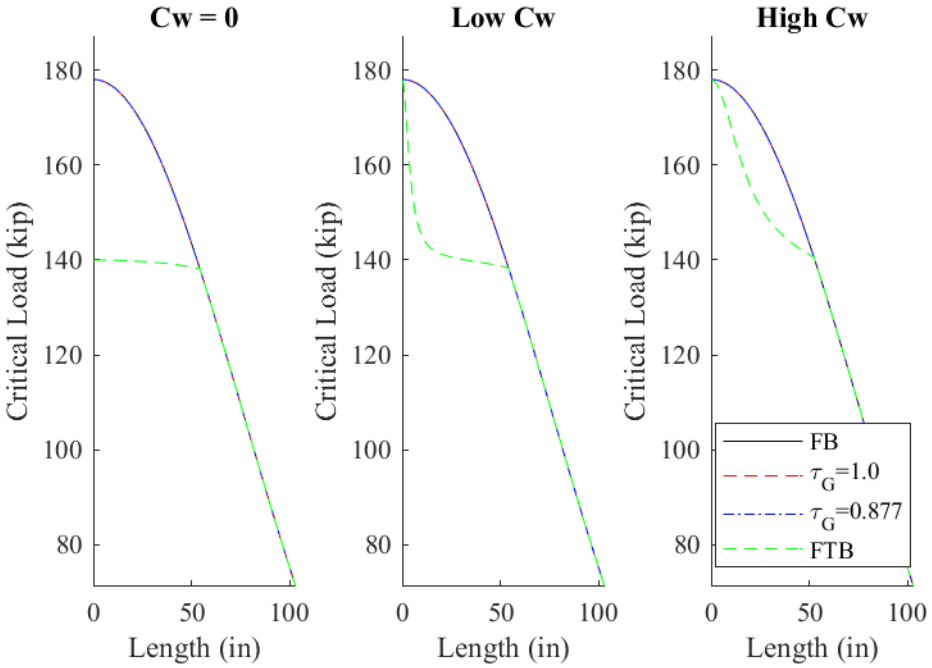

Figure C.45: Inelastic buckling of 2-L3"x3"x0.313"

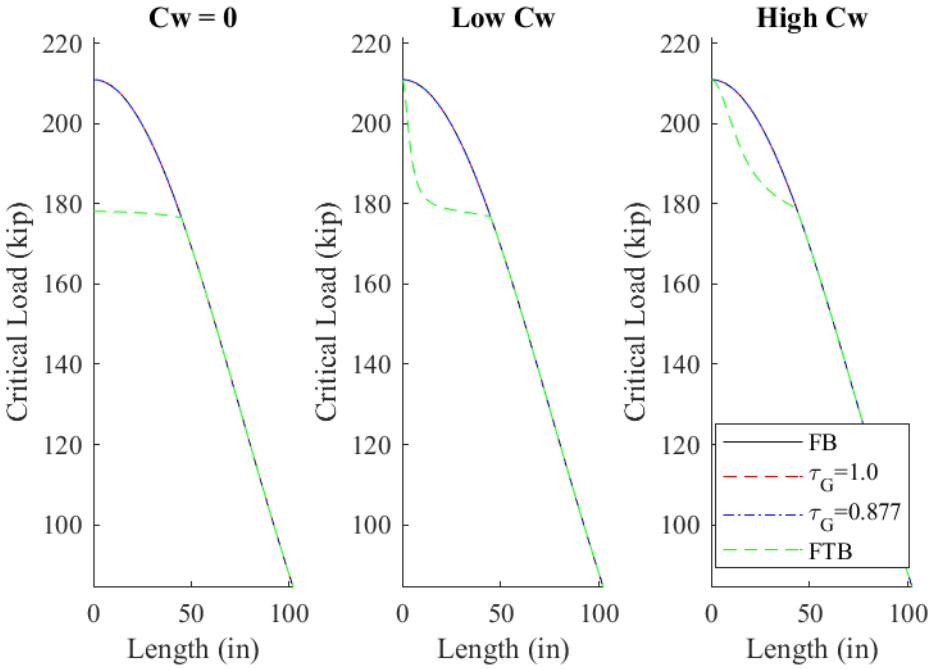

Figure C.46: Inelastic buckling of 2-L3"x3"x0.375"

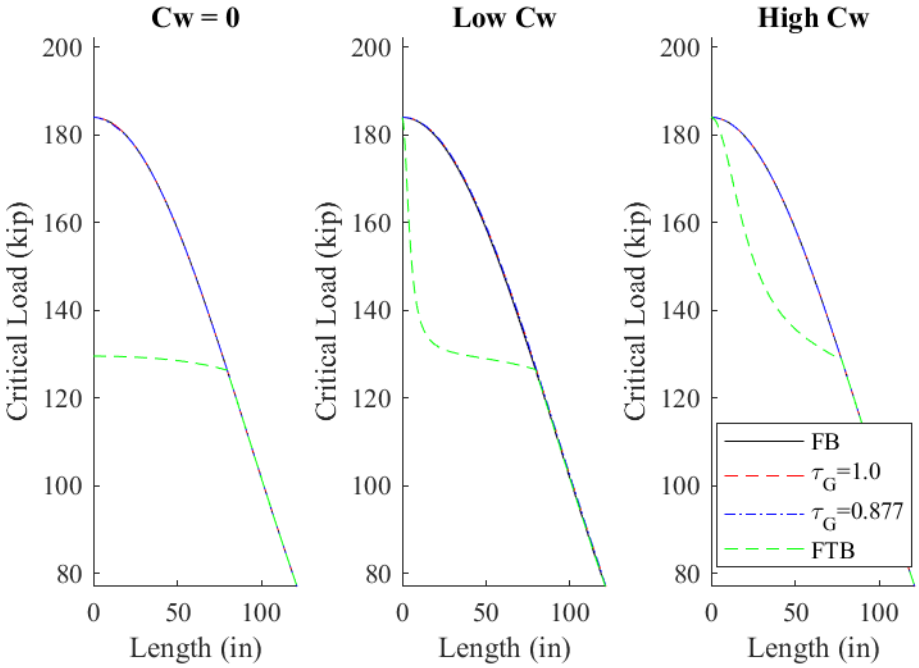

Figure C.47: Inelastic buckling of 2-L3.5"x3.5"x0.287"

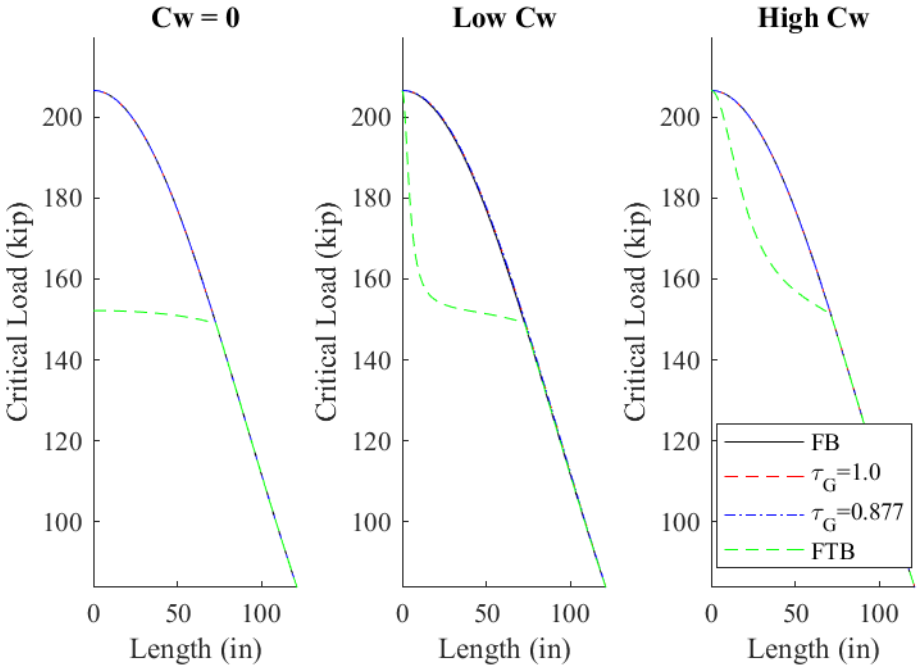

Figure C.48: Inelastic buckling of 2-L3.5"x3.5"x0.313"

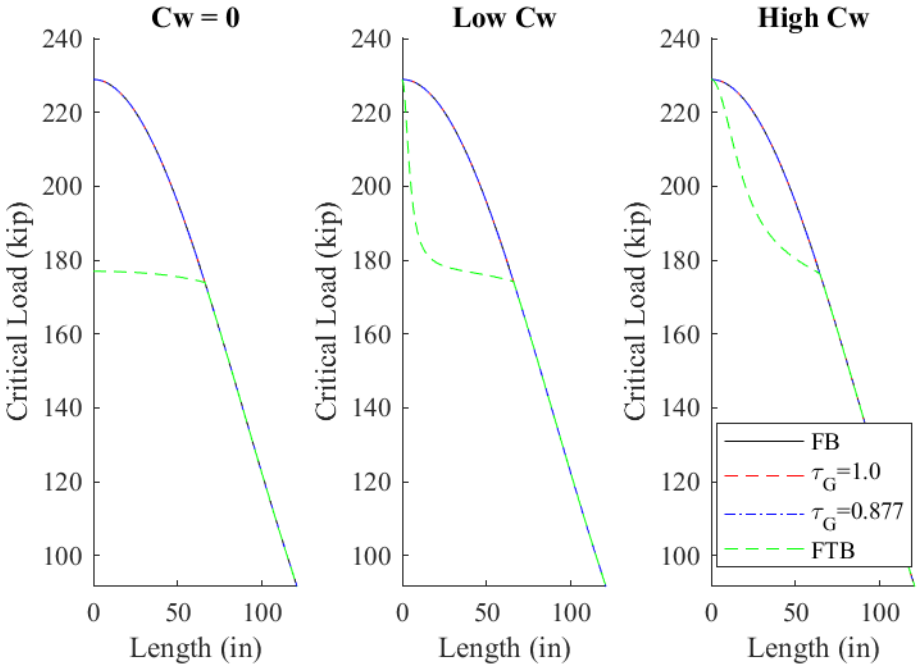

Figure C.49: Inelastic buckling of 2-L3.5"x3.5"x0.344"

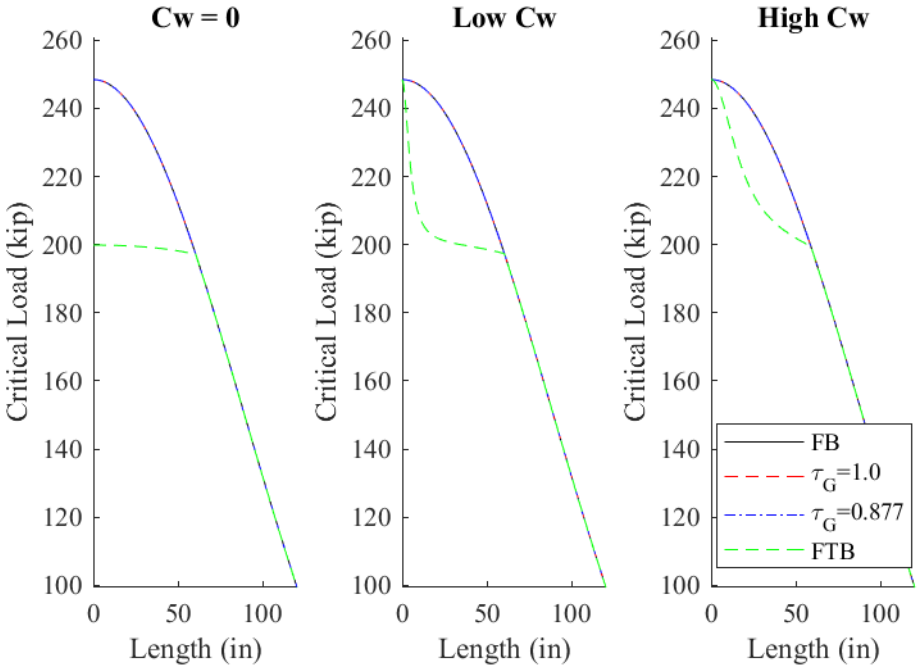

Figure C.50: Inelastic buckling of 2-L3.5"x3.5"x0.375"

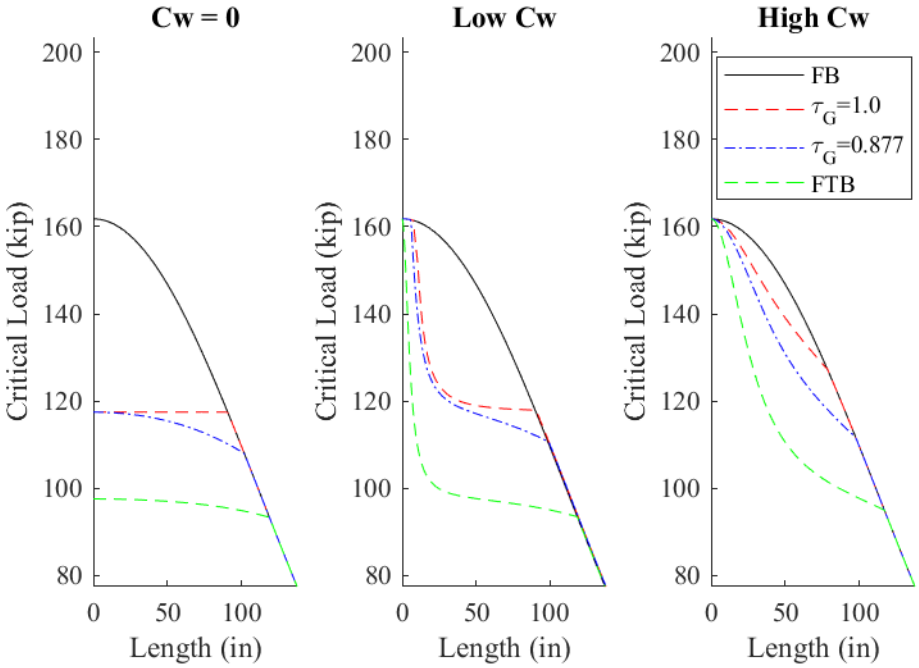

Figure C.51: Inelastic buckling of 2-L4"x4"x0.25"

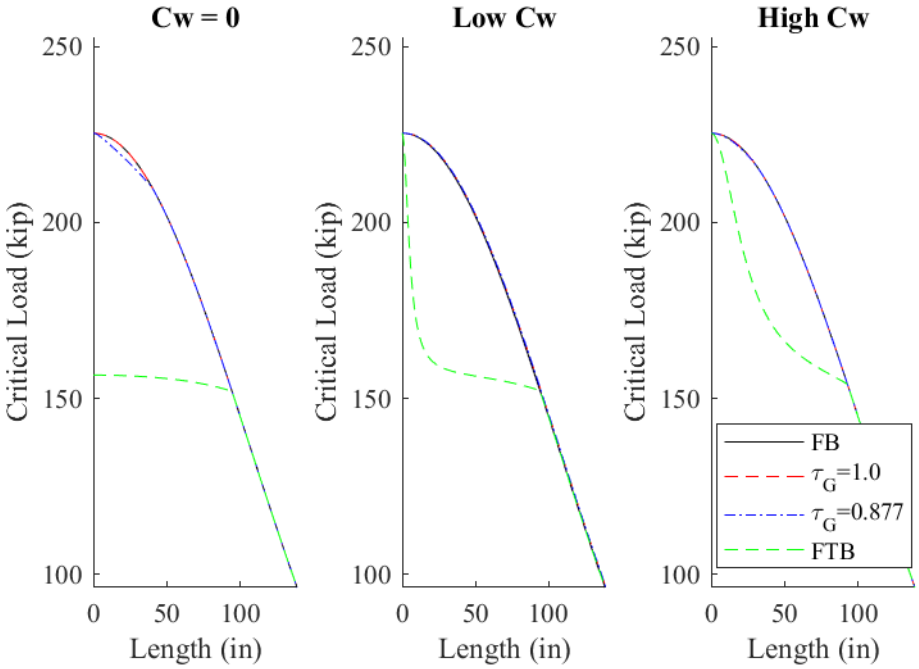

Figure C.52: Inelastic buckling of 2-L4"x4"x0.313"

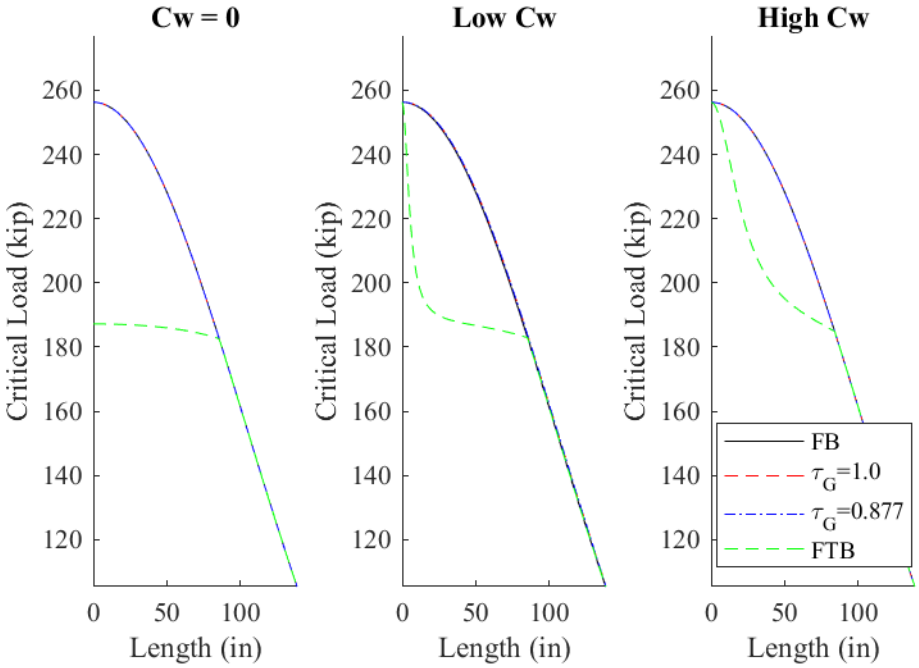

Figure C.53: Inelastic buckling of 2-L4"x4"x0.344"

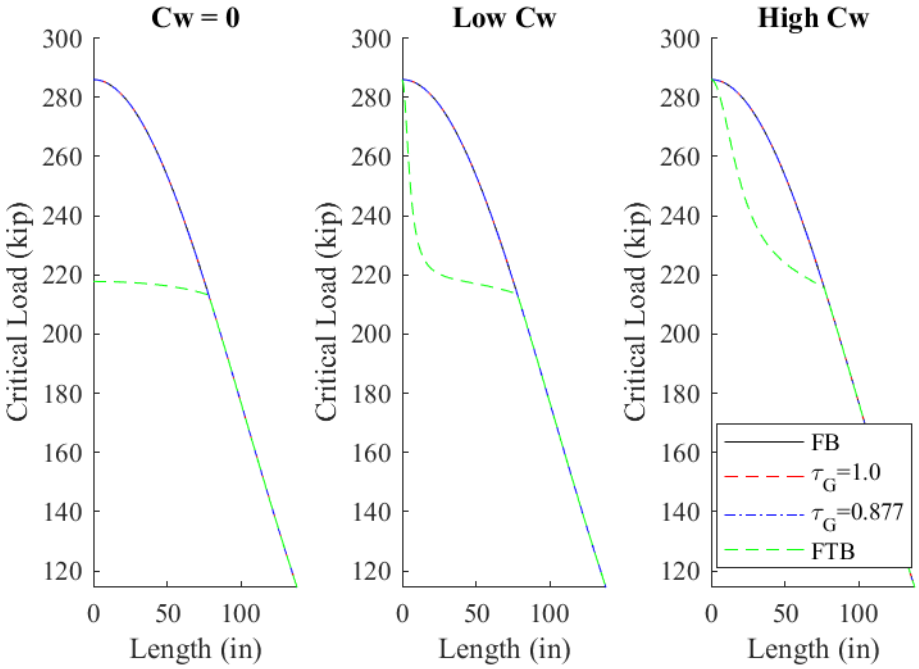

Figure C.54: Inelastic buckling of 2-L4"x4"x0.375"

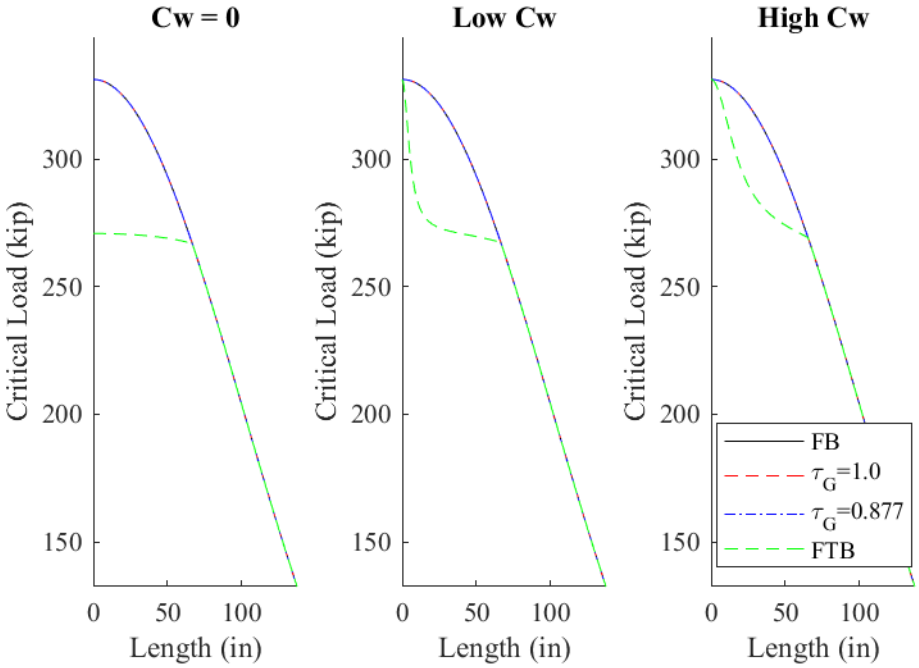

Figure C.55: Inelastic buckling of 2-L4"x4"x0.438"

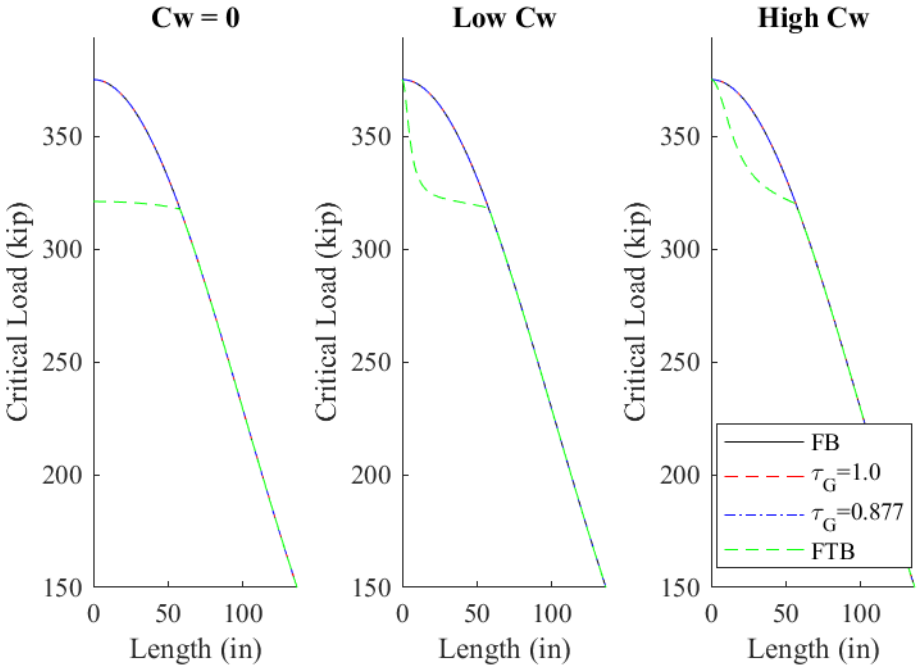

Figure C.56: Inelastic buckling of 2-L4"x4"x0.5"

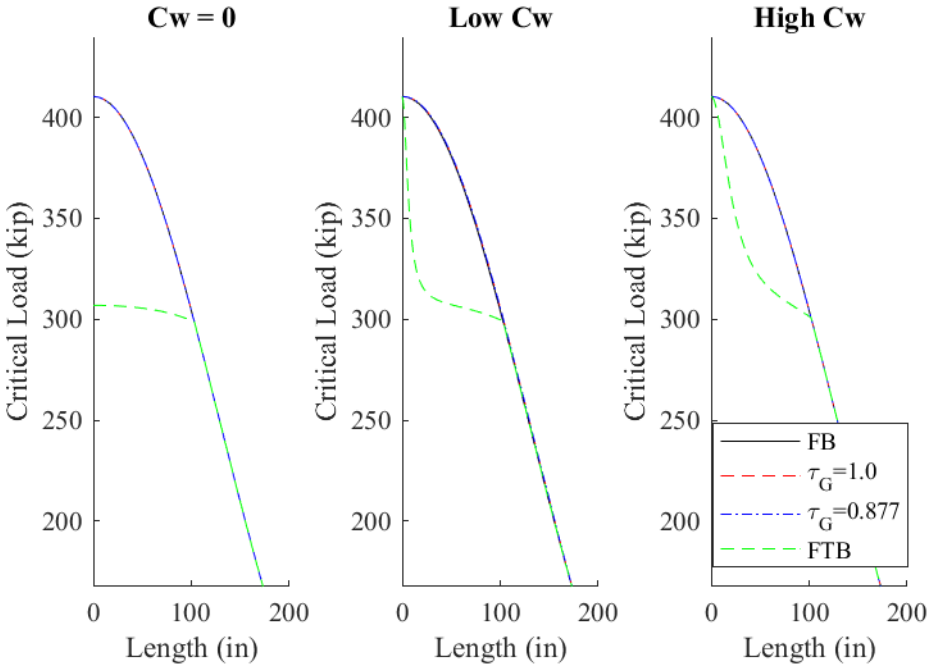

Figure C.57: Inelastic buckling of 2-L5"x5"x0.438"

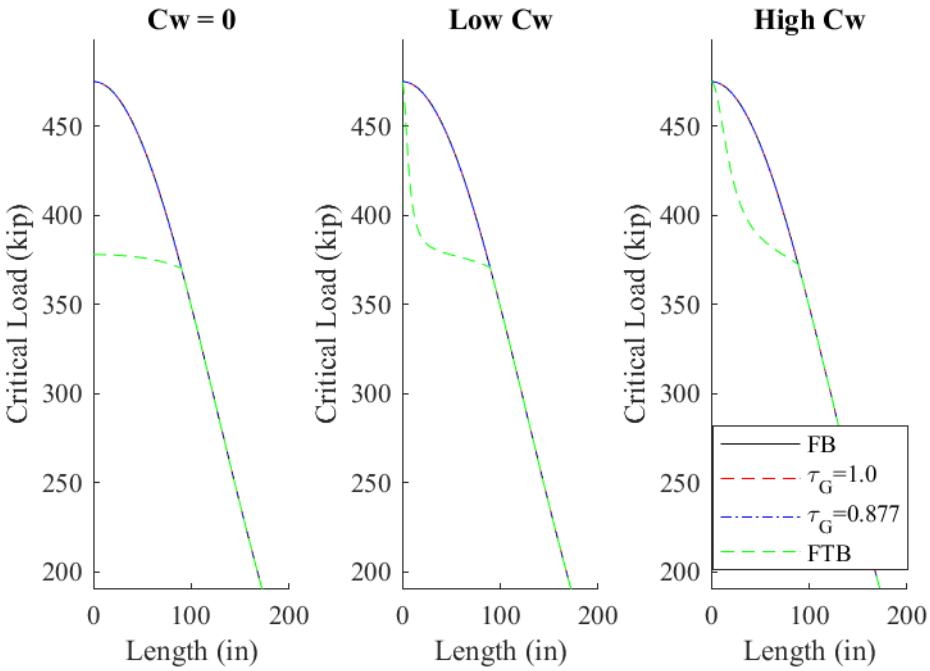

Figure C.58: Inelastic buckling of 2-L5"x5"x0.5"

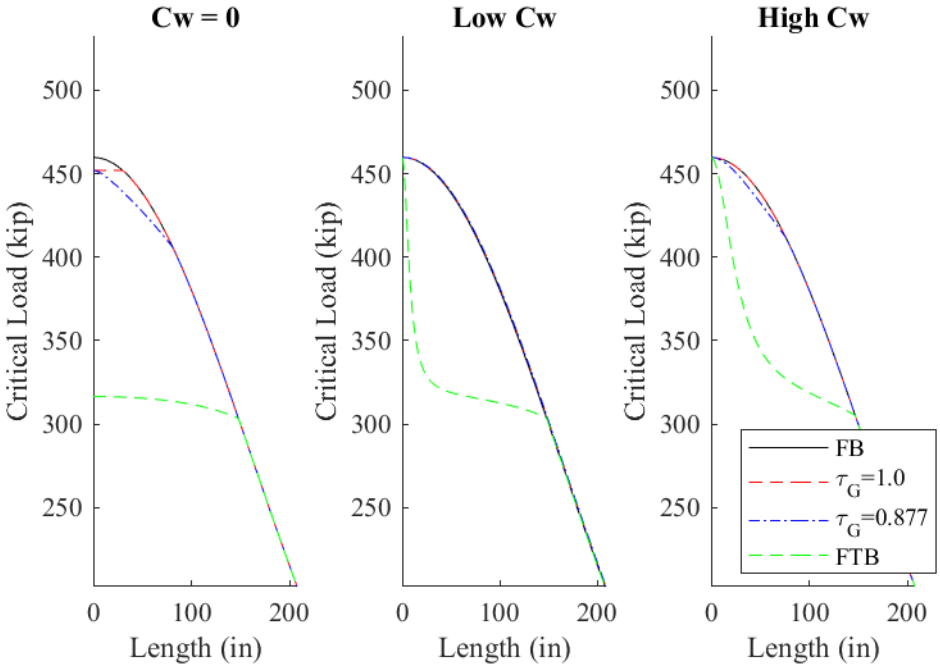

Figure C.59: Inelastic buckling of 2-L6"x6"x0.438"

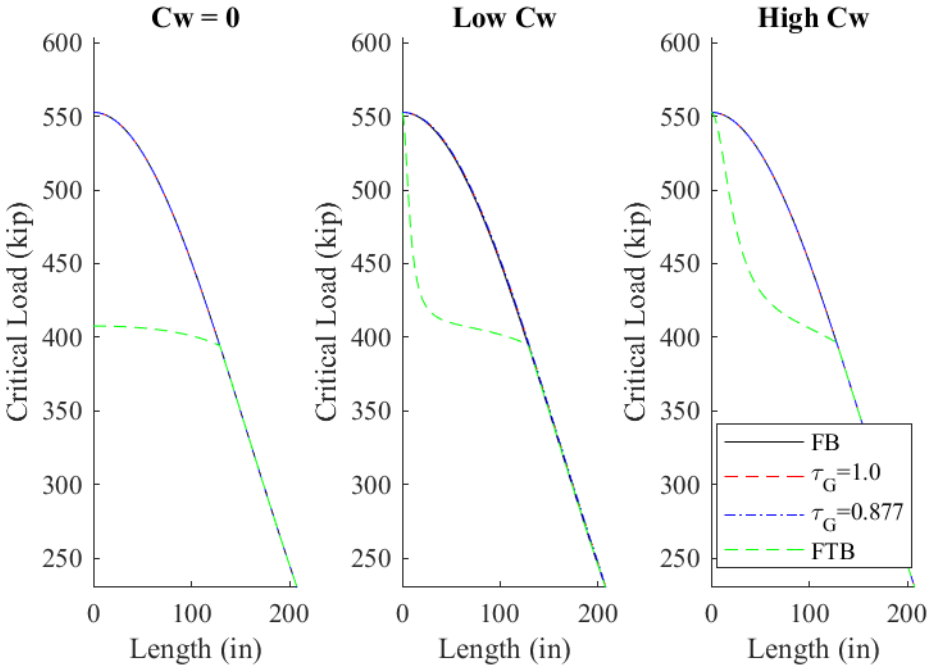

Figure C.60: Inelastic buckling of 2-L6"x6"x0.5"

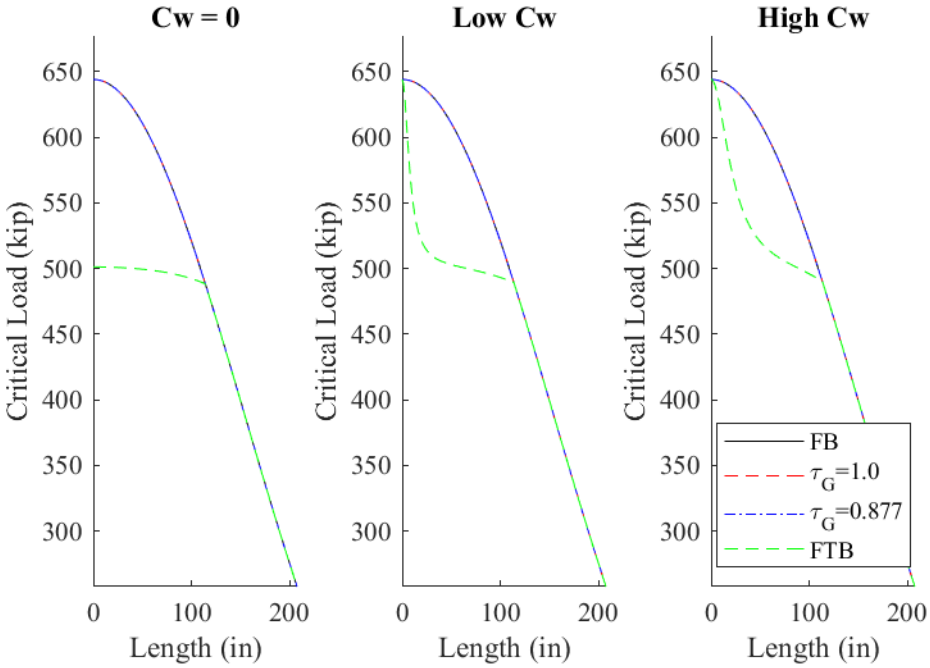

Figure C.61: Inelastic buckling of 2-L6"x6"x0.563"

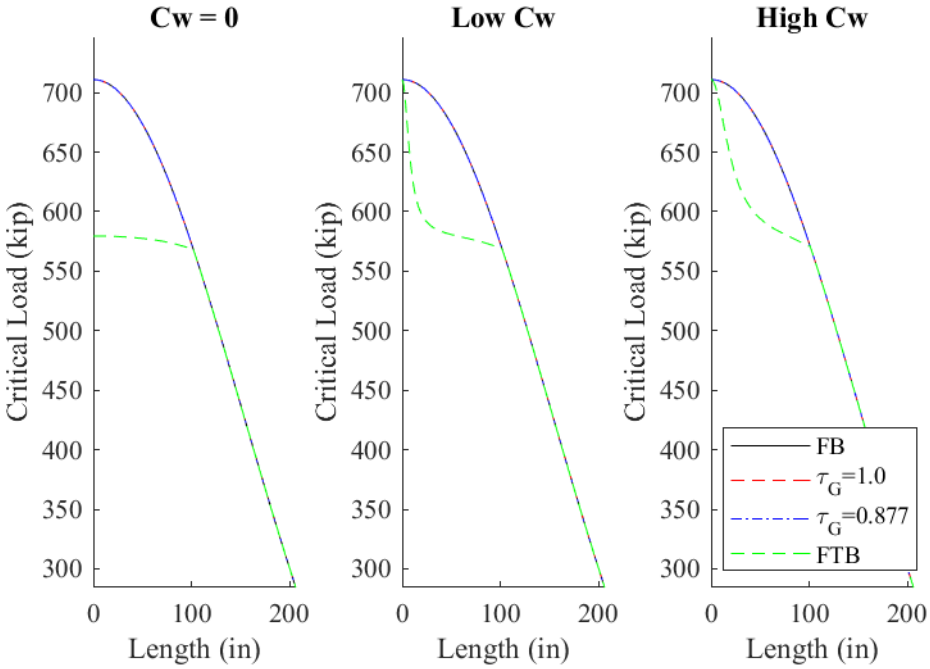

Figure C.62: Inelastic buckling of 2-L6"x6"x0.625"

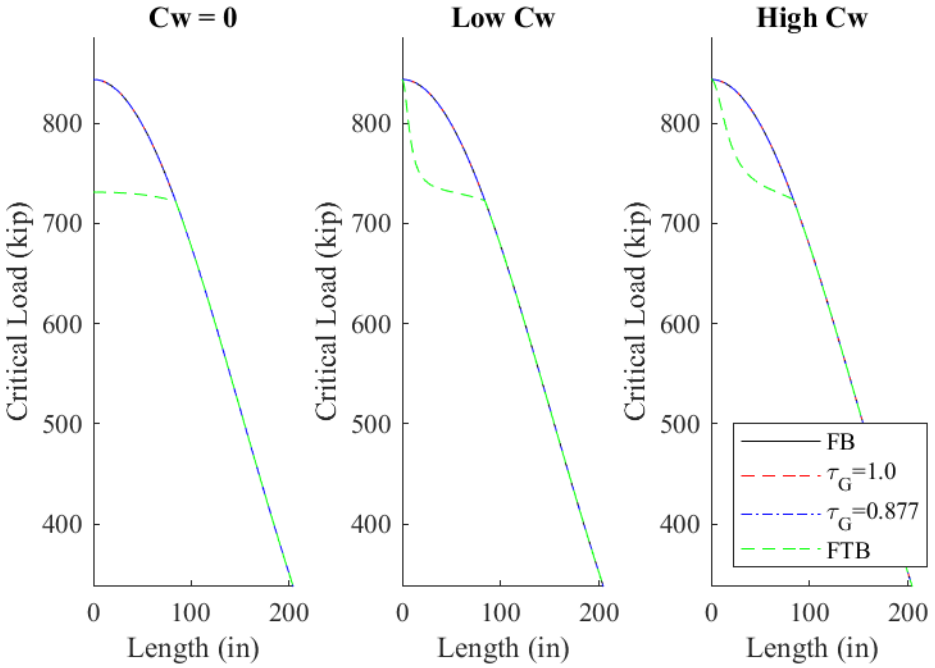

Figure C.63: Inelastic buckling of 2-L6"x6"x0.75"

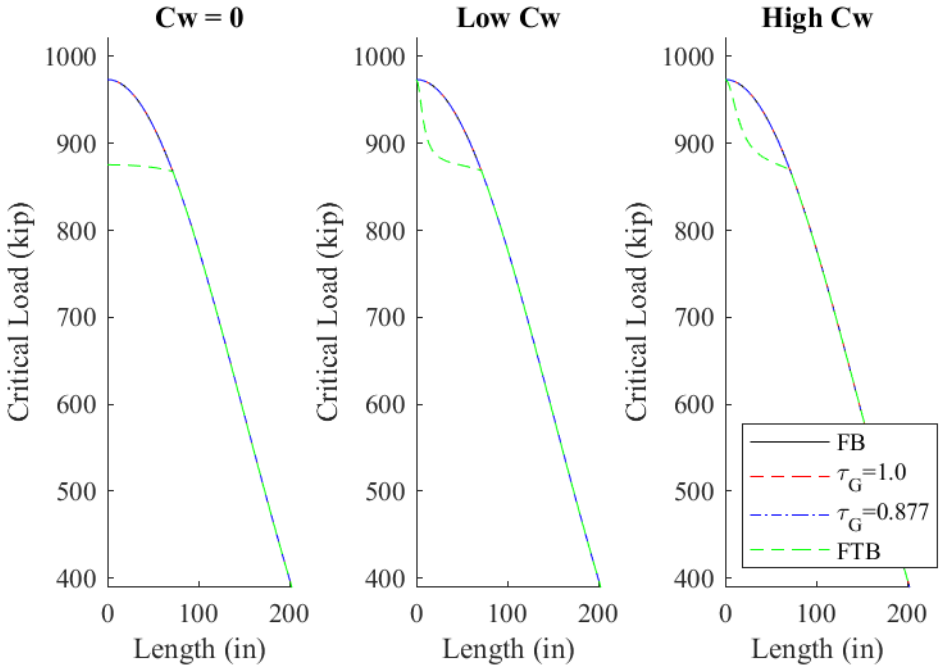

Figure C.64: Inelastic buckling of 2-L6"x6"x0.875"

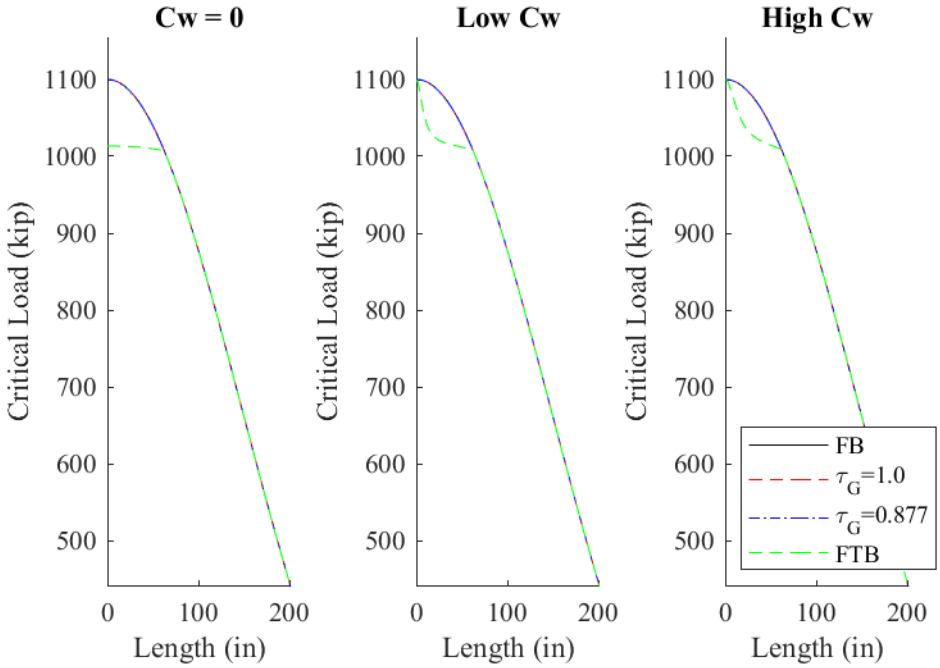

Figure C.65: Inelastic buckling of 2-L6"x6"x1"

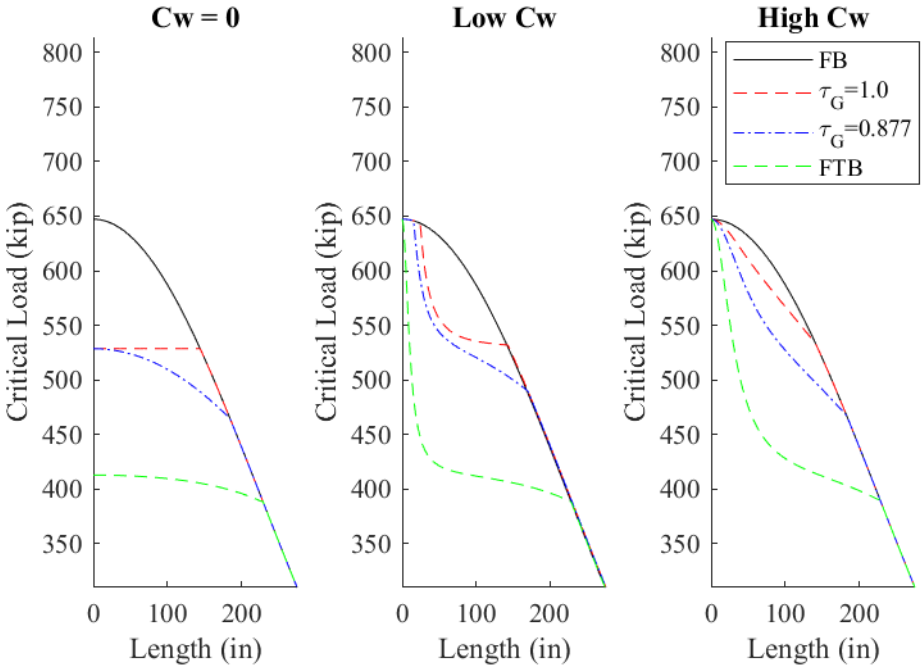

Figure C.66: Inelastic buckling of 2-L8"x8"x0.5"

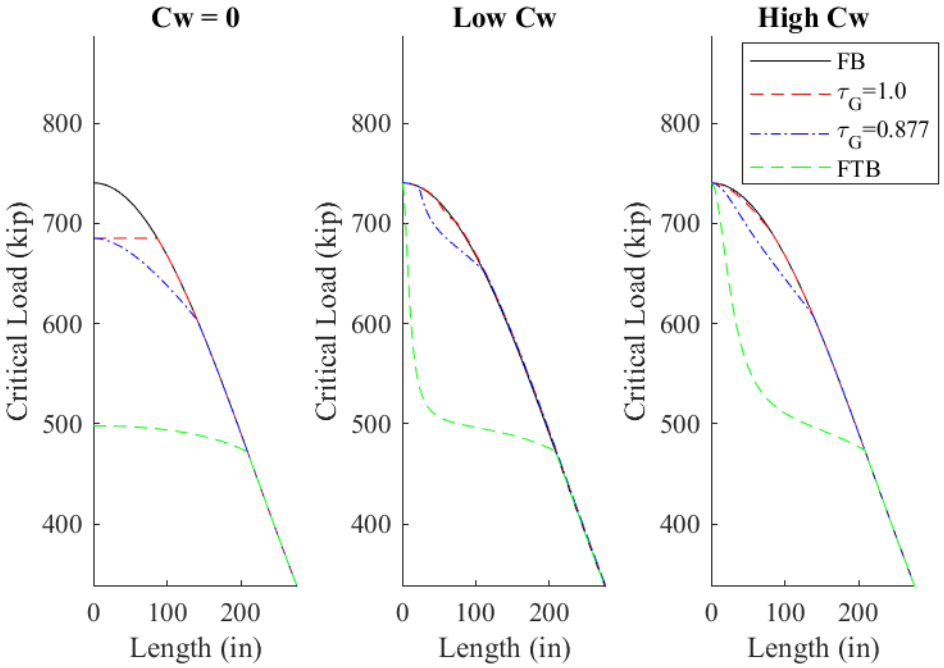

Figure C.67: Inelastic buckling of 2-L8"x8"x0.546"

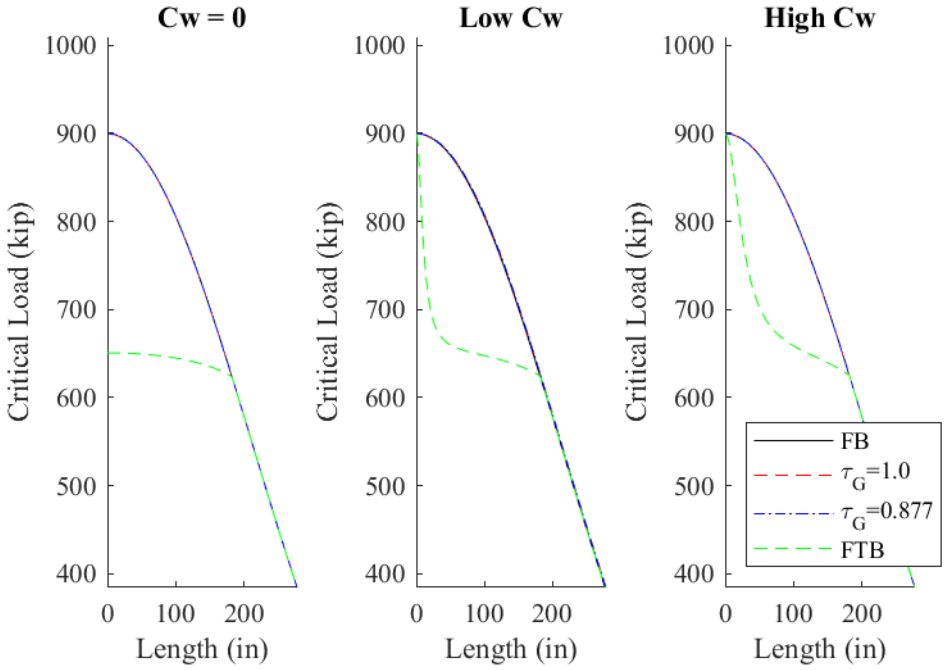

Figure C.68: Inelastic buckling of 2-L8"x8"x0.625"

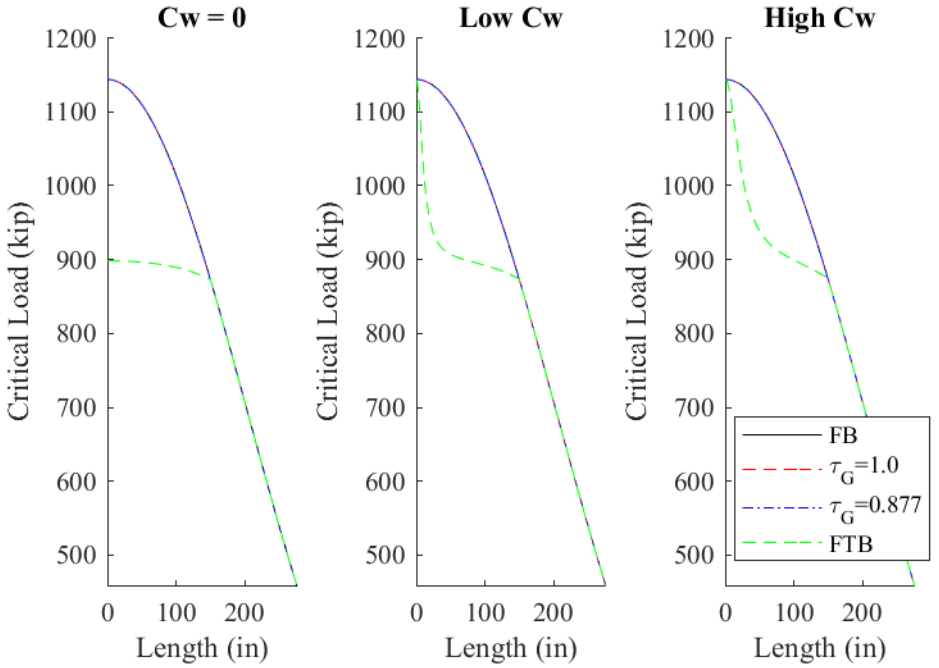

Figure C.69: Inelastic buckling of 2-L8"x8"x0.75"

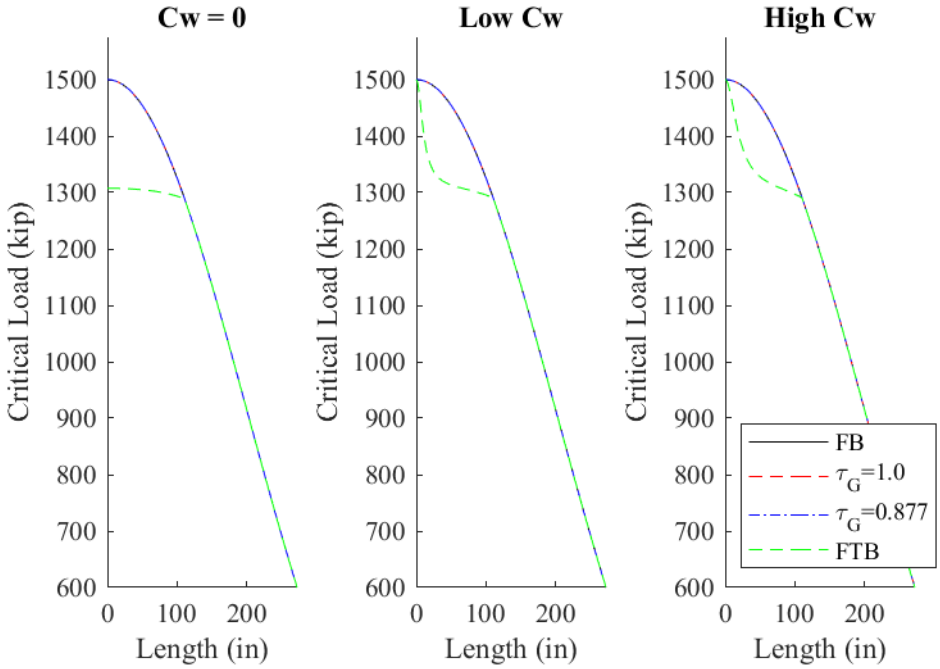

Figure C.70: Inelastic buckling of 2-L8"x8"x1"

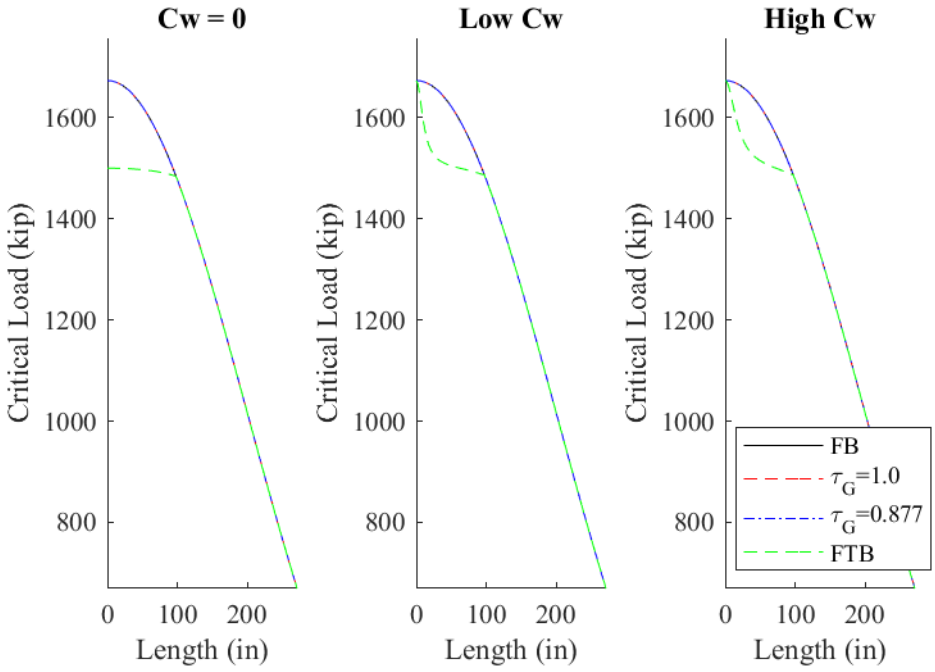

Figure C.71: Inelastic buckling of 2-L8"x8"x1.125"

D. Buckling of Chord Segments

This Appendix contains the results of the chord segment buckling study detailed in Chapter 5. The results are divided into Section D.1 that summarizes the elastic response and Section D.2 that summarizes the inelastic response.

D.1. Elastic Buckling Behavior of Double Angle Chord Segments

The following tables summarize the first 5 elastic buckling modes that were observed for the different members. The buckling modes were categorized into flexural, flexural-torsional, and local buckling behaviors according to the labels listed in Table D.1. Local buckling was observed as either twisting deformations in both flanges of one chord angle, which was classified as individual angles exhibiting flexural-torsional buckling, or different deformations in the horizontal and vertical flanges resulting in the a non-90° angle between the flanges, which was classified as a distortional buckling mode. Global flexural-torsional buckling was only identified when the ties rotated along with the angles.

Table D.1: Elastic buckling mode classification

Label	Description
g-FB	Global flexural buckling of the full double angle
i-FB	Individual flexural buckling of the angles
g-FTB	Global flexural-torsional buckling of full double angle*
	*Required composite movement across a tie
i-FTB	Individual flexural-torsional buckling of the angles
D	Distortion**
	**Vertical and horizontal flanges moved causing a non-90° angle to form

Table D.2: Elastic buckling of 2-L2"x2"x0.125" simply supported chord segment

Mode		Ties					
		0	1	3	7	15	23
1	P_{cr}	31.7 k	39.5 k	44.4 k	45.9 k	46.3 k	46.5 k
	Shape	g-FB+i-FTB	g-FB+i-FTB	g-FB	g-FB	g-FB	g-FB
2	P_{cr}	40.1 k	43.8 k	51.5 k	71.3 k	95.8 k	98.9 k
	Shape	g-FTB	i-FTB	i-FTB	i-FTB	D	D
3	P_{cr}	42.6 k	44.5 k	51.9 k	71.9 k	95.8 k	99.0 k
	Shape	i-FTB	i-FTB	i-FTB	i-FTB	D	D
4	P_{cr}	42.6 k	44.9 k	52.3 k	72.6 k	97.5 k	100.7 k
	Shape	i-FTB	i-FTB	i-FTB	i-FTB	D	D
5	P_{cr}	44.5 k	46.3 k	52.5 k	73.1 k	97.6 k	100.8 k
	Shape	i-FTB	g-FTB	i-FTB	i-FTB	D	D

Table D.3: Elastic buckling of 2-L2"x2"x0.125" fixed end chord segment

Mode		Ties					
		0	1	3	7	15	23
1	P_{cr}	18.8 k	32.7 k	39.2 k	44.4 k	45.8 k	46.0 k
	Shape	i-FB	g-FTB	g-FTB	g-FB	g-FB	g-FB
2	P_{cr}	18.8 k	38.6 k	39.3 k	47.5k	65.3 k	84.5 k
	Shape	i-FB	i-FTB	g-FB+i-FTB	g-FTB	g-FTB	g-FTB
3	P_{cr}	33.4 k	38.8 k	43.1 k	51.1 k	70.6 k	89.7 k
	Shape	i-FTB	g-FB+i-FTB	g-FTB	i-FTB	i-FTB	g-FB
4	P_{cr}	33.4 k	39.8 k	43.3 k	51.3 k	70.8 k	90.7 k
	Shape	i-FTB	g-FTB	i-FTB	i-FTB	i-FTB	D
5	P_{cr}	38.1 k	39.8 k	43.7 k	51.5 k	71.1 k	90.8 k
	Shape	i-FB	i-FTB	g-FTB	i-FTB	i-FTB	D

Table D.4: Elastic buckling of 2-L2"x2"x0.115" simply supported chord segment

Mode		Ties					
		0	1	3	7	15	23
1	P_{cr}	26.8 k	32.9 k	39.1 k	42.5 k	42.9 k	43.0 k
	Shape	g-FB+i-FTB	g-FB+i-FTB	g-FB+i-FTB	g-FB	g-FB	g-FB
2	P_{cr}	31.8 k	34.4 k	40.3 k	56.0 k	75.2 k	77.6 k
	Shape	g-FTB	i-FTB	i-FTB	i-FTB	D	D
3	P_{cr}	33.5 k	34.9 k	40.6 k	56.4 k	75.2 k	77.6 k
	Shape	i-FTB	i-FTB	i-FTB	i-FTB	D	D
4	P_{cr}	33.5 k	35.2 k	41.0 k	57.0 k	76.5 k	79.0 k
	Shape	i-FTB	i-FTB	i-FTB	i-FTB	D	D
5	P_{cr}	34.9 k	36.8 k	41.1 k	57.3 k	76.6 k	79.0 k
	Shape	i-FTB	g-FTB	i-FTB	i-FTB	D	D

Table D.5: Elastic buckling of 2-L2"x2"x0.115" fixed end chord segment

Mode		Ties					
		0	1	3	7	15	23
1	P_{cr}	17.4 k	26.5 k	32.2 k	38.9 k	42.4 k	42.5 k
	Shape	i-FB	g-FTB	g-FTB	g-FB	g-FB	g-FB
2	P_{cr}	17.4 k	31.4 k	32.7 k	39.5 k	55.4 k	71.2 k
	Shape	i-FB	i-FTB	g-FB+i-FTB	g-FTB	i-FTB	D
3	P_{cr}	27.3 k	31.7 k	34.1 k	40.0 k	55.5 k	71.2 k
	Shape	i-FTB	i-FTB	i-FTB	i-FTB	g-FTB	D
4	P_{cr}	27.3 k	32.1 k	34.4 k	40.2 k	55.6 k	71.4 k
	Shape	i-FTB	g-FB+i-FTB	i-FTB	i-FTB	i-FTB	D
5	P_{cr}	30.8 k	32.6 k	34.8 k	40.2 k	55.8 k	71.4 k
	Shape	i-FTB	g-FB+i-FTB	g-FTB	i-FTB	i-FTB	D

Table D.6: Elastic buckling of 2-L2"x2"x0.109" simply supported chord segment

Mode		Ties					
		0	1	3	7	15	23
1	P_{cr}	23.8 k	28.7 k	34.4 k	40.3 k	40.8 k	41.0 k
	Shape	g-FB+i-FTB	g-FB+i-FTB	i-FTB	g-FB	g-FB	g-FB
2	P_{cr}	27.3 k	29.5 k	34.5 k	47.9 k	64.3 k	66.3 k
	Shape	g-FTB	i-FTB	g-FB+i-FTB	i-FTB	D	D
3	P_{cr}	28.7 k	29.8 k	34.6 k	48.2 k	64.3 k	66.3 k
	Shape	i-FTB	i-FTB	i-FTB	i-FTB	D	D
4	P_{cr}	28.7 k	30.1 k	35.0 k	48.8 k	65.4 k	67.5 k
	Shape	i-FTB	i-FTB	i-FTB	i-FTB	D	D
5	P_{cr}	29.9 k	31.6 k	35.1 k	49.0 k	65.5 k	67.6 k
	Shape	i-FTB	g-FTB	g-FB+i-FTB	i-FTB	D	D

Table D.7: Elastic buckling of 2-L2"x2"x0.109" fixed end chord segment

Mode		Ties					
		0	1	3	7	15	23
1	P_{cr}	16.0 k	22.3 k	27.3 k	32.8 k	38.8 k	39.0 k
	Shape	i-FB	g-FTB	g-FTB	g-FB+i-FTB	g-FB	g-FB
2	P_{cr}	16.0 k	26.1 k	27.5 k	33.0 k	45.7 k	58.7 k
	Shape	i-FB	i-FTB	g-FB+i-FTB	i-FTB	i-FTB	D
3	P_{cr}	23.0 k	26.3 k	28.2 k	33.1 k	45.9 k	58.7 k
	Shape	i-FTB	i-FTB	i-FTB	i-FTB	i-FTB	D
4	P_{cr}	23.0 k	26.9 k	28.5 k	33.1 k	46.0 k	58.9 k
	Shape	i-FTB	g-FB+i-FTB	i-FTB	g-FB+i-FTB	i-FTB	D
5	P_{cr}	25.6 k	27.0 k	28.9 k	33.2 k	46.1 k	58.9 k
	Shape	i-FTB	i-FTB	g-FB+g-FTB	i-FTB	i-FTB	D

Table D.8: Elastic buckling of 2-L2"x2"x0.094" simply supported chord segment

Mode		Ties					
		0	1	3	7	15	23
1	P_{cr}	16.4 k	18.9 k	22.1 k	30.9 k	35.4 k	35.6 k
	Shape	g-FB+i-FTB	g-FB+i-FTB	i-FTB	i-FTB	g-FB	g-FB
2	P_{cr}	17.8 k	19.0 k	22.2 k	31.0 k	41.3 k	42.5 k
	Shape	g-FTB	i-FTB	i-FTB	i-FTB	D	D
3	P_{cr}	18.5 k	19.1 k	22.3 k	31.4 k	41.3 k	42.6 k
	Shape	i-FTB	i-FTB	i-FTB	i-FTB	D	D
4	P_{cr}	18.5 k	19.3 k	22.4 k	31.5 k	42.0 k	43.3 k
	Shape	i-FTB	i-FTB	i-FTB	i-FTB	D	D
5	P_{cr}	19.2 k	20.4 k	22.6 k	32.2 k	42.1 k	43.4 k
	Shape	i-FTB	g-FTB	i-FTB	i-FTB	D	D

Table D.9: Elastic buckling of 2-L2"x2"x0.094" fixed end chord segment

Mode		Ties					
		0	1	3	7	15	23
1	P_{cr}	14.4 k	15.8 k	18.7 k	21.9 k	30.5 k	35.0 k
	Shape	i-FB	g-FTB	g-FB+i-FTB	i-FTB	i-FTB	g-FB
2	P_{cr}	14.4 k	17.6 k	18.9 k	21.9 k	30.6 k	39.1 k
	Shape	i-FB	i-FTB	i-FTB	i-FTB	i-FTB	D
3	P_{cr}	16.1 k	17.7 k	18.9 k	22.0 k	30.6 k	39.1 k
	Shape	i-FTB	i-FTB	g-FTB	i-FTB	i-FTB	D
4	P_{cr}	16.1 k	18.0 k	19.0 k	22.0 k	30.8 k	39.3 k
	Shape	i-FTB	i-FTB	i-FTB	i-FTB	i-FTB	D
5	P_{cr}	17.4 k	18.0 k	19.2 k	22.0 k	30.8 k	39.3 k
	Shape	i-FTB	i-FTB	i-FTB	i-FTB	i-FTB	D

Table D.10: Elastic buckling of 2-L1.75"x1.75"x0.125" simply supported chord segment

Mode		Ties					
		0	1	3	7	15	23
1	P_{cr}	24.3 k	29.3 k	30.3 k	30.7 k	30.9 k	31.1 k
	Shape	g-FB+i-FTB	g-FB+i-FTB	g-FB	g-FB	g-FB	g-FB
2	P_{cr}	40.4 k	45.8 k	56.4 k	76.4 k	95.5 k	105.4 k
	Shape	g-FTB	g-FTB	i-FTB	i-FTB	g-FB	g-FB
3	P_{cr}	46.2 k	47.2 k	56.9 k	77.2 k	106.3 k	110.4 k
	Shape	i-FTB	i-FTB	i-FTB	i-FTB	D	D
4	P_{cr}	46.2 k	48.7 k	57.0 k	77.4 k	106.3 k	110.5 k
	Shape	i-FTB	i-FTB	i-FTB	i-FTB	D	D
5	P_{cr}	46.3 k	49.7 k	57.0 k	77.7 k	107.5 k	111.9 k
	Shape	i-FTB	i-FTB	g-FTB	g-FTB	D	D

Table D.11: Elastic buckling of 2-L1.75"x1.75"x0.125" fixed end chord segment

Mode		Ties					
		0	1	3	7	15	23
1	P_{cr}	12.4 k	26.2 k	29.2 k	30.3 k	30.6 k	30.7 k
	Shape	i-FB	i-FB	g-FB	g-FB	g-FB	g-FB
2	P_{cr}	12.4 k	29.2 k	36.0 k	43.0 k	55.1 k	60.9 k
	Shape	i-FB	g-FB	g-FB+g-FTB	g-FB+g-FTB	g-FB	g-FB
3	P_{cr}	25.3 k	29.3 k	40.9 k	53.1 k	60.2 k	66.5 k
	Shape	i-FB	g-FB+i-FTB	g-FTB	g-FTB	g-FB	g-FB
4	P_{cr}	25.3 k	33.0 k	43.1 k	53.2 k	74.2 k	94.8 k
	Shape	i-FB	g-FTB	g-FTB	g-FB+i-FTB	g-FTB	g-FTB
5	P_{cr}	30.7 k	36.0 k	44.3 k	54.1 k	75.5 k	97.5 k
	Shape	i-FTB	i-FTB	i-FTB	g-FTB	i-FTB	D

Table D.12: Elastic buckling of 2-L1.75"x1.75"x0.115" simply supported chord segment

Mode		Ties					
		0	1	3	7	15	23
1	P_{cr}	21.9 k	26.7 k	28.0 k	28.4 k	28.7 k	28.9 k
	Shape	g-FB+i-FTB	g-FB+i-FTB	g-FB	g-FB	g-FB	g-FB
2	P_{cr}	33.6 k	37.5 k	44.2 k	60.0 k	83.4 k	86.6 k
	Shape	g-FTB	i-FTB	i-FTB	i-FTB	D	D
3	P_{cr}	36.7 k	37.8 k	44.6 k	60.5 k	83.4 k	86.6 k
	Shape	i-FTB	g-FTB	i-FTB	i-FTB	D	D
4	P_{cr}	36.7 k	38.4 k	44.6 k	60.7 k	84.4 k	87.8 k
	Shape	i-FTB	i-FTB	i-FTB	i-FTB	D	D
5	P_{cr}	38.0 k	39.1 k	44.8 k	61.2 k	84.4 k	87.9 k
	Shape	i-FTB	i-FTB	i-FTB	i-FTB	D	D

Table D.13: Elastic buckling of 2-L1.75"x1.75"x0.115" fixed end chord segment

Mode		Ties					
		0	1	3	7	15	23
1	P_{cr}	11.5 k	24.2 k	26.6 k	28.0 k	28.4 k	28.4 k
	Shape	i-FB	i-FB	g-FB	g-FB	g-FB	g-FB
2	P_{cr}	11.5 k	26.0 k	31.4 k	37.4 k	47.7 k	56.1 k
	Shape	i-FB	g-FTB	g-FB+g-FTB	g-FB+i-FTB	g-FB	g-FB
3	P_{cr}	23.5 k	26.6 k	34.1 k	43.4 k	55.2 k	57.9 k
	Shape	i-FB	g-FB+i-FTB	g-FTB	g-FB+i-FTB	g-FB	g-FB
4	P_{cr}	23.5 k	27.3 k	35.5 k	44.0 k	59.2 k	76.5 k
	Shape	i-FB	g-FTB	g-FTB	i-FTB	i-FTB	i-FTB
5	P_{cr}	26.0 k	32.4 k	36.4 k	44.0 k	59.5 k	76.9 k
	Shape	i-FTB	i-FTB	i-FTB	i-FTB	i-FTB	D

Table D.14: Elastic buckling of 2-L1.75"x1.75"x0.109" simply supported chord segment

Mode		Ties					
		0	1	3	7	15	23
1	P_{cr}	20.3 k	25.0 k	26.5 k	27.1 k	27.3 k	27.5 k
	Shape	g-FB+i-FTB	g-FB+i-FTB	g-FB	g-FB	g-FB	g-FB
2	P_{cr}	29.3 k	32.3 k	37.8 k	51.4 k	71.4 k	74.1 k
	Shape	g-FTB	i-FTB	i-FTB	i-FTB	D	D
3	P_{cr}	31.6 k	32.9 k	38.1 k	51.7 k	71.4 k	74.1 k
	Shape	i-FTB	i-FTB	i-FTB	i-FTB	D	D
4	P_{cr}	31.6 k	33.2 k	38.1 k	51.9 k	72.2 k	75.1 k
	Shape	i-FTB	g-FTB	i-FTB	i-FTB	D	D
5	P_{cr}	32.9 k	33.6 k	38.3 k	52.3 k	72.2 k	75.2 k
	Shape	i-FTB	g-FTB	i-FTB	i-FTB	D	D

Table D.15: Elastic buckling of 2-L1.75"x1.75"x0.109" fixed end chord segment

Mode		Ties					
		0	1	3	7	15	23
1	P_{cr}	10.6 k	22.1 k	24.0 k	25.6 k	26.0 k	26.1 k
	Shape	i-FB	g-FTB	g-FB	g-FB	g-FB	g-FB
2	P_{cr}	10.6 k	22.1 k	27.2 k	32.7 k	41.8 k	51.0 k
	Shape	i-FB	i-FB	g-FB+g-FTB	g-FB+g-FTB	g-FB+g-FTB	g-FB
3	P_{cr}	21.5 k	23.9 k	29.4 k	36.0 k	48.7 k	51.5 k
	Shape	i-FB	g-FB	g-FTB	i-FTB	i-FTB	g-FB
4	P_{cr}	21.5 k	24.3 k	30.2 k	36.3 k	49.1 k	63.1 k
	Shape	i-FB	g-FB+g-FTB	g-FTB	i-FTB	i-FTB	D
5	P_{cr}	22.4 k	27.8 k	30.5 k	36.3 k	49.1 k	63.5 k
	Shape	i-FTB	i-FTB	i-FTB	i-FTB	i-FTB	D

Table D.16: Elastic buckling of 2-L4"x4"x0.375" simply supported chord segment

Mode		Ties					
		0	1	3	7	15	31
1	P_{cr}	451 k	573 k	646 k	659 k	664 k	669 k
	Shape	g-FB+i-FTB	g-FB+i-FTB	g-FB+i-FTB	g-FB	g-FB	g-FB
2	P_{cr}	543 k	593 k	689 k	839 k	1162 k	1385 k
	Shape	g-FTB	g-FTB	g-FTB	g-FTB	g-FTB	D
3	P_{cr}	598 k	625 k	789 k	949 k	1244 k	1387 k
	Shape	i-FTB	i-FTB	i-FTB	g-FTB	g-FTB	D
4	P_{cr}	598 k	642 k	795 k	1057 k	1265 k	1434 k
	Shape	i-FTB	i-FTB	g-FTB	g-FTB	D	D
5	P_{cr}	640 k	653 k	822 k	1114 k	1266 k	1440 k
	Shape	i-FTB	i-FTB	i-FTB	D	D	D

Table D.17: Elastic buckling of 2-L4"x4"x0.375" fixed end chord segment

Mode		Ties					
		0	1	3	7	15	31
1	P_{cr}	274 k	460 k	520 k	595 k	658 k	660 k
	Shape	i-FB	g-FTB	g-FTB	g-FTB	g-FB	g-FB
2	P_{cr}	274 k	538 k	563 k	638 k	753 k	1076 k
	Shape	i-FB	i-FTB	g-FB+i-FTB	g-FTB	g-FTB	g-FTB
3	P_{cr}	460 k	551 k	564 k	646 k	794 k	1124 k
	Shape	i-FTB	i-FTB	g-FTB	g-FB	g-FTB	g-FTB
4	P_{cr}	460 k	552 k	604 k	701 k	853 k	1178 k
	Shape	i-FTB	g-FB+i-FTB	g-FTB	g-FTB	g-FTB	g-FTB
5	P_{cr}	529 k	565 k	610 k	755 k	901 k	1212 k
	Shape	i-FTB	i-FTB	i-FTB	g-FTB	g-FTB	g-FTB

Table D.18: Elastic buckling of 2-L4"x4"x0.344" simply supported chord segment

Mode		Ties					
		0	1	3	7	15	31
1	P_{cr}	377 k	476 k	558 k	610 k	615 k	620 k
	Shape	g-FB+i-FTB	g-FB+i-FTB	g-FTB	g-FB	g-FB	g-FB
2	P_{cr}	429 k	477 k	588 k	686 k	971 k	1087 k
	Shape	g-FTB	g-FTB	g-FB+i-FTB	g-FTB	g-FTB	D
3	P_{cr}	467 k	490 k	620 k	774 k	1003 k	1088 k
	Shape	i-FTB	i-FTB	i-FTB	g-FTB	D	D
4	P_{cr}	467 k	500 k	633 k	857 k	1004 k	1128 k
	Shape	i-FTB	i-FTB	i-FTB	g-FTB	D	D
5	P_{cr}	501 k	509 k	652 k	892 k	1022 k	1131 k
	Shape	i-FTB	i-FTB	g-FTB	D	g-FTB	D

Table D.19: Elastic buckling of 2-L4"x4"x0.344" fixed end chord segment

Mode		Ties					
		0	1	3	7	15	31
1	P_{cr}	254 k	372 k	416 k	477 k	609 k	611 k
	Shape	i-FB	g-FTB	g-FTB	g-FTB	g-FB	g-FB
2	P_{cr}	254 k	428 k	451 k	512 k	613 k	900 k
	Shape	i-FB	i-FTB	g-FTB	g-FTB	g-FTB	g-FTB
3	P_{cr}	372 k	433 k	466 k	566 k	646 k	937 k
	Shape	i-FTB	i-FTB	g-FB+i-FTB	g-FTB	g-FTB	g-FTB
4	P_{cr}	372 k	445 k	480 k	586 k	695 k	978 k
	Shape	i-FTB	i-FTB	i-FTB	g-FB+i-FTB	g-FTB	g-FTB
5	P_{cr}	417 k	445 k	483 k	608 k	735 k	990 k
	Shape	i-FTB	i-FTB	g-FTB	i-FTB	g-FTB	D

Table D.20: Elastic buckling of 2-L4"x4"x0.313" simply supported chord segment

Mode		Ties					
		0	1	3	7	15	31
1	P_{cr}	301 k	371 k	442 k	549 k	563 k	569 k
	Shape	g-FB+i-FTB	g-FB+i-FTB	g-FTB	g-FTB	g-FB	g-FB
2	P_{cr}	328 k	372 k	473 k	558 k	769 k	827 k
	Shape	g-FTB	i-FTB	i-FTB	g-FB	D	D
3	P_{cr}	354 k	373 k	482 k	617 k	769 k	828 k
	Shape	i-FTB	g-FTB	i-FTB	g-FTB	D	D
4	P_{cr}	354 k	378 k	492 k	676 k	787 k	860 k
	Shape	i-FTB	i-FTB	g-FB+i-FTB	g-FTB	g-FTB	D
5	P_{cr}	379 k	384 k	503 k	692 k	793 k	861 k
	Shape	i-FTB	i-FTB	i-FTB	D	D	D

Table D.21: Elastic buckling of 2-L4"x4"x0.313" fixed end chord segment

Mode		Ties					
		0	1	3	7	15	31
1	P_{cr}	233 k	290 k	323 k	373 k	487 k	560 k
	Shape	i-FB	g-FTB	g-FTB	g-FTB	g-FTB	g-FB
2	P_{cr}	233 k	327 k	351 k	401 k	513 k	738 k
	Shape	i-FB	i-FTB	g-FTB	g-FTB	g-FTB	g-FTB
3	P_{cr}	291 k	330 k	362 k	446 k	554 k	758 k
	Shape	i-FTB	i-FTB	g-FB+i-FTB	g-FTB	g-FTB	D
4	P_{cr}	291 k	337 k	366 k	464 k	557 k	759 k
	Shape	i-FTB	i-FTB	i-FTB	i-FTB	g-FB	D
5	P_{cr}	319 k	337 k	374 k	469 k	586 k	761 k
	Shape	i-FTB	i-FTB	i-FTB	i-FTB	g-FTB	D

Table D.22: Elastic buckling of 2-L4"x4"x0.25" simply supported chord segment

Mode		Ties					
		0	1	3	7	15	31
1	P_{cr}	167 k	194 k	250 k	328 k	408 k	435 k
	Shape	i-FTB	i-FTB	i-FTB	g-FTB	D	D
2	P_{cr}	173 k	196 k	252 k	366 k	409 k	435 k
	Shape	g-FTB	i-FTB	i-FTB	g-FTB	D	D
3	P_{cr}	184 k	196 k	258 k	374 k	423 k	452 k
	Shape	i-FTB	i-FTB	g-FTB	D	D	D
4	P_{cr}	184 k	199 k	260 k	375 k	426 k	454 k
	Shape	i-FTB	i-FTB	i-FTB	D	D	D
5	P_{cr}	197 k	210 k	262 k	376 k	446 k	459 k
	Shape	i-FTB	g-FTB	g-FTB	D	D	D

Table D.23: Elastic buckling of 2-L4"x4"x0.25" fixed end chord segment

Mode		Ties					
		0	1	3	7	15	31
1	P_{cr}	159 k	161 k	180 k	211 k	287 k	402 k
	Shape	i-FTB	g-FTB	g-FTB	g-FTB	g-FTB	D
2	P_{cr}	159 k	173 k	192 k	229 k	304 k	402 k
	Shape	i-FTB	i-FTB	i-FTB	g-FTB	g-FTB	D
3	P_{cr}	169 k	174 k	193 k	245 k	329 k	404 k
	Shape	i-FTB	i-FTB	i-FTB	i-FTB	g-FTB	D
4	P_{cr}	169 k	176 k	193 k	27 k	349 k	406 k
	Shape	i-FTB	i-FTB	i-FTB	i-FTB	g-FTB	D
5	P_{cr}	176 k	176 k	195 k	248 k	368 k	409 k
	Shape	i-FTB	i-FTB	i-FTB	i-FTB	g-FTB	D

Table D.24: Elastic buckling of 2-L4"x4"x0.188" simply supported chord segment

Mode		Ties					
		0	1	3	7	15	31
1	P_{cr}	74 k	83 k	108 k	162 k	177 k	187 k
	Shape	i-FTB	i-FTB	i-FTB	D	D	D
2	P_{cr}	75 k	84 k	108 k	163 k	178 k	187 k
	Shape	g-FTB	i-FTB	i-FTB	D	D	D
3	P_{cr}	79 k	84 k	112 k	166 k	185 k	195 k
	Shape	i-FTB	i-FTB	i-FTB	D	D	D
4	P_{cr}	79 k	85 k	112 k	170 k	186 k	196 k
	Shape	i-FTB	i-FTB	i-FTB	D	D	D
5	P_{cr}	84 k	94 k	117 k	171 k	193 k	199 k
	Shape	i-FTB	g-FTB	i-FTB	g-FTB	D	D

Table D.25: Elastic buckling of 2-L4"x4"x0.188" fixed end chord segment

Mode		Ties					
		0	1	3	7	15	31
1	P_{cr}	70.5 k	74.1 k	82.3 k	104.2 k	149.9 k	174.0 k
	Shape	i-FTB	g-FTB	i-FTB	g-FTB	g-FTB	D
2	P_{cr}	70.5 k	74.6 k	82.7 k	105.9 k	159.2 k	174.5 k
	Shape	i-FTB	i-FTB	i-FTB	i-FTB	g-FTB	D
3	P_{cr}	73.0 k	74.7 k	82.7 k	106.3 k	159.7 k	175.2 k
	Shape	i-FTB	i-FTB	i-FTB	i-FTB	D	D
4	P_{cr}	73.0 k	75.2 k	83.0 k	106.7 k	160.0 k	176.4 k
	Shape	i-FTB	i-FTB	i-FTB	i-FTB	D	D
5	P_{cr}	75.3 k	75.2 k	83.8 k	107.1 k	160.4 k	177.7 k
	Shape	i-FTB	i-FTB	i-FTB	i-FTB	D	D

Table D.26: Elastic buckling of 2-L8"x8"x0.75" simply supported chord segment

Mode		Ties					
		0	1	3	7	15	31
1	P_{cr}	2134 k	2442 k	2759 k	3181 k	3923 k	4053 k
	Shape	g-FB+i-FTB	g-FTB	g-FTB	g-FTB	g-FTB	g-FB
2	P_{cr}	2294 k	2610 k	3119 k	3556 k	4032 k	5008 k
	Shape	g-FTB	i-FTB	i-FTB	g-FTB	g-FB	g-FTB
3	P_{cr}	2527 k	2697 k	3242 k	3968 k	4279 k	5255 k
	Shape	i-FTB	i-FTB	i-FTB	g-FTB	g-FTB	g-FTB
4	P_{cr}	2527 k	2729 k	3426 k	4003 k	4569 k	5286 k
	Shape	i-FTB	g-FB+i-FTB	g-FTB	g-FB	g-FTB	D
5	P_{cr}	2785 k	2822 k	3506 k	4266 k	4778 k	5373 k
	Shape	i-FTB	i-FTB	i-FTB	D	D	D

Table D.27: Elastic buckling of 2-L8"x8"x0.75" fixed end chord segment

Mode		Ties					
		0	1	3	7	15	31
1	P_{cr}	1705 k	2026 k	2219 k	2455 k	2877 k	3605 k
	Shape	i-FB	g-FTB	g-FTB	g-FTB	g-FTB	g-FTB
2	P_{cr}	1705 k	2260 k	2357 k	2597 k	3028 k	3788 k
	Shape	i-FB	i-FTB	i-FTB	g-FTB	g-FTB	g-FTB
3	P_{cr}	2026 k	2300 k	2486 k	2809 k	3237 k	3995 k
	Shape	i-FTB	i-FTB	i-FTB	g-FTB	g-FTB	g-FTB
4	P_{cr}	2026 k	2364 k	2508 k	2976 k	3397 k	4018 k
	Shape	i-FTB	i-FTB	i-FTB	g-FTB	g-FTB	g-FB
5	P_{cr}	2222 k	2365 k	2550 k	3124 k	3605 k	4136 k
	Shape	i-FTB	i-FTB	g-FB+i-FTB	i-FTB	g-FTB	g-FTB

Table D.28: Elastic buckling of 2-L8"x8"x0.625" simply supported chord segment

Mode		Ties					
		0	1	3	7	15	31
1	P_{cr}	1318 k	1496 k	1717 k	2030 k	2605 k	3258 k
	Shape	g-FB+i-FTB	g-FTB	g-FTB	g-FTB	g-FTB	D
2	P_{cr}	1367 k	1551 k	1931 k	2249 k	2777 k	3263 k
	Shape	g-FTB	i-FTB	g-FTB	g-FTB	g-FTB	D
3	P_{cr}	1485 k	1587 k	1955 k	2488 k	2886 k	3393 k
	Shape	i-FTB	i-FTB	i-FTB	g-FTB	g-FTB	D
4	P_{cr}	1485 k	1632 k	2090 k	2635 k	2962 k	3405 k
	Shape	i-FTB	i-FTB	i-FTB	g-FTB+D	D	D
5	P_{cr}	1641 k	1654 k	2120 k	2814 k	3097 k	3424 k
	Shape	i-FTB	i-FTB	g-FTB	D	D	g-FB

Table D.29: Elastic buckling of 2-L8"x8"x0.625" fixed end chord segment

Mode		Ties					
		0	1	3	7	15	31
1	P_{cr}	1240 k	1241 k	1349 k	1510 k	1825 k	2399 k
	Shape	i-FTB	g-FTB	g-FTB	g-FTB	g-FTB	g-FTB
2	P_{cr}	1240 k	1350 k	1431 k	1596 k	1916 k	2505 k
	Shape	i-FTB	i-FTB	g-FTB	g-FTB	g-FTB	g-FTB
3	P_{cr}	1323 k	1365 k	1499 k	1734 k	2049 k	2626 k
	Shape	i-FTB	i-FTB	i-FTB	g-FTB	g-FTB	g-FTB
4	P_{cr}	1323 k	1391 k	1512 k	1843 k	2150 k	2701 k
	Shape	i-FTB	i-FTB	g-FTB	g-FTB	g-FTB	g-FTB
5	P_{cr}	1391 k	1391 k	1533 k	1888 k	2275 k	2774 k
	Shape	i-FTB	i-FTB	g-FB+i-FTB	i-FTB	g-FTB	g-FTB

Table D.30: Elastic buckling of 2-L8"x8"x0.546" simply supported chord segment

Mode		Ties					
		0	1	3	7	15	31
1	P_{cr}	904 k	1040 k	1208 k	1454 k	1922 k	2242 k
	Shape	g-FB+i-FTB	g-FTB	g-FTB	g-FTB	g-FTB	D
2	P_{cr}	925 k	1051 k	1344 k	1603 k	2004 k	2244 k
	Shape	g-FTB	i-FTB	i-FTB	g-FTB	g-FTB	D
3	P_{cr}	998 k	1068 k	1353 k	1756 k	2029 k	2353 k
	Shape	i-FTB	i-FTB	g-FTB	g-FTB	g-FTB	D
4	P_{cr}	998 k	1102 k	1426 k	1839 k	2064 k	2369 k
	Shape	i-FTB	i-FTB	i-FTB	D	D	D
5	P_{cr}	1104 k	1111 k	1475 k	1949 k	2150 k	2415 k
	Shape	i-FTB	i-FTB	i-FTB	D	D	D

Table D.31: Elastic buckling of 2-L8"x8"x0.546" fixed end chord segment

Mode		Ties					
		0	1	3	7	15	31
1	P_{cr}	850 k	855 k	929 k	1050 k	1303 k	1780 k
	Shape	i-FTB	g-FTB	g-FTB	g-FTB	g-FTB	g-FTB
2	P_{cr}	850 k	915 k	988 k	1113 k	1367 k	1851 k
	Shape	i-FTB	i-FTB	g-FTB	g-FTB	g-FTB	g-FTB
3	P_{cr}	895 k	922 k	1019 k	1215 k	1462 k	1928 k
	Shape	i-FTB	i-FTB	i-FTB	g-FTB	g-FTB	g-FTB
4	P_{cr}	895 k	936 k	1041 k	1295 k	1533 k	1969 k
	Shape	i-FTB	i-FTB	i-FTB	g-FTB	g-FTB	g-FTB
5	P_{cr}	936 k	936 k	1044 k	1301 k	1618 k	1998 k
	Shape	i-FTB	i-FTB	i-FTB	i-FTB	g-FTB	g-FTB

Table D.32: Elastic buckling of 2-L8"x8"x0.5" simply supported chord segment

Mode		Ties					
		0	1	3	7	15	31
1	P_{cr}	703 k	815 k	962 k	1171 k	1574 k	1749 k
	Shape	g-FB+i-FTB	i-FTB	g-FTB	g-FTB	g-FTB	D
2	P_{cr}	715 k	821 k	1052 k	1286 k	1602 k	1752 k
	Shape	g-FTB	g-FTB	i-FTB	g-FTB	D	D
3	P_{cr}	770 k	825 k	1069 k	1396 k	1602 k	1840 k
	Shape	i-FTB	i-FTB	g-FTB	g-FTB	D	D
4	P_{cr}	770 k	851 k	1117 k	1452 k	1633 k	1858 k
	Shape	i-FTB	i-FTB	i-FTB	D	D	D
5	P_{cr}	852 k	856 k	1150 k	1532 k	1691 k	1870 k
	Shape	i-FTB	i-FTB	i-FTB	D	D	D

Table D.33: Elastic buckling of 2-L8"x8"x0.5" fixed end chord segment

Mode		Ties					
		0	1	3	7	15	31
1	P_{cr}	662 k	669 k	728 k	829 k	1046 k	1467 k
	Shape	i-FTB	g-FTB	g-FTB	g-FTB	g-FTB	g-FTB
2	P_{cr}	662 k	709 k	777 k	880 k	1098 k	1521 k
	Shape	i-FTB	i-FTB	g-FTB	g-FTB	g-FTB	g-FTB
3	P_{cr}	693 k	713 k	791 k	965 k	1174 k	1574 k
	Shape	i-FTB	i-FTB	i-FTB	g-FTB	g-FTB	g-FTB
4	P_{cr}	693 k	722 k	807 k	1019 k	1231 k	1580 k
	Shape	i-FTB	i-FTB	i-FTB	i-FTB	g-FTB	D
5	P_{cr}	722 k	722 k	808 k	1030 k	1296 k	1582 k
	Shape	i-FTB	i-FTB	i-FTB	g-FTB	g-FTB	D

Table D.34: Elastic buckling of 2-L8"x8"x0.438" simply supported chord segment

Mode		Ties					
		0	1	3	7	15	31
1	P_{cr}	479 k	554 k	683 k	844 k	1112 k	1198 k
	Shape	g-FB+i-FTB	i-FTB	g-FTB	g-FTB	D	D
2	P_{cr}	485 k	558 k	726 k	923 k	1114 k	1201 k
	Shape	g-FTB	i-FTB	i-FTB	g-FTB	D	D
3	P_{cr}	520 k	574 k	740 k	986 k	1156 k	1265 k
	Shape	i-FTB	g-FTB+i-FTB	i-FTB	g-FTB	D	D
4	P_{cr}	520 k	576 k	785 k	1014 k	1157 k	1271 k
	Shape	i-FTB	i-FTB	i-FTB	D	g-FTB	D
5	P_{cr}	576 k	580 k	789 k	1064 k	1176 k	1273 k
	Shape	i-FTB	g-FTB	i-FTB	D	D	D

Table D.35: Elastic buckling of 2-L8"x8"x0.438" fixed end chord segment

Mode		Ties					
		0	1	3	7	15	31
1	P_{cr}	453 k	462 k	504 k	580 k	752 k	1091 k
	Shape	i-FTB	g-FTB	g-FTB	g-FTB	g-FTB	D
2	P_{cr}	453 k	481 k	540 k	619 k	789 k	1094 k
	Shape	i-FTB	i-FTB	i-FTB	g-FTB	g-FTB	D
3	P_{cr}	470 k	483 k	541 k	683 k	845 k	1097 k
	Shape	i-FTB	i-FTB	g-FTB	g-FTB	g-FTB	g-FTB
4	P_{cr}	470 k	488 k	547 k	705 k	885 k	1101 k
	Shape	i-FTB	i-FTB	i-FTB	i-FTB	g-FTB	g-FTB
5	P_{cr}	488 k	488 k	549 k	720 k	927 k	1108 k
	Shape	i-FTB	i-FTB	i-FTB	i-FTB	g-FTB	D

Table D.36: Elastic buckling of 2-L8"x8"x0.375" simply supported chord segment

Mode		Ties					
		0	1	3	7	15	31
1	P_{cr}	304 k	351 k	459 k	575 k	718 k	766 k
	Shape	g-FB+i-FTB	i-FTB	g-FTB	g-FTB	D	D
2	P_{cr}	307 k	353 k	468 k	624 k	718 k	768 k
	Shape	g-FTB	i-FTB	i-FTB	g-FTB	D	D
3	P_{cr}	328 k	363 k	474 k	649 k	756 k	807 k
	Shape	i-FTB	i-FTB	i-FTB	D	D	D
4	P_{cr}	328 k	364 k	505 k	661 k	758 k	808 k
	Shape	i-FTB	i-FTB	i-FTB	D	D	D
5	P_{cr}	363 k	380 k	508 k	693 k	784 k	811 k
	Shape	i-FTB	g-FTB	i-FTB	D	D	D

Table D.37: Elastic buckling of 2-L8"x8"x0.375" fixed end chord segment

Mode		Ties					
		0	1	3	7	15	31
1	P_{cr}	288 k	299 k	328 k	382 k	510 k	702 k
	Shape	i-FTB	g-FTB	g-FTB	g-FTB	g-FTB	D
2	P_{cr}	288 k	305 k	343 k	411 k	536 k	704 k
	Shape	i-FTB	i-FTB	i-FTB	g-FTB	g-FTB	D
3	P_{cr}	297 k	305 k	346 k	455 k	574 k	709 k
	Shape	i-FTB	i-FTB	i-FTB	i-FTB	g-FTB	D
4	P_{cr}	297 k	308 k	349 k	458 k	601 k	714 k
	Shape	i-FTB	i-FTB	i-FTB	g-FTB	g-FTB	D
5	P_{cr}	308 k	308 k	350 k	463 k	626 k	721 k
	Shape	i-FTB	i-FTB	i-FTB	i-FTB	g-FTB	D

D.2. Inelastic Buckling Behavior of Double Angle Chord Segments

The following tables summarize the inelastic buckling loads that were observed for the different members. Each finite element model was evaluated in a Riks inelastic analysis with an imperfection of $L/1000$ using the first elastic buckling mode. As the angles acted independently in the fixed end model with 0 ties, the second elastic buckling mode was also included in these models to apply the same imperfection in both angles. If the symmetry of the imperfection lead to solver issues, a small (0.0001") imperfection of the next buckling mode was incorporated. Lastly, it was found that some inelastic buckling results were greater than the results of the same chord size with additional ties. In an attempt to verify this was a result of the chosen methodology for initial imperfection, an alternative elastic buckling mode was considered and the resulting reduced buckling capacities are noted in the footnotes. This was of greater concern with the fixed end chord buckling as the initial buckling modes exhibited less local behavior.

Table D.38: Inelastic buckling load of simply supported chords for Group 1

Cross Section	Axial buckling load (kip) for (#) ties					
	0	1	3	7	15	23
2-L2"x2"x0.125"	26.2	34.4	36.4	36.9	36.9	36.9
2-L2"x2"x0.115"	23.0	31.0	33.3	34.1	34.1	34.1
2-L2"x2"x0.109"	21.0	28.8 [1]	25.3	32.4	32.4	32.4
2-L2"x2"x0.094"	16.3	20.8 [2]	18.3	19.6	28.0	28.0
2-L1.75"x1.75"x0.125"	19.3	25.0	26.3	26.7	26.7	26.7
2-L1.75"x1.75"x0.115"	17.3	22.8	24.3	24.7	24.7	24.7
2-L1.75"x1.75'x0.109"	16.1	21.5	23.0	23.5	23.5	23.5

* Evaluations with different elastic buckling mode resulted in reduced buckling load

[1] Mode 2 = 25.7 k

[2] Mode 4 = 18.5 k

Table D.39: Inelastic buckling load of fixed end chords for Group 1

Cross Section	Axial buckling load (kip) for (#) ties					
	0	1	3	7	15	23
2-L2"x2"x0.125"	17.4	31.4	36.7 [1]	35.6	36.2	44.6
2-L2"x2"x0.115"	16.1	25.9	30.8 [2]	30.7	33.4	41.1
2-L2"x2"x0.109"	15.3	22.8	27.3	26.6	31.6	31.8
2-L2"x2"x0.094"	12.6	16.0	19.2	21.5	23.4	27.4
2-L1.75"x1.75"x0.125"	11.7	21.3	25.5	26.1	26.3	26.4
2-L1.75"x1.75"x0.115"	10.8	19.7	23.3	24.1	24.4	24.4
2-L1.75"x1.75'x0.109"	10.3	21.5	22.0	22.9	23.2	23.2

* Evaluations with different elastic buckling mode resulted in reduced buckling load

[1] Mode 4 = 35.6 k

[2] Mode 3 = 29.8 k

Table D.40: Inelastic buckling load of simply supported chords for Group 2

Cross Section	Axial buckling load (kip) for (#) ties					
	0	1	3	7	15	31
2-L4"x4"x0.375"	272	273	271	271	271	271
2-L4"x4"x0.344"	250	253	257	250	250	250
2-L4"x4"x0.313"	226	230	232	235	228	228
2-L4"x4"x0.25"	159 [1]	156	156	184 [2]	179	178
2-L4"x4"x0.188"	85.8 [3]	82.7	87.4	115	119	121

* Evaluations with different elastic buckling mode resulted in reduced buckling load

[1] Mode 2 = 148 k

[2] Mode 4 = 179 k

[3] Mode 3 = 76.4 k

Table D.41: Inelastic buckling load of fixed end chords for Group 2

	Axial buckling load (kip) for (#) ties					
Cross Section	0	1	3	7	15	31
2-L4"x4"x0.375"	213	277	282	284	270	270
2-L4"x4"x0.344"	197	255	259	261	249	249
2-L4"x4"x0.313"	180	230	234	237 [1]	239	227
2-L4"x4"x0.25"	153	153	167	179	190 [2]	183
2-L4"x4"x0.188"	77.1 [3]	74.9	87.0	101	128	128

[*] Evaluations with different elastic buckling mode resulted in reduced buckling load
[1] Mode 4 = 227 k
[2] Mode 4 = 186 k
[3] Mode 3 & 4 = 71.7 k

Table D.42: Inelastic buckling load of simply supported chords for Group 3

	Axial buckling Load (kip) for (#) ties					
Cross Section	0	1	3	7	15	31
2-L8"x8"x0.75"	1120	1130	1130	1130	1130	1110
2-L8"x8"x0.625"	932	931	944	948	952	948
2-L8"x8"x0.546"	781	783	809	824	833 [1]	816
2-L8"x8"x0.5"	659 [2]	644	717	743	764 [3]	738
2-L8"x8"x0.438"	491 [4]	486	572	606	628	626
2-L8"x8"x0.375"	350 [5]	346	418	475	498	505

[*] Evaluations with different elastic buckling mode resulted in reduced buckling load
[1] Mode 2 = 824 k
[2] Mode 4 = 617 k
[3] Mode 3 = 742 k
[4] Mode 4 = 457 k
[4] Mode 4 = 321 k

Table D.43: Inelastic buckling load of fixed end chords for Group 3

	Axial buckling load (kip) for (#) ties					
Cross Section	0	1	3	7	15	31
2-L8"x8"x0.75"	1008	1125	1136	1139	1141	1142
2-L8"x8"x0.625"	933	935	947	952	956	959
2-L8"x8"x0.546"	774	778	803	821	834	841
2-L8"x8"x0.5"	638	638	679	718	758	771
2-L8"x8"x0.438"	462 [1]	459	499	544	625	657
2-L8"x8"x0.375"	323 [1]	319	344	389	458	517

[*] Evaluations with different elastic buckling mode resulted in reduced buckling load
[1] Mode 3 & 4 = 443 k
[2] Mode 3 & 4 = 306 k

E. Double Angle Chord Torsion Study

This Appendix summarizes the results of the torsional buckling study discussed in Section 5.4. The initial evaluation determined the torsional reaction moment required to support a consistent 0.01 rad rotation. This moment was used to determine effective torsional section properties, either an effective torsional constant, J_e, or an effective warping constant, $C_{w,e}$. The J_e was determined assuming no warping stiffness inline with the relationship shown in Eq. E.1. The $C_{w,e}$ was determined using Eq. E.2 which incorporated the theoretical torsional constant, J, and fixed warping at both end of the member [21].

$$J_e = \frac{TL}{G\theta} = \frac{TL}{11{,}154 \text{ ksi } (0.01 \text{ rad})} \tag{E.1}$$

$$\theta = \frac{Ta}{GJ}\left(tanh\frac{L}{2a}\left(cosh\frac{L}{a} - 1\right) - sinh\frac{L}{a} + \frac{L}{a}\right) \tag{E.2}$$

where

$$a = \frac{EC_{w,e}}{GJ} \tag{E.3}$$

Table E.1: Equivalent torsional stiffness of Group 1 - Joist A

Section	J (in^4) Theory	J_e (in^4) for (#) ties 0	1	3	7	15	23
2-L2"x2"x0.125"	0.00505	0.00611	0.00735	0.00966	0.0136	0.0211	0.0284
2-L2"x2"x0.115"	0.00394	0.00491	0.00607	0.00821	0.0119	0.0190	0.0257
2-L2"x2"x0.109"	0.00336	0.00428	0.00538	0.00743	0.0110	0.0177	0.0242
2-L2"x2"x0.094"	0.00215	0.00293	0.00391	0.00572	0.00895	0.0150	0.0208
2-L1.75"x1.75"x0.125"	0.00439	0.00506	0.00612	0.00826	0.0121	0.0196	0.0269
2-L1.75"x1.75"x0.115"	0.00343	0.00405	0.00504	0.00703	0.0107	0.0177	0.0245
2-L1.75"x1.75'x0.109"	0.00293	0.00352	0.00445	0.00636	0.00986	0.0166	0.0231

Table E.2: Equivalent torsional stiffness of Group 2 - Joist girder B

Section	J (in^4) Theory	J_e (in^4) for (#) ties 0	1	3	7	15	31
2-L4"x4"x0.375"	0.268	0.293	0.318	0.369	0.457	0.634	0.975
2-L4"x4"x0.344"	0.208	0.230	0.253	0.297	0.374	0.533	0.841
2-L4"x4"x0.313"	0.156	0.177	0.196	0.234	0.300	0.439	0.714
2-L4"x4"x0.25"	0.081	0.096	0.110	0.136	0.183	0.284	0.492
2-L4"x4"x0.188"	0.0343	0.0448	0.0537	0.0700	0.100	0.166	0.306

Table E.3: Equivalent torsional stiffness of Group 3 - Joist girder C

Cross Section	J (in^4) Theory	J_e (in^4) for (#) ties 0	1	3	7	15	31
2-L8"x8"x0.75"	4.29	4.61	4.87	5.37	6.21	7.74	10.41
2-L8"x8"x0.625"	2.50	2.76	2.95	3.32	3.96	5.16	7.27
2-L8"x8"x0.546"	1.68	1.88	2.03	2.33	2.85	3.84	5.63
2-L8"x8"x0.5"	1.29	1.47	1.60	1.85	2.30	3.18	4.78
2-L8"x8"x0.438"	0.87	1.01	1.11	1.31	1.67	2.40	3.75
2-L8"x8"x0.375"	0.55	0.66	0.73	0.88	1.16	1.73	2.83

Table E.4: Equivalent warping stiffness of Group 1 - Joist A

Cross Section	C_w (in^6) Theory	$C_{w,e}$ (in^6) for (#) ties 0	1	3	7	15	23
2-L2"x2"x0.125"	0.00158	0.0338	0.1107	0.274	0.563	1.116	1.651
2-L2"x2"x0.115"	0.00124	0.0344	0.1092	0.262	0.534	1.053	1.553
2-L2"x2"x0.109"	0.00106	0.0347	0.1074	0.254	0.516	1.014	1.492
2-L2"x2"x0.094"	0.00068	0.0342	0.1019	0.234	0.471	0.920	1.346
2-L1.75"x1.75"x0.125"	0.00104	0.0167	0.0776	0.227	0.511	1.059	1.600
2-L1.75"x1.75"x0.115"	0.00082	0.0178	0.0777	0.219	0.486	1.001	1.506
2-L1.75"x1.75"x0.109"	0.00070	0.0183	0.0771	0.213	0.470	0.965	1.449

Table E.5: Equivalent warping stiffness of Group 2 - Joist girder B

Cross Section	C_w (in^6) Theory	$C_{w,e}$ (in^6) for (#) ties 0	1	3	7	15	31
2-L4"x4"x0.375"	0.3247	0.649	2.311	6.964	16.38	36.46	75.60
2-L4"x4"x0.344"	0.2537	0.698	2.293	6.530	14.96	32.96	68.39
2-L4"x4"x0.313"	0.1926	0.725	2.227	5.990	13.37	29.23	60.86
2-L4"x4"x0.25"	0.1010	0.721	1.957	4.720	10.04	21.65	45.62
2-L4"x4"x0.188"	0.0437	0.645	1.567	3.390	6.822	14.40	30.59

Table E.6: Equivalent warping stiffness of Group 3 - Joist girder C

Cross Section	C_w (in^6) Theory	$C_{w,e}$ (in^6) for (#) ties 0	1	3	7	15	31
2-L8"x8"x0.75"	20.78	18.68	54.19	155.0	365.7	793.2	1570
2-L8"x8"x0.625"	12.32	18.76	50.30	134.3	305.3	648.4	1268
2-L8"x8"x0.546"	8.34	17.55	45.38	116.4	259.6	547.3	1071
2-L8"x8"x0.5"	6.47	16.57	41.75	104.5	230.9	486.7	955.9
2-L8"x8"x0.438"	4.40	14.87	36.07	87.59	190.6	402.7	799.0
2-L8"x8"x0.375"	2.79	12.90	29.97	69.58	149.4	317.4	640.9

F. Inelastic Buckling with Effective Section Properties

F.1. Model-Based Section Properties

The following is a summary of the updated design buckling provisions accounting for the increased shear stiffness, the measured C_w from finite element modeling, and a variable effective torsional length factor, 1.0 and 0.5. Additionally, the tangential buckling response without the local buckling reduction is provided for reference. All eighteen cross sections included in the finite element study are listed below.

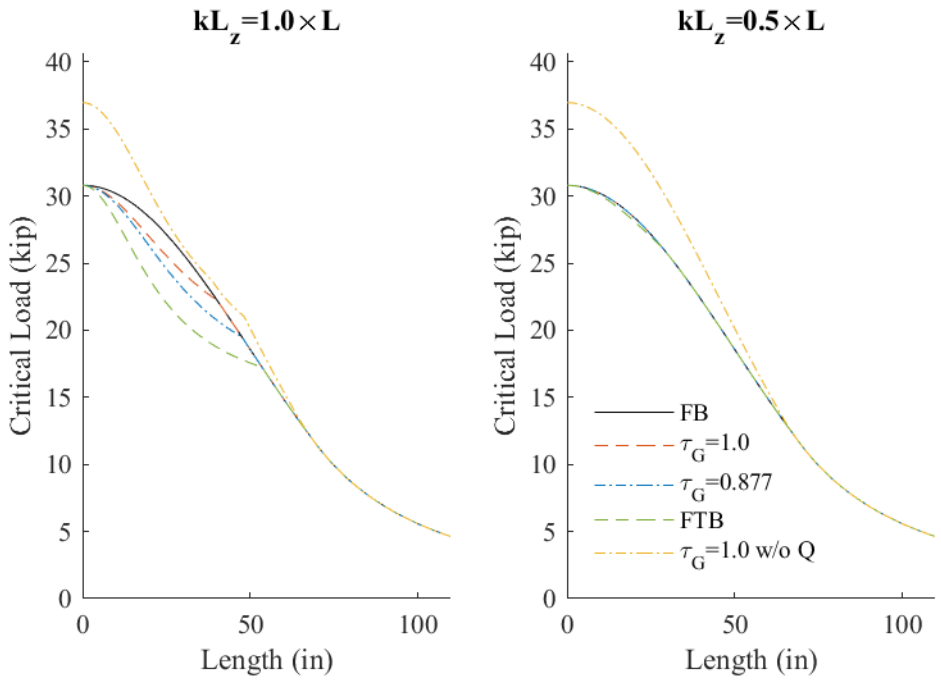

Figure F.1: Inelastic buckling of 2-L1.75"x1.75"x0.109" with measured C_w

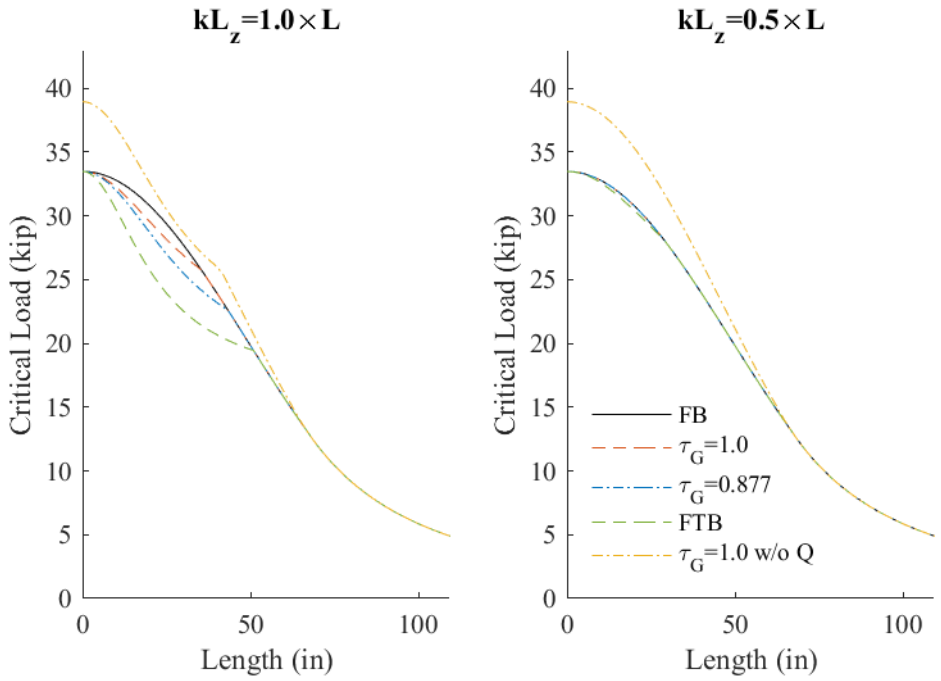

Figure F.2: Inelastic buckling of 2-L1.75"x1.75"x0.115" with measured C_w

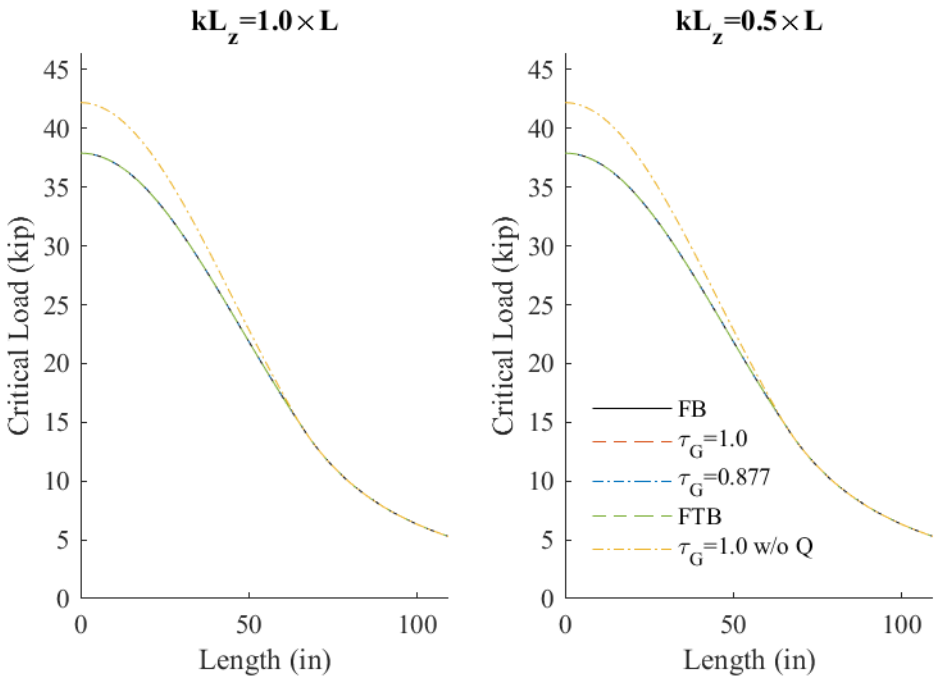

Figure F.3: Inelastic buckling of 2-L1.75"x1.75"x0.125" with measured C_w

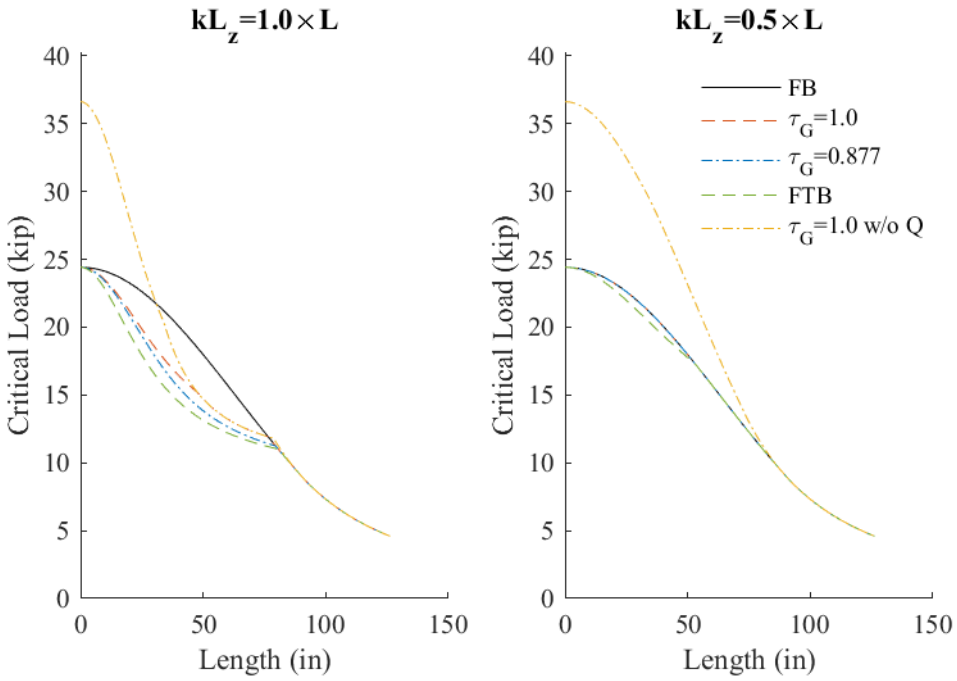

Figure F.4: Inelastic buckling of 2-L2"x2"x0.09375" with measured C_w

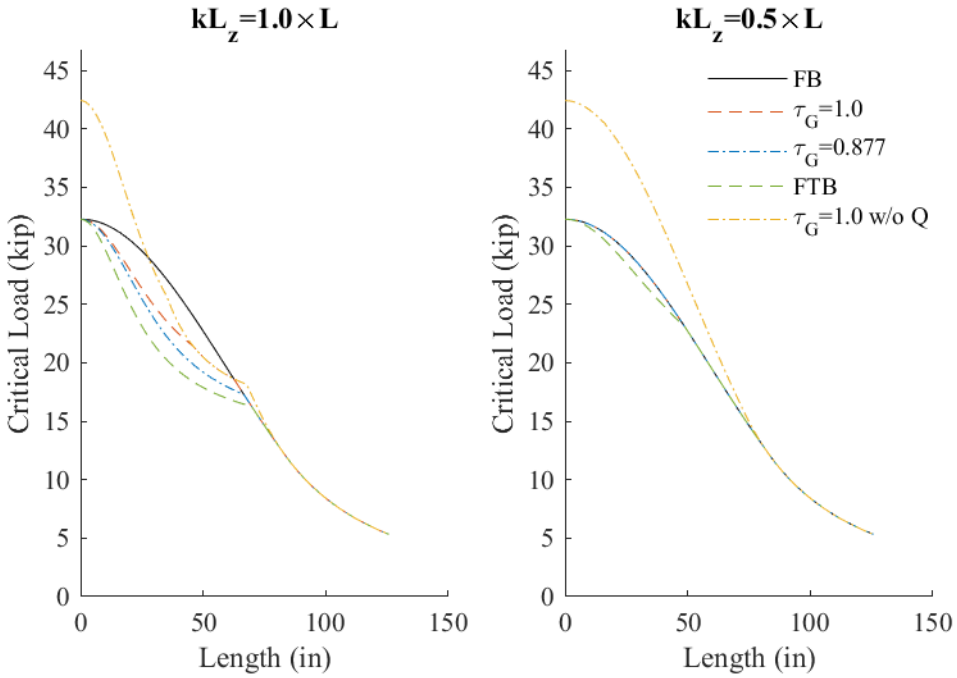

Figure F.5: Inelastic buckling of 2-L2"x2"x0.109" with measured C_w

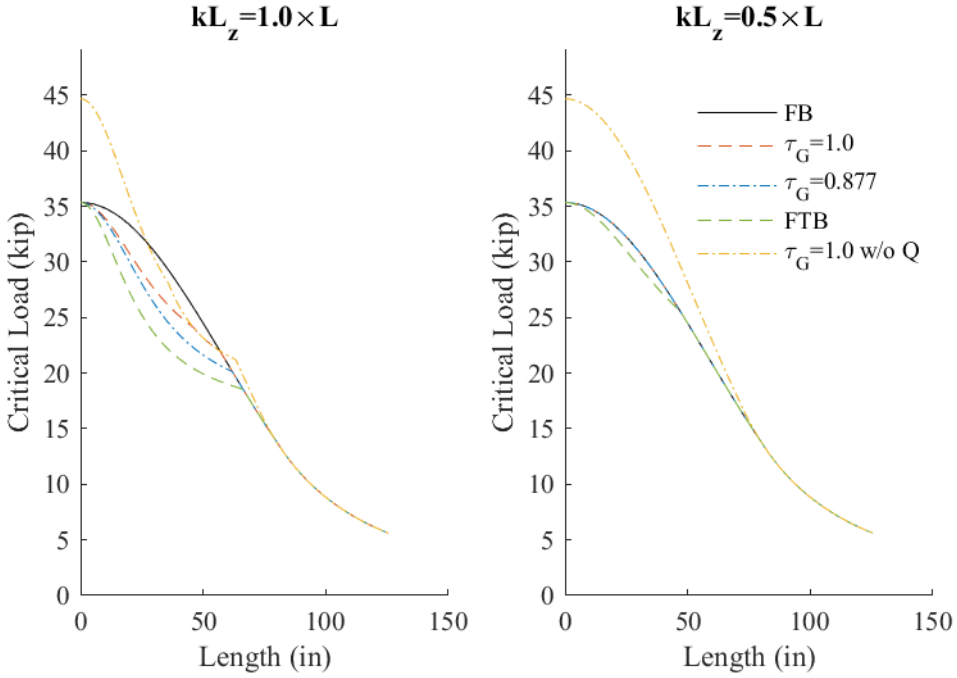

Figure F.6: Inelastic buckling of 2-L2"x2"x0.115" with measured C_w

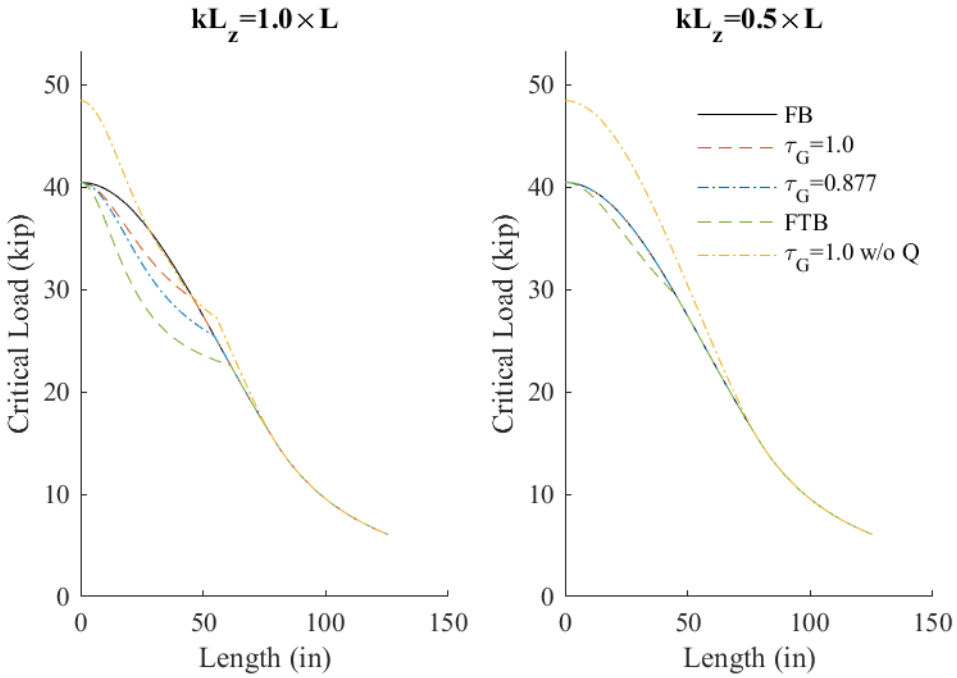

Figure F.7: Inelastic buckling of 2-L2"x2"x0.125" with measured C_w

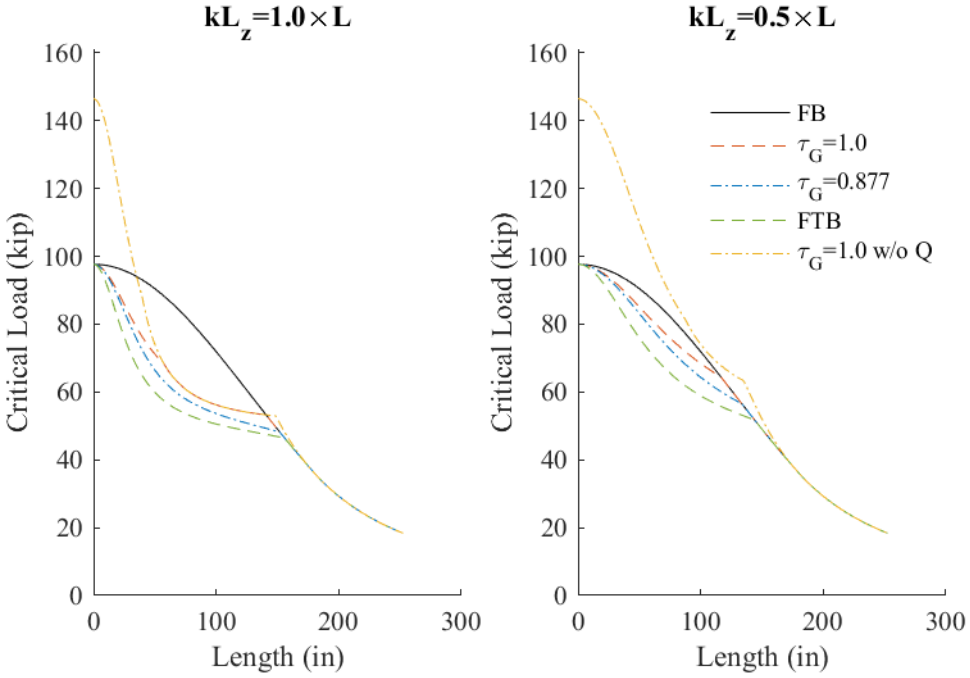

Figure F.8: Inelastic buckling of 2-L4"x4"x0.1875" with measured C_w

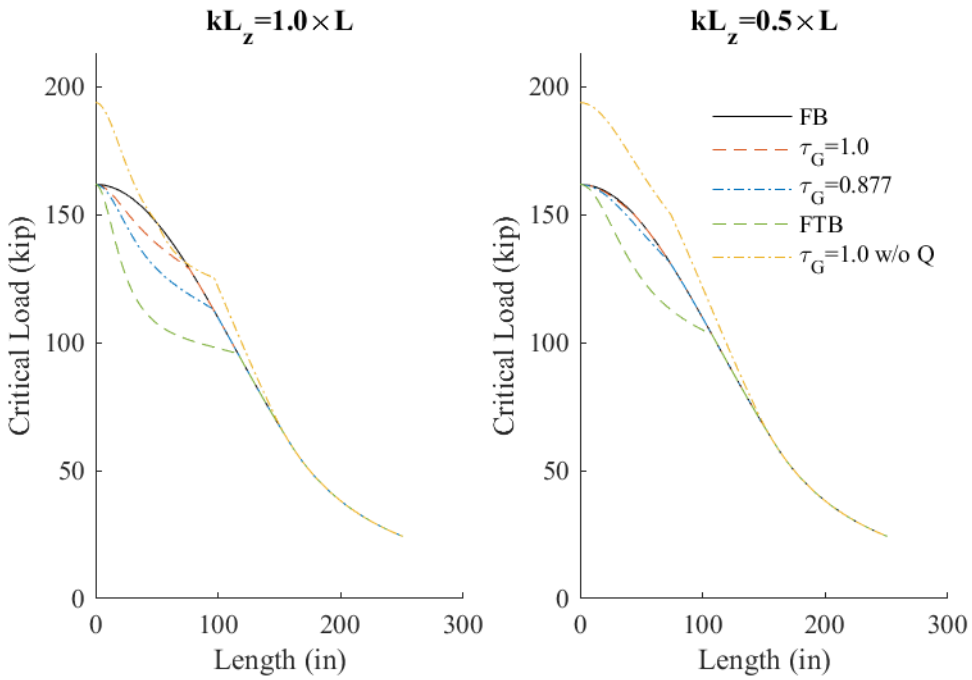

Figure F.9: Inelastic buckling of 2-L4"x4"x0.25" with measured C_w

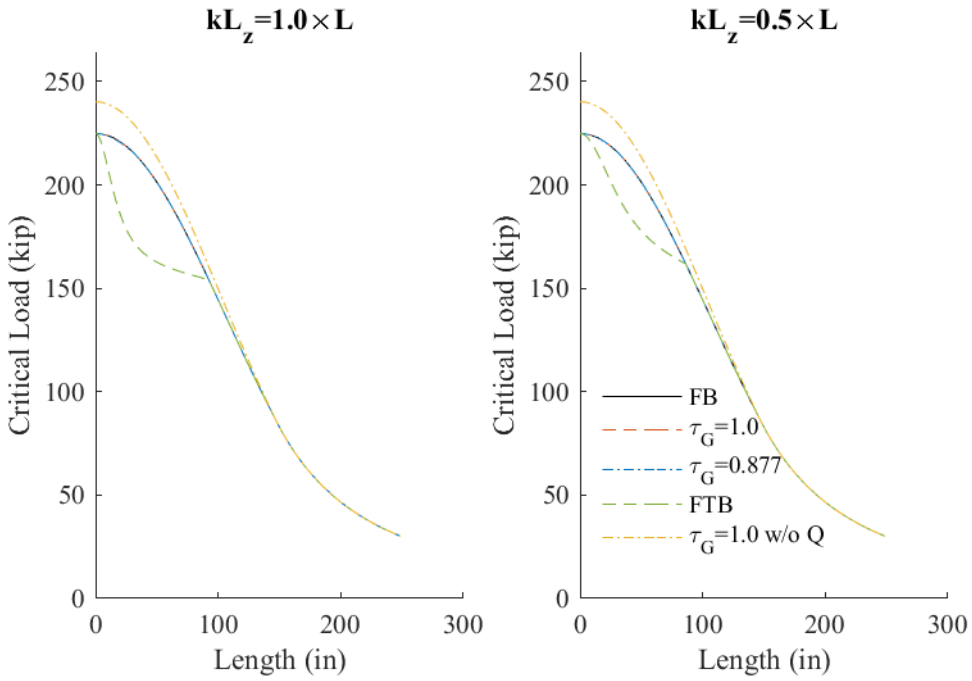

Figure F.10: Inelastic buckling of 2-L4"x4"x0.3125" with measured C_w

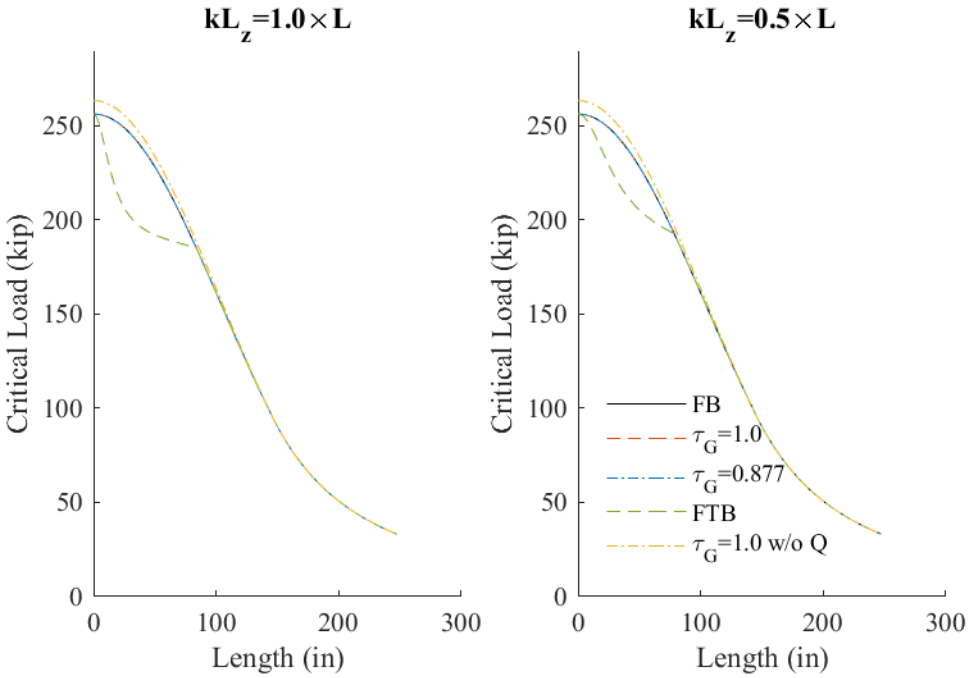

Figure F.11: Inelastic buckling of 2-L4"x4"x0.344" with measured C_w

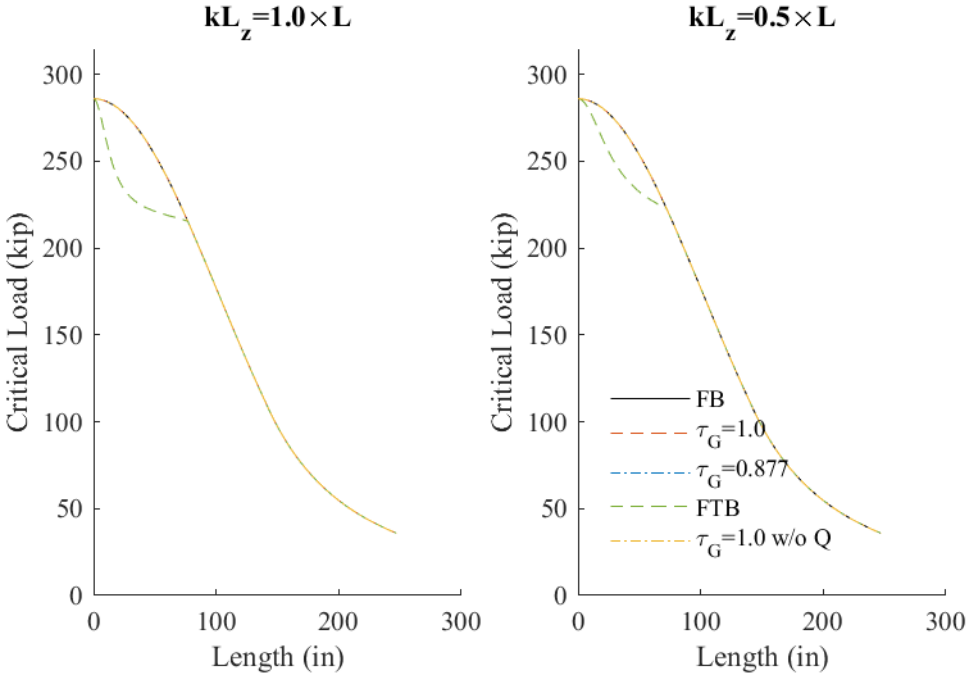

Figure F.12: Inelastic buckling of 2-L4"x4"x0.375" with measured C_w

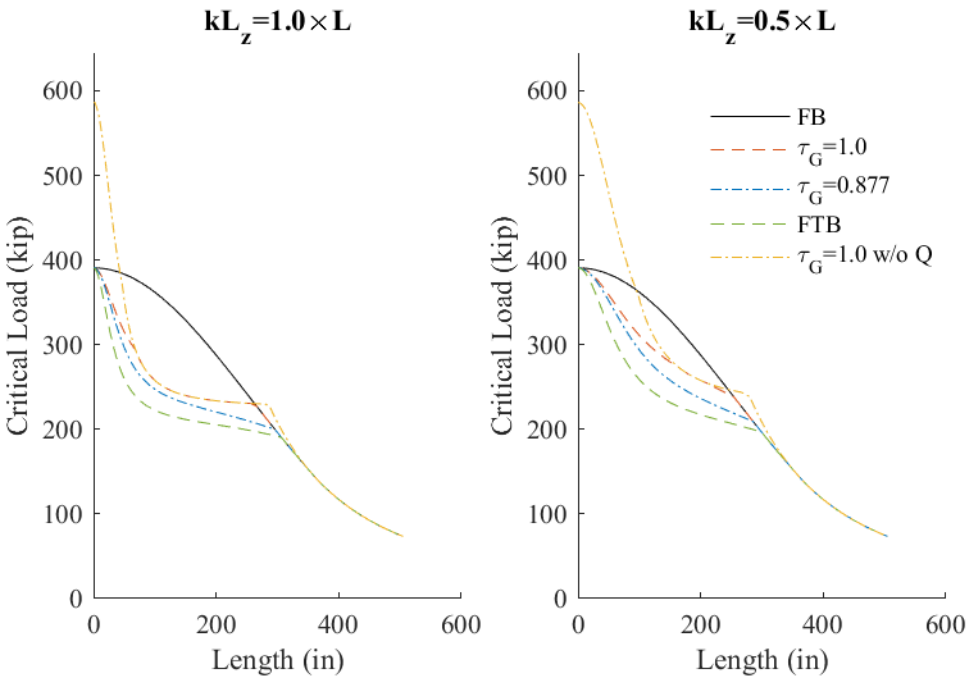

Figure F.13: Inelastic buckling of 2-L8"x8"x0.375" with measured C_w

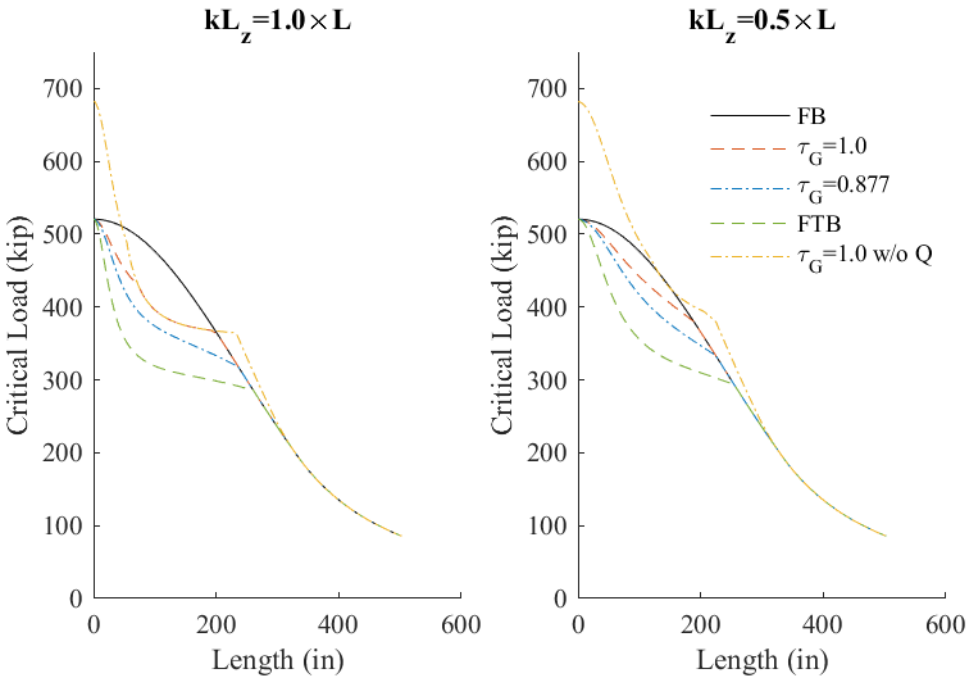

Figure F.14: Inelastic buckling of 2-L8"x8"x0.438" with measured C_w

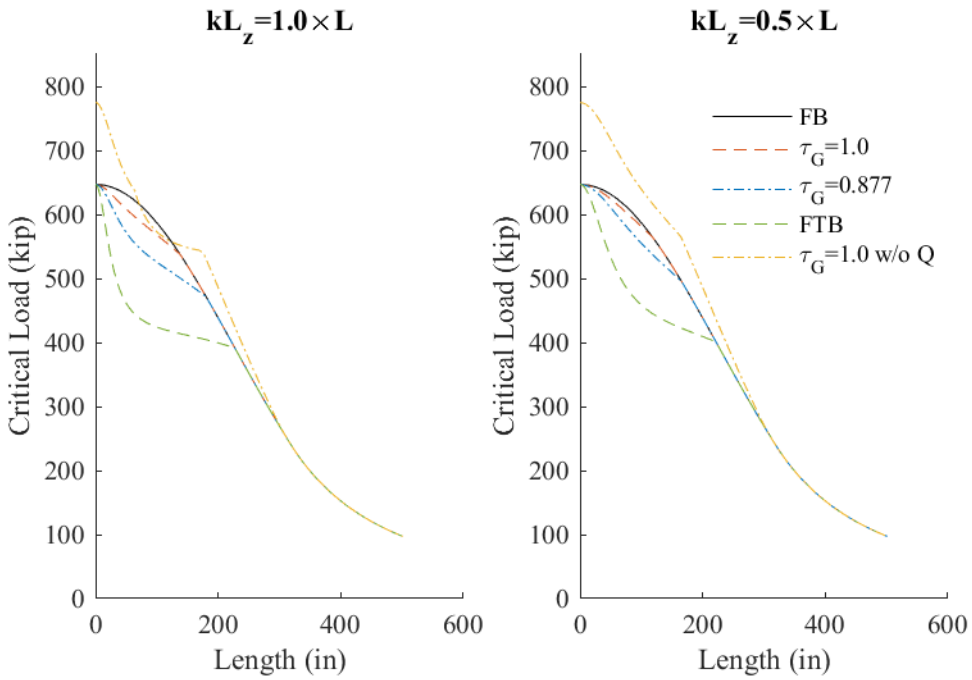

Figure F.15: Inelastic buckling of 2-L8"x8"x0.5" with measured C_w

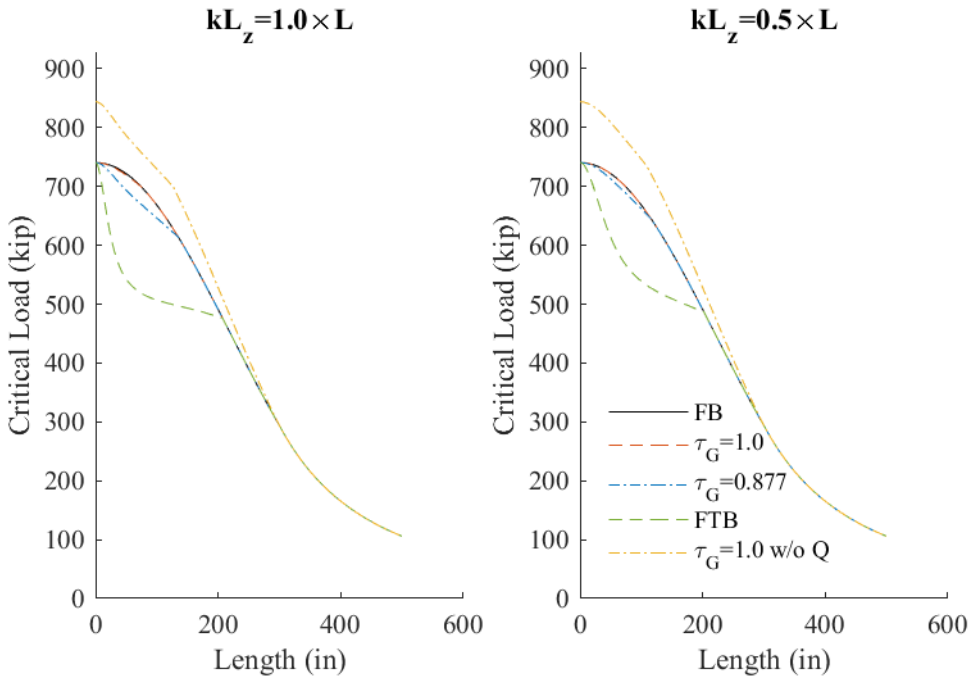

Figure F.16: Inelastic buckling of 2-L8"x8"x0.546" with measured C_w

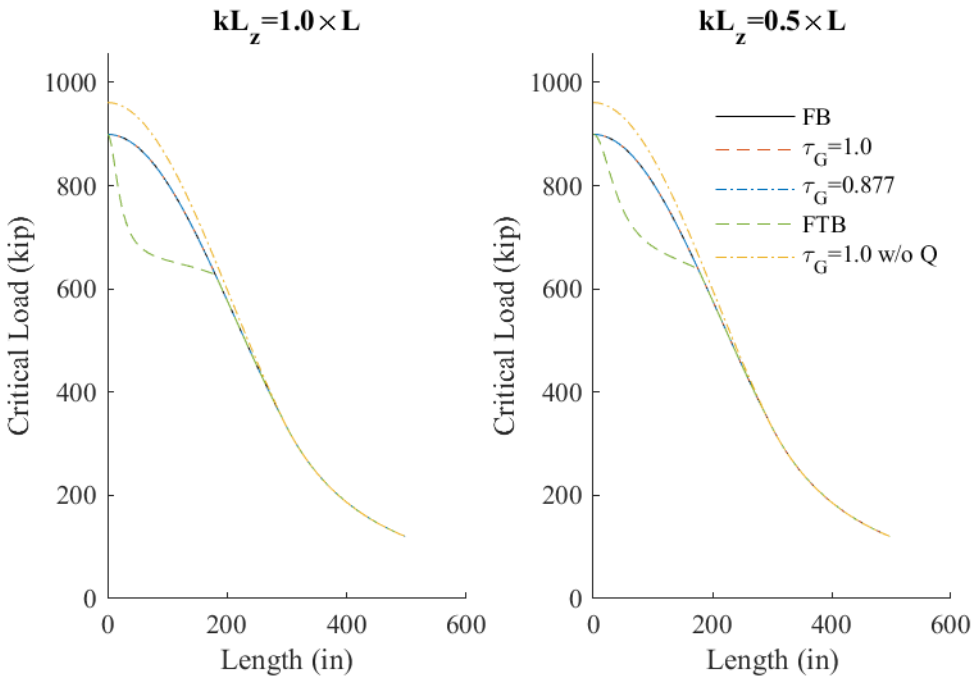

Figure F.17: Inelastic buckling of 2-L8"x8"x0.625" with measured C_w

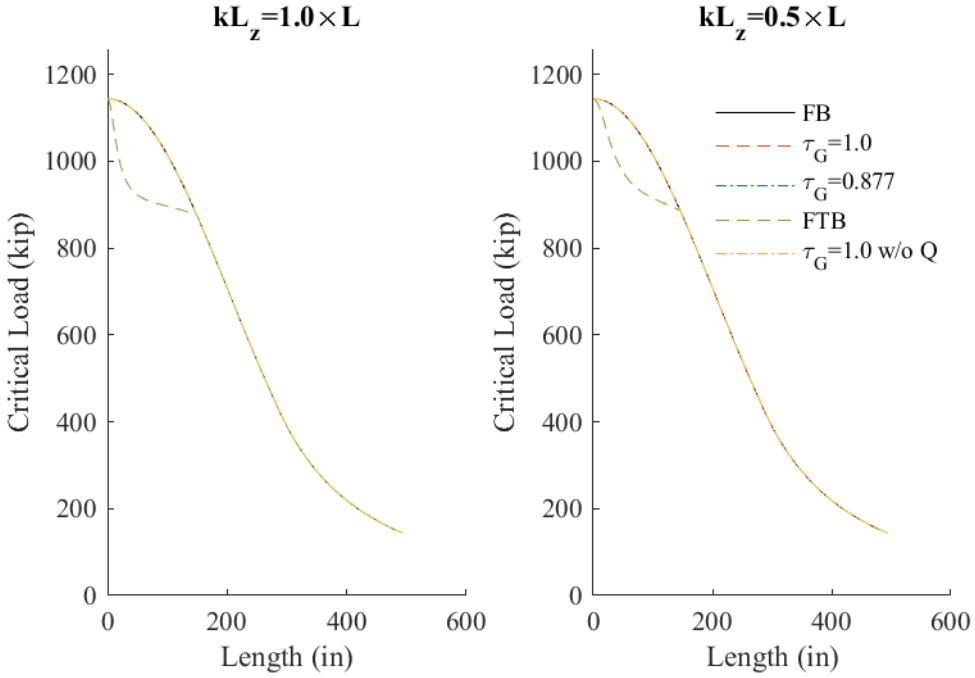

Figure F.18: Inelastic buckling of 2-L8"x8"x0.75" with measured C_w

F.2. Approximated Section Properties

The following is a summary of the updated design buckling provisions accounting for the increased shear stiffness, an approximate composite C_w, and an effective torsional length factor of 0.7 to account for fixed warping boundary conditions. The evaluation was completed for all double angle sections listed in Table 2.1. The composite C_w was taken as 70% of the "High C_w" from Appendix A based on the average of the C_w calculated using finite element analysis. The majority of the cross sections were observed be now be controlled by flexural buckling. Only results where the $\tau_G = 1$ or $\tau_G = 0.877$ buckling results were not equal to the flexural buckling mode are provided.

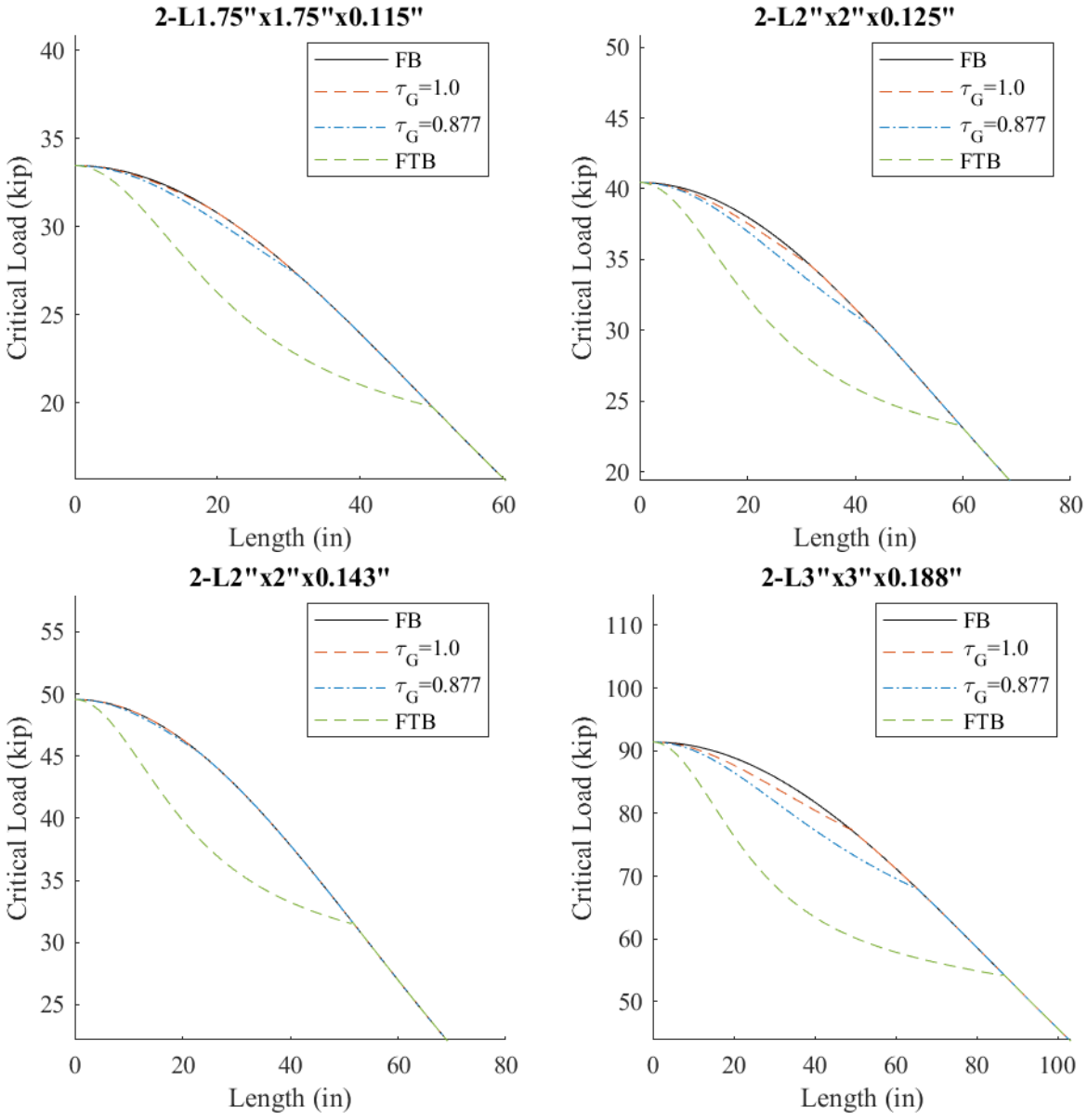

Figure F.19: Inelastic buckling of smaller angles with estimated C_w

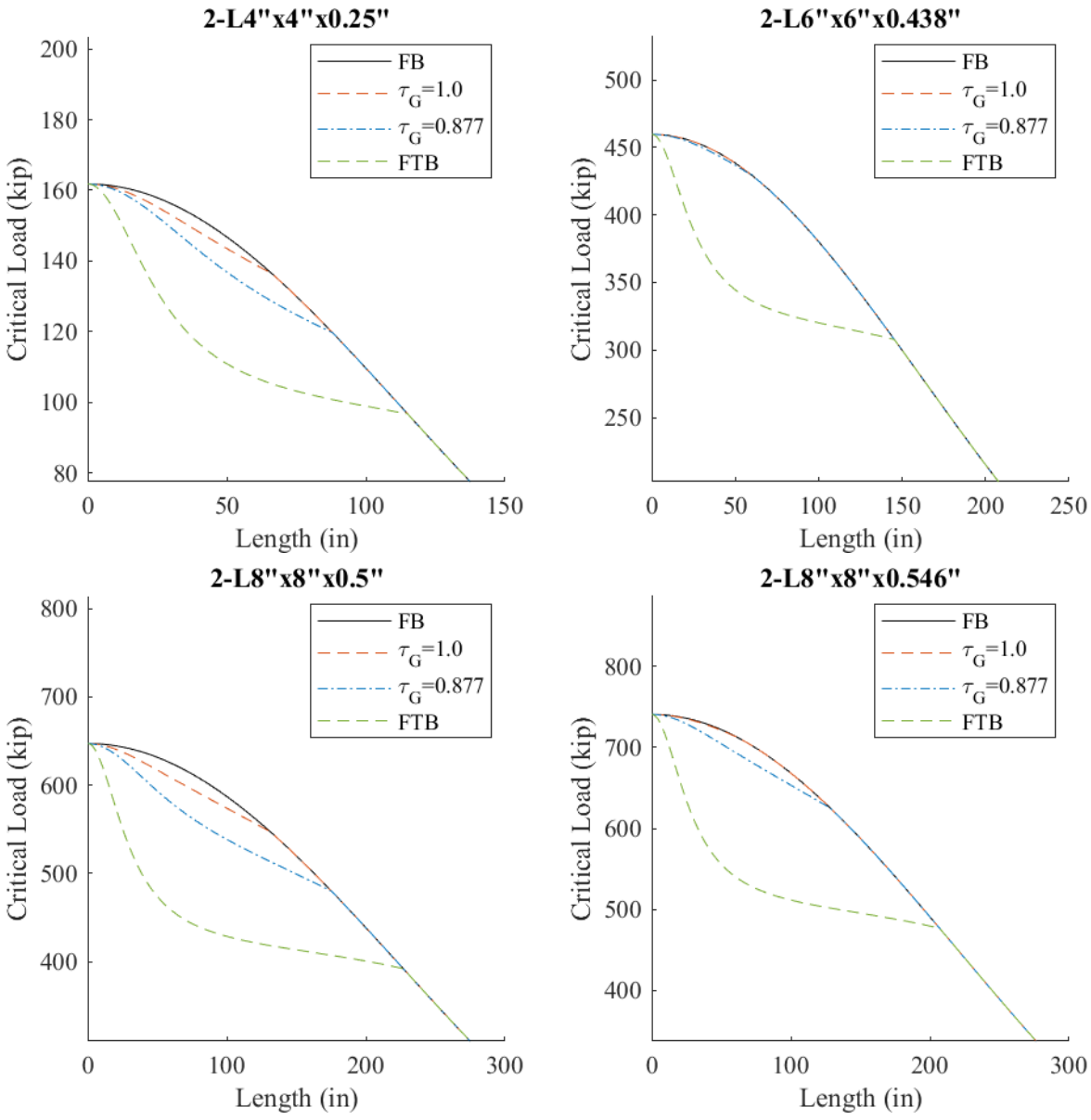

Figure F.20: Inelastic buckling of larger angles with estimated C_w